The constitution, microstructure and mechanical properties of some experimental cast nickel superalloys

- by -

JAMES EDWARD RESTALL

A dissertation submitted in partial fulfilment of the requirements for the degree of Doctor of Philosophy

The Faculty of Engineering
University of London

Acknowledgements

Apart from the brief account of introductory work in this programme already published in References 17, 18 and 71, the information contained in this Thesis is for the most part new and embodies the results of the author's own research and observations. Most of the experimental work on optical- and electron-metallography was initially done by the author, although some routine assistance was provided by his colleague Mr. E. C. Toulson, who worked under the author's instruction. Specialist services for chemical analysis and X-ray diffraction analysis were provided. Some of the X-ray films were provided for the author to calculate separately the lattice parameters of some phases. In addition a consultant statistician developed the linear regression equations quoted in this work.

The author wishes to express appreciation for the assistance of the following:

The Director of The National Gas Turbine Establishment, for the use of the laboratory facilities which made this study possible.

My Director of Studies at Imperial College, Dr. D. R. F. West, for his continued encouragement and stimulating discussions throughout this study.

My Supervisor, Dr. R. J. E. Glenny, Head of Materials Department, Royal Aircraft Establishment, for his helpful consultations throughout the programme of work.

Dr. M. G. Cockcroft, Head of Materials Science Department, National Gas Turbine Establishment, for encouragement and constructive advice.

Mr. E. C. Toulson of the National Gas Turbine Establishment, for performing some of the routine practical work, which included preparation of materials for metallographic examination, separately checking electron microprobe analysis data and carrying out specified heat-treatments of materials.

Mr. R. Freeman, Fulmer Research Institute Ltd., and Mr. D. Clark, Royal Aircraft Establishment, for their X-ray diffraction analyses.

Mr. W. R. Nall, Ministry of Defence, Bragg Laboratory, and Mr. D. Nicholas, Fulmer Research Institute Ltd., for supplying the chemical analysis data.

Dr. V. Ramaswamy, for assistance in operating the EM7 electron microscope at Imperial College.

Mr. J. H. Cadwell, Mathematical Services Department, Royal Aircraft Establishment, for processing the linear regression equations.

Finally, my Wife, for her constant support and encouragement during these five years of study.

CONTENTS

		Page
Acknowledgements		1
Synopsis		10
Chapter 1	Introduction	11
Chapter 2	Review of the literature	14
	Constituents of nickel superalloys	15
	The matrix phase	16
	The gamma-prime phase	17
	Minor element additions	19
	The carbides	20
	Topologically close packed phases	23
	Prediction and control of sigma phase formation in nickel superalloys	25
Chapter 3	Constitution and microstructure of experimental materials	31
	Materials and experimental procedures	
	Melting and casting procedures	33
	Preparation for metallographic and other examinations	33
	Results	
	General metallographic features of the alloys	34
	Chemical and electron microprobe analyses	36
	X-ray examinations	39
	Electron microscopy	40
	Discussion	
	General observations on the materials	41
	Distribution of elements	42
	Correlation of X-ray diffraction and other analyses	45
	Electron microscope investigations	47
	Phacomp relationships	50
	Conclusions	53
Chapter 4	Mechanical properties and microstructure	56
	Materials and experimental procedures	56
	Mechanical testing	56
	Metallographic and other observations	57
	Results	58
	Differential thermal analysis	59
	Hardness tests	59
	Miniature Charpy impact tests	60
	Tensile test results	61
	Creep-rupture tests	61
	Metallographic observations after creep and tensile testing	64
	Electron microprobe analysis	67

CONTENTS (cont'd)

		Page
	Discussion of results	68
	Mechanical properties	69
	Conclusions	74
Chapter 5	Metallurgical observations on factors influencing the mechanical behaviour	76
	General strengthening mechanisms operating in the matrix phase	76
	Some aspects of strengthening of the gamma-prime phase	80
	Strength of $\gamma + \gamma'$ alloys (general)	82
	Alloy design for creep-resistance	89
	Deformation mechanisms observed during creep	92
	Tertiary creep and grain boundary effects	96
	Grain size effects	100
	Summary and overall conclusions	101

TABLES

No.	Title	Page
1	Typical compositions of selected commercial nickel superalloys	119
2	Chemical composition of experimental alloys	120-123
3	Details of materials used in alloy manufacture	124
4	Quantitative electron microprobe analysis data for the dendrite, gamma, eutectic gamma-prime and MC carbides compared with the alloy compositions (as-cast)	125-129
5	Comparative analyses of gamma-prime phases in nickel alloys (as-cast)	130-133
6	Composition of gamma phasesin nickel alloys (as-cast and heat-treated)	134-136
7	Analyses of eutectic gamma-prime and MC carbides in nickel alloys (as-cast and heat-treated)	137-140
8	Measured and calculated lattice parameters of phases in nickel alloys (as-cast)	141-144
9	X-ray diffraction (lattice parameter) data for phases in as-cast and heat-treated alloys	145-148
10	Comparison of measured and calculated densities of cast alloys	149-150
11	Linear regression equations for constitution of gamma matrices, eutectic gamma-prime and mono-carbide phases in relation to the parent alloy composition (as-cast)	151
12	Mean electron vacancy number of alloys	152-153
13	Results of gamma-prime solvus temperature measurement by differential thermal analysis	154
14	Vickers hardness data (30 kg) for alloys (i) as-cast (ii) heat-treated 2000 hours at 850°C and (iii) heat-treated 200 hours at 1050°C	155-156
15	Miniature Charpy impact test results (ft lbf)	157-158
16	Tensile test data for experimental cast superalloys	159

TABLES (cont'd)

No.	Title	Page
17	Creep-rupture properties of conventionally-cast experimental alloys	160-167
18	Linear regression equations for creep-rupture tests on conventionally-cast alloys at 850°C, 1000°C and 1040°C	168-170
19	Creep-rupture properties of conventionally-cast and UDS alloys	171-172
20	Typical creep-rupture properties of selected experimental alloys in comparison to some commercial superalloys (IN100 and MarM246) tested at NGTE	173-174
21	Temperature, °C, to produce rupture in 100 hours at given stress level for conventionally-cast and UDS alloys	175

ILLUSTRATIONS

Fig. No.	Title	Page
1	Typical optical micrographs of the structure of the experimental superalloys (as-cast)	176
2	Electron micrographs (replicas) showing typical 'as-cast' structures	177
3	The nickel-chromium-aluminium phase diagram Isothermal sections for 750°C, 850°C and 1150°C	178
4	Ni_3Al solid solution field at approximately 2100°F (1150°C) for various ternary alloys	179
5	PHACOMP prediction of matrix compositions of U700 and IN713C in the Ni-Co-Cr and Ni-Cr-Mo systems	180
6	Typical mould assemblies of (a) conventionally-cast (b) unidirectionally solidified alloys	181
7	Optical microstructures of Nimonic 115 alloy blade and MarM246 alloy creep testpiece	182
8	Typical structures of as-cast alloys from transmission electron microscopy (1 MeV)	183
9	Typical thin foil microstructures of as-cast alloys using 100 KeV electron microscope	184
10	Typical electron micrographs of the structures of experimental alloys after heat-treatment for 2000 hours at 850°C	185
11	Typical electron micrographs showing the micro-structure of the Nimonic 115 alloy blade (100 KeV)	186
12	Nimonic 115 alloy blade structure (thin foil) using 1 MeV microscope	187
13	Thin foil microstructure of MarM246 alloy testpiece, water-quenched after 200 hours exposure at 1050°C	188
14	Electron micrographs of MarM246 alloy single crystal after creep/rupture testing at 1050°C	189
15	Schematic differential thermal analysis of a cast nickel superalloy	190
16	VPN data versus lattice constant mismatch ($\gamma - \gamma'$) Å for individual alloys	191

ILLUSTRATIONS (cont'd)

Fig. No.	Title	Page
17	Typical creep-rupture curves at 30 tsi/850°C	192
18	Typical creep-rupture curves at 10 tsi/1000°C	193
19	Typical creep-rupture curves at 7 tsi/1040°C	194
20	Relationship between times to 0.5%, 1% creep strain and time to produce rupture versus γ' solvus temperature at 30 tsi/850°C	195
21	Relationship between times to 0.5%, 1% creep strain and time to produce rupture versus γ' solvus temperature at 10 tsi/1000°C	196
22	Relationship between times to 0.5%, 1% creep strain and time to produce rupture versus γ' solvus temperature at 7 tsi/1040°C	197
23	Relationship between time to produce 0.5%, 1% creep strain and rupture at 850°C versus 'as-cast' hardness	198
24	Relationship between time to produce 0.5%, 1% creep strain and rupture at 1000°C versus 'as-cast' hardness	199
25	Relationship between time to produce 0.5%, 1% creep strain and rupture at 1040°C versus 'as-cast' hardness	200
26	Typical optical micrographs showing microcracks in conventionally-cast alloys after creep-rupture testing at 30 tsi/850°C	201
27	Typical optical micrographs showing microcracks in conventionally-cast alloys after creep-rupture testing at 10 tsi/1000°C	202
28	Typical optical micrographs showing microcracks in conventionally-cast alloys after creep-rupture testing at 7 tsi/1040°C	203
29	Thin foil microstructures of R8 alloy (a) deformed 0.2% and (b) fractured in tensile tests at room temperature	204
30	Thin foil microstructures of R6 alloy fractured in a tensile test at 750°C	205

ILLUSTRATIONS (cont'd)

Fig. No.	Title	Page
31	Thin foil microstructures of R6 alloy fractured after creep testing at 760°C	206
32	Thin foil microstructures of R8 alloy fractured in a creep-rupture test at 760°C	207
33	Thin foil microstructures of W36 alloy creep-rupture tested at 850°C	208
34	Thin foil microstructures of R8 alloy deformed 0.3% in a creep test at 1000°C	209
35	Thin foil microstructures of R6 alloy creep tested at 1040°C	210
36	Thin foil microstructures of MarM246 alloy single crystal creep-rupture tested at 1040°C (longitudinal section)	211
37	Typical grain boundary regions of MarM246 alloy after 200 h heat-treatment at 1050°C	212
38	Typical appearance of dendritic region of W44 alloy creep-rupture tested at 1000°C as revealed by EPMA	213
39	(a) Section through Ni-Cr-Al ternary at 75 a/o Ni illustrating alloys investigated[110].	214
	(b) and (c) Effects of v/o γ' and temperature on flow stress	215

The constitution, microstructure and mechanical properties of some experimental nickel cast superalloys

Synopsis

A series of experimental nickel base casting alloys has been studied to explore the relationship between constitution, microstructure and selected mechanical properties. The programme involved a study of phase equilibria, creep-rupture strengths, and tensile and impact properties of some experimental variants of a model heat-resistant alloy which had been proved to be too heavy for use as turbine blading. Lighter alloys were devised by substituting equi-atomic percentages of titanium and niobium for tantalum, and molybdenum for tungsten in the parent material.

In the first stage of the work the way in which the elements partitioned between the principal phases, matrix, gamma-prime, and MC-carbides, was studied for each alloy in the as-cast condition and after heat-treatments. Good correlations were obtained for the compositions of the gamma-prime phases derived from electron microprobe analysis, spectrographic and other chemical techniques. Relationships between phase composition and lattice constants measured by X-ray diffraction were explored. Structural examination of the alloys showed that they were not susceptible to the precipitation of undesirable embrittling phases during thermal exposure. Comparison was made with commercial alloys withdrawn from service. The implications regarding the PHACOMP predictions of instability were tentatively explored.

The second phase of work was principally concerned with the measurement of mechanical properties. Comparison information was obtained on commercially available alloys. Several experimental alloys were identified which exhibited good creep-rupture properties, combined with useful levels of toughness and microstructural stability.

Finally, metallurgical observations were made on the factors influencing the strengths of the individual phases, and how the constituent elements affected the alloy characteristics as a whole. Microstructural changes induced by tensile and creep deformation were in accord with observations made in the literature. The major parameters which correlated with the creep-rupture properties were the solvus temperature of the gamma-prime precipitate and the 'as-cast' hardness.

CHAPTER 1

Introduction

During the evolution of the gas turbine engine successive generations of nickel- and cobalt-base high temperature alloys, hereafter referred to as superalloys, have been developed to meet the stringent property requirements of components used in the hot parts of the engine. These developments are described in more detail in References 1 to 10. Today's advanced cast nickel superalloys offer approximately 300°C improvement in short-time (100 h) creep-rupture strength over that of the simple nickel-chromium superalloys of 30 years ago. Coupled with the strength benefits are the advances in foundry technology that have enabled cast turbine blades containing a variety of cooling channels to be produced. This has maintained their viability as major engine structural materials in face of competition from more refractory metallic and ceramic materials. Despite their successful record of performance in service to date there is a need for further improving the high temperature capability of superalloys to match the operating requirements and permit improved performance of advanced engines. It should be realised that comparatively small gains in creep performance are effectively doubled when the benefits of blade cooling are taken into account, thus 10°C improvement in creep-rupture strength will permit an increase of approximately 20°C in turbine entry temperature.

Even though superalloy components have survived for times approaching 50,000 h in some engines, there have been problems of deterioration in mechanical properties and premature failure in service which can be attributed to unanticipated changes occurring in the microstructure. Instability in nickel-base alloys has to be avoided because of the danger of precipitation of topologically close-packed (tcp) phases, such as sigma, or others such as the μ-phase of closely related structure[11]. These phases, based on transition element intermetallic compounds, are hard and brittle and generally adopt a plate-like morphology which provides easy paths for crack propagation. This type of precipitation is also disadvantageous because it depletes the matrix of important alloying elements such as cobalt, chromium, molybdenum and tungsten which are needed for strengthening, oxidation resistance etc[12]. The formation of eta carbide (M_6C) phases in the microstructure should also be avoided as it

involves the wastage of comparatively expensive and dense refractory metal elements such as molybdenum and tungsten. Fortunately a computer calculation technique known as PHACOMP[12] has been developed which predicts the susceptibility of an austenitic alloy to precipitate intermetallic compounds usually identified as tcp phases. The development of the PHACOMP procedure is discussed in more detail in Chapter 2. The basic concept of PHACOMP is that the undesirable phases σ, μ, R, X and also Laves forming in the superalloys are electron compounds, or as in the case of Laves phases electron bonding plays a strong role. Because such phases are characterised by a narrow range of electron-atom ratio, their formation can be predicted if the composition of the solid solution generating the compound can be determined. Certain guidelines have been laid down concerning the order in which the phases are precipitated and their composition to facilitate calculation of a cut-off electron vacancy number ($\bar{N}v$) representing the critical margin between safe (free of tcp phases) and 'unsafe' alloys which precipitate these phases. The electron vacancy number, Nv, of an element represents the number of electron 'holes' in the third subshell of transition metal elements. After success with initial work on alloys* such as Udimet 700 and René 100 for which a critical $\bar{N}v$ at or near 2.5 was established many investigators assumed that this was a "universal electron vacancy number" applicable to all superalloys regardless of assumed metallurgical reactions. When it was found that some nickel superalloys deviated markedly from the norm, some forming sigma phase at $\bar{N}v$ values significantly less than the previously accepted 'safe' values, conversely others having an unsafe $\bar{N}v$ but not forming sigma phase, changes were made in the assignment of vacancy numbers of individual elements in the alloy matrices in order to get them to conform to the unique $\bar{N}v$ of about 2.5 (References 5, 6, 13 to 16). PHACOMP still represents the best available means for predicting the propensity of an alloy composition to precipitate tcp phases in the microstructure, however discrepancies have arisen through insufficient knowledge of the partitioning of elements between the phases in the microstructure, irregularity in the movement of phase boundaries (e.g. $\gamma/\gamma + \sigma$) with time and temperature, and differences in opinion as to the electron vacancy numbers assigned to individual elements.

---

* The compositions of selected commercial superalloys are given in Table 1

As an introduction to the work described in this Thesis preliminary studies on superalloys were personally conducted, the results of which are discussed in the two already published papers (References 17 and 18 - see also appended copies).

The work in this Thesis was devised to study the constitution, microstructure and mechanical properties of selected commercial and experimental nickel cast superalloys from which it was hoped to develop new materials with better specific strength (strength/density) and improved structural stability during long term exposure at high temperatures. In attempting to optimise the composition of experimental alloys attention was given to retention of microstructural stability coupled with a reduction in specific gravity. The first part of this programme was designed to provide information on how different metallic elements alloy with the three principal phases found in a range of experimental casting alloys. These alloys were prepared by systematically replacing, in part or wholly, other elements for tantalum and tungsten in a creep-resistant superalloy. Such information should contribute to the basic understanding needed for rational design of nickel-base superalloys which demands that use is made of an optimal balance of lightweight, cheap elements that are of little strategic importance, whilst retaining the maximum benefit from alloying additions that promote strengthening without embrittling the materials. In addition it was hoped to obtain a better understanding of the phase equilibria pertinent to alloyed Ni_3Al (gamma-prime). This intermetallic compound is attracting interest by virtue of its strength, ductility and good oxidation resistance[19]. The first part of this study is described in Chapter 3. The second part of the programme, concerned with the measurement of some mechanical properties: impact, tensile and creep-rupture behaviour is described and discussed in Chapter 4. Finally, in Chapter 5 metallurgical observations, and pertinent evidence based on the alloy compositions and relevant physical measurements made in the experimental programme are briefly assessed against similar observations and ideas expressed in the literature on the factors governing the mechanical behaviour of polycrystalline cast superalloys.

CHAPTER 2

Review of the literature

The reader is referred to the many excellent and comprehensive reviews, in particular References 1 to 11, tracing the technological development of successive generations of nickel- and cobalt-base superalloys through the past few decades. To avoid needless repetition of these details a brief summary will be outlined of the pertinent factors relating to the development of nickel superalloys and to their current status as turbine rotor blades in advanced gas turbines. This discussion is confined to nickel superalloys as these have formed the basis for the study in the experimental programme described in the Chapters following.

Historically, the first nickel superalloy of any significance was probably Nimonic* 75 alloy, which is essentially a solid solution of chromium in nickel; it also contains dispersed MC-type carbides. Nimonic 75 alloy was developed in the UK at approximately the same time as a comparable alloy, designated Inconel, was developed in the USA. These alloys possessed a better combination of strength and oxidation resistance than did the stainless steels. The next significant step in superalloy development was the addition of titanium and aluminium to the nickel-chromium matrix to form a precipitate of the intermetallic compound Ni_3 (Al-Ti), gamma-prime. Nimonic 80 alloy introduced circa 1941 was basically an 80 w/o nickel-20 w/o chromium alloy** with the addition of 2.25 w/o titanium and 1 w/o aluminium which enhanced the creep properties relative to Nimonic 75 alloy. This development satisfied the immediate engineering demand for a material with greater creep strength at temperatures up to about 870°C combined with good oxidation resistance and the alloy was forgeable. As forging technology advanced it was capable of accommodating stronger alloys containing additions of refractory metals and increased levels of aluminium and titanium which produced larger volume fractions of gamma-prime (γ'). With these newer alloys the limits of conventional forging technology were rapidly being approached at a time when the reliability of investment castings had improved to the extent where design engineers became more ready to accept precision cast components. This stimulated further alloy development based on the use of progressively increasing additions of refractory metals and higher volume fractions of

---

* Trademark of International Nickel Ltd.

** w/o = weight percentage

gamma-prime designed to improve the high temperature creep strength. Such advanced alloys are typified by IN-738, B1900, MarM246 and IN-100; the latter two alloys are included as reference materials in the experimental programme described later. In the search for new materials continuing emphasis was given to improving the high temperature creep-rupture properties as the primary engineering requirement. Because the rate of progress in developing a more fundamental understanding of the effects of various alloying constituents on deformation mechanisms that regulate mechanical properties was slow and yielded little practical understanding, alloy development became rather empirical. The most immediate solution to the problem of improving the high temperature capability of alloys appeared to be to increase the number of alloying additions regardless of their effects on other properties of the materials. Thus the alloys steadily became more complex with respect to the microconstituents and the microstructural reactions that occurred as the true alloy phase equilibria was approached during exposure at high temperature. These efforts also led to alloys more suceptible to high temperature corrosion because in order to achieve strength improvements chromium, the element principally responsible for conferring corrosion resistance, was being replaced by the heavier refractory metal elements. With the recognition that no single property controls alloy performance and thereby engineering viability, development efforts centred around optimising strength, microstructural stability and corrosion resistance. Nevertheless today's nickel superalloys may contain a dozen or more alloying elements with each purporting to serve a specific role in controlling some aspect of behaviour. This practice has resulted in certain instances in extremely complicated microstructures which are difficult to interpret and for which the establishment of a clear correlation of structure with mechanical behaviour has been almost impossible. The need for a more basic understanding of the relationship between constitution microstructure and mechanical properties of these materials is evident if their engineering viability is to be guaranteed with any measure of confidence.

Constituents of nickel superalloys

The microstructure of as-cast nickel superalloys consists essentially of a continuous matrix phase, designated gamma solid solution, from

which is precipitated a fine, uniform dispersion of gamma-prime (Ni_3Al type compound) with inter-dendritic regions of primary MC carbide and areas of "white-etching" kidney shaped gamma-prime that result from eutectic solidification. The MC particles are present at the grain boundaries and dispersed to some extent in the dendrites. Small amounts of nitrides, borides and sulphides or other minor phases are generally in the inter-dendritic regions. These features are illustrated in the optical and electron micrographs of Figures 1 and 2. The continuous phase is the nickel solid solution (gamma) containing gamma-prime precipitate which may appear in the form of cuboids 0.2 to 0.8μm in size, or finer (tertiary gamma-prime) depending on cooling rate. The large chunky so-called eutectic gamma-prime formed from the liquid is composed of massive Ni_3Al particles separated by thin lamellae of gamma. The crystal structures of the matrix and gamma-prime phases are both face-centred cubic (fcc), their lattice parameters are very similar, and both phases have essentially identical orientation, that is, are coherent.

Decker[9], Sims[5] and others have pointed out that all superalloys exposed to high temperatures are chemically dynamic structures. Under the influence of high temperature service therefore marked transformations in the 'as-cast' microstructure would be anticipated, whereby not only the size, morphology and distribution of the three principal phases may alter, but, depending on the alloy composition a wide variety of new phases may appear in the microstructure. An appreciation of these changes may be gained from the existing state of knowledge of alloy constitution.

The matrix phase

In nickel superalloys the austenitic matrix phase, or gamma, is a solid solution of alloying elements in nickel. From phase analysis of commercial superalloys[20,21] the matrix phase, γ, is clearly capable of accommodating simultaneously a broad range of substitutional alloying elements, namely, carbon, chromium, cobalt, molybdenum, tungsten, iron, aluminium, titanium, niobium, vanadium and tantalum. From consideration of binary and ternary phase diagrams it is possible to predict the solubility of single, or a binary combination of elements in nickel, it is impossible to predict the solubility of the combination of alloying elements detected in the matrices of more complex superalloys.

One effect of these solute elements is to increase the lattice parameter of nickel, the rate of expansion per solute addition being the greatest for the refractory metal elements Nb, W and Mo and decreasing through Ti, Al, Cr to a minimum for Co[22]. Thus although the rate of hardening per solute addition has been related to the atomic diameter oversize, there is also an additional superimposed effect of these elements that can be attributed to positions in the periodical table (or Nv)[23,24]. Part of this extra effect may be the consequence of the reduction of stacking fault energy by alloying elements which would make cross-slip more difficult in the matrix phase. In binary nickel-base alloys correlations have been obtained between Nv with stacking fault energy and change in flow stress (yield stress) at room temperature per unit change in lattice constant[25,26]. These solid solution hardening effects are assumed to be additive in more complex alloys and have been shown to persist to 0.6 Tm,* above which temperature high temperature creep occurs and strengthening of nickel is diffusion dependent. Slow diffusing elements, molybdenum and tungsten, are believed to be potent hardeners per se, and as shown by Pridantsev[27] they lowered the diffusivity of titanium and chromium in a Ni-22 w/o Cr-2.8 w/o Ti-3.1 w/o Al alloy at 900°C.

The gamma-prime phase (γ')

With the exception of IN-718 alloy that is strengthened by the Ni_3Nb compound, by far the most important strengthening mechanism operating in commercial nickel superalloys is provided by the uniform precipitation of the intermetallic compound (γ') based on Ni_3Al. This gamma-prime phase occurs as a finely divided precipitate that is coherent with the matrix, both phases having a face-centred-cubic crystal structure, and their difference in lattice parameter is very slight, usually less than 0.5 per cent[28]. Ni_3Al is an ordered compound with Ni atoms occupying the cube faces and Al atoms at the cube corners; long range order is exhibited to near its melting point (1385°C). Although the nominal composition of gamma-prime is Ni_3Al, in commercial alloys this A_3B compound frequently contains numerous alloying elements that substitute for either Ni or Al atoms in the parent lattice. Studies by Taylor and Floyd[29,30] and others[31] of the phase relationships in the Ni-Cr-Al, Ni-Cr-Ti and Ni-Ti-Al system showed that Ni_3Al can dissolve appreciable quantities of Cr and Ti. It

---

*Tm = melting point K

was found that Ti could replace up to 60 per cent of the Al atoms with no change in crystal structure and only a slight increase (less than 1 per cent) in lattice parameter of the γ' (reference 32). Figure 3 illustrates the phase equilibria of the Ni-Cr-Al system that are pertinent to superalloys. The diagram has been constructed to illustrate the effects of temperature particularly with respect to the movement of the gamma-prime phase boundary. The significance of the tie lines XX will be discussed later.

Ternary phase equilibria studies of the Ni_3Al-X system were extended by Guard and Westbrook to include Co, Cu, Fe, Cr, Mo, Si, V, etc., and by others[33-35] to include elements such as Nb, Ta and W that are relevant to the experimental programme. A schematic isothermal ternary section has been constructed in Figure 4 showing the solubility of selected elements in Ni_3Al at 1150°C. Elements similar in size and electronic configuration to Ni, such as Co and Cu have a horizontal phase field and would be expected to substitute primarily for Ni. As demonstrated by a phase field running diagonally from Ni_3Al to Ni_3X, elements further along the first, second and third transition series towards Ti, Nb and Ta would be expected to substitute to a greater extent for the Al positions in the ordered structure. The Group VI elements, Cr, Mo and W with phase fields at an intermediate position may substitute randomly between the Ni and Al sites in the Ni_3Al lattice. The probability of site occupancy in the A_3B structure by different elements has been examined in detail by Guard and Westbrook, and separately by Karg, Fornwalt and Kriege[36]. Clearly the greatest uncertainties are associated with the behaviour of the Group VI elements. In ternary and more heavily alloyed form one would expect the lattice parameter, degree of ordering and melting point of Ni_3Al to be affected. In commercial superalloys the size, shape and distribution of γ' precipitate are affected by composition[37] and separately by heat treatment. These effects are complex and will be discussed in more detail later.

The work of Guard and Westbrook[31] on the mechanical behaviour (hardness) of Ni_3Al containing ternary alloying additions showed that as with terminal solid solutions, lattice strain played a major role in solid solution hardening. They noted that strain ageing, defect hardening, or

softening at high temperature, appeared to be as important as solid solution hardening. More recent ideas acknowledge the importance of lattice defects such as vacancies, dislocations, grain boundaries etc., but more importance is attached to anti-phase domain boundaries in influencing mechanical behaviour. Details of these effects are reserved for discussion in Chapter 5. In addition to solid solution and fault hardening of gamma-prime, Ham, Cooke and Purdy[38] have studied gamma-prime alloys which utilise precipitation of gamma-phase for strengthening. The latter development is an interesting example of the reversal of the normal role played by the phases in superalloys.

Minor element additions

Additions of small amounts of elements such as carbon, boron, magnesium and zirconium are made that are responsible for affecting the behaviour near grain boundaries[9]. For example, in the case of Udimet 500 alloy additions of 0.009 w/o B and 0.01 w/o Zr increased the creep life thirteen times, rupture stress approximately two-fold, elongation seven-fold and n, the stress dependence of creep, approximately four-fold at 870°C (Reference 39). The precise mechanisms by which the minor elements operate have not been established but one suggestion was that B and Zr occupy sites in grain boundaries, thereby stabilising the structure by diminishing the number of vacancies available for dislocation climb. In one superalloy controlled additions of Zr and B controlled the rate of agglomeration of $M_{23}C_6$ and gamma-prime at grain boundaries, that resulted in adjacent zones being depleted of γ' precipitate and causing intergranular microcracking at the grain boundaries transverse to the applied stress. Zirconium is occasionally detected as an MC carbide, or as a complex sulphide or sulphocarbide (the H-phase described in Reference 40). Because of the small quantity of zirconium added to the parent alloy, the solubility of residual amounts in both matrix and gamma-prime phases must be extremely restricted. In the case of boron additions the solubility limit is often exceeded and in most nickel superalloys the excess boron can be detected as a blocky grain boundary phase of the M_3B_2 type. The M radical in the M_3B_2 phase is predominantly either chromium or molybdenum, alloyed with lesser amounts of Ti, Ni and Co. Although there is no direct evidence that small amounts of boride are detrimental, the

levels of B and Zr need to be fairly strictly controlled in order to avoid undesirable grain boundary effects such as brittleness, hot-shortness etc.

The carbides

The role of carbides in superalloys is complex and opinions vary on whether they are to be tolerated or essential to influence behaviour at, or near, grain boundaries. It appears that sufficient carbon must be present during solidification to make certain that injurious trace elements such as oxygen and sulphur do not collect in the grain boundaries and produce brittle films. For example Boesch[41] found that when carbon was completely removed from a wrought nickel superalloy the ductility dropped to zero and the rupture strength was markedly reduced. When the carbon level is low (<0.02 w/o) cast alloys are often susceptible to premature intergranular failure during testing. Betteridge et al[1,42] used carbon additions to promote the formation of carbide networks which inhibited grain-boundary motion, thus increasing the creep and stress-rupture properties of superalloys. The effects of carbides upon high temperature properties are dependent on both the type of carbides present and their morphology and distribution i.e. factors that are determined by alloy composition and heat-treatment. Although no overriding opinion can be expressed concerning the most desirable type and morphology of carbide, such phases as M_6C influence the chemical stability and creep strength of the matrix through the removal of reactive elements such as Mo and W, a better understanding of the desirable chemistry, class and morphology of these phases is critical to the alloy designer.

The three types of carbides most commonly found in nickel superalloys[1-7] are MC, $M_{23}C_6$ and M_6C. In simple alloys that are low in chromium and refractory metal content a metastable M_7C_3 carbide can form which can be readily transformed to $M_{23}C_6$ by heat-treatment. Carbon can also be combined as a complex titanium carbonitride phase, or as a sulphocarbide. The most stable carbide in nickel superalloys is the MC phase where the M radical is predominantly titanium, niobium or tantalum, depending upon alloy composition. Group VI elements Cr, Mo and W can partly substitute for Ti, Nb or Ta in the MC phase, although when combinations of the latter three elements are present in an alloy only small amounts of Cr etc. are

detectable in the MC phase. Ti, Nb and Ta can readily substitute for each other, as in the compound (Ti, Ta, Nb) C. In practice the preferred order of formation for MC carbides has been determined to be TaC, NbC, TiC in order of decreasing stability whereas the order indicated by thermodynamics is TiC, TaC, NbC. The MC carbides have an fcc crystal lattice of the Na Cl type[22], with a lattice parameter (a_o) corresponding to stoichiometric TiC, NbC, TaC or for which a simple mixture-law relationship pertains[17,18]. In commercial alloys a_o for MC can range from 4.253Å to 4.356Å depending upon alloy composition and heat-treatment. The MC phase is usually stable to temperatures close to the fusion point of an alloy, hence its shape and distribution in the microstructure is only marginally affected by heat treatment. MC carbides generally occur as discrete particles that are evenly distributed throughout the microstructure in intergranular and transgranular sites, and often in the interdendritic regions of the matrix. In wrought alloys MC occurs as rounded or cube-shape particles, whereas in casting alloys their morphology and size depends on cooling rate. At rapid cooling rates the carbides in the chill zone may appear as small blocky particles, whereas under slow cooling they may develop a dendritic morphology, giving the so-called "Chinese-script" structure.

Although the MC phase is considered to have little direct influence on the mechanical properties it provides a major source of carbon that may be utilised during heat-treatment to improve the mechanical properties of both wrought and cast alloys. In order to maximise the creep resistance and ductility of superalloys heat-treatments have been devised to decompose the MC phase by reaction with the matrix and produce $M_{23}C_6$ thus:

$$MC + \gamma \rightarrow M_{23}C_6 + \gamma' \qquad \ldots.(1)$$

or

$$(Ti\ Mo)C + Ni\ Cr\ Co\ Al \rightarrow Cr_{21}Mo_2C + Ni_3(Al\ Ti) \qquad \ldots.(2)$$

The microstructural features of this decomposition generally show a white-etching γ' phase and discrete $M_{23}C_6$ particles at the periphery of the MC phase. Also, $M_{23}C_6$ can form by reaction with soluble residual carbon in the austenitic matrix. This carbide forms most readily at grain boundaries, although it has been observed at twin boundaries, stacking faults

and intergranular regions. In order to optimise the creep-rupture properties the preferred morphology of $M_{23}C_6$ at grain boundaries is as discrete particles. If the $M_{23}C_6$ develops in a cellular, platelet or sheet form, or as acicular particles which are formed intergranularly, the stress-rupture properties are impaired. The M radical in $M_{23}C_6$ is predominantly chromium, although in commercial alloys molybdenum, tungsten etc., can be included. The crystal structure of $Cr_{23}C_6$ is a complex fcc with 116 atoms per unit cell and a_o of 10.66Å (Reference 22). Substitution of other alloying elements for Cr generally increases the lattice parameter, and values up to 10.74Å have been reported[43].

In superalloys containing relatively high proportions i.e. more than six atomic percent, of molybdenum or tungsten the M_6C carbide (also called the η-carbide) tends to form in preference to $M_{23}C_6$. Analysis of commercial superalloys heat-treated above 1500°F (815°C) has shown that $M_{23}C_6$ and M_6C phases can co-exist in the microstructure[44-46]. In the η-carbide the M radical is generally composed of a refractory metal combined with transition elements, typical formulae are $(Ni\ Co)_3Mo_3C$, and $(Ni\ Co)_2W_4C$. Silicon and chromium have also been detected in η-carbides. Unlike the $M_{23}C_6$ carbide the composition of M_6C can vary widely and in at least one alloy, René 41, the existence of two M_6C carbides has been observed. The crystal structure of M_6C is face-centred-cubic with a lattice parameter in the range of about 10.9Å to about 11.1Å. This similarity in crystal structure makes M_6C and $M_{23}C_6$ phases difficult to distinguish by X-ray diffraction, but electron microprobe analysis and stain-etching techniques aid their identification in the microstructure.

M_6C can form in a similar manner to $M_{23}C_6$, as a product of the following reaction:

$$MC + \gamma \rightarrow M_6C + \gamma' \qquad \ldots.(3)$$

or $$(Ti\ Mo)C + Ni\ \ Co\ \ Al\ \ Ti \rightarrow Mo_3\ (Ni\ Co)_3\ C + Ni_3\ (Al\ \ Ti) \qquad \ldots.(4)$$

When precipitated directly from the matrix phase the morphology of M_6C is similar to that of $M_{23}C_6$, forming discrete particles, platelets exhibiting an acicular morphology, or as a grain boundary network. Since M_6C phases are stable at higher temperatures they are assumed to exert a beneficial

stabilising effect at grain boundaries during high temperature creep. This advantage may be offset by removal of solid solution strengthening effects afforded by refractory metal elements that are combined in the M_6C phases.

Topologically close packed (TCP) phases

As nickel superalloys approach microstructural stability during high temperature service a group of structurally related phases μ, x, R and Laves, sometimes precipitate in the microstructure. The presence of these intermetallic compounds, which have been characterised as topologically-close-packed phases[11] has been found to be detrimental to some alloy properties such as low temperature ductility and creep-rupture strength. These phases are hard, brittle and crystallographically complex, and frequently adopt a plate-like morphology in the microstructure. TCP phases are characterised by close-packed layers of atoms forming in kagomé (basket weave) nets aligned with the octahedral planes of the austenitic matrix. Following the work of Laves and Wallbaum[47,48] on binary alloys of transition metals, the tcp phases correspond to the formula AxBy, where the A-elements are those to the left of manganese, and B-elements are transition elements to the right of manganese in the portion of the Periodic Table following. Thus

	IV	V	VI	VII	VIII			I	II	III	
A	Ti	V	Cr	Mn	Fe	Co	Ni	Cu	Zn	Ga	B
elements	Zr	Nb	Mo	Tc	Ru	Rh	Pd	Ag	Cd	In	elements
→	Hf	Ta	W	Re	Os	Ir	Pt	Au	Hg	Tl	←

In these compounds manganese can act as either an A- or B-element depending on the element with which it is alloyed. The A atoms in these compounds e.g. Ti, V, Nb, Ta are larger than the B atoms e.g. Ni and Co.

The best known of these phases occurring in nickel superalloys is the sigma phase, which is a hard, brittle compound first discovered in the Fe-Cr system by Bain and Griffith[49]. Hall and Algie[50] defined the sigma phase as an intermetallic compound of one element in Group Va or VIa of

the periodic system and one of the first, second or third long periods. The sigma phase found in commercial superalloys is generally a ternary or quarternary phase based on Cr-Co-Mo, or Cr-Co-Mo-Ni. It can exist over wide ranges in composition represented by the formula $(Cr\ Mo)_x\ (Ni\ Co)_y$ where x and y can vary from 1 to 7 (Reference 3). Sigma phase is characterised by a specific complex tetragonal crystal structure with 30 atoms per unit cell and a $\frac{c}{a}$ of 0.52. The lattice constants of the Fe - 46.5 at. percent Cr sigma phase are: a = 8.799Å, c = 4.554Å, and $\frac{c}{a}$ = 0.517 (Reference 51). Among other examples of the identification of sigma phase in superalloys Mihalisin et al[52] detected a complex Co Cr - Mo Ti sigma phase in IN-100 alloy with a_o of 8.83Å, c_o 4.56Å and $\frac{c}{a}$ = 0.52. In the same work a Ni-Cr-Co type sigma phase was identified in Nimocast 713C alloy. The sigma phase found in nickel superalloys generally adopts a platelet morphology and appears as needles, often running in a Widmanstätten pattern from grain boundary to grain boundary. The two common nucleation sites observed for sigma phase are the grain- and second-phase particle- (usually carbide) boundaries.

Laves phases of the AB_2 type have also been observed in the microstructure of nickel superalloys, IN 718 (Reference 53) and IN 901 (Reference 54) being two examples. One criterion for the formation of Laves phases in binary metallic alloys is that the radius ratio of the constituent elements may be in the range 1.08 to 1.32 and ideally $\frac{R_A}{R_B}$ = 1.225 (References 55 to 57). The main reason for the existence of Laves phases is geometrical and at selected lattice positions of a close packed structure the larger A atoms can be substituted for one third of the B positions so that the packing is not disturbed. The resulting structure corresponds to the approximate formula AB_2, and depending on the packing sequence a cubic or hexagonal crystal structure may result. Recently electronic effects have been suggested as also contributing to the Laves structures adopted by some ternary compounds[57]. The Laves phase observed in superalloys such as IN 901 alloy, is usually present in the form of intergranular platelets[54]. In this alloy and in IN 718 the Laves phases which are stable from about 700°C to 900°C adopt a hexagonal structure (C_{14} type). The composition of the Laves phase in IN 718 alloy from X-ray fluorescence analysis was shown to be rich in Nb, Mo and Ni with lesser amounts of Fe, Cr and Ti[53]. In

both of these superalloys the Laves phases did not appear detrimental to properties, in contrast to their effects on iron-based alloys.

The μ-phase corresponding to the formula A_6B_7 is another topologically close packed structured phase that has occasionally been detected in superalloys. The Co_7W_6 μ-phase occurring in the Co-W equilibrium phase diagram has a rhombohedral crystal lattice with 13 atoms per unit cell, a_o of 8.94Å and α of $30^o42'$. In terms of hexagonal co-ordinates this structure has 39 atoms per unit cell with a_o of 4.733Å and c_o of 25.53Å (Reference 58). Beattie and Hagel[54] detected the presence of μ-phase in both René 41 and Incoloy 901 aged for 1000 h in the temperature ranges 816°C to 927°C and 760°C to 927°C respectively. In both alloys the μ-phase has a rhombohedral crystal lattice with $a_o \simeq 4.8$Å and $c_o \simeq 25.7$Å. The elements common to both of these alloys are Ni, Fe or Co, Cr, Mo, Al and Ti and the μ-phase can correspond to the formula $Mo_6(Fe \text{ or } Co)_7$. Precipitation of μ-phase has often been observed at regions where carbides are decomposing in alloys susceptible to M_6C formation. In these alloys the excessive concentrations of Mo and Cr in the M_6C structure favour the formation of μ-phase whereas alloys which form $M_{23}C_6$ favour the formation of sigma phase[5]. Relative to the well-documented evidence of the effects of sigma phase on mechanical properties comparatively little work has been done with respect to the μ-phase.

Prediction and control of sigma phase formation in nickel superalloys

Once the harmful effects of tcp phases on the mechanical behaviour of those superalloys in which they formed was recognised it became imperative to develop methods to predict the likelihood of their formation in order to rationalise alloy design. The most successful theories accounting for the occurrence of tcp phases, and sigma phase in particular, have been based upon the suggestion that they are electron compounds in which bonding is promoted by the electrons in the outer (3d) subshells of the transition metal elements involved[59]. One of the earliest attempts to correlate sigma phases in binary alloys was based on the proposal that they may occur at a characteristic electron-to-atom ratio ($\frac{e}{a}$) where e was the number of electrons outside the inert gas core for each element[60]. Subsequently Hall and Algie[50] correlated the composition ranges of sigma phases as occurring in a band of $\frac{e}{a}$ ratios of 5.6 to 7.6.

Later, Sully[61] replaced the electron-to-atom correlation for characterising the composition ranges of binary sigma phases by substituting values of the electron vacancies in the 3d shell of the elements involved. The electron vacancy numbers (Nv) are, for the most part, related to the electron concentration $\frac{e}{a}$, by the expression: $Nv = 10.66 - \frac{e}{a}$. Sully's Nv values were based on Pauling's[62] theory developed to explain the magnetic properties of the transition elements, Cr, Mn, Fe, Co and Ni, of the first long period. The common features of these elements is their similarity in atomic size and the 3d electron shell remains only partially filled. Experimental measurements of the magnetic moment at the absolute zero for the ferromagnetic metals Fe, Co and Ni had given 2.22, 1.71 and 0.61 Bohr magnetons per atom, respectively. These numbers represent the average number of unpaired electron spins in the elements. To explain these numbers it had been previously assumed that the 3d shell of nickel was occupied by an average of 9.39 of the total 10 outer electrons, with 0.61 electron in the 4s shell. The hole, or electron vacancy of 0.61 electron in the nearly completed d shell was then assumed to give a corresponding magnetic moment to the atom. Pauling reasoned that some of the 3d orbitals might be unsuited to bond formation whilst the remainder might be combined with 4s and 4p orbitals to create metallic bonding. Empirical evidence indicated that the 5d orbitals of each spin divided into 2.44 non-bonding orbitals (i.e. with only weak interatomic interactions) whilst the remaining 2.56 hybridised with the s and p orbitals to provide bond orbitals. Pauling calculated the number of bonding electrons for the elements chromium to nickel to be all of the outer electrons except those in the d orbitals. For chromium 6 electrons can be obtained from the 3d and 4s shells of which 5.78 hybrid (spd) electrons are utilised in bonding, leaving a remainder of 0.22 electrons. These electrons occupy the 3d non-bonding orbitals taking up parallel spins as long as possible. Conversely, there are 2.44 non-bonding orbitals, corresponding to 4.88 holes in the d shell, which because of the addition of the 0.22 electrons, leaves 4.66 net holes for chromium. Pauling assumed that because of their similarity in atomic diameter the number of spd bonding electrons remained constant at 5.78 for Mn, Fe, Co and Ni, and this would cause an increase in non-bonding electrons to 1.22 for Mn, 2.22 for

Fe, 3.22 for Co and 4.22 for Ni. He then derived a density of states diagram for 3d orbitals, from which values of magnetic moment (equal to the average number of unpaired electrons at absolute zero) were predicted at 2.22 μB for Fe, 1.66 μB for Co and 0.66 μB for Ni.

Beck and co-workers[59,63] used Pauling's electron vacancy theory to predict the stability ranges of phases in binary and ternary alloys in the Cr-Co-Ni, Cr-Co-Fe, Cr-Co-Mo, Cr-Ni-Mo, Co-Ni-Mo, Co-Fe-Mo and Ni-Fe-Mo systems at a temperature of 1200°C. Using the formula $\bar{N}v = \Sigma Mi(Nv)i$ where Mi is the atomic fraction of element i in the alloy matrix, and (Nv)i its electron vacancy number, it was found that the range of sigma phase composition could be characterised by average electron vacancy number ($\bar{N}v$) in the range 3.16 to 3.66. This number was computed from the expression:

$$\bar{N}v = 4.66\,[Cr] + 4.66\,[Mo] + 3.66\,[Mn] + 2.66\,[Fe] + 1.71\,[Co] + 0.61\,[Ni]$$

where: 4.66 = Pauling's 3d electron vacancy number for chromium, and [ ] = atomic fraction of a particular element. It is difficult to assign meaningful Nv number to elements other than those in the first long period, but in this first expression Beck assumed that because Mo was in the same group as Cr in the periodic table their electron vacancy numbers should be identical. In a later refinement the designated Nv values of some elements such as Mo and V depended on composition. For example with alloys consisting of 100 per cent sigma phase the calculated $\bar{N}v$ values were in the range 3.35 to 3.68 if Nv of 5.6 was used for molybdenum. Boesch and Slaney[64] are credited with the first successful application of electron hole theory to predict the likelihood of formation of a tcp phase in a commercial superalloy, Udimet 500. They assumed that the tcp phase precipitated directly from the austenite matrix (gamma) whose composition could be expressed as an $\bar{N}v$ value that could be related to the $\gamma/\gamma + \sigma$ phase boundary. Their method of calculating the residual matrix composition was based on the assumption that all of the titanium, aluminium and some nickel from the parent alloy composition precipitated $Ni_3(Al, Ti)$, γ' phase. Using Beck and Rideout's expression for Nv for the elemental constituents of the residual austenite they set an $\bar{N}v$ value of 2.32 as a safe upper limit to avoid the formation of sigma phase in Udimet 500 alloy.

They recognised that coring in casting alloys would require a different critical $\bar{N}v$ value. In addition they realised that whenever carbon contents were sufficiently high to matter, the matrix composition would be altered to allow for loss of carbide-forming elements. Boesch and Slaney also successfully applied their $\bar{N}v$ criterion of 2.32 to Udimet 700 alloy. Woodyatt et al[12] used a similar, but more refined method, thereafter designated PHACOMP, which allowed for the precipitation of carbides and borides in addition to γ' phase in order to calculate the residual matrix compositions of superalloys. In their analysis of a number of superalloys a critical value of $\bar{N}v$ of 2.52 was set as the safe upper limit to avoid the formation of sigma phase. The first step of this analysis was to express the alloy composition in atomic percentage. The boron content was accounted for by the formation of a boride phase of an assumed composition $(Mo_{0.5}Ti_{0.15}Cr_{0.25}Ni_{0.10})_3 B_2$, one half the carbon formed an MC carbide with an order of decreasing stability TaC, NbC, ZrC, TiC, VC. The remaining carbon formed $M_{23}C_6$ or M_6C carbides - $Cr_{21}(Mo, W)C_6$ if Mo + W levels are less than 6 per cent, or $(Ni\ Co_2\ Mo_3)C$ if Mo + W are greater than 6 per cent. All the Al plus remaining Ti was combined with other elements to form gamma-prime whose composition was described as Ni_3 (Al, Ti, Nb, 0.1Cr), or in event of there being insufficient Ni remaining it was assumed that the β Ni(Al, Nb, Ti, Cr) phase formed together with γ'. The residual matrix composition was then scaled to 100 per cent and its average electron vacancy ($\bar{N}v$) calculated from the expression:

$$\bar{N}v = 4.66\,[Cr + Mo] + 1.71\,[Co] + 0.61\,[Ni]$$

From computer assessments it was found that wrought alloys with $\bar{N}v$ of less than 2.52 did not form sigma, whereas those with a higher $\bar{N}v$ value precipitated sigma phase.

After initial success in applying PHACOMP to nickel superalloys several exceptions were found for both cobalt-base and a few nickel-base alloys. For example the critical $\bar{N}v$ of about 2.70 is accepted for cobalt alloys. In the case of nickel alloys these exceptions have arisen from incorrect assumptions of the amount and composition of the gamma-prime phase and of the carbides. It is also generally assumed that temperature

has no significant effect on the compositional ranges of the phases and for simplicity the phase equilibria in superalloys is correlated with ternary Ni-Cr-X systems usually at extremely high temperatures (ca 1200°C). In practice the temperature capability of superalloys is considerably less than 1200°C and the gamma-prime phase would be expected to dissolve in the matrix at temperatures well below this level. Elemental electron vacancy numbers were initially assumed to be constant in any group of the periodic table regardless of the combinations and quantity of the elements in the alloy. It was also usually assumed that tcp phases formed primarily in the matrix phase, and non-transition metals e.g. Ti, had negligible effects on sigma formation. In order to partly redress this balance and obtain a better agreement between iso-electron vacancy lines and sigma phase fields different values of Nv have been ascribed to some elements. For example Mihalisin[52] suggested that the Nv for Mo and W could be as high as 9.66. In a study of the Cr-Co-W and Cr-Mo-W-Al systems Kirby[65] recommended that the value of Nv for Mo and W varied with temperature from 8.2 at 760°C and 843°C to 8.9 at 927°C. Further it was shown that the $\gamma/\gamma + \sigma$ phase boundary in the pseudo-ternary (Ni + Co)-Cr-(Mo, W) system could be described by Nv expressions similar to those in the literature. In Kirby's work the solvus line describing the compositions of the γ matrix after ageing at 843°C could be defined using an average value of Nv for Co and Ni thus:

$$\frac{0.61 + 1.71}{2}[Ni + Co] + 4.66[Cr] + x[Mo, W] = 2.52$$

where [ ] = atomic fraction of the particular element and x varied from 7.7 to 8.0. One of the major exceptions to the PHACOMP critical $\bar{N}v$ of approximately 2.5 occurs with the well-known Nimocast 713C alloy where sigma phase occurrence has been reported at $\bar{N}v$ values below 2.20, a considerable deviation from the normally expected behaviour for nickel superalloys. Nimocast 713C alloy does not intentionally contain cobalt and the composition of its residual matrix cannot therefore be on or close to the Ni-Cr-Co ternary (shown in Figure 5a) as for other superalloys, but as shown by Murphy et al[13] it lies on or near the Ni-Cr-Mo ternary (Figure 5b). However, because the iso-electron vacancy line at $\bar{N}v$ 2.49

in the Ni-Cr-Mo system is not parallel to the $\gamma/\gamma + \sigma$ boundary (a normally accepted requirement for PHACOMP treatment) but intersects it at approximately 30^{o}, Murphy arbitrarily constructed a line parallel to the two-phase boundary at $\bar{N}v - 0.2$, commencing at the phase boundary intersection with the Ni-Mo and Ni-Cr binaries in order to correlate the 713C alloy compositions and their propensity to form sigma phase. It was further proposed that the equation for the line separating σ-free and σ-prone compositions and parallel to the two-phase boundaries could be described by the following expression:

$$\bar{N}v = 2.49 = 0.6[Ni] + 4.66[Cr] + Nv[Mo]$$

from which Nv for Mo was found to have a value of approximately 10. In the PHACOMP calculations most attention has been given to the prediction of sigma phase. Although the data are sparse, Sims has shown that precipitation of other tcp phases such as μ or Laves in susceptible alloys can also be treated by PHACOMP although the $\bar{N}v$ in these cases is lower than that for sigma. The general rule of thumb developed for other tcp phases was that Laves or μ phase may be expected in susceptible alloys at $\bar{N}v \geq 2.30$ if $(Mo + \frac{W}{2}) \geq 6$ per cent, providing the Fe is less than 20 per cent and Co less than 30 per cent. The limitations of the various PHACOMP schemes have been reviewed by Murphy et al[14] and there have been many attempts to refine the models in order to develop a "universal" theory such as the ALLCOMP scheme mentioned but not detailed by Barrett[15]. However as Sabol and Stickler[6] have pointed out, if the PHACOMP calculations are performed diligently and with proper recognition of the limitations, it still represents the best available means of fixing the tcp phase field and locating the complex superalloys with respect to these phase boundaries. In order to make further progress in this field there is clearly a need to study the phase relationships in a larger variety of superalloys, particularly in respect of establishing the true compositions of the matrix, gamma-prime and carbide phases.

CHAPTER 3

Constitution and microstructure of experimental materials

This Chapter represents the first phase of the programme which was designed to provide information on how different metallic elements alloy with the three principal phases found in the microstructure of the experimental casting alloys. These were prepared by systematically replacing, in part or wholly, other elements for tantalum and tungsten in a creep-resistant superalloy selected from Reference 66 and designated HRA-376 alloy. Unfortunately its high density (9 g/cc) precluded HRA-376 alloy for turbine rotor blade applications, but it served as a useful model for studying the possibility of developing lighter alloys of creep strength comparable or better than existing alloys and which are not susceptible to the formation of tcp phases in the microstructure. The general scheme may be seen by reference to Table 2 and the "composition" sections of Table 8. Essentially the programme was concerned with examining the model superalloy designated HRA-376, or W37 in the Tables, which nominally contains three atomic percent* each of tantalum and tungsten in addition to nickel, chromium, cobalt and the other elements listed. The remainder of the alloys in the series, with the exception of R12, were designed by substituting combinations of titanium, niobium and molybdenum partly or wholly for the tantalum and tungsten in the parent HRA-376 alloy. Thus the series of alloys consisted of a "base" of atomic percentage* 0.11 B, 0.7 C, 13.0 Al, 7.0 Cr, 10.0 Co, 63.1 Ni and 0.07 Zr with variants adding to a total of three atomic percentage each of the groups (Ti, Nb, Ta) and (Mo, W). From previous work[17,18] it was found that the Ti, Nb, Ta group partitioned in a similar way between the phases present in the superalloy microstructure, whilst Mo and W tended to act similarly to each other. The alloy compositions were such as to produce similar quantities of gamma-prime and carbides in the as-cast microstructures. From Table 1 the alloy series may be subdivided into six groups, the first headed by W37, and in turn by W34, W43, W41, R4 and R12. The W37 group all contain two element variants each at the three atomic percent level, while the W34 group all contain three percent of either Mo or W with equal additions of two

*Unless otherwise indicated, compositions are reported in atomic percentage

elements from the (Ti, Nb, Ta) group. W34 and R3 represent alloys in which similar elements are present in equivalent proportions. Alloys R4 to R11 represent a range of concentrations of Ti/Nb/Ta and Mo/W together. R12 contains a similar amount of gamma-prime to the other alloys, but is free of Ti, Nb, Mo, Ta and W. The alloys were examined both in the as-cast condition and after 2000 hours heat-treatment at 850°C and 200 hours at 1050°C. These temperatures are relevant to service use. 850°C represents the temperature region where sigma phase would be expected to be stable in some superalloys, and 1050°C where M_6C phases may be stable.

Some additional materials examined for comparison were Nimonic 115 alloy* and MarM246**. The Nimonic 115 alloy samples were in the form of blades which had prematurely fractured in a brittle manner in two industrial turbine engines. One engine had operated for 1360 hours and the other for approximately 8000 hours. Later metallographic examination showed that extensive sigma phase precipitation had occurred in these Nimonic 115 alloy blades. Comparison was made with a Nimonic 115 alloy blade removed from a turbine engine after 950 hours service under similar operating conditions, but which was free of sigma phase. MarM246 alloy, creep-tested for 200 hours in air at 1050°C contained precipitated M_6C in the microstructure. The compositions of the commercial superalloys examined in this work are included in Table 2. The techniques used in the study were conventional optical metallography, electron microscopy, electron microprobe analysis, spectrographic and wet chemical analytical techniques and X-ray diffraction studies of the alloys.

Relationships between the composition of the parent alloys and the composition of the phases in the microstructure of as-cast and heat-treated alloys were established. Changes in the microstructure induced by heat-treatment in the laboratory, and those induced by service exposure for the Nimonic 115 alloy blades, were observed in detail by electron microscopy. Some observations were made on the relevance of PHACOMP to these experimental and commercial superalloys.

---

*Trademark of International Nickel Limited

**Trademark of Martin Marrietta Corporation

Melting and casting procedures

With the exception of zirconium and boron added as Ni : 50 wt % Zr and Ni : 11.5 wt % B hardeners, the alloys were prepared from sequential additions of pure elements to pure nickel. The alloys were vacuum-melted using a high frequency induction furnace of about 10 kg capacity. Approximately 5 kg of alloy constituents were pre-weighed with due allowance being made for melting losses. Details of the source, purity and types of alloying additions are given in Table 3.

At a melt temperature of about 1480°C the alloys were vacuum-cast in backed shell moulds preheated to about 900°C. The mould assembly was used to produce six 0.5 in. diameter × 6 in. high cylinders (from which tensile, creep/rupture and other testpieces were machined), six cast-to-size miniature Charpy impact testpieces (1.66 in. long × 0.11 in. sq.) and a central feeder from which samples for chemical analysis were taken.

All the alloys were conventionally-cast, this giving an essentially equiaxed grain structure; in addition some were unidirectionally solidified (UDS) using the modified Bridgman technique adopted by Northwood and Homewood[67]. Briefly, this involved the casting of molten alloy into a shell mould mounted on a water-cooled copper chill and centred in a separate resistance-heated furnace in the melting chamber. Control of the solidification of the 0.5 in. diameter testbars was effected by raising the hot furnace (1540°C) at a rate of about 15 in./h. Under these conditions columnar grain growth occurred with elimination of transverse boundaries and improvement in strength, ductility and soundness of the cast. Typical cast mould assemblies are shown in Figure 6.

Preparation for metallographic and other examinations

Testpieces were cut from the 0.5 in. diameter bar stock for examination in the as-cast or heat-treated condition. Those to be heat-treated for 2000 hours at 850°C (sigma formation) or 200 hours at 1050°C (M_6C formation) were sealed in quartz capsules in an argon atmosphere ($\frac{1}{2}$ atm pressure). In certain instances gamma-prime phase residues extracted from the alloys were sealed in a quartz capsule in an argon atmosphere and re-melted using induction heating. After metallographic preparation the fused material was microprobe analysed. Specimens for electron

microscopy were prepared as standard two stage replicas, extraction replicas or as thin foils. A TENUPOL jet-machiner was used for profiling (dishing) and final polishing of thin foils. Comparatively stain-free foils were produced using an electrolyte[68], consisting of 10% H_2SO_4, 1% HF and 1.5% HNO_3 by volume in methanol at a temperature of -15°C, at approximately 20 volts and 100 milliamp current. Microprobe analysis was carried out using a JEOLCO JXA-3A instrument; for electron microscopy the Philips EM300 (100 KeV) at NGTE, or the AEI EM7 (1 MeV) instrument at Imperial College was used.

X-ray diffraction studies were performed at Fulmer Research Institute Ltd., using a Philips 11.46 cm diameter camera and cobalt K_α radiation for specimens in powder form, or a flat plate camera for obtaining diffraction patterns from the polished surfaces of bulk alloys. Some X-ray diffraction analysis was done using a Philips diffractometer at the Royal Aircraft Establishment.

Chemical analyses of the bulk alloys, the extracted gamma-prime phases, and the gamma phases were done by Chemical Inspectorate (Woolwich and Sheffield) using conventional wet chemical, X-ray fluorescence and atomic absorption techniques.

Results

General metallographic features of the alloys

The optical microstructures of all the alloys in the as-cast condition were found to be very similar; examples are shown in Figure 1. The phases that are resolvable include primary dendrites of nickel solid solution (gamma) containing gamma-prime precipitate, with interdendritic regions of primary MC carbide and areas of the white-etching, kidney-shaped gamma-prime that result from eutectic solidification. The MC particles are present at the boundaries and dispersed to some extent in the dendrites. Small amounts of borides and sulphides are generally present in the interdendritic regions. More details of the microstructure showing the morphologies, distribution and size ranges of the gamma-prime in the as-cast microstructures were given in a previous paper[17,18]. The gamma-prime precipitated by solid state reaction appears in the form of cuboids up to about 1μm in size (secondary gamma-prime) and also as a very much finer dispersion (tertiary gamma-prime). In addition there is the large

chunky, so-called eutectic gamma-prime formed from the liquid which is composed of massive Ni_3Al particles separated by thin lamellae of gamma. The quantities of the phases present in the microstructure of the as-cast alloys were approximately as follows: eutectic gamma-prime 4 ±1 vol %, cuboidal gamma-prime 62 ±2.5 vol %, MC approximately 2 vol %, balance matrix. Thus despite the potential complexity resulting from the addition of up to 12 elements to the nickel the phase equilibria can to a large extent be represented by the ($\gamma + \gamma'$) regions of the binary Ni-Al, or ternary Ni-Cr-Al and Ni-X-Al diagrams (Figures 3 and 4) References 31 to 35. From the optical microscope examination of the experimental as-cast alloys, no major cavities or flaws were detected, but there was interdendritic shrinkage porosity (at a level of about 1.0 per cent on an area basis) more coarsely dispersed in the conventionally-cast than in the UDS materials.

Following extensive ageing treatment (2000 hours) in the temperature region where the sigma phase in superalloys would be expected to be stable ($\sim 850^{\circ}C$), only minor changes in the microstructure of the experimental alloys were detected. Using the special etching and polarised-light technique of Dreshfield and Ashbrook[69] and other electrolytes such as Kalling's reagent used by Johnson et al[70], there was no evidence of the Widmanstätten structure of sigma phase needles in the microstructure. Otherwise there appeared to be some general break-up of the eutectic gamma-prime and at higher magnifications slight spheroidisation of the secondary gamma-prime was evident. In contrast the microstructure of the fractured Nimonic 115 alloy blades, Figure 7, contained large amounts of acicular phase that showed a tendency towards a crystallographic growth habit within the microstructure. Using techniques to be detailed later, these platelets were identified as sigma phase.

After the heat-treatment for 200 hours at $1050^{\circ}C$ which produced extensive η carbide (M_6C) precipitation within the microstructure of the MarM246 alloy (Figure 7), apart from some coarsening of the secondary gamma-prime phase in the experimental alloys there was no evidence of formation of any acicular phase, or other significant changes in the microstructure.

Chemical and electron microprobe analyses

Table 2 lists the chemical analyses of the individual alloys. With the exception of the so-far unexplained differences in niobium content of alloys R7, R8 and R9, there was fairly close agreement between the nominal composition and actual bulk analysis data of the alloys. These data supplied by Chemical Inspectorate showed maximum differences (w/o)* of 0.07 C (R13, R14 alloy), 0.3 Al (W41, R7, R12), 0.2 Ti (R2, R3, R11), 0.4 Cr (R10), 0.4 Co (W47), 0.04 Zr (R12), 0.8 Nb (R8), 0.2 Mo (R9, R8, R11), 0.3 Ta (R9), 0.6 W (W50) and up to 1.5 w/o Ni by balance. These analyses were generally recorded as the mean of three determinations.

The quantitative electron probe micro-analysis data (EPMA) for the dendrite, eutectic gamma-prime and MC phases in-situ in relation to the parent alloy compositions are listed in Table 4. These results represent the mean of at least three separate determinations of composition, using pure element standards and the iterative computer correction procedure developed by the author[71] and discussed in the third paper appended. The mean dendrite composition includes both matrix gamma and the approximately 60 per cent by volume of secondary gamma-prime precipitate, that were individually beyond the resolution limit (on size) of the microprobe analyser. Measurements of dendrite compositions were used as a rough check of alloy composition throughout the series. Note that the MC analyses include the relatively small amounts of cobalt (1.4 at.% maximum for W41) and nickel (3.7 at.% maximum for R6) detected by microprobe analysis. Carbon was qualitatively detected in the carbide phases, but in the absence of accurate mass absorption data and general uncertainties in the values of other parameters necessary for the quantification of light element data, compositions have been calculated assuming that the carbide is stoichiometric. Small amounts of boron were often detected by EPMA in these MC carbides.

Table 4 also lists the compositions of the gamma matrices, based on bulk chemical analyses using colorimetric or atomic absorption techniques on the filtrate resulting from electrolytic extraction of the

---

*w/o = weight percentage

gamma-prime phase from the various alloys. The zirconium concentration is recorded at a nominally zero level in the gamma phases. Broad trends for the alloying elements to partition between the different phases are evident from these data as in the previous work[17,18], i.e. Ti, Nb and Ta tend to partition towards the gamma-prime (as would be expected from the phase diagram, Figure 4) and the MC phases, while Cr, Co, Mo and W tend to alloy preferentially with the matrices.

Table 5 gives a comparison of the composition of the gamma-prime phases in the as-cast alloys. Both the eutectic and re-fused gamma-prime (i.e. extraction residue gamma-prime dried and re-fused) were analysed by EPMA, whilst a combination of spectrographic and wet-chemical techniques were used as a check on the analyses of extracted gamma-prime phases. Compositions were also calculated, based on the bulk chemical analyses using the assumption that, after allowances are made for MC formation, the alloys contain 60% γ' : 40% γ by volume. For most alloys there was a fair measure of agreement between the results of the various analyses for aluminium-content of the gamma-prime phases. Throughout the alloy series there is a marked similarity in the partitioning behaviour of all the elements although the magnitude of the effect depends on the mechanism of formation of the gamma-prime, i.e. from the liquid or by solid-state reaction, the number of alloying elements in the phases, and uncertainties inherent in the particular analytical techniques (e.g. overlap of spectral emission lines, colour interference by other elements). The eutectic gamma-prime phases analysed by EPMA generally contained more Al, Ti, Cr, Nb, Ta and less Mo and W than the secondary gamma-prime phases.

From measurements of changes in the composition of selected matrix (gamma) phases as a function of heat-treatment, Table 6, it was found that exposure for 2000 hours at 850°C (to precipitate sigma if the alloy composition is appropriate) increases the solubility of aluminium, and of elements such as titanium, niobium and tantalum that contribute to the formation of gamma-prime, whilst the levels of chromium, cobalt, molybdenum and tungsten progressively decrease. Exposure for 200 hours at 1050°C (for M_6C precipitation where appropriate) increases further the solubility of elements such as Ti, Nb, Ta that partition to the gamma-prime, whereas the levels of the Group VI elements and Co that preferentially alloy with the austenitic matrix decrease. The concentration

of elements such as Ti, Nb and Ta detected in the nickel matrices after the heat-treatment at 1050°C were less than their original level in the parent alloy. After allowing for the amounts of these elements used in carbide formation it can be deduced from the compositions of the matrices in Table 6 that the solvus temperatures of the gamma-prime phases were in excess of 1050°C.

EPMA was carried out on the eutectic gamma-prime and MC phases in the alloys in the as-cast condition and after 200 hours exposure at 1050°C (see Table 7). Some analyses were also made of the MC phases after 2000 hours exposure at 850°C which did not appear significantly different to the as-cast analyses, although there did appear to be some break-up of the eutectic gamma-prime structure during this exposure. Eutectic gamma-prime was present after heat-treatment at 1050°C and there were some general fluctuations in the concentrations of the elements, but the changes were not considered to be significant. Changes did occur in the size, distribution and composition of the MC phases in some alloys (e.g. W44, W34, W50, R3), although X-ray techniques did not indicate that $M_{23}C_6$ or M_6C formed in the microstructure. For example the MC particles in alloys W44, W34, W50 and R3 were in the form of fine dispersions (<0.5μm) after the 1050°C heat-treatment, and owing to the ease of penetration and spread of a 25 kV electron microprobe beam, the surrounding matrix gave an artificially high concentration of nickel (although inadequate to give M_6C) in the compositions. In contrast MarM246 alloy heat-treated for 200 hours at 1050°C precipitated large platelets of M_6C with a composition corresponding to the formula $(Ni + Co)_4 (Cr + W + Mo)_2C$. No evidence was found for the formation of tcp phases such as the μ, Co_7W_6 compound. The grain boundary regions were found to be rich in Al and deficient in chromium and other Group VI elements, presumably a consequence of the decomposition of an MC phase.

From general trends in the change of composition of the MC phases with exposure at 1050°C it was clear that in the two element variants (viz the group headed by W37) pseudo-binary carbides containing Mo and W [i.e. (Ta/W) C, (Ti/Mo) C, (Ti/W) C] occurred in the as-cast microstructure, however it was only in the Ti-containing variants that the carbide

compositions remained unchanged with heat-treatment. In the other alloys Mo and W did not predominantly feature in the MC phases in the as-cast, or heat-treated materials. In the alloys where Ti, Nb and Ta were present as binary, or ternary combinations there were some localised variations in composition of the MC phases during exposure at 1050°C, however it was clear that Nb was generally as stable as Ta in the MC structure.

X-ray examinations

The results of the X-ray diffraction analyses of the structure of the three principal phases present in the as-cast microstructure of the alloys are listed in Table 8. All phases, with the exception of the complex carbide detected in R12 alloy, were found to be cubic. The binary Ni_3Al phase exhibits superlattice reflections, some of the alloyed gamma-prime phases in the experimental alloys did not. Lattice parameters of the gamma phases were calculated from the chemical analyses listed in Table 4; those for gamma-prime were based on the mean of the measured analyses, and those for MC were calculated from the mixture-law relationship with lattice parameter values for stoichiometric TiC, NbC, TaC, listed by Goldschmidt[72]. In R3 alloy carbide extraction residues, two MC (or possibly carbo-nitride) phases were detected and were indexed to give a lattice constant of 4.143Å that corresponded to a complex (Ti, Nb, Ta)C phase. Table 9 indicates the magnitude of the changes in lattice parameter of the three principal phases induced by heat-treatment at 850°C and 1050°C, and also registers the appearance of any new phases in the microstructure. Very small differences in lattice parameter between the matrix and gamma-prime phases were observed. Changes in lattice parameter for the MC phases with heat-treatment were apparent that became more marked after the 1050°C exposure. Sigma phase was not detected in any cast alloy after the 850°C heat-treatment nor was $M_{23}C_6$ detected in the extraction residues. The 1050°C treatment produced some extra lines of very low intensity for some of the alloys; these were indexed as possible M_6C structures generally, but in the W47 and W43 alloys lines corresponding to a hexagonal phase were detected. In comparison extraction residues from the Nimonic 115 alloy blade materials contained

relatively large amounts of a tetragonal phase typical of sigma ($a = 8.867\text{Å}$, $c = 4.592\text{Å}$, $\frac{c}{a} = 0.52$), in addition to MC ($a = 4.325\text{Å}$), gamma-prime ($a = 3.589\text{Å}$) and a phase with a cubic structure with a lattice parameter (2.884Å) very close to that of pure chromium (2.885Å). $M_{23}C_6$ was not detected in the extraction residues from this blade material. The MarM246 alloy exposed at 1050°C showed very strong M_6C ($a = 11.10\text{Å}$) reflections in addition to gamma-prime (3.587Å) and very weak MC (4.33Å) reflections.

Table 10 shows that fairly good agreement was obtained between the measured densities of the cast alloys and those calculated from the chemical and electron microprobe analysis data and lattice parameter data published for the pure elements. In order to make further use of the analysis data of the matrix, eutectic gamma-prime and MC phases, Mr. J. H. Cadwell, to whom the author is indebted for this service, developed a series of regression equations that express the concentrations of individual elements in the phases in terms of the overall compositions of the alloys. These equations are listed in Table 11.

Electron microscopy

Microstructures of thin foils typical of most alloys in the series in the as-cast condition are illustrated in Figures 8 and 9. These show the secondary (cuboidal) gamma-prime phase up to approximately 1μm in size with a finer dispersion (<0.01μm) of γ' precipitate in the matrix (gamma) phase. The relative proportions of these phases, by volume, are approximately 60% Ni_3Al to 40% matrix. Alloy R12, free of Ti, Nb, Mo and W, contained a finer size of gamma-prime precipitate than the other alloys in the series. Examination of the foil structures and analyses of the diffraction patterns showed the random orientation growth of dendrites in the conventionally-cast alloys compared with the preferred orientation growth [100] of the unidirectionally solidified alloys. The dark-field images were obtained using superlattice reflections (100), (300) from the Ni_3Al phases. Owing to the difficulty of preparing thin foil specimens to illustrate grain boundary regions in the alloys, details of these were revealed using replication techniques. The grain boundaries were lined with simple MC phases (although sulphide phases have been detected by EPMA) that were also irregularly dispersed throughout the dendrites.

Heat-treatment for 2000 hours at 850°C produced little change in the microstructure of the cast alloys (Figure 10) except for a tendency for the secondary gamma-prime to spheroidise, and a slight increase in the volume fraction of matrix phases i.e. increasing the volume fraction by up to approximately 5 per cent. No evidence of the presence of sigma, or other tcp phase was found in the microstructures. In comparison typical thin foil microstructures of the Nimonic 115 alloy blade materials illustrated in Figures 11 and 12 show the typical acicular morphology of sigma phase in a background of matrix and gamma-prime phase. Dark-field images were also obtained using a reflection from the sigma phase.

Heat-treatment for 200 hours at 1050°C produced discernible changes in the concentration, distribution, and sizes of the gamma-prime phase in the experimental materials typified by Figure 13. There was obvious coalescence of the secondary gamma-prime, and an additional point of interest was the presence of a fine dispersion of gamma-prime in the matrices of the various alloys after water-quenching from 1050°C. This heat-treatment also reduced the volume fraction of gamma-prime to about 50 per cent. Dislocation networks were apparent particularly in the two-phase ($\gamma + \gamma'$) regions. There was no evidence of the presence of acicular M_6C phases in the microstructure of the experimental materials. For comparison Figure 14 illustrates microstructural features of MarM246 alloy in single crystal form after creep testing for 200 hours at 1050°C. In common with the experimental alloys there was evidence of coalescence of the secondary gamma-prime, and the presence of a much finer γ' dispersion in the surrounding matrix. There was also a significant volume fraction of acicular M_6C phase identified separately by X-ray and electron diffraction analyses of the microstructure (Figure 14).

Discussion

General observations on the materials

The chemical analyses of the cast alloys were in fairly close agreement with the desired compositions. General optical metallographic examination showed the alloys to be of acceptable soundness with about 1 per cent interdendritic shrinkage porosity, and to contain similar levels of carbide and eutectic gamma-prime phases.

Heat-treatment for 2000 hours at 850°C caused partial decomposition of the eutectic gamma-prime and slight spheroidisation of the secondary gamma-prime. The tertiary gamma-prime was below optical microscope resolution i.e. <<0.5μm in size. In contrast the Nimonic 115 alloy blade microstructures contained large amounts of acicular platelets, some of which occupied the width of a particular grain. Using the technique of Dreshfield et al[69], these platelets were tentatively identified as sigma. Heat-treatment for 200 hours at 1050°C produced little change in the microstructure of the experimental alloys apart from some coalescence of the secondary gamma-prime and partial dissolution of some MC particles. The latter heat-treatment caused extensive precipitation of an acicular phase within the microstructure of MarM246, in addition to coarsening the secondary gamma-prime phases.

Distribution of elements

The phase compositions listed in Table 4 represent the mean of at least three separate determinations of composition. The pattern for elements in the same group of the Periodic Table to partition in fairly specific ways, as illustrated in the previous work[17,18] is evident, the Group V elements (Nb, Ta) alloying with the gamma-prime and MC phases, whilst the Group VI elements (Mo,W) preferentially alloy with the nickel base matrices. Titanium acts similarly to Nb and Ta and tends to partition to the gamma-prime and MC phases. In the two-element variants (headed by W37 alloy in Table 1), pseudo-binary alloy carbides could occur between Mo/W and Ti/Ta-containing alloys, whereas the Nb-containing alloys produced NbC as the principal MC phase. In more complex alloys containing binary or ternary combinations of Ti, Nb and Ta, the Group VI elements (Mo and W) did not significantly feature in the MC phases. Chromium (Group VI) was not present to any significant level (always less than that in the alloy composition) in the MC phases. Small amounts of boron were often associated with the MC particles.

The accuracy and reproducibility of EPMA data is indicated by the following figures; for the eutectic gamma-prime the accuracy for [Al] was typically ±1.0 at %, [Cr] ±0.3, [Co] ±0.5, [Nb] ±0.2, [Mo] ±0.2, [Ta] ±0.3, [W] ±0.3, at the level detected. For the carbide phases, depending on the complexity of the alloy compositions, measurable substitutions of Ti,

Nb and Ta could occur for each other; thus ranges for these data for M in MC were typically 4 at.% at 30 at.% level and 2 at.% at 10% level. [W] and [Mo] range from 2.0% at the 15% level of detection to 0.3% at the 2% level in the various MC phases. In common with the observations of Gregg and Piearcey[73] for MarM200 alloy, in the experimental alloys localised concentrations of heavy metal elements in addition to sulphur and boron were also detected in these interdendritic regions. Significant localised variations in the concentration of elements occurred at the boundaries with interdendritic regions.

The preferred alloying behaviour of Ti, Nb and Ta is with carbon (to form MC) and with the gamma-prime phases. Mo and W alloy with the nickel base matrices, except in the "two-variant" alloys previously mentioned where Ti and Ta alloy with Mo and W in the MC phases. From the chemical analysis data it is clear that significant quantities of Al, Ti, Nb and Ta are present in the various matrices (one factor generally ignored in simplified versions of PHACOMP). Comparison of analyses of gamma-matrices provided by Nall[74] and Nicholas[75] using a combination of classical colorimetric, atomic absorption and spectrographic methods gave typical variations for individual elements as follows: [Al] ±1.0 in 5 at.%, [Ti] ±0.1 in 0.5%, [Cr] ±0.5 in 10%, [Co] ±0.5 in 12%, [Mo] and [W] ±0.5 in 3%. Data for Zr were generally not given for H_3PO_4 based filtrates as zirconium phosphate is separated as an insoluble residue. From previous work, however, using a mixed ammonium sulphate-citric acid electrolyte, [Zr] in the gamma phase was detected at less than 0.01 at % level. There appeared to be significant conflict in the data for the comparatively low concentrations of Nb and Ta detected in the gamma matrices, but those from spectrographic analysis were adjudged to be the most unreliable.

The various analyses of gamma-prime phases showed differences that could be ascribed both to errors in a specific analytical technique, and to actual chemical differences, e.g. compositional differences between the eutectic phase and the mean composition of the various types of gamma-prime present in the microstructure. Thus the eutectic gamma-prime, uniquely analysed by microprobe analysis, contained more titanium, niobium, tantalum (and, generally chromium) and less molybdenum and tungsten than the

levels of these elements detected by EPMA or other techniques in electrolytic extractions. These differences are probably related to the differences in mechanism of formation of gamma-prime, the eutectic being formed directly on cooling from the liquid, the secondary and tertiary gamma-prime forming from solid material that is supersaturated with Al, Ti, Nb, Ta etc.

From a comparison of the data on electrolytically extracted gamma-prime from microprobe and other analyses it is clear that there are fluctuations in the levels of the individual elements detected for any alloy, but there are acceptable agreements, with few exceptions, in the whole series. The composition of the gamma-prime phases derived from simple law-of-mixtures relationships from the known compositions of the parent alloy, gamma and MC phases are generally in agreement with the measured values.

Table 6 shows the general trends for change in composition of the matrices with heat-treatment both at 850°C and 1050°C. The concentrations of the gamma-prime forming elements generally increased with exposure temperature for the series. Small exceptions to this rule were found in R8, and R6 alloy. In contrast the concentrations of the Group Vl elements, in the various matrices generally decreased progressively with increase in exposure temperature. These changes were associated with changes occurring in the microstructure i.e. partial dissolution of the gamma-prime and MC phases. These data are in accord with the increased solubility of aluminium with temperature in the gamma phase indicated by the phase diagram.

From the EPMA data there appear to be somewhat random fluctuations in the composition, particularly [Al] of the eutectic gamma-prime phase between the as-cast and heat-treated alloys. However these changes appear to have limited significance in view of the heavily-segregated nature of these products and the known thermal stability of this type of phase. For the experimental alloys there appeared to be a general reduction after heat-treatment in [Ti], and Group Vl elements Cr, Mo and W in the gamma-prime phases. Heat-treatment at 1050°C caused partial solution of MC particles in some of the alloys, but most were judged to be of sufficient size to have confidence in the accuracy of the EPMA data. For the

two-element variants (W37 Group), molybdenum and tungsten did not feature predominantly in niobium- or tantalum-containing carbides in the heat-treated alloys; however, the Group VI elements featured as pseudo-binary carbides in combination with titanium [(Ti/Mo)C, (Ti/W)C]. No evidence for the formation of M_6C or $M_{23}C_6$ phases was found at particle sizes amenable to EPMA after heat-treatment at 850°C or 1050°C.

Correlation of X-ray diffraction and other analyses

The accuracy of lattice parameter measurement of γ' and MC extractions using the powder camera and appropriate application of the Nelson-Riley Function [fθ] was quoted at an average of 0.0005Å, compared with an average accuracy of 0.002Å using the flat plate camera for the gamma phase. The diffractometer measurements on the γ' and MC extracts had an average accuracy of 0.001Å. However, as previously shown[35,76] apart from differences that may be attributed to a particular X-ray camera, the sample preparation has a significant effect on the measurement of lattice parameter. For example Decker and Mihalisin[35] found the percentage mismatch measured on ternary Ni-Al-X alloys (where X was Si, V, Nb or Ta) varied significantly depending on whether ¼ inch thick specimens, filings or electrolytic extractions were examined. Thus differences between a_o for γ and γ' phases for Ni-Al-Nb were 0.024Å for ¼ inch specimens, compared with 0.032Å for filings, whilst there was only 0.002Å difference in lattice parameter measured for γ' using filings and extracts. Very good correspondence (0.002Å maximum) was found between the lattice constants for matrix phases using bulk specimens or filings in the same work. Using a different superalloy Lemaire et al[76] reported that the constrained γ/γ' misfit i.e. difference in lattice parameter between matrix and gamma-prime phases in-situ was approximately an order of magnitude less than the unconstrained misfit.

The data in Tables 8 and 9 show that the lattice parameters of the matrix phases were higher than the accepted value for pure nickel (a_o = 3.5240Å) and with the exception of R12 alloy the lattice constants for the gamma-prime phases were higher than that given for stoichiometric Ni_3Al (a_o = 3.567Å). Such changes would be expected from additions of elements of larger atomic size. The maximum difference in lattice parameter measured for the gamma and gamma-prime phases was 0.22 per cent in

the as-cast alloys. Using law-of-mixture relationships with respect to the lattice constants of the pure elements, combined with the chemical analyses of the gamma phases, and the mean of the measured analyses for gamma-prime,very good agreement was obtained between measured and calculated lattice constants. For the MC phases acceptable agreement was obtained using the EPMA data and values of lattice constant for the stoichiometric compounds listed by Goldschmidt[72]. Measurable differences in lattice parameter generally occurred for the three principal phases after heat-treatment at either temperature. For the individual phases, the matrices generally appeared more affected than the gamma-prime after heat-treatment at both temperatures, an observation that to some extent reflects the stability of the age-hardening phase. However, because of the similarity of atomic sizes of Al, Ti, Nb, Mo, Ta and W the changes in lattice parameter induced by part-dissolution of the gamma-prime phases in the matrices at temperature may not have been very marked. It was also found that Δa_o, the measured differences in lattice parameter, between the γ and γ' tended to be reduced by both heat-treatments. For the MC phases the changes in lattice parameter were generally more marked after the 1050°C heat-treatment, although there was no obvious correlation with change of composition where the metal base of the MC altered (as in W37, cf W44 or R2). These changes in a_o for the MC phases could just as readily be accounted for by possible changes in the stoichiometry of the compounds, as reported in Reference 72, a_o TiC = 4.3280Å cf 4.3217Å at $TiC_{0.61}$, a_o NbC = 4.707Å cf 4.4318Å at $NbC_{0.77}$, a_o $TaC_{0.99}$ = 4.4555Å cf 4.4100Å at $TaC_{0.7}$. In W37 and W44 alloy two types of possible M_6C were detected. For W47 and W43 alloys there were some very faint lines that could have corresponded to hcp structures of the M_2C type i.e. (Nb, Ta Mo)$_2$C. For all experimental alloys there was no evidence of the presence of sigma or any other tcp phase from X-ray diffraction analyses. In contrast the model Nimonic 115 alloy blades exhibited very strong intensities of lines corresponding to both the sigma phase $\left(\frac{c}{a} = 0.52\right)$ and a phase with a cubic structure and a lattice parameter close to pure chromium (2.884Å). Similar observations have been reported by Lemaire et al[76] who detected precipitation of α-chromium and α-tungsten after heat-treatment of a superalloy. The $\frac{c}{a}$ value for the sigma phase in the Nimonic 115 alloy

correlates well with the X-ray data for Co Cr - Mo Ti type sigma $\left(\frac{c}{a} = 0.52\right)$ detected in IN100 alloy and Ni-Cr-Mo type sigma $\left(\frac{c}{a} = 0.54\right)$ in the work reported by Mihalisin et al, and that reported for sigma $\left(\frac{c}{a} = 0.517\right)$ in experimental superalloys by Kirby[65]. The MarM246 alloy creep-tested at 1040°C exhibited a much higher intensity of M_6C reflections than those for the MC phase in the X-ray measurements on electrolytic extractions.

Comparison between the calculated and measured densities of the cast alloys gave a generally acceptable level of agreement between the data; the maximum difference of 3 per cent occurring with R8 alloy.

Electron microscope investigations

It is evident from the literature that a great deal of attention has been addressed to the factors affecting gamm-prime precipitation in binary, ternary and in more complex superalloys. These factors include: nucleation, mismatch with the lattice and coherency, and the subsequent coarsening behaviour of the γ' phase. In commercial superalloys the shape of individual gamma-prime particles varies from spheres to perfect cubes although some precipitates have intermediate shapes. For example Hagel and Beattie[77] suggested that spherical particles were formed when the difference in lattice constants between matrix and precipitates was less than approximately 0.5 per cent, and cubes would result when the differences were in the range 0.5 to 1.0 per cent. When the disregistry was above 1 per cent, only discontinuous precipitation would occur. However, Heslop[78] showed that in Nimonic 115 alloy with a lattice misfit of less than 0.1 per cent, cuboidal γ' phase occurred, and the work by Havalda[79], Loomis et al[37] on the influence of tungsten and molybdenum on the morphology of γ' precipitation in nickel-base superalloys and evidence from the present work showed the Hagel-Beattie suggestion to be only partly valid.

From the present study there were three size ranges of gamma-prime particles present in the as-cast microstructures. The primary (or eutectic) γ' particles examined in replicas tended to be comparatively large i.e. many above 5μm, and generally of angular shapes. The secondary γ' particles assumed a cuboidal morphology and appeared as squares, triangles or trapezoids up to about 1μm in size. In certain alloys the

cuboidal particles appeared to be cut by three mutually perpendicular planes, each passing through the cube centre, thus giving eight sub-cubes of identical orientation. These appear as clusters of four cubes in the microstructure. Similar observations have also been recorded in the literature. In addition, even in unidirectionally solidified alloys, very fine dispersions of γ' ($<<0.1\mu m$) were observed in the as-cast microstructures. From examination of thin foils it was found that in the cubic morphology the γ' particles were aligned along preferred directions such that the faces of the cubes were parallel to both {100} γ and {100} γ'. In the UDS alloys (R6, R8, MarM246) the dendrites grew in the preferred <100> direction and because of the simple cuboidal geometry of the particles this also enabled easier and better accuracy of measurement of volume fraction of gamma-prime to be obtained. The occurrence of cuboidal γ' particles is not believed to indicate any fundamental difference in precipitation behaviour between alloys, but this shape is believed to be the most stable under given conditions of heat-treatment for a particular alloy. Udimet 700, Nimonic 115, IN100 and B1900 alloys contain both spherical and cuboidal γ' particles and a difference in strain energy and coherency of γ' would be expected from these size and morphological differences. From the present work on thin foils of alloys W37, W36, W49, W34, R14, R15, W41, R6, R8, MarM246, in the as-cast condition individual particles could not always be clearly resolved under bright field conditions (e.g. Figure 8). This was because of a number of factors, such as the coherent interface, coherency strains associated with the precipitates, foil thickness effects and slight staining that occasionally resulted from the difficult foil preparation procedures. Using selected precipitate reflections i.e. (100) in dark field mode, the shape and size of precipitates could be more accurately measured, but because of the variability in intensity of superlattice reflection between the alloys, the dark field work was sometimes tedious and did not always produce the desired improvement in resolution of the γ' phases. However, for all the experimental alloys examined in the as-cast condition there was no evidence of the need to relieve coherency strains by dislocations.

Heat-treatment for 2000 hours at 850°C caused the secondary γ' particles to spheroidise slightly and dissolve in the matrix. Small

changes also occurred in the shape of secondary γ'. From the replica studies the $\gamma - \gamma'$ eutectic found in the experimental alloys appeared to be unstable during the ageing treatment at 850°C. Although the reaction products were not identified, this effect has been reported for other cast superalloys (e.g. IN100 aged at 871°C) as being associated with the precipitation of a perovskite carbide[72] $Ni_3(Al\ Ti)C$ that has the same structure (fcc) as γ' and a lattice parameter of ≈3.6Å. Also, from work by Mihalisin et al[52] $M_{23}C_6$ particles were identified by electron diffraction in the primary γ' regions of IN100 after creep-exposure at 1500°F (816°C and 1114 hours exposure).

Although there was no evidence for the formation of sigma, or other acicular tcp phase in the experimental alloys, the Nimonic 115 alloy blade materials contained numerous acicular platelets that were identified by electron diffraction analysis as sigma. Confirmation was based on the evidence from thin foils using both the 1 MeV, and Philips EM300 microscopes, and from examination of extraction replicas. There were some difficulties in fully identifying sigma phase by selected-area-diffraction particularly in the direction of the c axis using the 1 MeV instrument, but for the extraction replicas using the 100 KeV microscope with the {001} planes normal to the electron beam these patterns could be indexed as sigma phase structures (a = 8.8Å).

From the examination of the experimental alloys heat-treated for 200 hours at 1050°C the size, shape and distribution of the gamma-prime phases altered significantly. The primary γ' phase was still present in roughly the same form as in the as-cast alloys, whereas the secondary gamma-prime tended to coalesce and its volume fraction was reduced in a similar way to the behaviour illustrated for MarM246 single crystal material in Figures 13 and 14. A further common point of interest between MarM246 and the experimental alloys was the presence of considerable quantities of tertiary gamma-prime in the structure even after water-quenching of specimens after heat-treatment had been completed. Although the cooling rate may have been too low to retain the ultra-fine precipitate particles in solid solution, there is the possibility that they are microstructurally stable at 1050°C. Dislocation networks were observed at the periphery of the secondary gamma-prime particles. There was a large variation in size and shape of the secondary gamma-prime particles in closely neighbouring areas of the same foil of MarM246 alloy.

Another difference between the experimental alloys and MarM246 after the 1050°C exposure was the apparent absence of acicular M_6C phases in the microstructure of the former.

PHACOMP relationships

One of the objectives of the present work was to investigate the ways in which the alloying elements partitioned between the phases in experimental superalloys in order to examine some of the assumptions or uncertainties used in the PHACOMP procedure. Apart from the work reported by Kreige and Baris[20], and that was concerned with the chemical partitioning of elements between the matrices and gamma-prime phases in commercial alloys, but which was not specifically orientated towards PHACOMP, and the work of Mihalisin and Pasquine[21], there appears to be little comprehensive information apart from that presented here, on the more detailed chemistry of the phases in superalloys. From these data it was clear that the titanium, niobium and tantalum alloyed preferentially with the carbon to form MC phases that were fairly stable during laboratory exposure at 850°C and 1050°C. These three elements, as expected from the available ternary phase diagrams, then alloyed with the gamma-prime phases in preference to the gamma matrices. The Group Vl elements chromium, molybdenum, tungsten, and separately cobalt, alloyed preferentially with the matrix phases. Among the Group Vl elements tungsten showed the least solubility in gamma-prime, this substantiated the data shown in Reference 34.

Apart from the model commercial alloys Nimonic 115 and MarM246, there was no marked propensity for any of the experimental materials to precipitate tcp or M_6C phases. With regard to PHACOMP the $\bar{N}v$ values for the parent cast alloys, evaluated by the Woodyatt method, Table 12, were too low to indicate the formation of sigma in the microstructure, but it may also be significant that neither $M_{23}C_6$ or M_6C were detected to any great extent by electron-beam or X-ray techniques. With the exception of the presence of the bcc phase in Nimonic 115 alloys the changes occurring in the microstructure of these materials and MarM246 alloy could have been anticipated from standard PHACOMP procedures. It is also noteworthy that IN100, Nimonic 115, TRW1900 and U700 have a sufficiently high $\bar{N}v$ value to predict the formation of sigma in the microstructure, whereas 713C and U500 alloy would be borderline cases.

The $\bar{N}v$ data calculated for all the alloys using the method of Woodyatt et al, but using Nv for constituent elements of 10.66 minus the Group Number (i.e. Nv Co = 1.66, Nv Ni = 2.66) gives a lower $\bar{N}v$ for all alloys, and the critical value to predict sigma formation appears to be above 2.50. Examination of the $\bar{N}v$ for the analysed gamma matrices in the as-cast or heat-treated condition using Nv Co 1.71, Nv Ni 0.66 and Nv = 10.66 - GN for the other elements gives fair agreement with the $\bar{N}v$ for the experimental alloys from the Woodyatt scheme, but a maximum difference of 0.6 electron "holes" occurs between the "matrix" and alloy composition for one Nimonic 115 blade material. Using the same calculation procedure for the alloyed gamma-prime phases the $\bar{N}v$ values are far higher than for the matrix phases for all materials and more closely approach the marginal value of 2.5 for sigma formation. Similar to the situation for the matrix phases, if $\bar{N}v$ of the gamma-prime is based on using Nv values of 10.66 - GN the $\bar{N}v$ are all lowered .. but there appears to be no obvious critical $\bar{N}v$ to indicate propensity to sigma formation. However, before attaching too much significance to these values of $\bar{N}v$ it should be appreciated that an error of 0.5 w/o Al in chemical analysis is equivalent to a change in $\bar{N}v$ of 0.08 and this change is an order-of-magnitude greater than for the same error in [Ni].

There is adequate evidence in the literature to suggest that the sigma phase does not precipitate directly from the γ-lattice, but is preceded by transition phases. The locations within the microstructure from which sigma appears to nucleate preferentially include grain boundaries, twin boundaries, and interfaces with second particles such as carbides and borides. For example $M_{23}C_6$ particles were observed to be the nucleation sites for σ in U520, Ni-18 w/o Cr-18 Co-15 Al (Reference 6) and Ni-20 w/o Cr-20 Co-5 Al-5 Ti alloy[80], η' carbide particles in René 41 alloy[45], and Ni_3Ti particles in Nimonic 115-type alloys[81]. It is generally accepted that the sigma has an epitaxial orientation with respect to the matrix such that the long axis of the sigma plates tend to parallel the <111> directions in the gamma phase. The σ plates often run boundary to boundary, possibly because the faces are coherent with the matrix.

From the present work sigma was observed and identified only in the two high $\bar{N}v$ Nimonic 115 blade alloys. It was extremely difficult to

identify precisely the original nucleation sites of this phase and the subsequent growth mode; because of etching effects causing relief at the boundaries of the sigma it was difficult to decide whether the sigma grew solely within the matrix phase. The writer believes that the observation of α-chromium platelets in the Nimonic 115 alloy samples was significant, as such particles could readily act at nuclei for sigma formation. Lemaire et al[76] also observed precipitation of α-chromium and α-tungsten both at the interfaces and in the mass of growing gamma-prime particles in a superalloy. Precipitation of Group V1 elements in the gamma-prime particles during heat-treatment may occur because of the decreasing solubility of Cr, Mo etc. with temperature (indicated by Figure 3). Dissolution of the gamma-prime precipitate in the nickel matrix may induce locally the development of high concentrations of Group V1 elements that react with Co etc. to form sigma and once nucleated the sigma phase particles may grow from such sites at the matrix/gamma-prime interface. Within the gamma-prime phase itself because of the limited solubilities of Group V1 elements and the movement of the phase boundary with temperature, precipitation of Cr, Mo and W may readily occur. Lemaire et al[76] reported such observations for a superalloy. In the present work very fine scale precipitation was observed within the gamma-prime cuboids in heat-treated alloys but the responsible species could not be identified. For the Nimonic 115 blade materials partly because of relief effects induced by electrolytic attack of the γ' and γ matrix around the sigma platelets, it was difficult to make observations with certainty, but it appears likely that the sigma phase grew coherently in both matrix and gamma-prime phases. From the present work and from the literature there is substantial evidence of sigma surrounded by gamma-prime.

Bulk gamma-prime alloys based on the analyses of Kreige and Baris[20] for IN100, and separately of Nimonic 115 and 713C alloys were arc-melted to produce 50 g buttons. After homogenising at 1270°C for 3 hours these alloyed gamma-prime materials were exposed for 2000 hours at 850°C. Precipitates of sigma phase were identified by X-ray diffraction in both Nimonic 115-type γ' and IN100-type γ' alloys, for the 713C-type γ' a bcc phase (a_o = 2.93Å), possibly a Cr-Mo rich phase, was identified. It is believed that the bcc phase in the 713C-type γ' would ultimately have

transformed to the sigma phase, hence supporting the general contention, also made by Mihalisin and Pasquine, that the alloyed γ' phase in super-alloys is at least as likely to precipitate sigma as a high $\bar{N}v$ matrix during exposure. Further studies of the role of alloyed gamma-prime may lead to a more complete understanding of PHACOMP. For a further point of interest typical analyses of γ' and matrices of the experimental alloys after heat-treatment at 850°C, one from each variant group of Tables 4 and 5, are plotted on the simple ternary phase diagram Figure 3. In these plots the phase compositions are based on the similarity in behaviour and hence grouping together of: (Ni + Co), (Cr + Mo + W), (Al + Ti + Nb + Ta). The analyses of the matrices and gamma-prime phases in the experimental alloys appear to be in fair accord with the phase-fields indicated by the simple Ni-Cr-Al diagram. In PHACOMP studies reported elsewhere the Nv value of Cr is accepted as 4.66 but those ascribed to Mo and W (4.66 to 9.66) have been a source of contention. From the ternary phase diagram with Ni and Al, it is obvious, but not so far explained, that the solubilities of Mo and W in the γ' phase are very much lower than that of chromium. Hence more attention to the role of γ' in PHACOMP studies may assist in understanding the apparent anomalous behaviour of Mo and W.

Conclusions

Twenty-four experimental alloys and two commercial alloys were studied to characterise the structure and composition of phases found in the microstructure.

1. For the experimental alloys in both the as-cast condition and after heat-treatment for 2000 hours at 850°C, or 200 hours at 1050°C, elements that tended to form monocarbide (MC) phases i.e. titanium, niobium and tantalum tended also to alloy preferentially with the gamma-prime phases.
2. Chromium, cobalt, molybdenum and tungsten alloy preferentially with the matrix phases.
3. Small amounts of boron were often associated with the monocarbide phases.
4. Generally good agreement was obtained between the chemical analyses and microprobe analysis data for the alloyed gamma-prime phases.

5. Good correlation was also obtained between the chemical composition, calculated and measured lattice constants of the phases and the measured and calculated densities of the parent alloys.

6. A series of linear regression equations was developed to relate the composition of the phases and parent alloys.

7. Apart from slight structural changes occurring within the microstructure that were anticipated from consideration of simple phase diagrams in the literature, none of the experimental alloys showed any tendency to precipitate tcp phases during exposure at 850°C, or significant precipitation of M_6C during exposure at 1050°C.

8. From the electron microscope examination of thin foils and replicas prepared from bulk testpieces it was found that the 850°C treatment caused slight dissolution of secondary gamma-prime and decomposition of eutectic gamma-prime phases.

9. Heat-treatment at 1050°C caused significant coalescence of the secondary gamma-prime phases.

10. Structures water-quenched after 200 hours exposure at 1050°C contained very fine tertiary gamma-prime that may have precipitated in the short duration of the quench.

11. In the as-cast condition i.e. including the unidirectionally solidified alloys, the matrix and γ' precipitates were coherent, there was little evidence of the presence of dislocations, but a very fine precipitate was present within some cuboids.

12. In comparison the Nimonic 115 alloy blade materials showed extensive precipitation of sigma platelets in the microstructure, and the MarM246 alloy also showed a typical Widmanstätten structure identified as M_6C platelets.

13. With reference to the PHACOMP analysis it was found from the measured compositions of the gamma-phases in these alloys that account should be taken of the aluminium, titanium, niobium and tantalum in the various matrices.

14. The γ' and MC in the experimental alloys appeared to be fairly stable and these observations are unlikely to apply for all superalloys.

15. Bulk gamma-prime alloys based on compositions taken from the literature have been shown to precipitate sigma phase during heat-treatment.

16. From observations of sites for sigma formation in the Nimonic 115 alloy blades it was considered that the phase grew continuously in both γ' amd matrix phases, and a mechanism was proposed for the nucleation (i.e. precipitation of Group Vl elements) and subsequent growth in both phases.

17. It is considered that a better understanding of the roles of molybdenum and tungsten in sigma precipitation may be obtained from the more detailed study of alloyed gamma-prime phases.

CHAPTER 4

Mechanical properties and microstructure

The second phase of the programme involved a limited study of the short-time creep-rupture strengths of a series of experimental superalloys in the conventionally-cast form. Selected alloys were also examined in the unidirectionally solidified condition. Some tensile tests were done. Hardness changes of the alloys and miniature Charpy impact values were measured after heat-treatments had been applied that would induce undesirable changes in the microstructure i.e. sigma-phase and M_6C precipitation in unstable alloys. Structural changes induced by creep and thermal exposure without stress were followed using optical and electron metallography. Factors governing the creep and short-time tensile behaviour i.e. coherency strains, stability of the precipitate (gamma-prime solvus temperature) and general microstructural features were tentatively explored.

Materials and experimental procedures

The melting and casting procedures for the experimental alloys outlined in Chapter 3 were used to produce the typical cast mould assemblies illustrated in Figure 6. Testpiece blanks were removed by slitting from these assemblies.

Mechanical testing

Constant load creep-rupture tests were carried out in air at three standardised conditions, 850°C/30 tsi, 1000°C/10 tsi and 1040°C/7 tsi on all alloys, except for the very weak R12 alloy, in the conventionally cast condition. At these and higher temperatures comparative tests were done on commercial alloys IN100 and MarM246. The stresses were sufficiently high to produce rupture in about 200 hours maximum. Some creep tests were done on the UDS alloys at the same conditions, with additional tests being done at intermediate temperatures (750/760°C) to explore the extent of primary creep under high stress conditions. Creep tests were repeated for aluminised-coated R6 alloy to explore the influence of oxidation processes on the short-time creep-rupture behaviour. The creep testpieces 63 mm long, with a gauge portion 20 mm long, a diameter of 3.99 mm and 8μ in. finish were prepared by conventional wet grinding processes.

The strain during tests was measured from extensometers clamped to the flanges machined at the ends of the testpiece gauge length.

In order to determine the susceptibility to microstructural instability i.e. sigma phase precipitation that may cause embrittlement of the alloys in service, miniature Charpy impact tests were done at room temperature on unmachined testpieces in the as-cast condition and after heat-treatments designed to precipitate sigma phase (2000 hours exposure at 850°C) and eta carbide, M_6C, (200 hours exposure at 1050°C) in the microstructure of susceptible alloys. For comparison impact tests were done on fully heat-treated Nimonic 115 alloy testpieces machined from bar stock and testpieces machined from turbine blades that had prematurely fractured in a brittle manner during service due to the presence of large amounts of sigma phase; one blade that had been in service but was free of sigma was also examined. The compositions of the Nimonic 115 alloy blade materials are listed in Table 2. Impact tests were also done on MarM246 alloy testpieces that contained M_6C precipitates. The impact testpieces were 1.7 in. (43 mm) and 0.11 in. (2.8 mm) square and unnotched.

A few tensile tests were done at room temperature and 750°C on two alloys R6 and R8 in the conventionally-cast and unidirectionally solidified condition. Hardness checks were made on alloys in the as-cast condition and after heat-treatments and creep-rupture tests had been completed to determine whether these measurements could be correlated with their creep-rupture behaviour.

Metallographic and other observations

In all instances the casting soundness was judged by the standard optical metallographic procedure described previously. In many instances structural changes induced by tensile or creep-processes were explored using replicas or thin foils, the latter spark-eroded from the gauge portion or heads of tensile-creep testpieces. Observations were also made on UDS MarM246 alloy single crystal and polycrystalline testpieces. These studies were supported by X-ray diffraction and electron probe microanalysis of the alloy microstructure. The solvus temperature of the gamma-prime precipitate in the various alloys was measured using commercially available differential thermal analysis equipment (Stanton 6-25). In

this technique a hollow, cylindrical testpiece approximately 12.5 mm × 7.5 mm diameter was spark machined to fit a quartz capsule that was pre-evacuated and pressurised (200 mm) with argon. The quartz capsule with a re-entrant bay accommodating a thermocouple was fitted to a similar capsule containing a platinum standard. In practice the solvus temperature was measured during heating of the alloys to above the liquidus (a maximum of about 1380°C) and subsequently during controlled cooling, and the mean of three determinations recorded. The equipment was calibrated by measuring the melting point of pure metal standards and by comparing gamma-prime solvus temperature data for commercial superalloys such as Nimonic 90, Nimonic 115, IN100, Nimocast 713C, MarM200 and MarM246 alloy. The accuracy of measurement for the melting point or liquidus of the various metals and alloys tested was estimated at ±5°C at about 1455°C, similar to that of the best data obtained for the gamma-prime solvus temperature. The gamma-prime solvus temperature measurement was supported by optical metallographic examination of testpieces water-quenched from about 15°C above that temperature.

Results

The general metallographic features of the experimental alloys have been described in Chapter 3. A pre-requisite for mechanical testing was a judgment on casting soundness i.e. in terms of freedom from gross defects such as unacceptable levels of microporosity and oxide inclusions, and uniformity of structure. Interdendritic shrinkage porosity was uniformly dispersed at about the 1.0 v/o level* in the conventionally-cast alloys which were also free from mould inclusions. The UDS alloys showed the typical columnar <100> growth pattern of the polycrystals, but with some non-planar solidification (growth faulting) and columnar grain boundaries following an irregular path between the interlocking dendrites i.e. with small sections of grain boundary becoming transverse or inclined to the principal growth direction. Regions containing small spherical holes (i.e. gaseous porosity) were detected in the UDS alloys, the amounts of which were presumably related to the furnace chamber pressure. The volume fraction of the gamma-prime phase was found to be similar to that

* v/o = volume percentage

in the conventionally cast alloys. Dendrite arm spacings of all the alloys, irrespective of the casting method, were in the range 60 to 80μm. Grain sizes of the conventionally cast alloys were similar, i.e. approximately 5 mm. The majority of grains extended over the entire length of the UDS alloys and were typically 150 mm long with a spread in diameter from about 3 mm at the base to about 6 mm near the top of the casting.

Differential thermal analysis

The DTA measurements of γ' solvus temperature during cooling of testpieces are listed in Table 13 for the experimental and some commercial superalloys. Solvus temperature data for the commercial alloys from the literature are given for comparison. For the experimental alloys the solvus temperature measured during cooling was about 35°C lower than that indicated during the heating cycle. The solvus temperature measurement during cooling was very much sharper on the trace of temperature difference versus average temperature, than that of the gradual endothermic change occurring during the heating cycle. A schematic DTA trace is shown in Figure 15.

Hardness tests

The hardness values of the experimental alloys in the as-cast and heat-treated conditions (850°C and 1050°C) are listed in Table 14. The data include both the range and mean of at least six measurements made within the dendrites (i.e. away from grain boundaries, large carbide particles etc). In the as-cast condition most of the alloys had VPN values above 320 VPN; three alloys W37, W34 and W41 had average VPN values in excess of 400, and the softest material (VPN 237 ±11) was R12 alloy which contained aluminium (as Ni_3Al) as the principal strengthening element. For all alloys there was a significant spread in hardness values for any condition examined. Mean values of hardness for the individual alloys in the as-cast and heat-treated condition are plotted as a function of lattice parameter mismatch between the matrix and gamma-prime phases in Figure 16. No significant correlation could be found between the alloy hardness and lattice parameter misfit between matrix and gamma-prime.

Heat-treatments for 2000 hours at 850°C, or 200 hours at 1050°C caused some change in the average VPN for most alloys. For some alloys

the effects were small and were masked by the scatter in results. The effects of the 850°C treatment were somewhat variable; the hardness of R5 and W47 alloy decreased by 45 and 36 VPN respectively, whilst the hardness of W44 alloy was increased by 33 VPN. The 1050°C treatment caused softening of most alloys, the effect being most marked for R7 alloy with a reduction of 47 VPN, whilst alloys W49 and R14 were not affected to any significant extent. The hardness ranges of the Nimonic 115 alloy blades containing sigma phase in the microstructure were higher than that of the sigma-free blade material, but were still within the hardness specification published by the alloy manufacturer. Resolution of the sigma phase by thermal exposure for ½ hour at 1000°C produced a decrease in hardness for the Nimonic 115 alloy. The MarM246 alloy testpieces showed a hardness decrease after exposure at 1050°C.

Miniature Charpy impact tests

Table 15 lists the miniature Charpy impact test data for plain (unnotched) testpieces in the as-cast condition and after heat-treatment at 850°C and 1050°C. Included for comparison are data on Nimonic 115 alloy testpieces machined from bar stock and from turbine rotor blades that had been prematurely removed from three different industrial engines. One set of industrial engine blades containing sigma had been operating for about 1360 hours with a mean temperature of the midspan, from which the testpieces were machined, of about 850°C. The other set of blades containing sigma phase operated under similar conditions for approximately 8000 hours, whereas the third blade set (sigma-free) had operated in the same temperature regime but for a shorter time (950 hours). From the chemical analyses given in Table 2 the calculated average electron vacancy numbers $\bar{N}v$ of the sigma-containing Nimonic 115 alloys were approximately 2.84 and 2.73 respectively compared to the borderline value for the sigma-free alloy of 2.54. MarM246 alloy testpieces cast under similar conditions to the experimental alloys were tested in the as-cast condition and after exposure for 200 hours at 1050°C.

In the as-cast condition the impact strength values of most of the experimental alloys were typical of those for other cast nickel superalloys i.e. MarM200, MarM246, 713C, IN100. There was a considerable spread in impact values for most alloys i.e. typically in the range of about 1.0 to

4.0 ft/lbf (1.3 to 5.2 J) with a few in excess of these values. Relative to the wrought Nimonic 115 alloy in the fully-heat-treated condition (1½ hours/1190°C/air cooled + 6 hours/1100°C/air cooled), with the exceptions of single testpieces in R1, W49 and the generally high values for R12 alloy, the cast alloys fractured at lower energy levels. Heat-treatment for 2000 hours at 850°C had negligible effect on the toughness of the experimental alloys, compared with the effect of service exposure on the Nimonic 115 alloy blades containing sigma phase (<0.1 ft/lbf) at room temperature. The comparative brittleness induced by sigma phase precipitate in the Nimonic 115 alloy blades was retained to a temperature of at least 750°C (0.1 ft/lbf) compared with values in the range 6 ft/lbf to over 10 ft/lbf for the fully heat-treated alloy in the unexposed condition, and about 8 ft/lbf for the sigma-free blade material. Heat-treatment for ½ hour at 1000°C redissolved the sigma phase, with minimal apparent effect on the gamma-prime morphology, and significantly improved the toughness (>3.5 ft/lbf) at room temperature. Heat-treatment of the experimental alloys and MarM246 alloy for 200 hours at 1050°C had some small effects on their impact behaviour at room temperature, but no significant embrittlement was observed despite the large amount of M_6C phase that precipitated in MarM246 alloy.

Tensile test results

The tensile test results for conventionally-cast and unidirectionally solidified R6 and R8 alloys are listed in Table 16. Values of 0.2 per cent proof stress and ultimate tensile strength for these experimental alloys were similar to those of other high strength casting alloys such as MarM200, MarM246 and MarM002 for any material and test condition. The two main features of the behaviour of these experimental alloys included the ductility improvement afforded by unidirectional solidification, and the reduction in tensile ductility which occurs in the intermediate temperature region (700 to 850°C) for most gamma-prime strengthened superalloys.

Creep-rupture tests

Table 17 lists the creep-rupture test data obtained at 850°C, 1000°C and 1040°C for all of the conventionally-cast alloys. The data are presented as times (h) to produce 0.1, 0.2, 0.5, 1.0 per cent creep strain, duration of secondary creep, rupture life and creep rate (per cent h^{-1});

also included are the levels of primary creep strain and the elongation at rupture. Representative creep-rupture curves for a range of alloys are shown in Figures 17 to 19 for each of the three test conditions, 30 tsi/850°C, 10 tsi/1000°C and 7 tsi/1040°C. Excluding R12 alloy test-pieces that prematurely fractured during loading, plots of the mean times to selected levels of creep strain (0.5 and 1.0 per cent) and rupture-life as a function of the gamma-prime solvus temperature are illustrated in Figures 20 to 22. The times taken to reach selected creep strain levels and rupture failure were related to the mean levels of 'as-cast' hardness of the various alloys (excluding R12) as shown by the linear regression lines included in Figures 23 to 25. Summaries of the relationships derived for expressing the creep-rupture properties as functions of the γ' solvus temperature and 'as-cast' hardness are given for the various test conditions in Table 18. No significant relationship was derived between creep rate and hardness or γ'-solvus-temperature for any test condition. It was also found that there was no obvious relationship between either the creep-rupture properties or the hardness and mismatch in lattice parameter between the matrix and gamma-prime phases. Examination of the creep-rupture data in Table 17 shows that W37 and W41 alloy clearly stand out relative to the other materials tested, but their strength advantage was offset by their higher specific gravity.

The results of the creep-rupture tests for conventionally-cast and unidirectionally-solidified alloys are compared in Table 19. Data are also included for a low carbon-content (LC) R6 alloy in which the titanium-content and the amounts of other carbide forming elements were proportionately reduced in relation to the carbon content. Tests were also done on pack-aluminised coated R6 alloy in the UDS condition to investigate the influence of a typical coating used in aero-engine practice.

These data and those illustrated in Figures 17 to 19 show that one of the principal benefits of UDS at any temperature is the improved ductility, recorded as elongation-at-rupture. At the lowest 'standard' test temperature i.e. 850°C, for both R6 and R8 alloy the durations to produce the given levels of creep strain were generally greater whilst the secondary creep rates were generally lower in the conventionally-cast condition. For both alloys the rupture lives were longer in the UDS condition, the

effect being more significant for R8 alloy (200 hours average for UDS cf 91 hours for conventionally-cast condition). The low-carbon version of R6 behaved similarly to its higher carbon-content parent. At 1000°C/ 10 tsi in the UDS condition for the one test done R6 alloy had the longest rupture life (218 hours), but that of the best conventionally-cast testpiece (149 hours) was close to those for the UDS low-carbon alloy (158 hours and 161 hours). The rupture-life of the UDS R8 alloy was similar (168 hours cf 167 hours) to the better of the two results for the conventionally cast condition. Durations of secondary creep were generally longer for both alloys in the conventionally-cast condition. At 7 tsi/ 1040°C the maximum rupture lives and time to 1 per cent strain for R6 in either condition were similar. The one test on R6 LC UDS gave longer durations to produce the given creep strains and a lower secondary creep rate, but no improvement in rupture life relative to the conventionally-cast R6 alloy. Because of the scatter in creep-rupture data at any test condition for the uncoated alloys, in the single test conducted on aluminised-coated R6 alloy testpieces it is difficult to separate any significant effects of the aluminising coating process on the short-time creep-rupture behaviour.

A few creep-rupture tests were done on R6 and R8 alloy at a high stress condition at intermediate (ca 760°C) and a higher temperature (1100°C) for general comparison with the behaviour of other superalloys. Particular interest was centred on the amount of primary creep occurring in UDS alloys at stress levels approaching the yield stress at about 760°C. Data for unidirectionally-solidified MarM200, IN100 and B1900 alloy tested elsewhere[83] at 1400°F (∿762°C) and 85 ksi (∿38 tsi) have shown that high levels of primary creep strain (>5 per cent) can occur. More detailed investigations[84] of the influence of stress on MarM200 alloy UDS have shown that approximately 4.0 per cent primary creep strain can occur in creep tests at about 45 tsi/762°C. In the NGTE tests at 42 tsi/ 750°C the primary creep strain levels for UDS R6 alloy including the aluminised-coated testpieces, were in excess of 4 per cent. Similar observations were made for both R6 and R8 in tests at 45 tsi/760°C.

A general comparison between the creep-rupture properties of R6 and R8 alloys, and commercial superalloys under similar test conditions, is given in Table 20. At 30 tsi/850°C in the conventionally-cast condition the durations to 0.5 per cent or 1.0 per cent creep strain for R6 alloy exceeded those for the other alloys listed. Apart from the very dense HRA-376 alloy the rupture-life of conventionally-cast R6 alloy was also the longest. In the UDS condition R6 and R8 alloy were considerably stronger than IN100, but their rupture lives were similar to that for MarM246 alloy. A similar pattern of behaviour was also observed in the creep-rupture tests at 7 tsi/1040°C. For the few available data at 4 tsi/1100°C it is clear that IN100 alloy is very weak in comparison to the other alloys. Relative to MarM246 alloy in the conventionally-cast or UDS condition both R6 and R8 alloy have a marked rupture-life advantage i.e. approximately 720 hours for UDS R8 cf 142 hours maximum for UDS MarM246. In one test at 4 tsi/1150°C one UDS R8 alloy testpiece ruptured in 22 hours and in the conventionally-cast condition ruptured in 16 hours. Table 21 lists the temperature capability of selected experimental and commercial superalloys for 100 hours rupture at three stress levels. On a specific strength (strength/density) basis IN100 is clearly the strongest material up to about 1050°C, above which alloys of the R6, R8 type appear more attractive.

Metallographic observations after creep and tensile testing

Figure 26 shows typical optical micrographs of sections taken near to the fracture surfaces of conventionally-cast alloys after creep-rupture testing at 850°C. In common with similar testpieces creep-rupture tested at 750°C, 1000°C (Figure 27) or 1040°C (Figure 28) and those fractured in tensile tests at room temperature it was noted that intergranular cracking occurred on the grain boundaries oriented normal to the principal stress axis. The microcracks away from the fracture surfaces often propagated through the carbide decorated regions at the periphery of the eutectic gamma-prime. These fissures in the creep testpieces were usually oxidised and the extent of oxidation attack was generally more marked with increasing test temperature. From an examination of ruptured testpieces there was some evidence of cavitation and void formation particularly at carbide particle boundaries and ahead of an advancing intergranular crack of the

type that is associated with creep-failure of wrought superalloys. For the unidirectionally-solidified alloys the columnar grain boundaries were not truly linear but followed the irregular paths between interlocking dendrites. In these creep testpieces cracking was often observed to have occurred along small transverse segments of the grain boundaries in the same way as in conventionally-cast alloys, and in certain instances the fracture paths followed the boundaries of the columnar grains.

Some structural changes were observed to have occurred during the creep-rupture tests at or above 1000°C. For example, there appeared to be some coarsening of the secondary gamma-prime precipitate into long stringers and other irregular (non-cubic) shapes. Partial dissolution occurred of small MC particles located at grain boundaries and within the dendrites. These appeared to be surrounded with a white etching phase (presumed to be γ') in some of the less creep-resistant alloys. After tests at 1040°C dissolution of MC particles was very marked with MarM246 alloy, the carbide particles randomly located within the dendrites and the grain boundaries being surrounded by a continuous 'white-etching' film (γ').

No significant changes in general microstructure of alloys creep-rupture tested at 750°C or 850°C were observable at optical microscope resolution (ca 0.5μm) apart from the oxide films which were present at the surfaces of all testpieces on termination of the tests. Below the surface oxide films were zones apparently free of gamma-prime precipitate and occasionally containing unidentified, very fine acicular precipitates that were presumed to be oxides or nitrides.

Electron microscope studies of thin foils machined from tensile and creep-rupture testpieces subjected to controlled levels of strain and after fracture showed more details of the microstructural deformation processes occurring within the bulk of the alloys. For example, in both conventionally-cast and UDS structures very fine dispersions of (tertiary) gamma-prime were observed between the secondary gamma-prime precipitates; they were identified as such from dark-field observations. These finer dispersions of gamma-prime appeared to play a very important role in controlling the dislocation substructure within the alloys. Figure 29 shows

typical microstructures of an alloy that has been lightly deformed (up to 0.2 per cent strain) in tensile tests at room temperature in comparison to some which were taken very close to a fracture surface of a similar testpiece after completion of a tensile test. In the foils machined from the lightly deformed alloy most of the dislocations were restricted to the regions between the secondary gamma-prime particles, although a few straight, apparently single dislocations and occasional stacking faults were observed in the secondary gamma-prime particles. For the foils machined near the fracture surfaces from the tensile testpieces, as deformation is inhomogeneous, the microstructure was variable. In regions lying between the slip bands there appeared to be a few single dislocations and occasional stacking faults associated with the secondary gamma-prime. The γ' precipitate boundaries were often delineated by heavy concentrations of dislocations that could not be individually resolved. It was noted that the apparent blackness in some micrographs was due to the presence of a large number of dislocations and is not a staining effect. Other foils showed that much of the deformation was concentrated in the slip bands with very dense tangles of dislocations in both "matrix" regions and secondary gamma-prime particles. The designation "matrix" refers to the material separating the individual (cuboidal) secondary gamma-prime particles and includes the dispersion of very fine (tertiary γ') particles in the matrix phase.

Thin foils prepared from tensile or creep-rupture testpieces after testing in the range 750°C to 850°C (Figures 30 to 33) had many similar features to those tensile-tested at room temperature. There were generally more stacking faults within the secondary gamma-prime particles, and a few apparently single dislocations compared against the "matrix" regions which were decorated with heavy concentrations of dislocations. Figure 32 shows very heavy tangles of dislocations in both matrix and gamma-prime. For the duration of these tests there was no obvious spheroidisation or dissolution of the secondary gamma-prime particles. Using the microscope in dark-field mode the tertiary gamma-prime particles were readily evident*.

---

*Additional spots are present in the selected area diffraction patterns (SADP) in all of these illustrations in consequence of dust particles picked up during the report reproduction process.

During the creep-rupture tests at 1000°C there was evident coarsening and some change in shape of the secondary gamma-prime particles in many alloys. The dislocations generally tended to form tangles and with few exceptions were unpaired (i.e. there were few resolvable super dislocations). In many instances the dislocations lay in loops apparently on the surfaces of the secondary gamma-prime particles.

After creep testing at 1040°C coalescence and distortion of the secondary γ' was more marked, but the dislocation substructure was generally similar to that after tests at 1000°C (see Figures 34 to 36). Some polygonal networks of dislocations were present at the interface of the matrix and secondary gamma-prime particles. Tertiary γ' particles were evident in all polycrystalline alloys examined and in the single crystal MarM246 alloy testpieces that could only be furnace-cooled (i.e. not quenched) after rupturing. It was of particular interest to note the change in morphology of the secondary gamma-prime particles in the foils machined in the longitudinal direction from the gauge length regions of all testpieces examined. The observations made on the morphology and distribution of gamma-prime phase in the thin foil work were also confirmed by the examination of replicas taken from the gauge length and heads of creep-rupture testpieces. From examination of replicas and scanning electron microscopy (SEM) of grain boundary and interdendritic regions near to fracture surfaces occasional cracking was observed for the experimental alloys. There was little evidence of the formation of a second phase (γ') nor any denudation of γ' precipitate from the matrix regions near the grain boundaries of the stronger alloys. In contrast MarM246 alloy testpieces showed apparently continuous grain boundary films of γ' after 1040°C creep-rupture tests (see Figure 37), but the mottled appearance of some of these regions suggested that they could be composed of two phases (matrix and tertiary γ').

Electron microprobe analysis

A JEOLCO JXA-3A electron microprobe analyser was used to supplement the general optical and electron metallographic observations of microstructural changes occurring during creep, relative to the effect of exposure at temperature in the absence of stress. In particular evidence was sought for the formation of grain boundary films of gamma-prime that has been

reported to occur in some superalloys, in addition to identifying $M_{23}C_6$ or M_6C phases that may have formed during exposure at temperature.

From examination of a number of alloys tested at 30 tsi/850°C there was no systematic variation in composition of the dendritic material (γ + secondary γ') at the boundaries, nor any marked change in the composition of the MC particles that were of sufficient size for electron probe microanalysis (EPMA). There was some evidence for an occasional increase in concentration of chromium at some grain boundaries, although if this was associated with precipitation of $Cr_{23}C_6$ particles these were too fine for positive identification by EPMA. Similarly there was occasional evidence for localised concentrations of molybdenum at some grain boundaries, but if associated with $M_{23}C_6$ or M_6C particles these also were too fine for identification. These general observations also applied to testpieces creep-tested at 1000°C or 1040°C. Generally, apart from intergranular oxidation associated with general propagation of creep cracks there were no obvious systematic compositional changes that could be identified by EPMA occurring in consequence of the applied stress in creep. Figure 38 shows the apparently unchanged structure of a dendrite decorated by tantalum and molybdenum-rich carbide particles after the alloy was creep-rupture tested for 101 hours at 1000°C.

In contrast to the experimental alloys, after heat-treatment or creep-rupture tests at 1040°C the grain boundary regions of MarM246 alloy, illustrated in Figure 37, were found to be high in aluminium which may have been associated with the formation of a film rich in γ'. The acicular precipitates and some grain boundary particles were found to be deficient in Ti, Nb, Ta, but rich in Mo and W, the Group Vl elements being associated with the formation of M_6C.

Discussion of results

The major objective of this work was to develop new alloys with better or equivalent high temperature creep-rupture properties compared to the model HRA-376 alloy, but with a lower specific gravity and without sacrifice to the ductility and good microstructural stability of the parent alloy. In the general scheme the choice of alloy compositions explored and the method of manufacture was constrained to a large extent by the composition of the parent alloy and the 'enlightened empiricism'

and technological and commercial restraints governing its method of manufacture. Ideally single crystal alloys would have been studied. The nature and quantity of alloying elements that were substituted in the experimental alloys were selected to have minimal effect on the structure and volume fraction of the phases found in the microstructure, but with lower density.

Mechanical properties

With the exception of the model R12 alloy (free of refractory metal hardeners) the range of hardness values listed for the experimental alloys in Table 14 was fairly typical of those obtained for the commercially available cast superalloys such as IN100, IN713C, MarM200, MarM246 and MarM002, developed for high temperature creep-resistance. The effects of heat-treatment for 2000 hours at 850°C or 200 hours at 1050°C generally caused some changes in the average hardness values for most alloys, but in most instances these were masked by the scatter in results. After exposure at 850°C the most marked changes in hardness occurred in three alloys: R5 and W47 alloy became softer (by 45 and 36 VPN respectively) while W44 showed a hardness increase of 33 VPN. No significant change in hardness occurred for two alloys (W49 and R14) after the 1050°C heat-treatment, whereas general softening occurred for most alloys, this effect being most marked for R7 alloy which showed a reduction of 47 VPN. With the exception of the so far unexplained increase in hardness of W44 alloy after exposure at 850°C the general softening that occurred throughout the alloy series was not associated with those microstructural changes that caused embrittlement, but was due to microstructural changes associated with overaging and dissolution of the gamma-prime precipitate. There was no obvious correlation between the hardness changes occurring in consequence of heat-treatment and the measured solution temperature of the γ' precipitate listed in Table 13. Empirical relationships were derived between alloy hardness and creep-rupture properties. This indicated that the as-cast hardness could be used as a sorting tool in cast superalloy development.

The miniature Charpy impact test data listed in Table 15 show a significant variation in fracture energy values for both the experimental

and commercial superalloys. All of the testpieces were fractured with the exceptions of one machined from fully heat-treated Nimonic 115 alloy bar, one from W49 alloy and two R12 alloy testpieces in the as-cast condition. The fractures were ductile and were associated with significant plastic deformation. Heat-treatment for 2000 hours at 850°C had a somewhat variable effect on the fracture energy values of the experimental alloys, but the testpieces fractured in a ductile manner. None broke in the brittle mode of the Nimonic 115 alloy blades containing the sigma phase precipitate in tests at room temperature or 750°C ($E \leq 0.1$ ft/lbf). Nimonic 115 alloy testpieces machined from bar stock in the fully heat-treated condition and those machined from a turbine rotor blade material free of sigma phase but engine tested under similar conditions to one of the sigma-containing alloys had very high fracture energy values at room temperature (E = 8.3/8.6 ft/lbf). Thus the embrittling effect of sigma phase, in the absence of any other identifiable microstructural change was established and could clearly be separated from observed creep-induced damage (viz extensive cavitation at grain boundaries that may have induced marked weakening). Heat-treatment for ½ hour at 1000°C redissolved the sigma phase precipitate with minimal effect on the morphology and distribution of the gamma-prime phase. It reduced the hardness and considerably improved the fracture energy values and ductility of the alloy. Heat-treatment of the experimental alloys for 200 hours at 1050°C had a variable effect on their room temperature impact behaviour. Three alloys R4, R7 and R9 had fracture energy values of less than 1.0 ft/lbf after the 1050°C exposure, but subsequent metallographic examination showed that the reduction in toughness was due to the presence of casting defects (cavities) caused by poor feeding during solidification, and was not a consequence of the presence of an embrittling phase being produced in the microstructure. It was significant that although M_6C precipitated in the MarM246 alloy during 1050°C exposure it did not embrittle the alloy, in fact the values of impact energy of the MarM246 alloy testpieces appeared to be increased by the 1050°C exposure. Subsequent metallographic examination showed that the carbide phases originally present at the grain boundaries had partially reacted with the surrounding matrix material and were encircled

by a 'white-etching' phase that was presumed to be rich in gamma-prime. Such reactions have been reported to occur in other superalloys and it is generally accepted that the gamma-prime reaction product improves the ductility (stress-redistribution capability) of the grain boundary regions. Thus these grain boundary effects may have had a predominating influence on the impact behaviour of MarM246 after high temperature exposure.

No detailed investigation was made of the tensile properties of any of the experimental alloys but a few tests were done on R6 and R8 at room and intermediate temperatures. The values obtained for 0.2 per cent Proof Strength, Ultimate Tensile Strength and elongation-at-fracture for R6 and R8 (Table 16) were in the same range as for other high strength cast superalloys, IN100, MarM200, MarM246 alloy.

Comparative creep-rupture data for the experimental alloys and commercial cast superalloys are listed in Tables 17, 19 and 20. In terms of the programme objectives there was a requirement for equivalent or better creep-rupture strength to HRA-376 alloy (W37) at a lower density (and preferably ≤ 8.6 g/cc) concomitant with the avoidance of microstructural instability that may cause premature failure. Data for the same test conditions were included for the commercial superalloys IN100 and MarM246. In assessing the relative creep-rupture performance, at stress levels found in turbine parts the amount of primary creep strain should be less than 0.5 per cent[83] and secondary creep rates should be minimal and maintained at a constant level for the longest possible duration. Taking as a basis for promising alloys being the achievement of 100 hours mean lifetime for each of the test conditions irrespective of alloy density then Table 17 shows that at 7 tsi/1040°C W41 alloy (233 hours) was the strongest, followed in turn by W37 (206 hours), R6 (188 hours), R3 (187 hours), R8 (177 hours), W50 (175 hours), W44 (173 hours), R10 (164 hours), R13 (164 hours), R5 (155 hours), W34 (148 hours), R7 (128 hours), R15 (125 hours), R4 (123 hours), R14 (120 hours) and R11 (117 hours). The superiority of W41 and W37 alloy over the other alloys at 7 tsi/1040°C was also demonstrated by their longer durations to 1 per cent creep strain and lower secondary creep rates. At 10 tsi/1000°C W37 alloy (258 hours) was the strongest of the alloys fulfilling the target

requirements. It was followed in turn by W41 (207 hours), W34 (146 hours), R5 (136 hours), R10 (136 hours), R6 (125 hours), R13 (115 hours), W44 (114 hours), W50 (114 hours), R7 (114 hours), R3 (110 hours), W43 (106 hours) and R11 (103 hours). In the tests at 30 tsi/850°C W34 (153 hours) was the strongest alloy closely followed by W37 (152 hours) and in turn by R13 (one test duration of 141 hours), R6 (one test duration of 125 hours) and W41 alloy (119 hours). The alloys satisfying the mean lifetime requirements of 100 hours for each of the three test conditions were W37, W34, R13, W41 and R6.

From the data listed in Table 17 and those following, Table 21 summarises the calculated temperature capability for 100 hours rupture lifetime for the conventionally-cast and UDS alloys at stress levels of 30 tsi, 7 tsi and 4 tsi respectively. At 30 tsi W37 was the strongest conventionally-cast alloy, offering a temperature advantage of 28°C over IN100 alloy and 20°C over MarM246 alloy; alloys R6 and R8 also showed temperature advantages over the two commercial alloys. At 7 tsi W41 was the strongest conventionally-cast alloy, followed by R6 and R8 alloy, the latter giving a temperature advantage of 10°C over MarM246 alloy. At 4 tsi conventionally-cast R6 alloy has a temperature advantage of about 25°C over MarM246 alloy. However, the more pertinent parameter chosen for selection of a turbine blade alloy is the specific strength properties (i.e. strength/density) and in terms of the Larson-Miller parameter $P = T (20 + \log t)$, where T is the test temperature (K) and t is the time (h) allowance may be made for alloy density. From the specific strength data, IN100 alloy was clearly the strongest conventionally-cast alloy at 30 tsi/100 hours life, offering about 35°C over MarM246 alloy, whereas R6 was marginally stronger than W37 alloy. In the tests at 7 tsi and allowing for alloy density W41 was the strongest conventionally-cast alloy, followed in turn by R10, R6, R8, W37 and IN100; MarM246 was the weakest alloy in the group. In the tests at 4 tsi R6 had about 25°C cf the 27°C advantage of R8 over MarM246 alloy for a 100 hours rupture life.

Examination of the creep-rupture data listed in Tables 17, 19 and 20 also illustrated in part in Figures 17 to 19, showed that one of the principal benefits accorded by unidirectional solidification was the

improvement in ductility (elongation at fracture) for any alloy and test condition. The effects of UDS on other creep-rupture test parameters, i.e. duration to specified creep strains, creep rate and rupture life or temperature capability, were more dependent on the alloy composition and test conditions. For example at 30 tsi/850°C the rupture life of R6 alloy was only marginally improved by UDS (30 hours or less in about 140 hours) whereas R8 alloy had its life doubled by UDS. The secondary creep rates were higher for both alloys but their durations to 1.0 per cent creep strain were shorter in the UDS condition. IN100 and MarM246 alloy at the same test condition generally had a lower secondary creep rate, and larger durations to 1.0 per cent strain and rupture in the UDS condition. At the high stress intermediate temperature conditions i.e. 42 to 45 tsi/ 750°C and 45 tsi/760°C, unidirectional solidification provided the expected improvements in ductility and rupture life for both R6 and R8 alloy. However, an additional feature of the creep behaviour of the UDS alloys was the presence of large primary creep strains very much in excess of that usually prescribed (<0.5 per cent) at the stress levels found in turbine components. This effect has been shown to occur for other UDS superalloys by Leverant and Duhl[84] who suggested that as the deformation is relatively heterogeneous at these temperatures the better perfection of microstructure of the UDS material permitted dislocations to glide large distances without leaving their slip plane. Some efforts were made to explore briefly the possibility of decreasing the level of primary creep strain and improving creep-rupture properties generally by developing a substructure within the material. One UDS R6 alloy testpiece was pre-stressed (30 tsi) in creep for sufficient time (300 hours) at 750°C to produce 0.1 per cent strain and the stress was then increased to 42 tsi. The primary creep strain for this testpiece was considerably reduced to near the level typical of a conventionally-cast structure; this pre-stressing treatment also gave a significantly improved lifetime. With the UDS R8 alloy one testpiece was pre-stressed in a tensile test to about 0.15 per cent strain at 760°C and cooled to room temperature before creep testing at 45 tsi/760°C. Under these conditions the testpiece showed a considerable diminution in rupture life with a significant increase in

the level of primary creep strain. The effect has been demonstrated of limiting the glide distance of dislocations in directionally-solidified material by introducing a fine scale substructure into MarM200 single crystals by shock loading[85]. After such treatment the primary creep strain at 100 ksi/1400°F [45 tsi/760°C] was only 0.33 per cent compared to 3.3 per cent for a virgin crystal of the same orientation.

In the creep-rupture tests done at 10 tsi/1000°C the rupture life and fracture elongation of R6 alloy were superior for the UDS condition, but the mean life was similar to that of the low carbon content alloy and only marginally above that of the conventionally-cast alloy. Apart from the improved rupture ductility little benefit was obtained from directional solidification. R8 behaved somewhat similarly to R6 alloy in creep-rupture tests at 10 tsi/1000°C. In the tests at 7 tsi/1040°C the expected improvements in rupture ductility from directional solidification showed for both R6 and R8 alloy, but only with the latter alloy was there any significant improvement in rupture life. Similarly the creep ductilities of MarM200 and IN100 alloy were improved, the beneficial effect on life being more marked for MarM246 alloy. In the tests at 4 tsi/1100°C significant improvements in time to produce 1 per cent creep strain, rupture ductility and life occurred with both R6 and R8 type alloys, i.e. rupture in 376 hours for UDS R6 cf 143 hours for conventionally-cast R6 alloy and rupture in approximately 720 hours for UDS R8 alloy. At 1100°C MarM246 alloy testpieces showed some improvement in rupture-life and ductility through UDS. Also at 1100°C a conventionally-cast IN100 alloy testpiece ruptured after extensive creep deformation (62 per cent) in only 2 hours, but no UDS testpieces were available for comparison. From the few tests done on the UDS R6 testpieces that were pack-aluminised (involving a coating heat-treatment cycle of about 16 hours at 870°C), with the possible exceptions of the test results at 42 tsi/750°C (improved life at 763 hours) and 10 tsi/1000°C (slight decrease in rupture life at 138 hours) it was difficult to detect any significant effects of the coating process on the short-term creep-rupture behaviour.

Conclusions

Twenty-four experimental alloys and three commercial alloys were investigated.

1. Among the experimental alloys two designated R6 and R8 had tensile and creep-rupture properties comparable to the best commercial alloys.

2. All the alloys were designed to be stable on thermal exposure and it was confirmed that this was in fact the case.

3. Stability in other samples, for instance taken from service components, showed that sigma phase precipitation in Nimonic 115 alloy blades ($\bar{N}v \simeq 2.84$ and 2.73 respectively) led to serious degradation of mechanical properties whereas another sample of slightly different composition ($\bar{N}v \simeq 2.54$) was not degraded. This observation emphasises the importance of the modern practice of Nv control in alloy production.

4. MarM246 alloy testpieces showed a propensity for precipitation of M_6C phase during high temperature exposure which detracted from creep-resistance but had minimal effect on impact strength.

5. Comparison was made in some cases between conventionally-cast and UDS materials. The general observations were that the tensile properties and creep-rupture properties at temperatures up to 1040°C were similar to those of the strongest commercial casting alloys. UDS improved the elongation-at-fracture values and creep-rupture lifetime of all alloys tested but the level of improvement was found to be dependent on alloy composition and test conditions. The best performance among the experimental alloys was shown by UDS R8 alloy which at 4 tsi/1100°C exhibited more than 40°C improvement in 100 hours capability over MarM246 alloy.

6. Vickers hardness values of the experimental alloys were in the range typical of commercial casting alloys which behaved similarly during heat-treatments.

7. Correlations have been obtained between durations to produce given levels of creep strain and rupture, and the solvus temperature of the gamma-prime precipitate. Regression equations were also developed relating the creep-rupture properties to alloy hardness.

8. No correlation was observed in the case of creep-rupture properties, alloy hardness values and coherency strain occurring between the various matrices and gamma-prime phases.

9. Exploratory studies of one alloy using a pack-aluminised protective coating showed no effect on properties.

CHAPTER 5

Metallurgical observations on factors influencing the mechanical behaviour

In this Chapter the metallurgical observations made of the structure of the experimental cast superalloys and the Nimonic 115 alloy turbine blades, alloy compositions and relevant property measurements will be compared with observations and ideas expressed in the literature on the factors influencing the mechanical behaviour of polycrystalline cast superalloys. Amongst others a Paper by Davies and Johnston[87] entitled "The metallurgical design of a superalloy" appeared to be particularly relevant.

General strengthening mechanisms operating in the matrix phase

From the chemical and electron microprobe analyses of the three principal phases, matrix, γ' and carbide, in the various experimental alloys a fairly clear idea was obtained of the way in which the alloying elements partitioned. For example Mo and W partitioned preferentially to the matrix phases, where because of their atomic diameter oversize relative to nickel internal strains would be generated in the parent lattice. According to the Mott and Nabarro[88] model of hardening by elastic misfit the yield stress for a dilute solid solution is given by:

$$\tau = 2G \varepsilon C \qquad \ldots.(1)$$

where G is the shear modulus, ε the lattice parameter misfit between pure solvent and solute atom and C the solute atom concentration. It has also been shown[89] that the lattice parameter mismatch may be approximated by the relative difference in atomic volume V between solvent and solute, thus:

$$\varepsilon = \frac{1}{a}\frac{da}{dc} \sim \frac{V\ (\text{solute}) - V\ (\text{solvent})}{V\ (\text{solvent})} \qquad \ldots.(2)$$

where a = lattice parameter.

On the basis of difference in atomic size, Al, Ti, Nb, Mo and W would be expected to give solid solution strengthening in the nickel matrix, whilst a somewhat smaller influence may be expected from elements such as Cr and Co that have a similar atomic diameter to nickel. While

for any single solute element in nickel, a linear relationship is obeyed between flow-stress and lattice parameter change, as shown by Pelloux and Grant[23] the magnitude of the change in yield stress for solutes in nickel is not a linear function of lattice parameter but depends on the position of the solute in the periodic table or electron vacancy number (Nv). For equivalent lattice strains the larger the difference in Nv between solute and solvent, the greater was the hardening and increase in yield stress. Fleischer[89,90] suggested that effects of valency on strength could be accounted for by the differences in modulus between solute and solvent which would affect the work needed to force a dislocation through hard or soft regions in the matrix. It was argued that because the self energy of a dislocation depends on shear modulus G, if G of the solute is larger than that of the solvent (matrix) an extra stress will be required to move the dislocation. Point values of the moduli will depend on the local compositions and are related to the interatomic interaction energies. Anisotropy in the elastic constants must also be taken into consideration, according to Fine[91]. A quantitative theory concerning this effect has not been developed yet.

It is well known that a simple lattice dislocation of the $\frac{a}{2}$ <110> type in a face-centred-cubic lattice can dissociate in the {111} glide plane as follows:

$$\frac{a}{2}[1\bar{1}0] = \frac{a}{6}[1\bar{2}1] + \frac{a}{6}[2\bar{1}\bar{1}] \qquad \ldots.(3)$$

This dissociation lowers the energy of the resultant extended dislocation. The two partial dislocations bounding the extended dislocation will repel each other and an intervening region of stacking fault will be produced. At some equilibrium separation (d) the total energy is minimised by the balance occurring between the elastic repulsive forces between the extended dislocations and the attractive force supplied by the finite energy of the stacking fault. The equilibrium separation is given by:

$$d = \frac{Ga^2}{48\pi \cdot \gamma} \cdot K \qquad \ldots.(4)$$

where G is the shear modulus, a the cube cell edge, γ = stacking fault energy (SFE) and K is a constant for a given material which is dependent on b, the Burgers vector[7]. It is clear that the stacking fault energy is the principal factor influencing the extent of dissociation of dislocations in a fcc matrix. Work by Beeston and France[25] has shown that additions of Fe, Cr, Al and Ti lower the stacking fault energy of nickel. It was observed that Co, which is generally reported as an alloying addition whose role is that of lowering the stacking fault energy of nickel alloys, was less effective than Ti, Al or Cr. In the same work Beeston and France applied their observations from binary alloys to some more highly alloyed Nimonic compositions and correlated Nv with stacking fault energy and shear strengths in a series of alloys. In low stacking fault energy matrices cross-slip is more difficult than in high stacking fault energy matrices and dislocations tend to be confined to their own slip plane. Reference 92 illustrates some examples of the type of dislocation structure occurring in cobalt alloys of different SFE. Alloys with a low SFE show a substructure with a high density of widely extended dislocations with marked dissociation as cross-slip was almost totally inhibited, whereas matrices with high SFE in which cross-slip was very easy tended to show a cellular dislocation structure and dislocation tangles.

Solid solution hardening effects in nickel alloys have been shown to persist to 0.6 Tm, above which high temperature creep occurs and the strengthening of nickel is diffusion dependent. At the higher temperatures the slow diffusing elements such as W and Mo would be potent hardeners per se, and as shown by Pridantsev[27] they lower the diffusivity of Ti and Cr in a superalloy at 900°C. However the amount of alloying elements that can be added to nickel to develop solid solution strengthening is generally limited because of the need for microstructural stability and in the case of Mo and W because of limitations on density.

Heavily alloyed solid solutions are likely to exhibit short-range-order which causes an increase in flow stress because of the extra energy required to cause shearing. Nordheim and Grant[93] have suggested that short-range-order strengthening may occur in fairly high chromium content

alloys (ca 20/25 w/o* Cr alloys) which is in the composition range of Hastelloy X, Inconel 625 (22 w/o Cr) and alloys in the early Nimonic series that are comparatively lean in the elements forming gamma-prime.

With the exception of IN718 alloy that is strengthened by the Ni_3Nb-type compound, by far the most important strengthening mechanism operating in commercial nickel superalloys is provided by the uniform precipitation of the intermetallic phase (γ') based on Ni_3Al. In these compositions the gamma-prime frequently contains numerous alloying elements that substitute for either Ni or Al atoms in the parent lattice. From the work of Taylor and Floyd[29,30] on Ni-Cr-Ti, Ni-Cr-Al and Ni-Ti-Al systems, that of Guard and Westbrook[31] and others in ternary phase equilibria studies on the Ni_3Al-X system and those by the author[17,18] on more complex alloys, elements similar in size and electronic configuration to Ni, such as Co and Cu would be expected to substitute primarily in the Ni positions, whereas elements further along the first, second and third transition series towards Ti, Nb and Ta would be expected to substitute to a greater extent for the Al positions in the Ni_3Al lattice. Gamma-prime is an ordered compound, possessing the Cu_3Au ($L1_2$)-type structure and exhibits long range order to near its melting point (1385°C); in ternary and more heavily alloyed form one would expect the degree of ordering and the melting point to be affected. In superalloys generally the γ' phase is coherent with the nickel base matrices; both phases have a fcc crystal-structure and differences in lattice constants are usually very small (<0.5 per cent). This means that the interfacial energy is very small which in turn has a marked effect on the stability of the dispersion (by reducing the rate of coarsening of the precipitate) and improving the creep-resistance of superalloys. These factors will be discussed later in the text after separately examining some current ideas on the deformation behaviour of ordered intermetallics of the Ni_3Al type.

---

*w/o = weight percentage

Some aspects of strengthening the gamma-prime phase

At low temperatures unalloyed gamma-prime deforms by slip confined essentially to the {111} system, superdislocations of screw character cross-slip onto {100} planes where they generally remain immobile. Edge dislocations do not interact with the screw dislocation debris and remain mobile so that their mean free path for motion at small strains is high. Ni_3Al manifests behaviour atypical of fcc metals with a low strain rate sensitivity and its flow stress is unusually low[87], slip along {111} is extremely heterogeneous at low temperature but at 400°C and above {111} slip is fine and uniform. The flow stress of γ' increases rapidly with temperature which may be associated with the emergence of {100} slip which has been observed at 400°C and predominates at 700°C (Reference 94). This raises the opportunity for multiple slip interaction hardening in which the mean free path of edge dislocations is reduced by the rapid generation of dipoles, edge and screw dislocation debris within glide bands. Dislocation debris anneals out so rapidly at temperature above 900°C that little steady creep occurs and the resistance offered by the Ni_3Al lattice itself to the motion of dislocations is too small to provide adequate creep resistance. Hence at high temperatures no strain-hardening mechanism is available and the flow stress of gamma-prime will give an indication of initial transient creep behaviour but can lead to erroneous conclusions with respect to long term creep resistance[87].

The work of Guard and Westbrook on the mechanical behaviour (hardness) of Ni_3Al containing ternary alloying additions showed that as with terminal solid solutions, lattice strain played a major role in solid solution hardening. They noted that strain ageing (defect hardening, or softening at high temperature) appeared to be as important as solid solution hardening. More recent ideas acknowledge the importance of lattice defects such as vacancies, dislocations, grain boundaries etc., but more importance is attached to antiphase domain boundary faults in influencing the mechanical behaviour of gamma-prime. These boundaries generally contain wrong bonds between nearest neighbour atoms, but certain cases can exist such as between the (001) [110] boundary in the Cu_3Au structure where nearest neighbour relations are correct but some bonds between

second neighbours are incorrect[95,96]. Since antiphase boundaries (APB) contain wrong bonds they represent regions of higher energy, the value of which depends on crystal orientation. APBs would be expected to lie preferentially in planes of lowest energy and this has been shown experimentally for annealed Cu_3Au (Ll_2 structure) to be the $\{100\}\ \frac{a}{2}\ \langle 110\rangle$ shear-type boundary[97]. In addition to APB faults, (whose specific energy is about ten times greater than the γ/γ' interfacial energy in superalloys) superlattice intrinsic and superlattice extrinsic faults (produced by shear displacements of the type $\{111\}\ \frac{1}{3}\ \langle 112\rangle$) of lower energy than that of the APB, and complex faults which may be regarded as a superposition of APB and complex intrinsic faults[98] play a significant role in the deformation of superalloys.

A somewhat simplified representation of the model for APB strengthening of an ordered alloy involves the following factors. An ordinary dislocation passing under stress through an ordered lattice will leave a plane of disorder in its wake. Because the energy required to form an APB is generally non-zero it is harder to move a dislocation through an ordered region than through a disordered region. A second (following) dislocation can then move through more easily and erase the disorder created by the leading dislocation. The width of the APB fault is determined by the balance between the elastic repulsion of the two dislocations of like sign and the attraction due to the surface tension of the antiphase boundary. The equilibrium separation, τ, of the two dislocations has been calculated for various orientations of dislocations in both isotropic and anisotropic elasticity theory. The separation of the dislocations may be represented by a simplified expression of the following type:

$$\tau = C/S \qquad \ldots.(5)$$

where C is a constant incorporating the Burgers vector and elastic constants of the material and S the surface tension of the antiphase boundary which is a function of the number of wrong bonds intercepting the boundary. Koehler and Seitz[98] were the first to suggest that the superdislocation

configuration (i.e. pair of dislocations with associated strip of APB) could move through an ordered region more easily than an ordinary dislocation. The factors determining the manner in which superdislocations move in particular alloys i.e. short and long-range-order, crystal structure and composition are discussed more fully by Beeler[96] and others.

In addition to solid solution and fault hardening of gamma-prime, from electron microscope observations in the present work and those reported elsewhere[76,99-103] very fine scale precipitation of a second phase can occur within the secondary gamma-prime particles in superalloys. These observations will be discussed later. Ham, Cooke and Purdy[38] have studied bulk gamma-prime alloys that utilise precipitation of gamma-phase for strengthening.

Strength of $\gamma + \gamma'$ alloys (general)

Most of the factors suggested to account for the mechanical behaviour separately of the matrix and gamma-prime phases have been outlined. From the literature it is evident that progress has been made in applying these ideas and in certain cases quantifying the individual contributions of the phases found in the microstructure to account for the strength of superalloys under a variety of experimental conditions (stress, strain rate and temperature). These factors include coherency strains, differences in elastic moduli between particles and matrix, state of order in the particles, differences in stacking-fault energy of particles and matrix, energy required to form additional particle-matrix interface, and increase in lattice resistance of particles with temperature. A brief outline follows of the pertinent ideas that have been developed to account for the strengthening of casting alloys (high v/o gamma-prime) similar in type to the experimental alloys in this programme. More detailed descriptions of models representing these and other superalloys strengthened by low volume fractions of gamma-prime are summarised in the literature (see particularly References 1, 2, 4 and 9).

The two main ideas put forward to explain the strength of superalloys are concerned with APB, and coherency strain respectively. Williams[104], Merrick[105], Gleiter and Hornbogen[106], and more recently Copley and Kear[107] have applied APB strengthening to a number of different

alloys. Briefly it is considered that dislocations $\left(\bar{b} = \frac{a}{2} \langle 110 \rangle\right)$ glide in pairs during shearing of the gamma-prime particles i.e. by a super-dislocation mechanism, producing a net addition to shear strength. One of the earliest detailed analysis of APB strengthening in superalloys is attributed to Gleiter and Hornbogen who derived a mathematical relationship that would account for the complete ageing curve for a model Ni-Cr-Al alloy containing a low volume fraction of gamma-prime. Copley and Kear studied a high volume fraction gamma-prime alloy (MarM200) and were able to account for its increase in critical resolved shear stress due to APB energy, using a relationship of the form:

$$\Delta\tau APB = \frac{\gamma APB}{2b} \qquad \ldots.(6)$$

where γAPB is the APB energy and b the Burgers vector. More than two-thirds of the critical resolved shear stress of MarM200 was attributable to the APB energy. More recently[108] it has been shown that APB should be replaced by the fault energy (Γ) for (111)-type shear in γ'. The value of Γ would depend upon APB, complex fault, and superlattice intrinsic and extrinsic fault. According to Decker[9] a probable shortcoming of the gamma-prime fault theories is that neither of the fault energy terms, $\frac{\Gamma}{2b}$ or $\frac{APB}{2b}$ term allow for variation of the volume fraction of γ' in superalloys. From consideration of the critical temperature for ordering of their Ni_3X phases Decker deduced that titanium, niobium and tantalum additions to γ' would not increase the APB energy significantly. However because of the stacking fault correlation with Nv and elastic misfit between alloying elements in γ', titanium and possibly niobium and tantalum could increase other components of Γ. In contrast to the APB strengthening ideas, Decker and Mihalisin[35] re-emphasised the importance of γ/γ' coherency strain both in the case of dislocations cutting and by-passing gamma-prime particles. By substitution of carefully chosen elements (V, Nb, Ta, Ga, Mn, Si, C) for Al in gamma-prime in experimental ternary alloys they were able to correlate hardness increases with increase in lattice mismatch. Their results were found to be in accord with the theory of Gerald and Haberkorn[109] on increase of CRSS* ($\Delta\tau$cs) arising from coherency strains.

*Critical resolved shear stress

Thus: $$\Delta\tau_{cs} = 3\,G\varepsilon^{\frac{3}{2}}\left(\frac{hf}{2b}\right)^{\frac{1}{2}} \quad \ldots.(7)$$

where G is the shear modulus of the γ phase, ε is the constrained lattice mismatch, h is the particle diameter and f the volume fraction of γ'. The value of CRSS should increase with coherency strain, volume fraction and particle size of γ'. This coherency strain argument was used to account for the strengthening of a number of commercial superalloys that could be separated into two groups: alloys with high coherency strain ($a_o\gamma' > a_o\gamma$) such as IN718, Nimonic 80A and Nimonic 90, and those with low coherency strain such as PE16, IN713C, Nimonic 105 and Nimonic 115 and casting alloys such as MarM200 and IN100. Alloys with high coherency strain are used at temperatures below about 0.6 Tm, and those with low coherency strain are generally stronger at higher temperatures.

Elegant experiments pertinent to a large range of commercial superalloys were designed by Beardmore et al[110] to illustrate the effects of both the volume fraction of gamma-prime and the temperature on the flow-stress of simple Ni-Cr-Al alloys. The alloy compositions were carefully selected (see Figure 39) to produce during ageing at 900°C microstructures containing 0 per cent γ' (i.e. 100 per cent matrix γ) to 100 per cent γ'. It was found that the size of γ' particles produced during equilibrium ageing treatments increased as its volume fraction was increased, ranging from 0.2μm at low volume fractions up to about 0.8μm at the highest volume fraction. These are typical of the sizes obtained in commercial superalloys. The 100 per cent matrix alloy showed a continuously decreasing flow-stress with temperature, apart from the 'hump' in the 500/700°C range which was due to strain ageing effects as evidenced by serrated stress-strain curves. At and above 900°C there appeared to be a simple monotonic correlation between flow stress and the volume fraction of γ' in the alloy, the greater the amount of γ' the stronger the alloy. At low temperatures the flow-stress/temperature characteristics for the two-phase and 100 per cent γ' alloy could be divided into

three basic types. Low v/o γ' alloys, containing up to 20 v/o γ', were characterised by an essentially constant flow-stress to about 700°C followed by a rapid decrease with further temperature increase. With the increasing v/o of γ' from 10 to 20 per cent the strength increment was independent of temperature. Alloys containing 40 to 60 v/o γ' exhibited a flow-stress/temperature dependence typical of many commercial alloys, with a constant flow-stress to intermediate temperatures, increasing at higher temperatures, followed by a rapid decrease at the highest testing temperatures. The curves for the 80 v/o and 100 v/o γ' alloys were very similar exhibiting an increasing flow-stress with temperature to about 900°C followed by a rapid decrease in strength with further temperature rise.

Electron microscope examination showed significant differences in deformation behaviour occurring in tests up to 500°C (low temperature) and above 800°C (high temperature) respectively. For example the test-pieces tested at low temperatures deformed by localised slip bands of varying width with little or no dislocation structure in the γ' particles. Increasing the amount of γ' had an effect similar to that of an increase in temperature, producing more diffuse slip bands and a cell-like sub-structure with dislocations being stored in the γ matrix during low temperature deformation. The 100 v/o γ' alloy was found to deform in a uniform manner at low temperatures as shown by uniform, fine slip markings and relatively uniform distribution of apparently-single dislocations i.e. the separation of the superdislocation pairs was too small to be resolved in the electron microscope. In contrast the 100 per cent matrix alloy (single phase) deformed by localised slip and the remnant dislocations appeared to be arranged in pairs. When the alloys were tested at high temperature, regardless of the volume fraction of γ', the deformation was homogeneously distributed. The dislocation structure, in general, appeared as a uniform tangle and there was no tendency for the dislocations in the matrix to be paired. In low v/o γ' alloys dislocation loops were observed around the γ' particles, and the dislocations were stored primarily in the matrix. In high v/o γ' alloys dislocations were unable to loop around the γ' particles and dark field studies showed intensely tangled dislocation structures stored in the matrix. High temperature deformation of the 100 v/o γ' alloys produced

a uniform distribution of superdislocations. By ageing the alloy that consisted of 100 v/o γ matrix at 900°C at a lower temperature (700°C) Beardmore et al precipitated a small volume fraction ($\sim$3 v/o) of very fine (<300Å) γ', and were able to calculate its contribution to the low temperature strength of the dilute superalloys. The hyperfine γ' particle size was stated to be small enough for deformation to occur by dislocations cutting through particles, since the critical particle diameter for a changeover from cutting to bowing by the Orowan mechanism is at least 300Å. The strengthening afforded to the matrix by virtue of the cutting of the hyperfine γ' precipitate by dislocations was based on the following relationship:

$$\sigma = \frac{\pi S r}{b l} \qquad \ldots.(8)$$

where σ is the flow-stress, b the Burgers vector, l the distance between the precipitates, S the energy of the interface produced by dislocations cutting the precipitate. Using measured values of r and l, and assuming values of b (2.53Å) and S (160 erg cm^{-2}) a value of approximately 70,000 psi was derived for flow stress[110].

To account for the relationship between v/o γ' and mechanical properties of their alloys Beardmore et al concluded that at the equilibrium ageing temperature, 900°C and above, the microstructure of the alloys consisted of a dispersion of large (0.5µm) strong γ' particles in a weak single-phase γ matrix and as the flow-stress was a function of v/o γ' the 100 v/o γ' alloy was always the strongest under these test conditions. At lower temperatures (<500°C) the microstructure consisted of a bimodal dispersion of large ($\sim$0.5µm) γ' particles of low strength and a hyperfine γ' precipitate ($\sim$75Å) that was responsible for strengthening the matrix. With increasing temperature above 700°C the hyperfine γ' would re-dissolve in the matrix and would not contribute to the alloy strength. At low temperatures the flow stress of the alloys was not simply related to the volume fraction of γ' in the alloys but showed a peak in strength at about 25 v/o γ'. Copley and Kear[107] originally suggested that the drop in flow-stress of γ - γ' alloys above 760°C was

a consequence of a reduction in APB energy due to disordering. However Corey et al[111] have shown that Ni_3Al does not disorder until at least 1100°C.

The electron microscope observations on the low temperature deformation behaviour of the Ni-Cr-Al alloys by Beardmore et al were in direct agreement with those of Kear et al for MarM200 alloy and with those arising in the present investigation of experimental cast superalloys. For example Figure 29 shows that in alloys moderately deformed (0.2 per cent strain) in tensile tests at room temperature most of the dislocations were restricted to the regions between the secondary γ' particles. In contrast foils machined close to the fracture surfaces of tensile testpieces had a variable microstructure because of the inhomogeneous deformation. Between the slip bands the γ' precipitate boundaries were often delineated by heavy concentrations of dislocations whereas the γ' itself had a few single dislocations and occasional stacking faults. Other foils showed that particularly in the slip bands very dense tangles of dislocations occurred in both matrix and secondary gamma-prime particles. Similar features were also observed in the foils machined from tensile or creep-rupture testpieces that had been tested in the range 750°C to 850°C (Figures 30 to 33) viz a few, apparently single, dislocations with generally more stacking faults being generated within the secondary γ' particles and a somewhat heavy decoration of the "matrix" regions between the 'cuboidal' γ'. These "matrix" regions contained the very much finer dispersions of γ' reported by Beardmore et al, which appeared to play an important role in controlling the dislocation substructure within the experimental alloys to very much higher temperatures than those relevant to the simpler alloys studied in Reference 94. The gamma-prime solvus temperatures for the experimental alloys (Table 13) were all in excess of 1040°C which was the general maximum test temperature used in creep-testing; and fine dispersions of γ' were found to be present in MarM246 alloy exposed for 200 hours at 1050°C and subsequently water-quenched.

A further complication to the observation of deformation processes occurring in the experimental superalloys, but which was not mentioned by Beardmore et al, was the appearance of an extremely fine dispersion of a

second phase in the secondary gamma-prime particles. These dispersions appeared to increase only slightly in size with the times and temperatures involved in the experimental programme, but although expected to exert some influence on the dislocation substructure they were still too fine to permit positive identification. They may be gamma phase, or precipitates of Group VI elements.

From the observation of thin foils machined from the heads and gauge length regions of testpieces creep tested at 1000°C and 1040°C (Figures 34 to 36) it was clear that the secondary gamma-prime particles were changing their shape and size. At these higher temperatures the deformation appeared to be more homogeneous, presumably because climb and cross-slip can readily occur, and stacking faults were rarely observed. The dislocation activity was confined to the interface regions of the secondary gamma-prime particles, or the two phase (gamma + tertiary γ') regions at these higher temperatures. A particularly interesting feature common to Figures 35 and 36 was the obviously heavy deformation of secondary γ' occurring in the gauge length regions of R8 and MarM246 alloy during creep tests at 1040°C. The highly deformed appearance of the secondary gamma-prime particles was similar to that illustrated by Decker[9] occurring in consequence of creep deformation of Nimocast 713 alloy at 815°C.

Details of the investigations into the effect of orientation and sense of applied uniaxial stress (i.e. tension or compression) on the morphology of gamma-prime precipitates in both single crystal and polycrystalline Udimet 700 alloy are described in References 112 to 114. Briefly, after stress-annealing of solution-treated and aged Udimet 700 alloy testpieces at 22.5 ksi, 1750°F (955°C) the gamma-prime agglomerated and formed plates with broad faces aligned perpendicular to the [001] tensile stress axis and sides perpendicular to the remaining cube directions. In contrast compressive annealing produced parallelopipeds oriented parallel to the stress axis. A general thermodynamic analysis was developed to account for the free energy changes due to changes in bulk precipitation strain, effective modulus, coherency strain energy and total inter-phase boundary area. It was shown that within the

constraints imposed by coherency strain energy the dominant driving force (free energy change) was due to changes in bulk precipitation strain. The analysis predicted that minimising the mismatch in lattice constant of the matrix and precipitate phases by alloying would suppress stress-induced morphological changes. Further, if the elastic constants of the matrix and precipitate were equal, stress-induced morphological changes could be completely precluded. In the present work the gamma-prime particles were considerably distorted and their final shape and size gave the appearance of joined-up (welded) platelets. Dislocation cutting and climb processes during creep at 1040°C would be expected to make a contribution to this shape change of the secondary γ', but if as appears to be the case, several cuboids weld together, a significant diffusional mass-transport of atoms must occur involving the flow of stress generated vacancies and atoms in opposite directions by a Nabarro-Herring mechanism[115,116].

Alloy design for creep-resistance

From the literature concerned with the design of creep-resistant alloys at high temperatures attention is usually drawn to the following principal factors[117-119]. The volume fraction of γ' should be at least 30 v/o; Pridantsev[27] noted that the optimum amount of γ' was approximately 60 v/o, Guard[119] and separately Davies and Johnston[87] found that the maximum creep-resistance in the Ni-Cr-Al system occurred at approximately 60 v/o γ'. Interparticle spacing should be in the range of about 500Å and therefore the particle size should be small. Sorokina and Yuganova[120] observed that in Ni-Cr-Al-Ti alloys containing 10 to 20 v/o γ' the alloy with the best long term creep strength at 700°C had the smallest γ' particle size; in addition the particle size effect appeared more important than the volume fraction of γ' in determining creep life. The particle should have a strength greater than that of the matrix to minimise cutting-through. The γ' dispersion has to remain finely distributed and stable under the influence of stress. In superalloys generally the γ' is coherent with and has almost the same lattice parameter as the matrix. As the strain energy per unit area of γ/γ' interface arising from lattice mismatch is one of the most significant driving forces for growth and

coalescence of the γ' particles, a large mismatch with a correspondingly large interfacial strain energy would tend to produce unstable γ' dispersions at high temperature.

Measures that minimise coarsening (increase in average particle size) and hence make more difficult the by-passing of precipitates will help to retain long term creep-resistance. The important variables involved in the growth of large particles at the expense of small ones are solute solubility, solute diffusion coefficient and specific interfacial energy between particles and matrix. Fleetwood[121] has applied Wagner's theory of Ostwald ripening to γ' in superalloys thus:

$$h^3 = \frac{64\ \gamma_e\ D\ C_e\ V_m^2\ t}{9RT} \qquad \ldots.(9)$$

where h is the mean particle diameter, γ_e the specific interfacial free energy, D the γ' solute diffusion coefficients in γ, C_e the equilibrium molar concentration of γ' solute in γ, V_m is the molar volume of γ' and R the gas constant. Because γ_e is small the rate of growth obtained by differentiating Equation (9) is also small. From the analysis of experimental data on γ' coarsening in Ni-Al alloys by Ardell[122], values of interfacial energy deduced from the slope of the lines relating the average particle size $\left(\frac{\bar{a}}{2}\right)$ as a function of time $\left(t^{\frac{1}{3}}\right)$ was found to be extremely small, approximately 14 erg cm^{-2}. Compositional effects in superalloys affect the values of γ_e, C_e and D in Equation (9). In Ni-Cr-Ti-Al alloys the rate of coarsening of γ' decreased[121] as the chromium content was increased from 10 to 37 per cent. This effect was related partly to reduced C_e and partly to the reduction of coherency strain and consequent reduction of γ_e/D. In higher Ti-Al alloys increases in γ' ripening rates were associated with increased coherency strain. Mitchell[123] observed no effect of Co, Mo and Fe additions on the growth rate of γ' in a Ni-Cr-Ti-Al alloy, however increasing the Nb content from 2 to 5 per cent markedly decreased the coarsening rate despite the increase in coherency strain. This effect has been accounted for on the basis of the reduction of C_e and D caused by the Nb partitioning to the γ' being more influential than the increased coherency strains with increasing Ti-Al ratio.

Table 9 lists the lattice constants measured at room temperature for the matrix and gamma-prime phases in the experimental alloys in the as-cast and in the heat-treated condition. It was observed that the differences in lattice parameter were very small in the as-cast condition and were only slightly affected, in those alloys for which measurements were made, by exposure at high temperatures. The smallness of the lattice parameter difference is related to the preferential partitioning of elements of similar atomic size such as Mo and W (atomic radius r = 1.40Å and 1.41Å respectively) to the matrix, and Ti, Nb and Ta (r = 1.47Å, 1.46Å and 1.46Å) to the gamma-prime phases. Whilst these alloying elements effectively nullify coherency strain to a large extent, they will also be expected to contribute to microstructural stability and hence creep-resistance because of their low diffusivity D. No correlation could be found between the mismatch in lattice parameter (Δa) between the matrix and gamma-prime for the experimental alloys and either the room temperature hardness measurements or any creep-rupture parameter. Whilst low lattice parameter mismatch is important for its contribution to controlling the rate of coarsening of the γ' precipitate, in alloys with $\Delta a = 0$, dislocations passing through the γ' particles will produce ledges at the particle/matrix interface which may enhance particle growth. Davies and Johnston observed that a number of superalloys terminated steady state creep at approximately the same strain level (1 per cent) at 1700°F (927°C) irrespective of time at temperature. It was suggested that at this strain level a sufficient number of ledges could be introduced into the interfaces to start γ' growth. The process then became autocatalytic since γ' growth weakens the alloy and allows more coarsening; thus at this point tertiary creep begins to emerge.

Two further factors are relevant to the effects of alloy chemistry on the creep-rupture behaviour of the experimental alloys. Firstly because the testpieces were polycrystalline small amounts of the so-called minor elements C, B and Zr were added because of their well known effects on controlling the mechanical behaviour at, or near, grain boundaries. Secondly there are the effects of substitutional solid-solution elements as they affect the microstructural stability of the γ' precipitate and

MC phases and hence the creep-rupture behaviour of the alloys. Before discussing these chemical effects per se on the creep-rupture behaviour of the alloys simplified ideas from the literature on creep mechanisms, and their relevance to metallographic observations made on various creep-rupture testpieces from the experimental programme will be discussed.

Deformation mechanisms observed during creep

Leverant, Kear and Oblak[85,124,125] have studied the creep mechanisms of MarM200 alloy single crystals occurring in the temperature range 1400°F (760°C) to 1800°F (982°C). In tests at 760°C the levels of primary creep strain and creep rate were markedly orientation dependent. The creep curve for the crystal with an orientation near [001] displayed extensive primary creep in contrast to the absence of primary creep in orientations near [011] and [111]. In addition the rupture life and ductility varied from 5 hours and 30 per cent RA* for [011] to over 1900 hours and 14 per cent RA near [001]. At 871°C and 982°C a definite, but less-pronounced improvement in creep and stress-rupture properties occurred for orientations approaching [001] and [111]. At 760°C slip occurred on {111}, but several Burgers vectors were observed. Dislocations of the $\frac{a}{2}$ <112> were generated and then dissociated into $\frac{a}{3}$ <112> and two $\frac{a}{6}$ <112> partials. The deformation mode at 760°C was found to be very sensitive to strain rate; during creep viscous slip of intrinsic/extrinsic fault pairs with net Burgers vector a <112> occurred through both γ and γ' phases, the γ' particles being sheared by $\frac{a}{3}$ <112> partials. Intersecting {111} <112> slip led to network formation at the γ/γ' interface during steady state creep. In tensile tests at the same temperature, slip occurred on widely spaced bands by shear of $\frac{a}{2}$ <110> superlattice pairs through both γ and γ' phases. Thus primary creep proceeded by the motion of pairs of superdislocations coupled with extrinsic fault pairs at a rate controlled by diffusion, at high strain rates deformation occurred by slip. At 857°C it was found that shear of the γ' precipitate by pairs of $\frac{a}{2}$ <110> dislocations controlled deformation in both primary and steady state creep. At 982°C the creep strength was much less dependent on orientation, and was rationalised in terms of slip on cube planes as well as octahedral planes.

---

*Reduction of cross-sectional area

One of the simplest and earliest models of secondary creep was that a balance was being maintained between dislocation - producing strain hardening processes and dislocation - reducing recovery processes. The steady state creep-resistance of crystalline single phase solids, which depends on the diffusivity D, stacking fault energy γSFE, elastic modulus E, temperature T, and stress σ, has been described by a formula such as[126,127]:

$$\dot{\varepsilon} = \left(\frac{\sigma}{E}\right)^n f(\gamma SFE)\, e^{-\frac{Q}{RT}} \qquad \ldots.(10)$$

where $f(\gamma SFE)$ is a function of SFE and Q is the activation energy for creep. For solid solution alloys n has values in the range 3 to 7, and Q is equal to the activation energy for self-diffusion above 0.5 Tm. Consequently high creep strength is favoured by solute additions that raise the modulus or reduce the SFE and which lower the diffusivity. When second phase particles are present, the activation energy for creep is much higher than the activation energy (for self diffusion) of the matrix. Ansell and Weertman[126] first suggested that the rate-controlling process in multi-component alloys is dislocation climb around particles. At stresses (σ) above $\frac{Gb}{\lambda}$ (where G is the γ shear modulus, b the Burgers vector and λ the mean planar interparticle separation) dislocations will move past particles by looping. Loops will thereby build up and exert back-stresses to prevent more looping until recovery occurs by the climb of the first dislocation loop around the γ' particle. The creep rate is given by:

$$\dot{\varepsilon} = \frac{\pi\sigma^4\ \lambda^2\ D}{r_0\ G^3 \cdot kT} \qquad \ldots.(11)$$

where D is the matrix self diffusion coefficient, r_0 the particle size, k is Boltzmann's constant and T the temperature. The factors favouring high creep resistance under these circumstances are small interparticle spacing (large v/o γ'), decreased D (obtained by adding W or Mo to Ni) and increased particle size.

At low stresses $\left(<\frac{Gb}{\lambda}\right)$ dislocations can climb over or around γ' particles without the necessity of pile-ups around the particles and the creep rate is given by:

$$\dot{\epsilon} = \frac{\pi\sigma\, b^3\, D}{8k\, Tr_0^4} \qquad \ldots.(12)$$

Low creep rate is predicted to be favoured by low diffusivity and large particle size.

Leverant, Duhl[84] and others have explored the effect of stress, temperature, and creep mechanisms for a variety of polycrystalline superalloys: IN100, MarM200, and B1900 in the conventionally-cast and directionally solidified condition. In tests at 760°C the UDS alloys tended to show large levels of primary creep strain at high stresses, whereas at somewhat higher temperature, $\geq$ 843°C, primary creep strains were small (e.g. 0.3 per cent at 871°C/75 ksi). At 760°C primary creep occurred by viscous glide of intrinsic/extrinsic stacking fault pairs with a net Burgers vector of a <112>. This deformation was heterogeneous permitting dislocations to glide large distances without leaving their slip plane. Steady state creep was reached only when sufficient intersections had occurred between the {111} <112> slip systems to limit the glide distance of dislocations to the scale of a few γ' particles. Consequently columnar-grained materials, with a large grain size (diameter of about 0.1 inch), and single crystals exhibited large primary creep strains. In contrast, in conventionally-cast alloys where grain boundary barriers to slip are more closely spaced there was less primary creep for the same stress[84]. At higher temperatures homogeneous dislocation arrays were generated at small strains and consequently the glide distances were quite limited from the outset of the creep test. Hence the primary creep strains were generally comparable for directionally-solidified and conventionally-cast alloys.

In the metallographic observations[85,125] of structures of MarM200 alloy deformed in creep at 857°C extensive networks of $\frac{a}{2}$ <110> dislocations formed at the γ/γ' interfaces. Two modes of dislocation shear occurred within the γ' precipitate. The first, of lesser importance, was identical

to that observed at 760°C and consisted of the creation of low energy superlattice extrinsic and intrinsic stacking faults by the viscous glide of $\frac{a}{3}$ <112> partial dislocations through γ'. The second and principal mode of shear involved the cutting of γ' by constricted $\frac{a}{2}$ <110> dislocation pairs which were quite difficult to resolve individually. At 982°C deformation of the γ' took place by shear and climb of paired $\frac{a}{2}$ <110> dislocations which could at times be individually resolved in the paired loops on (111).

The microstructural changes occurring during creep-rupture tests for the experimental alloys were studied using thin foils and replicas in the electron microscope, but the dislocation analysis was not as detailed as those of Kear et al. Because of difficulties associated with the thinning of grain boundary regions,the thin foil work was confined to studying the microstructural features of the grain interiors (i.e. bulk dendritic regions). The general features were similar to those reported in the literature for other superalloys. For example as illustrated in Figure 29 during low temperature deformation the dislocations were largely confined to the interfaces between the matrix and secondary gamma-prime particles. At intermediate temperatures (750/850°C) the microstructures usually showed a large number of stacking faults that were absent from the structures of the gauge length and head-sections of creep testpieces that were tested at 1000°C and above. The morphology of the secondary gamma-prime particles was not significantly altered by creep or tensile deformation at intermediate temperatures. However, depending on the alloy, the position from which the foils were machined from a testpiece, and the test temperature, a range of morphologies and sizes of secondary gamma-prime was observed after creep tests at and above 1000°C. Within immediately adjacent regions of foils machined from the heads of creep testpieces after tests at 1000°C the secondary gamma-prime particles tended to undergo a slight spheroidisation and comparatively few dislocations were present in the structure. In comparison foils machined from the gauge length region of the same testpieces (e.g. see Figure 34) showed extensive networks of dislocations particularly concentrated in the "matrix" (i.e. γ + tertiary γ') regions between the secondary γ'

particles. A few dislocations were present in the secondary gamma-prime and one particle in the micrographs, Figure 34(b) and (c) shows two super dislocations. It should be noted that the creep testpieces were not quenched from the test temperature and thus recovery effects would contribute to the appearance of the microstructure. In Figure 34(a) the dislocation networks which appear to be similar to those found in typical "matrix" regions are believed to be located in the γ phase adjacent to the secondary gamma-prime particles. Foils machined from the heads of creep testpieces tested at 1040°C showed a range of sizes and shapes of secondary gamma-prime particles i.e. cuboids, lenticular shapes and rods, similar to that observed from the previous work with MarM246 alloy testpieces exposed in the absence of stress for 200 hours at 1050°C and water quenched to room temperature. However, these structures were comparatively free of dislocations relative to the heavily-deformed material in the gauge lengths of testpieces creep-tested at 1040°C. Figures 35 and 36 show microstructural features common to most of the alloys creep-rupture tested at 1040°C; the secondary gamma-prime particles were heavily deformed and took on the appearance of a series of drawn-out and "welded" cuboids. Dislocation networks were largely confined to the two-phase γ + tertiary gamma-prime regions whereas the secondary γ' particles were comparatively dislocation-free.

Tertiary creep and grain boundary effects

All of the alloys showed a tertiary stage of creep. This part of the creep curve is usually associated with coalescence of voids to form larger cavities that agglomerate until the material isolated between them is insufficient to support the applied load, and the testpieces ultimately fracture. All the creep testpieces in this programme fractured in a ductile manner. Formation of cavities during creep has been observed in a variety of metallic materials, in magnesium alloys at about 200°C with an increase in cavity population with temperature to a maximum at about 300°C. Similar effects have been observed in copper-base (α-brass), iron-base and nickel-base alloys[127]. Cavitation preferentially occurs at boundaries subjected to a tensile stress. Such sites are known to be efficient sources or sinks of vacancies and also there is a general denudation of precipitate relative to grain interiors. An indication of the

importance of grain boundary denudation effects occurs in the high strength aluminium alloys e.g. (Al + Zn + Mg) where it can lead to brittleness, susceptibility to stress cracking[128,129] and poor fatigue properties[130]. Sims[3], Gresham[131] and others[9,132-135], have shown the importance of grain boundary denudation effects in suppressing or delaying grain boundary sliding and cavitation that usually cause intergranular failure of nickel superalloys during high temperature creep. The mechanisms controlling this behaviour of superalloys is not fully understood at this time, but the chemical effects of the so-called minor elements, C, B and Zr, and more recently Hf (not studied here) and the control of the morphology of the phases by heat-treatment play a very important part in controlling the behaviour at or near grain boundaries. For example, carbon is added to the alloys in order to produce blocky carbides which are desirable to inhibit grain boundary sliding during creep at intermediate temperatures. Unfortunately these carbide particles are often faulted and pre-cracked and are potential nucleation sites for grain boundary cracking. Heat-treatments have been developed for some superalloys that cause breakdown of MC particles into discreet, blocky $M_{23}C_6$ particles enveloped in a more or less continuous film of ductile gamma-prime. The ductile film can accommodate plastic deformation around the carbide particles as the boundary shears thereby enhancing the intermediate temperature creep life. Too much carbon added to nickel superalloys, or incorrectly applied heat-treatments, may produce undesirable morphologies and continuous carbide networks at grain boundaries which causes embrittlement. The precise mechanisms by which boron and zirconium additions contribute to the creep properties of superalloys remains the cause of much speculation. Decker et al[134] appear to have been the original discoverers of the beneficial effects afforded by trace amounts of B and Zr in improving the hot-workability and creep strength of superalloys. They suggested that because of the large size discrepancy relative to the other components of superalloys that B and Zr would preferentially be accommodated at grain boundaries, which are regions of high irregularity of the crystal lattice. Thus small amounts of B and Zr were visualised as locally "healing" the grain boundary, thereby decreasing the available "flaws" and retarding the segregation of other odd-sized elements such as

carbon. In the absence of B and Zr an experimental superalloy failed in creep at 1600°F (870°C) because of agglomeration of $M_{23}C_6$ particles at grain boundaries normal to the applied stress. The adjacent matrix became depleted in γ' precipitate and microcracks formed at the interface of the $M_{23}C_6$ particles and linked together to cause early brittle fracture. Optimal quantities of B and Zr retarded the rate of agglomeration of $M_{23}C_6$ and γ' at grain boundaries, delayed microcracking from late in primary creep until well into tertiary creep, and improved the rupture life and creep-ductility. As in the case of carbon, the levels of B and Zr need to be strictly controlled in order to avoid undesirable grain boundary effects such as brittleness, hot-shortness etc. The effects of B and Zr additions to superalloys have been reproduced to some extent by the addition of small quantities of Ag to Al-Zn-Mg alloys[136]. In this case the Ag produced a refinement of precipitate structure to produce a smaller and more uniform interparticle spacing in the grain boundaries than in alloys without silver. Essentially the addition prevented coarsening of the structure, and this has been used for other metallic materials e.g. the addition of Co to Cu-Be alloys[137]. The action may be by reducing the mobility of vacancies, by altering the precipitate-matrix interfacial energy, or by the formation of small amounts of an additional precipitate which hinders boundary migration and hence retards discontinuous precipitation[138]. Nield and Quarrel[139] have proposed that the incidence of cavitation during creep of aluminium alloys is governed by a balance between grain boundary sliding and grain boundary migration and that vacancy diffusion is not a primary process.

Cavities have also been observed within the grains themselves and low temperature crack initiation in nickel superalloys occurs at microstructural defects such as pores and brittle second phases (i.e. carbides). From the present work and that reported by Kear et al[140] crack initiation and final rupture was intergranular. The cracks frequently followed a crystallographic path through the γ/γ' eutectic regions which contain significant amounts of carbides, borides and sulphides. From the mechanical test results it is clear that the levels of C, B and Zr used in the experimental alloys did not detract significantly from their ductility or

toughness. However no overriding statement can be made about the optimisation of minor element composition, or the mechanism of operation of B and Zr in particular, in controlling grain boundary behaviour.

From examination of electron micrographs of ruptured testpieces, there was little evidence for the occurrence of grain boundary decomposition of MC particles and formation of γ' films, or γ'-precipitate-denuded matrix films for any creep-test condition up to 1040°C for the very strong alloys i.e. W37, W41, R6 and R8. Some of the weaker alloys showed occasional breakdown of MC particles (surrounded by γ') after about 100 hours creep exposure at 1000°C. In contrast to these effects the Nimonic 115 alloy blade materials contained blocky carbide particles encompassed by γ' films at grain boundaries, and the MarM246 alloy testpieces invariably showed M_6C particles and a grain boundary film containing γ' after creep exposure at 1040°C. From the experimental work two batches of Nimonic 115 alloy contained sigma phase precipitates in the microstructure. X-ray diffraction analyses of residues electrolytically-extracted from creep-ruptured testpieces did not show any significant quantities of $M_{23}C_6$ or M_6C phases to be precipitated in the microstructure. A feature common to all the creep-rupture testpieces after failure at any test condition was the presence of oxide-decorated microcracks at grain boundaries and the extent of this oxidation damage increased with both time and temperature. For most polycrystalline superalloys the depth of oxidation damage was usually greater at grain boundary regions than in the matrix. This was because of structural discontinuities allowing greater rates of diffusion and because of the presence of carbides with comparatively poor oxidation characteristics relative to the matrix. Intergranular penetration of oxygen would be expected to detract from the creep-rupture properties of the alloys, but may not have had an over-riding influence in this programme as evidenced by the similar duration to failure of uncoated and pack-aluminised testpieces in creep.

Grain size effects

The effect of grain size (d) on creep rate has been incorporated into the equation:

$$\dot{\varepsilon} = A\sigma^n d^m \exp\left(-\frac{Q}{RT}\right) \quad \ldots.(13)$$

where Q is the appropriate (diffusional) activation energy and A is a material constant. More recently theories have been presented[141-143] wherein σ in Equation (13) is replaced by an "effective stress" responsible for driving the local glide process. In particle hardened materials the "effective stress" is dependent on the opposing stress from particles experienced by the dislocations and an extra back stress which arises because of the additional dislocation line length created as the dislocation segment bows out around the particles. At temperatures of about 0.5 Tm and below a small grain size is usually associated with reduced steady state creep[141]. At temperatures above 0.5 Tm the typical behaviour of metallic materials seems to be that the creep rate increases with decreasing grain size at small grain sizes. In some special cases for instance in Monel and austenitic stainless steel[141] where slightly above 0.5 Tm it is possible to get an increasing creep rate at large and small grain sizes with a minimum at an intermediate grain size. It is generally accepted that the increased creep strength with decreasing grain size at low temperatures has the same origin as the well-known strengthening of grain boundaries in low-temperature deformation. It has been suggested that the weakening effect of grain boundaries at high temperatures is caused by the increased contribution of grain boundary sliding to the creep strain with decreasing grain size and measurements have in some cases supported this proposal. The creep strength of superalloys is dependent upon the grain structure, but it is extremely difficult to vary grain size per se whilst retaining the same microstructural features. Richards[144] found that the rupture life and creep-resistance of a wrought superalloy increased with grain size provided that the ratio of component thickness to grain size was kept constant. A cast superalloy showed a similar dependence of creep-rupture properties upon thickness

to grain size ratio. However, because of the difficulty of controlling closely the grain size of the casting alloys by varying the casting temperature alone, the section size to grain size relationship with creep-rupture properties was not so distinct.

For the experimental alloys examined in the present programme no systematic attempt was made to vary the grain size or microstructure of the alloys, which may otherwise have had a significant effect on their creep-rupture strengths. For most practical purposes the distribution of phases e.g. carbides, borides that would be expected to initiate mechanical failure, were similar.

Summary and overall conclusions

Metallurgical observations have been made on the relationship between the constitution, microstructure and selected mechanical properties of a series of experimental nickel-base casting alloys designed for high temperature creep resistance. The investigation involved a limited study of phase equilibria and selected mechanical properties; tensile, short-term creep-rupture strengths, hardness and impact properties of a series of experimental variants of a model heat-resistant alloy, designated HRA-376, whose high density (≈9 g/cc) precluded it for use as turbine blading. Similar observations were made for the commercial nickel casting alloy MarM246 using testpieces cast under laboratory conditions, and for Nimonic 115 alloy turbine blades that had been withdrawn from service engines. Two sets of blades manufactured when control of alloy composition by PHACOMP procedures was not employed contained sigma phase precipitates in the microstructure. Comparison was made with Nimonic 115 alloy blades withdrawn from an engine with a similar service history, but which were free of sigma phase.

In addition to a base of boron, carbon, aluminium, chromium, cobalt, nickel and zirconium, HRA-376 alloy contains three atomic percentage each of tantalum and tungsten. The experimental variants were designed by systematically replacing, titanium and niobium for tantalum, and molybdenum for tungsten. A further model alloy free of Ti, Nb, Mo, Ta and W but containing sufficient Al to produce a similar volume fraction of gamma-prime was included. The principal objectives were to

devise lighter alloys which had equivalent or superior creep-rupture strength to the model parent alloy and which retained microstructural stability during long term exposure at high temperatures.

1. In the first stage of the experimental programme 24 experimental alloys and 2 commercial alloys were studied to characterise the structure and composition of phases found in the microstructure. The three principal phases, matrix, gamma-prime and MC carbides were analysed by spectrographic and other chemical techniques in addition to electron microprobe analysis.

2. For the experimental alloys in both the as-cast condition and after heat-treatment for 2000 hours at 850°C, or 200 hours at 1050°C, elements that tended to form monocarbide (MC) phases i.e. titanium, niobium and tantalum, tended also to alloy preferentially with the gamma-prime phases.

3. Chromium, cobalt, molybdenum and tungsten alloy preferentially with the matrix phases.

4. Small amounts of boron were often associated with the monocarbide phases.

5. Generally good agreement was obtained between the chemical analyses and the microprobe analysis data for the alloyed gamma-prime phases. These analyses have formed the basis for developing a new family of alloys based on the gamma-prime phase. In bulk form these alloys have been shown to possess a good combination of creep-strength and toughness, also combined with excellent oxidation resistance.

6. Good correlation was also obtained between the chemical composition, calculated and measured lattice constants of the phases and calculated densities of the parent alloys.

7. A series of linear regression equations was developed to relate the compositions of the phases and parent alloys.

8. Apart from slight structural changes occurring within the microstructure that were anticipated from consideration of simple phase diagrams in the literature, none of the experimental alloys showed any tendency to precipitate tcp phases during exposure at 850°C, or significant precipitation of M_6C during exposure at 1050°C.

9. From the electron microscope observation of thin foils and replicas prepared from bulk testpieces it was found that the 850°C treatment caused slight dissolution of secondary gamma-prime and decomposition of eutectic gamma-prime phases.

10. Heat-treatment at 1050°C caused significant coalescence of the secondary gamma-prime phases.

11. Structures water-quenched after 200 hours exposure at 1050°C contained very fine tertiary gamma-prime that may have precipitated in the short duration of the quench.

12. In the as-cast condition i.e. including the unidirectionally solidified alloys, the matrix and γ' precipitates were coherent; there was little evidence of the presence of dislocations, but a very fine precipitate was present within some gamma-prime cuboids.

13. In comparison two Nimonic 115 alloy blade materials showed extensive precipitation of sigma platelets in the microstructure, and the MarM246 alloy also showed a typical Widmanstätten structure identified as M_6C platelets.

14. With reference to the PHACOMP analysis it was found from the measured compositions of the gamma phases in these alloys that account should be taken of the aluminium, titanium, niobium and tantalum in the various matrices.

15. The γ' and MC in the experimental alloys appeared to be fairly stable but these observations are unlikely to apply for all superalloys.

16. Bulk gamma-prime alloys based on compositions taken from the literature have been shown to precipitate sigma phase during heat-treatment.

17. From observations of sites for sigma formation in the Nimonic 115 alloy blade materials it was considered that the phase grew continuously in both γ' and matrix phases, and a mechanism was proposed for the nucleation (i.e. precipitation of Group Vl elements) and subsequent growth in both phases.

18. It is considered that a better understanding of the roles of molybdenum and tungsten in sigma precipitation may be obtained from the more detailed study of alloyed gamma-prime phases.

The second phase of the programme involved a limited study of the short-term creep-rupture strengths, hardness changes and miniature Charpy impact values after heat-treatments had been applied to the experimental alloys. Some tensile tests were done. Comparisons were made with two commercial alloys, IN100 and MarM246. Microstructural changes induced by creep and thermal exposure without stress were followed using optical and electron metallography. Factors governing the creep and short-term tensile behaviour i.e. coherency strain, stability of the gamma-prime precipitate and general microstructural features were tentatively explored.

19. Among the experimental alloys two, designated R6 and R8, had tensile and creep-rupture properties comparable to the best commercial alloys. The 100 hour creep-rupture strengths of R6 and R8 were very close to that of the model parent alloy HRA-376.

20. All the alloys were designed to be stable on thermal exposure and it was confirmed that this was in fact the case.

21. Stability in other samples, for instance, those taken from service components, showed that sigma phase precipitation in two samples of Nimonic 115 alloy ($\bar{N}v \simeq 2.73$ and 2.84 respectively), led to serious degradation of mechanical properties whereas another sample of slightly different composition ($\bar{N}v \simeq 2.54$) was not degraded. This observation emphasises the importance of the modern practice of Nv control in alloy production.

22. MarM246 alloy testpieces showed a propensity for precipitation of M_6C phase during high temperature exposure which detracted from creep-resistance, but had minimal effect on impact strength.

23. Comparison was made in some cases between conventionally-cast and unidirectionally solidified alloys. The general observations were that the tensile properties and creep-rupture properties at temperatures up to 1040°C were similar to those of the strongest commercial casting alloys. UDS improved the elongation-at-fracture values and creep-rupture lifetime of all alloys tested but the level of improvement was found to be dependent on alloy composition and test conditions. The best performance among the experimental alloys was shown by UDS R8 alloy which at 4 tsi/1100°C exhibited more than 40°C improvement in 100 hours capability over MarM246 alloy.

24. Vickers hardness values of the experimental alloys were in the range typical of commercial casting alloys which behaved similarly during heat-treatments.

25. Correlations have been obtained between durations to produce given levels of creep strain and rupture, and the solvus temperature of the gamma-prime precipitate. This is believed to be the first time that the solvus temperature of the major strengthening phase has been employed to express the creep-rupture properties of alloys. Regression equations were also developed relating the creep-rupture properties to alloy hardness.

26. No correlation was observed in the case of creep-rupture properties and alloy hardness values with respect to coherency strain occurring between the various matrices and gamma-prime phases.

27. Exploratory studies of one alloy using a pack-aluminised protective coating showed no effect on properties.

Finally, the metallurgical observations made of the structure, composition and mechanical properties of the alloys examined in this work were compared with ideas expressed in the literature on factors influencing the mechanical behaviour of cast nickel superalloys.

28. The contribution made by the alloying elements to the strength of the nickel matrix and separately to the gamma-prime phase was examined. For example, because of their atomic size differences Al, Ti, Nb, Mo and W would be expected to give solid solution strengthening in the nickel matrix at temperatures to 0.6 Tm. At high temperatures slow diffusing elements such as Mo and W would be expected to improve the creep resistance of nickel. Ti, Nb and Ta preferentially alloy with and stabilise the gamma-prime phase at high temperatures. The fortuitous partitioning of Co and the Group Vl elements Cr, Mo and W to the matrix phase and Ti, Nb and Ta to the gamma-prime phase produced alloys with low coherency strain and good creep-resistance.

29. Microstructural changes occurring in consequence of tensile and creep deformation were in accord with those in the literature. At optical microscope resolution no obvious microstructural instabilities, demonstrated by the appearance of acicular phases etc. occurred in the

experimental alloys. After creep-rupture tests at or above 1000°C changes in size and shape of the secondary gamma-prime precipitate occurred in most alloys. Acicular phases were observed in the commercial alloys. These were identified as sigma phase in two Nimonic 115 blade alloys and eta-carbide in MarM246 alloy creep tested at 1040°C. Fracture modes during tensile or creep-rupture tests were invariably intergranular. Transmission electron microscopy showed that during room temperature deformation the dislocations were found in the two phase matrix (γ + tertiary γ') regions located between the secondary gamma-prime precipitates. At temperatures in the range 750/850°C extensive stacking faults within the gamma-prime precipitate were evident. In this temperature range deformation is relatively heterogeneous due to the glide of intrinsic/extrinsic fault pairs for which cross-slip is exceedingly difficult. At 1000°C and above, creep deformation occurring within the grains was more homogeneous, stacking faults were absent and the secondary γ' precipitate had coalesced and had a general drawn-out stringer appearance. At these higher temperatures shearing of the secondary γ' particles by dislocations was evident, and networks of dislocations were observed at the γ'/matrix interfaces and within the two-phase matrix-plus-tertiary γ' regions. Although the secondary γ' particles appeared comparatively free of dislocations after high temperature creep this effect could have been in consequence of the slow rate of cooling on termination of the tests. Very fine scale precipitates that were not positively identified were often observed within the secondary γ' particles which could have affected the ease with which the γ' could otherwise be sheared in creep.

30. Attempts were made to correlate the creep-rupture strength of the alloys with compositional effects, general microstructural features, coherency strain, γ' precipitate stability etc. It is concluded that the high temperature creep resistance of these polycrystalline alloys is dependent on both compositional effects and manufacturing history. Creep deformation occurred both within the grains and at the grain boundaries where fracture ultimately occurred. No correlation could be made between creep-rupture properties and coherency strain, whereas the solvus temperature of the gamma-prime precipitate and alloy hardness could be correlated with creep resistance.

REFERENCES

No.	Author(s)	Title, etc.
1	W. Betteridge J. Heslop	The Nimonic Alloys E. Arnold Ltd., London, 1959
2	W. Betteridge	The Nimonic Alloys E. Arnold Ltd., London, 1974
3	C. T. Sims	A contemporary view of nickel-base superalloys J. of Metals, 18, 1119-1130, 1966
4	C. T. Sims	The role of refractory metals in austenitic superalloys 6th Plansee Seminar, 1968
5	C. T. Sims W. C. Hagel	The Superalloys J. Wiley & Sons, 1972
6	G. P. Sabol R. Stickler	Microstructure of nickel-based superalloys Phys. Stat. Sol. 35, 11-52, 1969
7	P. S. Kotval	The microstructure of superalloys Metallography, 1, 251-285, 1969
8	C. P. Sullivan M. J. Donachie F. R. Morral	Cobalt-base superalloys Monograph Series Cobalt Information Centre, 1970
9	R. F. Decker	Strengthening mechanisms in nickel-base superalloys AMAX Symposium on steel-strengthening mechanisms, 1969
10	C. T. Sims	ASME 70-GT-24, 1971
11	H. J. Beattie W. C. Hagel	Trans. Met. Soc. ASME, 233, No. 2, 277-287, 1965
12	L. R. Woodyatt C. T. Sims H. J. Beattie	Trans AIME, 236, 519 1966
13	H. J. Murphy C. T. Sims A. M. Beltran	J. Metals, 20, 46 1968
14	H. J. Murphy C. T. Sims A. M. Beltran	International Symposium on Structural Stability in Superalloys ASM 1968

REFERENCES (cont'd)

No.	Author(s)	Title, etc.
15	C. S. Barrett	Some industrial alloying practice and its basis J. Inst. Metals, 100, 65, 1972
16	C. H. Lund M. J. Woulds J. Hocking	Cobalt and sigma, participant, spectator or referee J. Inst. Metals, 100, 65, 1972
17	J. E. Restall E. C. Toulson	Constitution and microstructure of certain cast nickel superalloys Part I. Metals and Materials, 134-139, 1973
18	J. E. Restall E. C. Toulson	Ibid, Part II, 187-194, 1973
19	J. E. Restall M. J. Weaver	Improvements in or relating to tri-nickel aluminide base alloys Brit. Pat. Spec. 1381859, 29 January 1975
20	O. H. Kriege J. M. Baris	Trans. ASM Quarterly, 62, No. 1, 195-200, 1969
21	J. R. Mihalisin D. L. Pasquine	Phase transformations in nickel-base superalloys As Reference 14
22	W. B. Pearson	Handbook of lattice spacings and structures of metals and alloys Pergamon Press, 1958
23	R. M. N. Pelloux N. J. Grant	Trans. Met. Soc. AIME, 218, 232-237, 1960
24	E. R. Parker T. H. Hazlett	"Principles of solution hardening" Relation of properties to microstructure ASM, 30, 1954
25	B. E. P. Beeston L. K. France	J. Inst. Metals, 96, 105, 1968
26	B. E. P. Beeston I. L. Dillamore R. G. Smallman	Metal Sci. J. 2, 12, 1968
27	M. V. Pridantsev	Izv. Akad. Nauk. SSSR, Metal (5), 115, 1967

REFERENCES (cont'd)

No.	Author(s)	Title, etc.
28	C. H. Lund	Physical metallurgy of nickel base superalloys, DMIC Rept. 153, 1961
29	A. Taylor R. W. Floyd	The constitution of nickel-rich alloys of the nickel-titanium-aluminium and nickel-chromium-aluminium systems
30	Ibid	J. Inst. Metals, 81, 25-32 and 451-464 1952-53
31	R. W. Guard J. H. Westbrook	Alloying behaviour of Ni_3Al (γ' phase) Trans. Met. Soc. AIME, 215, 807-814 1959
32	R. Nordheim N. J. Grant	Trans. AIME 200, 211, 1954
33	R. W. Guard E. A. Smith	Constitution of the Ni-Mo-Al system J. Inst. Metals, 88, 283-287, 1959
34	P. B. Budberg	Study of alloys in the ternary system Ni-Al-W, Zhur, Neorg Khimi 3(3) 694-698 1958 Also DMIC Rept. 183 1963
35	R. W. Decker J. R. Mihalisin	Coherency strains in γ' hardened nickel alloys Trans. ASM 62, 481-489 1969
36	A. V. Karg D. E. Fornwalt O. H. Kreige	The effect of alloying elements on the intensity of superlattice reflections of Ni_3Al J. Inst. Metals 99, 301-305 1971
37	W. T. Loomis J. W. Freeman D. L. Sponseller	The influence of molybdenum on the γ' phase in experimental nickel-base superalloys Met. Trans. 3, 989-1000, 1972
38	R. K. Ham R. H. Cooke G. R. Purdy	Solidification behaviour and gamma precipitation in nickel-rich γ' (Ni_3Al, Ti) Met. Sci. J., 6, 73-77, 1972
39	R. F. Decker J. W. Freeman	Trans. AIME 218, 277 1960
40	W. Wallace T. Tereda	The nature of sulfo-carbides observed in nickel-base superalloys Metallography 6, 511-526, 1973

REFERENCES (cont'd)

No.	Author(s)	Title, etc.
41	W. J. Boesch (Private communication to) C. T. Sims	Nickel alloys - the heart of gas turbine engines ASME 70-GT-24 1970
42	A. W. Franklin W. Betteridge	J. Inst. Metals 85, 473 1956/57
43	W. C. Hagel H. J. Beattie	Trans. AIME 215, 967, 1959
44	B. J. Piearcey R. W. Smashey	Trans. AIME 239, 451, 1967
45	H. J. Beattie F. L. VerSnyder	Trans. ASM 49, 883, 1957
46	H. E. Collins	Relative stability of carbide and intermetallic phases in nickel-base superalloys International Symposium on Structural Stability in Superalloys ASM 1968
47	F. Laves J. J. Wallbaum	Naturwissenschaften 27, 674, 1939
48	J. J. Wallbaum	Naturwissenschaften 31, 91, 1943
49	E. C. Bain W. E. Griffiths	Trans. TMS-AIME 75, 1927
50	E. O. Hall S. H. Algie	The sigma phase Met. Rev. 11, 61, 1966
51	D. P. Shoemaker B. G. Bergman	J. Am. Chem. Soc. 72, 5793, 1950
52	J. R. Mihalisin C. G. Bieber R. T. Grant	Sigma - its occurrence, effect and control in nickel-base superalloys Trans. Met. Soc. AIME 242, 2399, 1968
53	H. L. Eiselstein	Advances in the technology of stainless steels and related alloys ASTM STP 369, 62 1965
54	H. J. Beattie W. C. Hagel	Trans. AIME 221, 28 1961

REFERENCES (cont'd)

No.	Author(s)	Title, etc.
55	L. V. Azaroff	Introduction to solids McGraw-Hill 1960
56	T. B. Massalski	in, Theory of alloy phases ASM Cleveland 1965 (p63)
57	K. Kuo	Acta metall. 1, 720, 1953
58	R. G. Barrows	The occurrence of sigma-type phases in heat-resisting alloys, with special emphasis on the Co-Cr-W systems Ph.D. Thesis, University of Denver, 1970
59	D. K. Das S. P. Rideout P. A. Beck	Intermediate phases in the Mo-Fe-Co, Mo-Fe-Ni and Mo-Ni-Co ternary systems Trans AIME, 194, 1071, 1952
60	A. H. Sully T. J. Heal	An electron compound in alloys of the transition metals Research, 1, 288, 1948
61	A. H. Sully	The sigma phase in binary alloys of the transition elements J. Inst. Metals, 80, 173-179, 1951-52
62	L. Pauling	The nature of the interatomic forces in metals Phys. Rev. 54, 899, 1938
63	S. P. Rideout W. D. Manly E. L. Kamen B. S. Lement P. A. Beck	Intermediate phases in ternary alloy systems of transition elements Trans. AIME, 872-876 1951
64	W. J. Boesch J. S. Slaney	Metal Progress, 86, 109 1964
65	G. N. Kirby	The relative effects of chromium, molybdenum and tungsten upon the occurrence of sigma phase precipitation in nickel-base alloys Ph.D Thesis, University of Michigan, 1971
66	G. Llewelyn T. D. Weaver M. J. Weaver P. W. Wildgoose	Nickel-base alloys Brit. Pat. Spec., 1,011, 785 1965

REFERENCES (cont'd)

No.	Author(s)	Title, etc.
67	J. E. Northwood T. Homewood	Controlled solidification of gas turbine alloys Proc. tenth annual conference of the British Investment Casters Technical Association, May 1970
68	B. J. Piearcey B. H. Kear R. W. Smashey	Correlation of structure with properties in a directionally solidified nickel-base superalloy Trans. ASM 60, 634-645, 1967
69	R. L. Dreshfield R. L. Ashbrook	NASA TN-D-6015 September 1970
70	J. J. Johnson J. Walsh M. J. Donachie	The sigma phase formed in nickel-base UDIMET 700 J. Inst. Metals, 95, 379-381, 1967
71	J. E. Restall	An examination of correction procedures for quantitative electron-probe micro-analysis Metallurgia Vol LXXX, No. 479, 121-125 1969
72	H. J. Goldschmidt	Interstitial alloys Butterworths 1967
73	R. A. Gregg B. J. Piearcey	Solute distribution and eutectic formation in as-cast nickel-base superalloys Trans. Met. Soc. AIME, 230, 599-600, 1964
74	W. Nall	Private communication
75	D. Nicholas	Ibid, Fulmer Research Institute Ltd
76	L. Lemaire D. E. Fornwalt B. H. Kear	Co-precipitation of γ' (Ni_3Al) and α-Cr in a nickel-base alloy Microstructures 13-16 December/January 1971
77	H. J. Beattie W. C. Hagel	Iron and Steel Institute Special Report No. 64, 1959
78	J. Heslop	Cobalt, 24, 128, 1964

REFERENCES (cont'd)

No.	Author(s)	Title, etc.
79	A. Havalda	Investigation of the influence of tungsten on the morphology of the γ' precipitation in nickel-base superalloys Trans. ASM, 62, No. 2, 477-480, 1969
80	J. R. Mihalisin	Trans. AIME 239, 180, 1967
81	J. Billingham J. Lauridsen	Nucleation of sigma phase in a complex nickel-base superalloy Metallography 6, 85-90, 1973
82	A. Taylor	X-ray Metallography John Wiley and Sons Inc. 1961
83	F. L. VerSnyder M. E. Shank	The development of columnar grain and single crystal high temperature materials through directional solidification Mater. Sci. Eng. 6, 213-247, 1970
84	G. R. Leverant D. N. Duhl	The effect of stress and temperature on extent of primary creep in directionally-solidified nickel-base superalloys Met. Trans. 2, 907-908, 1971
85	G. R. Leverant B. H. Kear	The mechanism of creep in gamma-prime precipitation hardened nickel-base alloys at intermediate temperatures Met. Trans. 1, 491-498, 1970
86	C. Morizot Y. Honnorat	Etude d'alliages superrefractaires pour solidification unidirectionelle. Memoires Scientifique Rev. Metallurg, LXIX, No. 11, 1972
87	R. G. Davies T. L. Johnston	The Metallurgical Design of a Superalloy, Ford Motor Company, Dearborn, Michigan 1969
88	N. F. Mott F. R. N. Nabarro	Report of the conference on strength of solids Physical Society, 1 to 19, 1948
89	R. L. Fleischer	The strengthening of metals, p.93 Edited by D. E. Peckner, Reinhold, New York 1964

REFERENCES (cont'd)

No.	Author(s)	Title etc.
90	R. L. Fleischer	Acta. Met., 11, 203-209, 1963
91	M. E. Fine	The strengthening of metals Edited by D. E. Peckner, Reinhold, New York 1964
92	P. S. Kotval	Trans. Met. Soc. AIME 242, 1651 1968
93	R. Nordheim N. J. Grant	J. Inst. Metals 82, 440-444 1954
94	P. H. Thornton R. G. Davies T. L. Johnston	Met. Trans. 1, 207-218 1970
95	P. A. Flinn	Intermetallic Compounds (Chapter 14) Edited by J. H. Westbrook John Wiley and Sons Inc. 1967
96	J. R. Beeler	Intermetallic Compounds (Chapter 14) Edited by J. H. Westbrook John Wiley and Sons Inc. 1967
97	P. A. Flinn	Trans. AIME 218, 145, 1960
98	J. S. Koehler F. Seitz	J. Appl. Mech. 14, 217 1947
99	J. F. Radavich W. H. Couts	Trans. ASM 54, 591 1961
101	J. F. Radavich W. H. Couts	Rev. High Temp. Mater, 1, 55, 1971
102	J. M. Oblak J. E. Doherty A. F. Giamei B. H. Kear	Precipitation of γ in the γ' of nickel-base superalloys Met. Trans. 5, 1252-1255 1974
103	H. F. Merrick	Precipitation within γ' particles in nickel-base superalloys Met. Trans. 4, 885 to 887, 1973
104	R. O. Williams	Acta. Met. 5, 241, 1957

REFERENCES (cont'd)

No.	Author(s)	Title, etc.
105	H. F. Merrick	Deformation of nickel-chromium base alloys Proc. Third European Reg. Conf. Electron Microscopy, Prague 1964
106	H. Gleiter E. Hornbogen	Theory of the interaction of dislocations with coherent ordered zones Phys. Status Solidi. 12, 235, 1965
107	S. M. Copley B. H. Kear	A dynamic theory of coherent precipitation hardening with application to nickel-base superalloys Trans. AIME 239, 984-992, 1967
108	B. H. Kear A. F. Giamei J. M. Silcock R. K. Ham	Scripta Met. 2, 287 1968
109	V. Gerold H. Haberkorn	Phys. Status Solidi. 16, 675, 1966
110	P. Beardmore R. G. Davies T. L. Johnston	On the temperature dependence of the flow stress of nickel base alloys Trans. Met. Soc. AIME 245, 1537-1545 1969
111	C. L. Corey B. Lisowsky	Trans. Met. Soc. AIME 239, 239-243 1967
112	J. K. Tien S. M. Copley	The effect of uniaxial stress on the periodic morphology of coherent gamma-prime precipitates in nickel-base superalloy crystals Met. Trans. 2, 215-219, 1971
113	J. K. Tien S. M. Copley	The effect of orientation and sense of applied uniaxial stress on the morphology of coherent gamma-prime precipitates in stress annealed nickel-base superalloy crystals Met. Trans. 2, 543-553, 1971
114	J. K. Tien R. P. Gamble	Effects of stress coarsening on coherent particle strengthening Met. Trans 3, 2157-2162, 1972

REFERENCES (cont'd)

No.	Author(s)	Title, etc.
115	F. R. Nabarro	Deformation of crystals by the motion of ions. Strength of solids. The Physical Society, London, 75 1948
116	C. Herring	Diffusional viscosity of a polycrystalline solid J. Appl. Phys. 21, 437, 1950
117	R. F. Decker R. R. Dewitt	J. of Metals 17, 139 1965
118	R. W. Cahn	Modern practice in the design of strong alloys J. of Metals 28 to 37, February 1973
119	R. W. Guard	Mechanical behaviour of materials at elevated temperatures Edited by J. E. Dorn, McGraw Hill New York, 1961
120	Yu G. Sorokina S. A. Yuganova	Met. Science and Heat Treatment 5/6 456-457, 1968
121	M. J. Fleetwood	Private communication to R. F. Decker (9)
122	A. J. Ardell	The mechanism of phase transformations in crystalline solids. IOM Monograph No. 33, p.111 Institute of Metals, London, 1969
123	W. I. Mitchell	Z. Metallk 55, 613, 1964
124	B. H. Kear G. R. Leverant J. M. Oblak	Trans. ASM 62, 639-650 1969
125	G. R. Leverant B. H. Kear J. M. Oblak	Creep of precipitation-hardened nickel-base alloy single crystals at high temperature Met. Trans. 4, 355-362, 1973
126	G. S. Ansell J. W. Weertman	Trans. Met. Soc. AIME 215, 838-843 1959

REFERENCES (cont'd)

No.	Author(s)	Title, etc.
127	A. J. Kennedy	Processes of creep and fatigue in metals 261 ff Publisher Oliver and Boyd, London, 1962
128	P. C. Varley N. K. B. Day A. Sendorek	J. Inst. Metals, 86, 337 1957-58
129	R. Chadwick N. B. Muir H. B. Grainger	Stress-corrosion of wrought ternary and complex alloys of the aluminium-zinc-magnesium system J. Inst. Metals, 85, 161, 1956-57
130	P. J. E. Forsyth	J. Aust. Inst. Metals 8, 52, 1963
131	H. E. Gresham	Metals and Materials 3,433, 1969
132	C. P. Sullivan M. P. Donachie	Some effects of microstructure on the mechanical properties of nickel-base superalloys Metals Eng. Quart. 7, 36, 1967
133	D. McLean	A note on the metallography of cracking during creep J. Inst. Metals 85, 468, 1956/57
134	R. F. Decker J. P. Rowe J. W. Freeman	Boron and zirconium from crucible refractories in a complex heat-resistant alloy NASA Report 1392 1958
135	J. K. Tien R. P. Gamble	The influence of applied stress and stress sense on grain boundary precipitate morphology in a nickel-base superalloy during creep Met. Trans. 2, 1663-1667, 1971
136	I. J. Polmear	The properties of commercial Al-Zn-Mg alloy J. Inst. Metals 89, 51, 193, 1960/61
137	A. R. Entwistle J. K. Wynn	Precipitation in commercial copper-beryllium alloys J. Inst. Metals 89, 24, 1960/61
138	A. Kelly	The strengthening of metals by dispersed particles Proc. Roy. Soc., London, 63-79, V282A 1964

REFERENCES (cont'd)

No.	Author(s)	Title, etc.
139	A. G. Quarrell B. J. Nield	Intercrystalline cracking in creep of some aluminium alloys J. Inst. Metals, 85, 480, 1956/57
140	B. H. Kear A. F. Giamie	Transverse grain boundary strengthening in a directionally solidified nickel-base alloy Proc. Third International Conference on the strength of metals and alloys The Institute of Metals and the Iron and Steel Institute (Cambridge, England) (134-138) August 1973
141	R. Lagneborg	Dislocation mechanisms in creep International Metallurgical Review 17, 130-145, 1972
142	R. Lagneborg	Bypassing of dislocations past particles by a climb mechanism Scripta Metallurgica 7, 605-614, 1973
143	J. P. Hirth	The influence of grain boundaries on mechanical properties Met. Trans. 3, 3047-3067 1972
144	E. G. Richards	J.Inst. Metals 96, 365, 1968

TABLE 1

Typical compositions of selected commercial nickel superalloys (percentage by weight)

Alloy	B	C	Al	Ti	Cr	Fe	Co	Ni	Zr	Nb	V	Mo	Hf	Ta	W
Nimonic 75	0.001	0.08		0.4	20.0	5.0 max		Bal	0.05						
Nimonic 80A	0.003	0.06	1.3	2.3	20.0	1.0 max	1.1	Bal	0.07						
Nimonic 90	0.003	0.09	1.4	2.4	20.0	1.0 max	16.0	Bal	0.07						
Nimonic 105	0.006	0.15	4.5	1.2	14.5	1.0 max	20.0	Bal	0.10			5.0			
Nimonic 115	0.016	0.15	5.0	4.0	15.0	1.0 max	15.0	Bal	0.05			4.0			
Udimet 500	0.005	0.08	3.0	3.0	19.0	4.0 max	19.0	Bal				4.0			
Udimet 700	0.03	0.08	4.3	3.5	15.0	1.0 max	18.5	Bal				5.2			
Incoloy 901	0.02	0.05	0.25	2.5	13.5	34.0		Bal				6.1			
Nimocast 713LC	0.012	0.05	6.0	0.7	12.0	0.5 max		Bal	0.10	2.0		4.5			
Nimocast PD16	0.02	0.13	6.0	0.5 max	6.0	0.5 max		Bal	0.12	2.0 max		2.0			11.0
Nimocast PD21	0.02	0.10	6.0	0.5 max	5.8	0.5 max		Bal		1.5		2.0			10.5
IN100	0.01	0.18	5.5	4.7	10.0	1.0 max	15.0	Bal	0.06		0.9	3.0			
IN738	0.01	0.17	3.4	3.4	16.0	0.5 max	8.5	Bal	0.10	0.9		1.8		1.8	2.6
MarM246	0.02	0.15	5.5	1.5	9.0	1.0 max	10.0	Bal	0.05			2.5		1.5	10.0
MarM002	0.02	0.15	5.5	1.5	9.0	0.5 max	10.0	Bal	0.05			0.5 max	1.5	2.5	10.0
B1900	0.02	0.10	6.0	1.0	8.0		10.0	Bal	0.08			6.0		4.3	

TABLE 2

Chemical composition of alloys

Alloy	Castcode	B	C	Al	Ti	Cr	Co	Ni*	Zr	Nb	Mo	Ta	W
W37	1 LD298	0.02	0.15	5.7	0	5.9	9.6	60.6	0.10	0	0	8.9	9.0
	2	0.02	0.14	5.9	0	5.9	9.6	60.0	0.11	0	0	9.0	9.3
	3	0.11	0.7	13.0	0	7.0	10.0	63.1	0.07	0	0	3.0	3.0
W36	1 LD300	0.02	0.15	6.0	0	6.2	10.1	63.2	0.10	4.8	0	0	9.4
	2	0.02	0.14	6.1	0	6.1	10.3	62.9	0.10	5.4	0	0	8.9
	3	0.11	0.7	13.0	0	7.0	10.0	63.1	0.07	3.0	0	0	3.0
W44	1 LD302	0.02	0.15	6.0	0	6.2	10.1	63.1	0.10	0	5.0	9.3	0
	2	0.03	0.13	6.1	0	6.0	10.3	63.3	0.10	0	4.9	9.1	0
	3	0.11	0.7	13.0	0	7.0	10.0	63.1	0.07	0	3.0	3.0	0
W47	1 LD304	0.02	0.15	6.2	0	6.5	10.5	66.2	0.10	5.1	5.2	0	0
	2	0.02	0.12	6.2	0	6.6	10.9	65.3	0.10	5.6	5.1	0	0
	3	0.11	0.7	13.0	0	7.0	10.0	63.1	0.07	3.0	3.0	0	0
R1	1 LD250	0.02	0.15	6.4	2.6	6.7	10.8	67.9	0.12	0	5.3	0	0
	2	0.02	0.10	6.3	2.8	6.5	10.8	67.9	0.11	0	5.5	0	0
	3	0.11	0.7	13.0	3.0	7.0	10.0	63.1	0.07	0	3.0	0	0
W49	1 LD306	0.02	0.15	6.1	2.5	6.4	10.3	64.8	0.10	0	0	0	9.6
	2	0.02	0.14	6.1	2.4	6.4	10.3	65.4	0.12	0	0	0	9.1
	3	0.11	0.7	13.0	3.0	7.0	10.0	63.1	0.07	0	0	0	3.0
W34	1 LD299	0.02	0.15	5.9	0	6.1	9.8	61.9	0.10	2.3	0	4.5	9.2
	2	0.02	0.12	5.8	0	5.9	10.0	61.6	0.10	2.7	0	4.6	9.1
	3	0.11	0.7	13.0	0	7.0	10.0	63.1	0.07	1.5	0	1.5	3.0
W50	1 LD305	0.02	0.15	5.9	1.2	6.1	10.0	62.6	0.10	0	0	4.6	9.3
	2	0.02	0.13	6.0	1.1	6.2	10.2	63.0	0.10	0	0	4.5	8.7
	3	0.11	0.7	13.0	1.5	7.0	10.0	63.1	0.07	0	0	1.5	3.0

TABLE 2 (cont'd)

Alloy	Castcode	B	C	Al	Ti	Cr	Co	Ni*	Zr	Nb	Mo	Ta	W
R13	1 LD308	0.02	0.15	6.1	1.3	6.3	10.2	64.0	0.11	2.4	0	0	9.5
	2	0.02	0.08	6.2	1.4	6.1	10.3	62.5	0.11	2.6	0	0	9.6
	3	0.11	0.7	13.0	1.5	7.0	10.0	63.1	0.07	1.5	0	0	3.0
R2	1 LD248	0.02	0.15	6.2	1.3	6.4	10.4	65.5	0.11	0	5.1	4.8	0
	2	0.02	0.10	6.1	1.5	6.4	10.4	65.3	0.11	0	5.2	4.9	0
	3	0.11	0.7	13.0	1.5	7.0	10.0	63.1	0.07	0	3.0	1.5	0
R14	1 LD307	0.02	0.15	6.4	1.3	6.6	10.7	67.0	0.11	2.5	5.2	0	0
	2	0.02	0.08	6.3	1.4	6.7	10.8	65.5	0.11	2.7	5.3	0	0
	3	0.11	0.7	13.0	1.5	7.0	10.0	63.1	0.07	1.5	3.0	0	0
R15	1 LD309	0.02	0.15	6.1	0	6.4	10.3	64.6	0.10	2.5	5.0	4.5	0
	2	0.02	0.09	6.1	0	6.2	10.5	64.0	0.09	2.5	4.9	4.7	0
	3	0.11	0.7	13.0	0	7.0	10.0	63.1	0.07	1.5	3.0	1.5	0
W43	1 LD303	0.02	0.15	6.0	0	6.2	10.1	64.4	0.10	2.4	2.5	4.6	3.5
	2	0.03	0.14	6.2	0	6.1	10.3	64.3	0.10	2.6	2.5	4.6	3.1
	3	0.11	0.7	13.0	0	7.0	10.0	63.1	0.07	1.5	1.5	1.5	1.5
R3	1 LD251	0.02	0.15	6.1	0.8	6.3	10.2	64.2	0.11	1.6	2.5	3.1	4.8
	2	0.01	0.11	6.2	1.0	6.2	10.1	63.4	0.12	1.9	2.6	3.2	5.2
	3	0.11	0.7	13.0	1.0	7.0	10.0	63.1	0.07	1.0	1.5	1.0	1.5
W41	1 LD301	0.02	0.15	5.9	0	6.1	9.8	61.8	0.10	0	2.4	9.1	4.6
	2	0.02	0.13	6.2	0	6.0	9.9	61.4	0.09	0	2.4	9.1	4.7
	3	0.11	0.7	13.0	0	7.0	10.0	63.1	0.07	0	1.5	3.0	1.5
R4	1 LD289	0.02	0.15	6.1	0.8	6.4	10.3	64.7	0.11	1.6	3.4	3.2	3.2
	2	0.02	0.14	6.1	0.9	6.3	10.3	64.1	0.11	1.8	3.4	3.3	3.5
	3	0.11	0.7	13.0	1.0	7.0	10.0	63.1	0.07	1.0	2.0	1.0	1.0

TABLE 2 (cont'd)

Alloy	Castcode	B	C	Al	Ti	Cr	Co	Ni*	Zr	Nb	Mo	Ta	W
R5	1 LD258	0.02	0.15	6.0	0.8	6.3	10.2	63.9	0.11	1.6	1.7	3.1	6.3
	2	0.02	0.14	6.0	0.9	6.2	10.1	63.1	0.11	1.8	1.7	3.2	6.7
	3	0.11	0.7	13.0	1.0	7.0	10.0	63.1	0.07	1.0	1.0	1.0	2.0
R6	1 LD255	0.02	0.15	6.0	0.4	6.3	10.2	63.8	0.11	2.0	2.5	3.9	4.8
	2	0.02	0.13	6.2	0.5	6.1	10.2	62.8	0.10	2.2	2.5	4.1	5.1
	3	0.11	0.11	13.0	0.5	7.0	10.0	63.1	0.07	1.25	1.5	1.25	1.5
R7	1 LD256	0.02	0.15	6.1	1.1	6.4	10.3	64.9	0.11	2.0	2.5	1.6	4.8
	2	0.02	0.14	5.8	1.2	6.3	10.2	64.0	0.11	2.7	2.6	1.8	5.1
	3	0.11	0.7	13.0	1.25	7.0	10.0	63.1	0.07	1.25	1.5	0.5	1.5
R8	1 LD257	0.02	0.15	6.1	1.0	6.3	10.2	64.1	0.11	0.8	2.5	3.9	4.8
	2	0.02	0.14	6.2	1.0	6.0	10.1	63.1	0.10	1.6	2.7	3.9	5.1
	3	0.11	0.7	13.0	1.25	7.0	10.0	63.1	0.07	0.5	1.5	1.25	1.5
R9	1 LD252	0.02	0.15	6.2	1.7	6.4	10.4	65.3	0.11	0.8	2.5	1.6	4.9
	2	0.02	0.13	6.1	1.8	6.1	10.3	64.9	0.11	1.1	2.5	1.9	5.0
	3	0.11	0.7	13.0	2.0	7.0	10.0	63.1	0.07	0.5	1.5	0.5	1.5
R10	1 LD253	0.02	0.15	6.1	1.7	6.4	10.3	65.6	0.11	0.8	1.6	1.6	6.4
	2	0.02	0.12	5.9	1.8	6.0	10.1	65.1	0.08	0.9	1.7	1.7	6.6
	3	0.11	0.7	13.0	2.0	7.0	10.0	63.1	0.07	0.5	1.0	0.5	2.0
R11	1 LD254	0.02	0.15	6.2	1.7	6.5	10.5	65.8	0.11	0.8	3.4	1.6	3.3
	2	0.02	0.14	6.3	1.9	6.3	10.4	65.2	0.11	0.9	3.6	1.7	3.5
	3	0.11	0.7	13.0	2.0	7.0	10.0	63.1	0.07	0.5	2.0	0.5	1.0
R12	1 LD249	0.02	0.02	8.6	0	7.1	11.5	72.5	0.12	0	0	0	0
	2	0.02	0.04	8.9	0	7.0	11.3	72.5	0.16	0	0	0	0
	3	0.11	0.10	16.8	0	7.3	10.4	65.3	0.07	0	0	0	0

TABLE 2 (cont'd)

Alloy Castcode		B	C	Al	Ti	Cr	Co	Ni*	Zr	Nb	Mo	Ta	W
Nimonic 115 alloy blades containing sigma phase (2)	(4)	0.014	0.15	5.05	4.05	14.85	15.0	57.2	0.05	0	3.67	0	0
	(5)	0.016	0.14	4.88	3.83	15.10	14.90	57.6	0.05	0	3.51	0	0
Nimonic 115 alloy blade (sigma free) (2)		0.018	0.15	4.40	4.04	14.95	14.60	58.7	0.04	0	3.18	0	0
MarM246	(2)	0.016	0.13	5.45	1.54	8.95	10.11	59.6	0.04	0	2.43	1.52	10.21

* Ni balance
(1) Nominal weight percentage
(2) Actual weight percentage
(3) Nominal atomic percentage
(4) Service life ≃ 8000 hours
(5) Service life ≃ 1360 hours

TABLE 3

Details of materials used in alloy manufacture

Material	Supplier	Typical level of impurities ppm (W/o)													
		C	Mg	Al	Si	S	Ti	Fe	Co	Cu	Zn	As	Sn	Sb	Pb
Nickel carbonyl pellets	Henry Gardner & Co Ltd	100	-	-	-	10	-	-	5	10	-	1	-	-	1
Cobalt electrolytic cathode grade	Brandhurst & Co Ltd	-	-	<2	-	20	-	20	-	-	3	-	-	<5	4-8
Aluminium super purity pellets	The British Aluminium Co Ltd	-	-	-	20	-	-	15	-	15	-	-	-	-	-
Ni-11.5 W/o Boron	Murex Ltd	300	<1000	<100	<2000	-	-	4000	-	-	-	-	-	-	10
Ni-50 W/o Zirconium															
Chromium pellets		200	-	500	400	40	-	1400	-	-	-	-	-	-	5
Niobium pellets		<1000	-	-	<400	-	<100	<300	-	-	-	-	<100	-	-
Molybdenum pellets		<500	-	<7500	<2000	<100	-	<500	-	<500	-	-	-	-	<20
Tantalum pellets		<1000	-	-	<200	-	<100	<200	-	-	-	-	<100	-	-
Tungsten pellets															
Carbon granular charcoal	British Drug Houses Ltd														

TABLE 4

Composition of dendrite, gamma, eutectic gamma-prime and MC carbides compared with alloy compositions - (as-cast)

Alloy	Phase	B	C	Al	Ti	Cr	Co	Ni	Zr	Nb	Mo	Ta	W
W37	Alloy	0.11	0.7	13.0	0	7.0	10.0	63.1	0.07	0	0	3.0	3.0
	Gamma	0	0	4.7	0	12.7	13.6	64.0	0	0	0	1.3	3.8
	Eutectic γ'	0	0	19.9	0	5.1	7.9	61.7	0.07	0	0	3.5	1.8
	MC	0	50.0	0	0	2.1	1.6	2.6	0.3	0	0	30.3	13.5
	Dendrite	0	0	12.4	0	7.0	9.6	66.2	0	0	0	2.4	2.8
W36	Alloy	0.11	0.7	13.0	0	7.0	10.0	63.1	0.07	3.0	0	0	3.0
	Gamma	0	0	5.0	0	12.9	13.4	63.7	0	1.8	0	0	3.3
	Eutectic γ'	0	0	19.2	0	4.2	7.1	64.3	0.07	3.5	0	0	1.7
	MC	0	50.0	0	0	4.3	1.8	3.0	0.5	38.5	0	0	1.9
	Dendrite	0	0	12.9	0	8.9	9.3	65.2	0	2.0	0	0	1.8
W44	Alloy	0.11	0.7	13.0	0	7.0	10.0	63.1	0.07	0	3.0	3.0	0
	Gamma	0	0	3.3	0	13.1	15.8	62.1	0	0	4.9	0.8	0
	Eutectic γ'	0	0	21.1	0	2.8	6.5	63.1	0.07	0	1.0	5.4	0
	MC	0	50.0	0	0	1.7	0.8	2.5	0.3	0	2.9	43.0	0
	Dendrite	0	0	13.9	0	7.7	11.4	61.6	0	0	2.6	2.7	0
W47	Alloy	0.11	0.7	13.0	0	7.0	10.0	63.1	0.07	3.0	3.0	0	0
	Gamma	0	0	4.8	0	11.2	13.3	65.4	0	0.8	4.5	0	0
	Eutectic γ'	0	0	18.7	0	3.2	6.8	65.4	0.07	4.8	1.1	0	0
	MC	0	50.0	0	0	0.3	0.4	2.6	0.2	45.2	1.6	0	0
	Dendrite	0	0	12.8	0	8.4	11.2	63.0	0	2.0	2.6	0	0
R1	Alloy	0.11	0.7	13.0	3.0	7.0	10.0	63.1	0.07	0	3.0	0	0
	Gamma	0	0	6.9	0.7	12.3	15.0	60.4	0	0	4.7	0	0
	Eutectic γ'	0	0	17.4	5.9	3.7	7.0	64.7	0.05	0	1.3	0	0
	MC	0	50.0	0	32.5	0.8	0.2	1.4	0.1	0	15.0	0	0
	Dendrite	0	0	13.0	2.3	8.2	10.9	62.6	0	0	3.0	0	0

TABLE 4 (cont'd)

Alloy	Phase	B	C	Al	Ti	Cr	Co	Ni	Zr	Nb	Mo	Ta	W
W49	Alloy	0.11	0.7	13.0	3.0	7.0	10.0	63.1	0.07	0	0	0	3.0
	Gamma	0	0	3.6	0.6	11.2	11.4	70.1	0	0	0	0	3.1
	Eutectic γ'	0	0	18.5	5.6	4.0	7.4	63.5	0.07	0	0	0	1.0
	MC	0	50.0	0	32.1	1.2	0.4	2.3	0.2	0	0	0	13.9
	Dendrite	0	0	12.5	2.0	8.1	10.3	63.4	0	0	0	0	3.8
W34	Alloy	0.11	0.7	13.0	0	7.0	10.0	63.1	0.07	1.5	0	1.5	3.0
	Gamma	0	0	3.5	0	10.7	13.2	67.4	0	0.9	0	0.8	2.8
	Eutectic γ'	0	0	19.9	0	3.6	7.0	64.3	0.07	1.5	0	2.1	1.6
	MC	0	50.0	0	0	0.1	0.1	2.0	0.2	32.1	0	16.0	1.4
	Dendrite	0	0	14.7	0	8.1	9.8	63.2	0	0.7	0	0.7	2.7
W50	Alloy	0.11	0.7	13.0	1.5	7.0	10.0	63.1	0.07	0	0	1.5	3.0
	Gamma	0	0	4.3	0.2	11.3	12.8	68.1	0	0	0	0.6	2.8
	Eutectic γ'	0	0	21.8	2.1	3.6	7.6	61.3	0.07	0	0	2.0	1.4
	MC	0	50.0	0	16.6	1.0	0.5	2.2	0.2	0	0	24.9	4.6
	Dendrite	0	0	14.5	1.0	8.2	11.1	61.4	0	0	0	1.3	2.6
R13	Alloy	0.11	0.7	13.0	1.5	7.0	10.0	63.1	0.07	1.5	0	0	3.0
	Gamma	0	0	7.2	0.6	14.4	14.6	58.5	0	0.9	0	0	3.8
	Eutectic γ'	0	0	18.2	2.9	3.7	7.9	63.6	0.06	2.2	0	0	1.5
	MC	0	50.0	0	12.5	0.4	0.1	1.8	0.2	33.0	0	0	2.0
	Dendrite	0	0	13.6	1.4	8.1	11.1	60.9	0	1.0	0	0	3.9
R2	Alloy	0.11	0.7	13.0	1.5	7.0	10.0	63.1	0.07	0	3.0	1.5	0
	Gamma	0	0	5.8	0.3	14.7	16.3	57.7	0	0	4.9	0.3	0
	Eutectic γ'	0	0	19.1	3.5	3.4	7.3	63.7	0.06	0	1.1	1.9	0
	MC	0	50.0	0	17.7	1.0	0.5	2.5	0.1	0	5.3	22.9	0
	Dendrite	0	0	13.1	1.3	8.0	10.5	63.1	0	0	3.1	0.9	0
R14	Alloy	0.11	0.7	13.0	1.5	7.0	10.0	63.1	0.07	1.5	3.0	0	0
	Gamma	0	0	7.2	0.6	12.9	15.1	58.5	0	0.9	4.8	0	0
	Eutectic γ'	0	0	16.8	3.0	3.4	7.5	65.7	0.05	2.2	1.4	0	0
	MC	0	50.0	0	10.7	0.5	0.3	1.9	0.1	32.1	4.4	0	0
	Dendrite	0	0	13.3	1.4	7.7	10.6	63.0	0	1.0	3.0	0	0

TABLE 4 (cont'd)

Alloy	Phase	B	C	Al	Ti	Cr	Co	Ni	Zr	Nb	Mo	Ta	W
R15	Alloy	0.11	0.7	13.0	0	7.0	10.0	63.1	0.07	1.5	3.0	1.5	0
	Gamma	0	0	5.6	0	13.1	16.2	59.1	0	0.8	4.8	0.4	0
	Eutectic γ'	0	0	18.3	0	3.0	7.5	65.3	0.06	2.2	1.4	2.3	0
	MC	0	50.0	0	0	0.7	0.7	2.8	0.2	28.8	2.9	13.9	0
	Dendrite	0	0	12.7	0	7.9	10.6	63.3	0	1.1	3.1	1.3	0
W43	Alloy	0.11	0.7	13.0	0	7.0	10.0	63.1	0.07	1.5	1.5	1.5	1.5
	Gamma	0	0	3.1	0	14.8	16.4	60.6	0	0.8	2.4	0.6	1.3
	Eutectic γ'	0	0	21.9	0	3.1	6.4	62.9	0.07	2.2	0.6	2.5	0.4
	MC	0	50.0	0	0	0.6	0.5	2.5	0.2	24.3	1.3	14.6	5.8
	Dendrite	0	0	12.5	0	6.5	9.8	64.7	0	1.0	1.1	0.5	1.2
R3	Alloy	0.11	0.7	13.0	1.0	7.0	10.0	63.1	0.07	1.0	1.5	1.0	1.7
	Gamma	0	0	7.7	0.3	12.5	14.3	59.8	0	0.7	2.6	0.2	1.9
	Eutectic γ'	0	0	18.8	2.3	3.3	7.0	64.8	0.05	1.3	0.8	1.3	0.4
	MC	0	50.0	0	11.2	0.8	0.8	3.3	0.3	15.6	1.9	14.6	1.5
	Dendrite	0	0	12.9	0.9	8.1	11.5	61.7	0	o.5	1.6	0.8	2.0
W41	Alloy	0.11	0.7	13.0	0	7.0	10.0	63.1	0.07	0	1.5	3.0	1.5
	Gamma	0	0	3.6	0	13.9	15.1	61.9	0	0	2.6	1.0	1.8
	Eutectic γ'	0	0	18.5	0	4.0	7.8	64.1	0.07	0	0.7	4.4	0.5
	MC	0	50.0	0	0	1.4	1.4	2.6	0.3	0	1.5	42.3	0.7
	Dendrite	0	0	13.6	0	6.8	9.8	63.2	0	0	1.1	3.2	1.6
R4	Alloy	0.11	0.7	13.0	1.0	7.0	10.0	63.1	0.07	1.0	2.0	1.0	1.0
	Gamma	0	0	5.3	0.2	14.0	15.2	59.8	0	0.6	3.6	0.2	1.1
	Eutectic γ'	0	0	18.8	2.1	3.1	7.1	62.7	0.05	1.5	0.9	1.4	0.4
	MC	0	50.0	0	9.8	0.7	0.6	2.6	0.1	17.7	2.5	15.0	1.0
	Dendrite	0	0	13.0	0.9	7.9	10.6	63.0	0	0.6	2.0	0.7	1.3
R5	Alloy	0.11	0.7	13.0	1.0	7.0	10.0	63.1	0.07	1.0	1.0	1.0	2.0
	Gamma	0	0	4.9	0.2	14.5	16.5	58.6	0	0.5	1.9	0.2	2.7
	Eutectic γ'	0	0	19.9	2.2	3.6	7.1	63.2	0.06	1.5	0.5	1.4	0.6
	MC	0	50.0	0	8.6	0.8	0.5	2.4	0.3	17.5	1.4	16.6	1.9
	Dendrite	0	0	13.5	0.8	8.0	11.0	61.7	0	0.5	1.0	0.7	2.8

TABLE 4 (cont'd)

Alloy	Phase	B	C	Al	Ti	Cr	Co	Ni	Zr	Nb	Mo	Ta	W
R6	Alloy	0.11	0.7	13.0	0.5	7.0	10.0	63.1	0.07	1.25	1.5	1.25	1.5
	Gamma	0	0	7.4	0.1	13.4	15.6	57.0	0	0.9	2.9	0.6	2.1
	Eutectic γ'	0	0	20.2	1.1	3.2	7.2	63.2	0.06	2.1	0.6	1.9	0.5
	MC	0	50.0	0	3.1	1.0	0.8	3.7	0.1	22.1	1.5	16.8	0.9
	Dendrite	0	0	12.9	0.4	8.0	10.8	63.0	0	0.8	1.4	0.9	1.8
R7	Alloy	0.11	0.7	13.0	1.25	7.0	10.0	63.1	0.07	1.25	1.5	0.5	1.5
	Gamma	0	0	6.5	0.4	12.3	13.6	61.7	0	0.4	2.8	0.2	2.1
	Eutectic γ'	0	0	19.5	2.6	3.3	7.4	62.8	0.06	2.2	0.8	1.0	0.4
	MC	0	50.0	0	10.4	0.5	0.6	2.8	0.2	23.0	2.0	9.3	1.2
	Dendrite	0	0	13.1	1.0	8.1	11.3	61.7	0	0.7	1.6	0.3	2.2
R8	Alloy	0.11	0.7	13.0	1.25	7.0	10.0	63.1	0.07	0.5	1.5	1.25	1.5
	Gamma	0	0	7.1	0.4	12.4	14.4	60.6	0	0.2	2.7	0.4	1.8
	Eutectic γ'	0	0	20.0	2.2	3.3	7.5	62.8	0.06	1.1	0.7	1.9	0.5
	MC	0	50.0	0	10.7	0.8	0.9	3.5	0.2	14.5	2.3	15.6	1.5
	Dendrite	0	0	13.4	0.9	8.0	10.9	62.0	0	0.3	1.5	0.8	2.2
R9	Alloy	0.11	0.7	13.0	2.0	7.0	10.0	63.1	0.07	0.5	1.5	0.5	1.5
	Gamma	0	0	6.9	0.8	12.5	13.8	60.9	0	0.3	2.4	0.2	2.2
	Eutectic γ'	0	0	17.9	3.6	3.4	7.1	65.1	0.05	0.8	0.7	0.9	0.5
	MC	0	50.0	0	18.2	0.6	0.5	2.8	0.1	11.4	2.9	11.5	2.0
	Dendrite	0	0	13.0	1.6	7.8	11.5	61.8	0	0.3	1.5	0.4	2.0
R10	Alloy	0.11	0.7	13.0	2.0	7.0	10.0	63.1	0.07	0.5	1.0	0.5	2.0
	Gamma	0	0	6.6	1.0	12.8	13.2	61.6	0	0.4	2.0	0.2	2.2
	Eutectic γ'	0	0	18.2	4.2	2.8	7.9	64.1	0.06	0.9	0.5	0.8	0.6
	MC	0	50.0	0	19.1	0.7	0.6	2.3	0.2	8.9	2.5	12.0	3.7
	Dendrite	0	0	12.9	1.7	7.7	10.8	62.5	0	0.3	1.2	0.5	2.4
R11	Alloy	0.11	0.7	13.0	2.0	7.0	10.0	63.1	0.07	0.5	2.0	0.5	1.0
	Gamma	0	0	6.8	0.8	11.7	13.0	62.0	0	0.3	3.6	0.3	1.5
	Eutectic γ'	0	0	18.4	4.0	3.4	6.9	65.2	0.05	0.8	0.3	0.7	0.3
	MC	0	50.0	0	20.0	0.7	0.5	1.9	0.3	9.6	4.0	11.1	1.9
	Dendrite	0	0	13.1	1.7	8.1	11.2	61.9	0	0.2	1.9	0.4	1.5

TABLE 4 (cont'd)

Alloy	Phase	B	C	Al	Ti	Cr	Co	Ni	Zr	Nb	Mo	Ta	W
R12	Alloy	0.11	0.10	16.8	0	7.3	10.4	65.3	0.07	0	0	0	0
	Gamma	0	0	10.4	0	10.3	13.5	65.8	0	0	0	0	0
	Eutectic γ'	0	0	27.7	0	6.3	7.9	58.1	0.05	0	0	0	0
	MC	complex M_7 C_3 phase detected											
	Dendrite	0	0	17.4	0	7.8	10.9	63.9	0	0	0	0	0

TABLE 5

Comparative analyses of gamma-prime phases in nickel alloys
(as-cast)

Alloy	Gamma-prime	Method	Al	Ti	Cr	Co	Ni	Zr	Nb	Mo	Ta	W
W37	1 Eutectic	spectro	19.9	0	5.1	7.9	61.7	0.07	0	0	3.5	1.8
	2 Re-fused		18.4	0	2.7	7.5	66.0	0.07	0	0	3.3	2.0
	3 Chemical/spectro		19.0	0	2.4	7.6	65.1	0.07	0	0	2.9	2.9
	4 Calculated		19.6	0	3.5	7.7	63.3	0.07	0	0	3.6	2.3
W36	1 Eutectic	spectro	19.2	0	4.2	7.1	64.3	0.07	3.5	0	0	1.7
	2 Re-fused		17.8	0	3.5	8.5	64.2	0.07	3.4	0	0	2.5
	3 Chemical/spectro		17.2	0	2.5	6.3	68.5	0.07	2.9	0	0	2.5
	4 Calculated		18.8	0	3.7	8.4	63.0	0.07	3.5	0	0	2.5
W44	1 Eutectic	spectro	21.1	0	2.8	6.5	63.1	0.07	0	1.0	5.4	0
	2 Re-fused		18.6	0	2.3	6.3	67.6	0.07	0	1.3	3.8	0
	3 Chemical/spectro		20.3	0	2.1	7.1	65.3	0.07	0	1.7	3.5	0
	4 Calculated		20.1	0	2.6	6.9	65.3	0.07	0	1.5	3.4	0
W47	1 Eutectic	spectro	18.7	0	3.2	6.8	65.4	0.07	4.8	1.1	0	0
	2 Re-fused		18.6	0	3.6	7.4	64.7	0.07	4.0	1.8	0	0
	3 Chemical/spectro		14.6	0	1.9	5.8	72.7	0.07	3.3	1.6	0	0
	4 Calculated		18.6	0	4.7	8.8	61.6	0.07	4.2	2.1	0	0
R1	1 Eutectic		17.4	5.9	3.7	7.0	64.7	0.05	0	1.3	0	0
	2 Re-fused		17.4	3.0	3.2	7.3	66.9	0.05	0	2.2	0	0
	3 Chemical/spectro		19.6	3.4	3.0	7.5	65.5	0.05	0	1.0	0	0
	4 Calculated		16.8	4.1	3.5	7.2	66.5	0.05	0	1.9	0	0
W49	1 Eutectic	spectro	18.5	5.6	4.0	7.4	63.5	0.07	0	0	0	1.0
	2 Re-fused		18.3	3.0	3.4	7.9	65.2	0.07	0	0	0	2.2
	3 Chemical/spectro		17.8	3.7	2.8	7.4	65.5	0.07	0	0	0	2.8
	4 Calculated		19.0	3.5	4.6	9.3	61.2	0.07	0	0	0	2.4

TABLE 5 (cont'd)

Alloy	Gamma-prime	Method	Al	Ti	Cr	Co	Ni	Zr	Nb	Mo	Ta	W
W34	1 Eutectic	spectro	19.9	0	3.6	7.0	64.3	0.07	1.5	0	2.1	1.6
	2 Re-fused		18.4	0	2.8	7.6	65.3	0.07	1.6	0	2.2	2.1
	3 Chemical/spectro		16.7	0	2.5	7.4	67.1	0.07	1.8	0	2.0	2.5
	4 Calculated		19.2	0	4.4	8.5	62.0	0.07	1.5	0	1.8	2.6
W50	1 Eutectic	spectro	21.8	2.1	3.6	7.6	61.3	0.07	0	0	2.0	1.0
	2 Re-fused		18.7	1.4	2.6	7.8	65.5	0.07	0	0	1.5	2.4
	3 Chemical/spectro		19.0	1.4	2.2	6.7	66.5	0.07	0	0	1.3	2.8
	4 Calculated		19.2	1.7	4.4	8.8	61.6	0.07	0	0	1.6	2.7
R13	1 Eutectic	spectro	18.2	2.9	3.7	7.9	63.6	0.06	2.2	0	0	1.5
	2 Re-fused		17.2	1.9	3.0	7.6	66.8	0.06	1.4	0	0	2.1
	3 Chemical/spectro		17.8	2.1	3.7	7.0	64.8	0.06	2.0	0	0	2.6
	4 Calculated		17.8	2.0	2.2	7.7	66.2	0.06	1.4	0	0	2.6
R2	1 Eutectic		19.1	3.5	3.4	7.3	63.7	0.06	0	1.1	1.9	0
	2 Re-fused		17.1	2.3	3.1	7.0	67.5	0.05	0	1.8	1.2	0
	3 Chemical/spectro		20.2	2.1	2.8	7.4	64.8	0.05	0	1.3	1.4	0
	4 Calculated		17.5	2.7	2.1	6.2	67.8	0.06	0	1.9	1.8	0
R14	1 Eutectic	spectro	16.8	3.0	3.4	7.5	65.7	0.05	2.2	1.4	0	0
	2 Re-fused		16.0	1.7	4.2	7.8	67.0	0.05	1.6	1.7	0	0
	3 Chemical/spectro		17.5	2.0	3.6	7.4	65.1	0.05	1.8	2.6	0	0
	4 Calculated		16.9	2.0	3.6	7.4	66.0	0.05	2.1	2.0	0	0
R15	1 Eutectic		18.3	0	3.0	7.5	65.3	0.06	2.2	1.4	2.3	0
	2 Re-fused		17.1	0	2.7	7.1	67.8	0.06	1.7	1.5	2.1	0
	3 Chemical/spectro		18.4	0	3.5	7.3	63.4	0.06	2.4	2.4	2.6	0
	4 Calculated		18.0	0	2.8	7.1	66.4	0.06	1.9	1.8	2.0	0

TABLE 5 (cont'd)

Alloy	Gamma-prime	Method	Al	Ti	Cr	Co	Ni	Zr	Nb	Mo	Ta	W
W43	1 Eutectic	spectro	21.9	0	3.1	6.4	62.9	0.07	2.2	0.6	2.5	0.4
	2 Re-fused		18.5	0	3.3	6.9	66.2	0.07	1.5	0.9	1.6	1.0
	3 Chemical/spectro		17.2	0	2.2	6.5	69.5	0.07	1.4	0.9	1.5	0.9
	4 Calculated		20.5	0	1.7	6.6	65.5	0.07	1.6	1.1	1.8	0.7
R3	1 Eutectic		18.8	2.3	3.3	7.0	64.8	0.05	1.3	0.8	1.3	0.4
	2 Re-fused		17.4	1.5	3.2	7.4	66.1	0.06	1.1	0.9	1.2	1.2
	3 Chemical/spectro		19.2	1.3	2.9	8.0	64.3	0.06	1.1	0.5	1.3	1.4
	4 Calculated		17.5	1.4	2.6	7.3	66.4	0.06	1.1	1.0	1.1	1.5
W41	1 Eutectic	spectro	18.5	0	4.0	7.8	64.1	0.07	0	0.7	4.4	0.5
	2 Re-fused		18.8	0	2.5	7.2	66.6	0.07	0	0.5	3.5	0.9
	3 Chemical/spectro		18.7	0	2.7	7.2	66.0	0.07	0	0.8	3.1	1.5
	4 Calculated		20.3	0	2.5	7.0	64.7	0.07	0	0.9	3.3	1.3
R4	1 Eutectic		18.8	2.1	3.1	7.1	62.7	0.05	1.5	0.9	1.4	0.4
	2 Re-fused		18.1	1.4	2.7	7.1	66.3	0.06	1.1	1.1	1.2	1.0
	3 Chemical/spectro		19.3	1.1	3.0	7.9	64.3	0.06	1.1	0.9	1.4	1.0
	4 Calculated		18.6	1.3	2.4	6.7	66.9	0.06	0.9	1.0	1.2	1.0
R5	1 Eutectic		19.9	2.2	3.6	7.1	63.2	0.06	1.5	0.5	1.4	0.6
	2 Re-fused		18.0	1.3	2.6	7.5	65.8	0.06	1.0	0.5	1.2	2.1
	3 Chemical/spectro		19.1	1.2	3.0	8.1	64.0	0.06	1.1	0.3	1.4	1.8
	4 Calculated		18.8	1.4	2.0	6.1	67.6	0.06	0.9	0.4	1.2	1.6
R6	1 Eutectic		20.2	1.1	3.2	7.2	63.2	0.06	2.1	0.6	1.9	0.5
	2 Re-fused		18.3	0.7	3.0	7.7	65.0	0.06	1.7	0.8	1.4	1.4
	3 Chemical/spectro		19.5	0.6	2.8	8.4	64.2	0.06	1.3	0.5	1.5	1.2
	4 Calculated		16.7	0.7	2.8	6.5	69.3	0.06	1.0	0.6	1.3	1.1

TABLE 5 (cont'd)

Alloy	Gamma-prime	Method	Al	Ti	Cr	Co	Ni	Zr	Nb	Mo	Ta	W
R7	1 Eutectic		19.5	2.6	3.3	7.4	62.8	0.06	2.2	0.8	1.0	0.4
	2 Re-fused		18.2	2.2	2.8	7.1	65.2	0.06	1.7	0.8	0.7	1.3
	3 Chemical/spectro		19.2	1.7	2.8	7.8	63.8	0.06	1.6	0.6	1.1	1.4
	4 Calculated		17.8	1.6	3.4	7.8	65.8	0.06	1.3	0.7	0.5	1.1
R8	1 Eutectic		20.0	2.2	3.3	7.5	62.8	0.06	1.1	0.7	1.9	0.5
	2 Re-fused		18.3	2.0	2.8	7.7	64.4	0.06	0.9	0.9	1.5	1.4
	3 Chemical/spectro		19.2	1.5	2.8	7.7	64.3	0.06	1.1	0.6	1.5	1.3
	4 Calculated		17.2	1.4	3.5	7.2	65.9	0.06	0.4	1.6	1.5	1.3
R9	1 Eutectic		17.9	3.6	3.4	7.1	65.1	0.05	0.8	0.7	0.9	0.5
	2 Re-fused		17.8	2.8	2.8	7.4	65.5	0.06	0.8	0.8	0.7	1.4
	3 Chemical/spectro		18.0	2.4	2.9	7.9	64.9	0.06	0.8	0.6	1.0	1.5
	4 Calculated		17.5	2.4	3.4	7.7	66.2	0.06	0.4	0.9	0.4	1.1
R10	1 Eutectic		18.2	4.2	2.8	7.9	64.1	0.06	0.9	0.5	0.8	0.6
	2 Re-fused		18.6	3.0	2.7	8.1	63.3	0.06	0.8	0.8	0.7	2.0
	3 Chemical/spectro	spectro	17.4	3.1	3.2	6.1	66.1	0.06	0.7	0.6	1.1	1.7
	4 Calculated		17.7	2.3	3.2	8.1	65.7	0.06	0.4	0.3	0.4	1.9
R11	1 Eutectic		18.4	4.0	3.4	6.9	65.2	0.05	0.8	0.3	0.7	0.3
	2 Re-fused		17.8	2.9	3.4	7.4	65.0	0.06	0.8	1.2	0.6	0.9
	3 Chemical/spectro	spectro	16.2	2.8	3.4	6.1	67.6	0.06	0.6	1.2	1.0	1.1
	4 Calculated		17.5	2.5	4.0	8.2	65.4	0.06	0.4	1.0	0.3	0.7
R12	1 Eutectic		27.7	0	6.3	7.9	58.1	0.05	0	0	0	0
	2 Re-fused		24.2	0	5.6	8.1	62.1	0.05	0	0	0	0
	3 Chemical/spectro		21.1	0	5.3	8.6	65.0	0.05	0	0	0	0
	4 Calculated		21.1	0	5.3	8.4	65.2	0.05	0	0	0	0

TABLE 6

Composition of gamma phase in nickel alloys - (as-cast and heat-treated)

Alloy	Analysis method	Condition	Al	Ti	Cr	Co	Ni	Nb	Mo	Ta	W
W37	1	As cast	4.7	0	12.7	13.6	64.0	0	0	1.3	3.8
	2 Spectro	H/T 2000h/850°C	6.2	0	10.3	12.5	66.5	0	0	1.4	3.1
	3	H/T 200h/1050°C	6.6	0	9.4	11.7	67.8	0	0	1.5	3.0
W36	1	As cast	5.0	0	12.9	13.4	63.7	1.8	0	0	3.3
	2	H/T 2000h/850°C	6.6	0	10.6	12.2	65.8	1.8	0	0	3.0
	3	H/T 200h/1050°C	7.3	0	9.6	11.2	66.9	2.0	0	0	3.0
W44	1	As cast	3.3	0	13.1	15.8	62.1	0	4.9	0.8	0
	2 Spectro	H/T 2000h/850°C	4.0	0	12.2	14.6	63.4	0	4.7	1.1	0
	3	H/T 200h/1050°C	4.4	0	11.2	13.4	65.5	0	4.2	1.3	0
W47	1	As cast	4.8	0	11.2	13.3	65.4	0.8	4.5	0	0
	2	H/T 2000h/850°C	6.9	0	10.7	12.5	65.1	0.9	3.9	0	0
	3	H/T 200h/1050°C	7.5	0	10.2	10.5	67.1	1.3	3.4	0	0
R1	1	As cast	6.9	0.7	12.3	15.0	60.4	0	4.7	0	0
	2	H/T 2000h/850°C	9.4	2.0	8.4	10.1	66.6	0	3.5	0	0
	3	H/T 200h/1050°C	10.0	2.4	8.1	9.9	66.5	0	3.1	0	0
W49	1	As cast	3.6	0.6	11.2	11.4	70.1	0	0	0	3.1
	2 Spectro	H/T 2000h/850°C	5.5	1.1	9.1	9.0	72.6	0	0	0	2.7
	3	H/T 200h/1050°C	6.6	1.4	8.0	8.1	73.1	0	0	0	2.8
W34	1	As cast	3.5	0	10.7	13.2	67.4	0.9	0	0.7	3.6
	2 Spectro	H/T 2000h/850°C	5.7	0	10.1	12.8	66.7	1.1	0	0.8	2.8
	3	H/T 200h/1050°C	7.1	0	8.2	11.3	68.1	1.2	0	1.0	3.1

TABLE 6 (cont'd)

Alloy	Analysis method	Condition	Al	Ti	Cr	Co	Ni	Nb	Mo	Ta	W
W50	1	As cast	4.3	0.2	11.3	12.8	68.1	0	0	0.5	2.9
	2	H/T 2000h/850°C	6.7	0.6	11.0	12.1	66.2	0	0	0.6	2.8
	3	H/T 200h/1050°C	7.3	0.9	10.4	10.8	66.9	0	0	0.8	2.9
R13	1	As cast	7.2	0.6	14.4	14.6	58.5	0.9	0	0	3.8
	2	H/T 2000h/850°C	9.7	1.0	8.7	9.4	66.8	1.3	0	0	3.1
	3	H/T 200h/1050°C	11.5	1.3	7.9	9.6	65.4	1.4	0	0	2.9
R2	1	As cast	5.8	0.3	14.7	16.3	57.7	0	4.9	0.3	0
	2	H/T 2000h/850°C	8.7	1.0	11.4	12.4	62.2	0	3.7	0.6	0
	3	H/T 200h/1050°C	11.2	1.3	8.9	10.0	64.5	0	3.1	1.0	0
R14	1	As cast	7.2	0.6	12.9	15.1	58.5	0.9	4.8	0	0
	2	H/T 2000h/850°C	8.6	1.1	8.7	12.2	65.0	1.1	3.3	0	0
	3	H/T 200h/1050°C	9.8	1.3	9.0	10.0	65.6	1.2	3.1	0	0
R15	1	As cast	5.6	0	13.1	16.2	59.1	0.8	4.8	0.4	0
	2	H/T 2000h/850°C	8.4	0	11.5	12.9	61.2	0.8	4.4	0.8	0
	3	H/T 200h/1050°C	10.9	0	8.8	10.4	63.9	1.2	3.6	1.2	0
W43	1	As cast	3.1	0	14.8	16.4	60.6	0.8	2.4	0.6	1.3
	2 Spectro	H/T 2000h/850°C	3.7	0	13.3	14.3	64.0	0.9	2.1	0.7	1.0
	3	H/T 200h/1050°C	5.1	0	11.2	13.5	65.4	1.0	2.0	0.8	1.0
R3	1	As cast	7.7	0.3	12.5	14.3	59.8	0.7	2.6	0.2	1.7
	2	H/T 2000h/850°C	9.5	0.8	9.6	12.2	63.5	0.6	1.8	0.5	1.5
	3	H/T 200h/1050°C	11.6	1.0	8.1	9.7	64.8	0.8	1.6	0.8	1.6
W41	1	As cast	3.6	0	13.9	15.1	61.9	0	2.6	1.0	1.8
	2	H/T 2000h/850°C	5.4	0	11.5	14.0	64.0	0	2.3	1.2	1.6
	3	H/T 200h/1050°C	6.5	0	10.9	13.5	64.2	0	2.1	1.2	1.6

TABLE 6 (cont'd)

Alloy	Analysis method	Condition	Al	Ti	Cr	Co	Ni	Nb	Mo	Ta	W
R6	1	As cast	7.4	0.1	13.4	15.6	57.0	0.9	2.9	0.6	2.1
	2 Spectro	H/T 2000h/850°C	3.4	0.1	11.5	16.4	62.8	0.6	2.8	0.8	1.6
	3	H/T 200h/1050°C	5.1	0.2	9.6	15.3	64.4	0.7	2.7	0.6	1.4
R8	1	As cast	7.1	0.4	12.4	14.4	60.6	0.2	2.7	0.4	1.8
	2 Spectro	H/T 2000h/850°C	4.2	0.3	10.5	12.3	68.3	0.3	2.0	0.5	1.6
	3	H/T 200h/1050°C	5.4	0.2	9.7	14.7	64.3	0.5	2.9	0.6	1.7

TABLE 7

Analyses of eutectic gamma-prime and MC carbides in nickel alloys - (as-cast and heat-treated)

Alloy	Phase		C	Al	Ti	Cr	Co	Ni	Zr	Nb	Mo	Ta	W
W37	γ'	1 As cast		19.9	0	5.1	7.9	61.7	0.07	0	0	3.5	1.8
		2 H/T 200h/1050°C		22.0	0	4.0	7.7	60.4	0.06	0	0	4.4	1.5
	MC	1 As cast	50.0	0	0	2.1	1.6	2.6	0.3	0	0	30.3	13.5
		2 H/T 200h/1050°C	50.0	0	0	1.8	2.4	4.2	0.4	0	0	39.5	1.7
W36	γ'	1 As cast		19.2	0	4.2	7.1	64.3	0.07	3.5	0	0	1.7
		2 H/T 200h/1050°C		16.5	0	4.0	7.8	66.1	0.06	4.4	0	0	1.2
	MC	1 As cast	50.0	0	0	4.3	1.8	3.0	0.5	38.5	0	0	1.9
		2 H/T 200h/1050°C	50.0	0	0	0.7	0.7	2.2	0.2	45.1	0	0	1.1
W44	γ'	1 As cast		21.1	0	2.8	6.5	63.1	0.07	0	1.0	5.4	0
		2 H/T 200h/1050°C		17.9	0	2.3	8.3	66.9	0.06	0	1.0	3.6	0
	MC	1 As cast	50.0	0	0	1.7	0.8	2.5	0.3	0	2.9	43.0	0
		2 H/T 200h/1050°C	50.0	0	0	2.1	1.5	3.0	0.3	0	5.6	37.5	0
W47	γ'	1 As cast		18.7	0	3.2	6.8	65.4	0.07	4.8	1.1	0	0
		2 H/T 200h/1050°C		19.7	0	2.7	8.0	64.0	0.06	3.7	1.9	0	0
	MC	1 As cast	50.0	0	0	0.3	0.4	2.6	0.2	45.2	1.6	0	0
		2 H/T 200h/1050°C	50.0	0	0	0.7	1.3	2.3	0.1	41.4	4.2	0	0
R1	γ'	1 As cast		17.4	5.9	3.7	7.0	64.7	0.05	0	1.3	0	0
		2 H/T 200h/1050°C		15.7	5.0	3.3	6.8	67.9	0.05	0	1.3	0	0
	MC	1 As cast	50.0	0	32.5	0.8	0.2	1.4	0.1	0	15.0	0	0
		2 H/T 200h/1050°C	50.0	0	33.2	0.8	0.2	1.2	0.1	0	14.5	0	0

TABLE 7 (cont'd)

Alloy	Phase		C	Al	Ti	Cr	Co	Ni	Zr	Nb	Mo	Ta	W
W49	γ'	1 As cast		18.5	5.6	4.0	7.4	63.5	0.07	0	0	0	1.0
		2 H/T 200h/1050°C		17.5	5.0	3.6	6.6	66.4	0.05	0	0	0	0.9
	MC	1 As cast	50.0	0	32.1	1.2	0.4	2.3	0.2	0	0	0	13.9
		2 H/T 200h/1050°C	50.0	0	31.8	0.8	1.9	3.3	0.1	0	0	0	12.1
W34	γ'	1 As cast		19.9	0	3.6	7.0	64.3	0.07	1.5	0	2.1	1.6
		2 H/T 200h/1050°C		20.2	0	3.8	7.2	63.2	0.06	2.3	0	2.2	1.1
	MC	1 As cast	50.0	0	0	0.1	0.1	2.0	0.2	32.1	0	16.0	1.4
		2 H/T 200h/1050°C	50.0	0	0	3.7	2.1	3.0	0.3	31.9	0	6.3	2.7
W50	γ'	1 As cast		21.8	2.1	3.6	7.6	61.3	0.07	0	0	2.0	1.0
		2 H/T 200h/1050°C		18.3	2.6	3.5	7.4	65.3	0.06	0	0	1.9	1.0
	MC	1 As cast	50.0	0	16.6	1.0	0.5	2.2	0.2	0	0	24.9	4.6
		2 H/T 200h/1050°C	50.0	0	18.3	0.7	1.4	2.4	0.2	0	0	22.6	4.6
R13	γ'	1 As cast		18.2	2.9	3.7	7.9	63.6	0.06	2.2	0	0	1.5
		2 H/T 200h/1050°C		18.4	2.1	3.7	8.1	63.8	0.06	2.2	0	0	1.7
	MC	1 As cast	50.0	0	12.5	0.4	0.1	1.8	0.2	33.0	0	0	2.0
		2 H/T 200h/1050°C	50.0	0	8.4	0.4	0.3	2.2	0.1	35.8	0	0	2.8
R2	γ'	1 As cast		19.1	3.5	3.4	7.3	63.7	0.06	0	1.1	1.9	0
		2 H/T 200h/1050°C		16.5	3.3	3.4	7.2	65.8	0.06	0	1.4	2.4	0
	MC	1 As cast	50.0	0	17.7	1.0	0.5	2.5	0.1	0	5.3	22.9	0
		2 H/T 200h/1050°C	50.0	0	16.7	1.5	1.5	2.4	0.2	0	4.2	23.5	0

TABLE 7 (cont'd)

Alloy	Phase		C	Al	Ti	Cr	Co	Ni	Zr	Nb	Mo	Ta	W
R14	γ'	1 As cast		16.8	3.0	3.4	7.5	65.7	0.05	2.2	1.4	0	0
		2 H/T 200h/1050°C		18.5	2.0	3.4	6.9	65.6	0.05	1.9	1.7	0	0
	MC	1 As cast	50.0	0	10.7	0.5	0.3	1.9	0.1	32.1	4.4	0	0
		2 H/T 100h/1050°C	50.0	0	8.9	1.2	0.7	6.0	0.2	27.8	5.2	0	0
R15	γ'	1 As cast		18.3	0	3.0	7.5	65.3	0.06	2.2	1.4	2.3	0
		2 H/T 200h/1050°C		18.1	0	2.8	6.8	66.7	0.06	2.2	1.1	2.3	0
	MC	1 As cast	50.0	0	0	0.7	0.7	2.8	0.2	28.8	2.9	13.9	0
		2 H/T 200h/1050°C	50.0	0	0	0.8	0.8	3.7	0.2	28.8	2.2	13.5	0
W43	γ'	1 As cast		21.9	0	3.1	6.4	62.9	0.07	2.2	0.6	2.5	0.4
		2 H/T 200h/1050°C		17.5	0	3.0	7.7	67.2	0.06	1.5	0.5	2.3	0.3
	MC	1 As cast	50.0	0	0	0.6	0.5	2.5	0.2	24.3	1.3	14.6	5.8
		2 H/T 200h/1050°C	50.0	0	0	0.8	1.0	2.5	0.2	27.0	1.5	16.5	0.5
R3	γ'	1 As cast		18.8	2.3	3.3	7.0	64.8	0.05	1.3	0.8	1.3	0.4
		2 H/T 100h/1050°C		18.5	2.0	3.0	7.4	64.7	0.06	1.5	0.7	1.7	0.5
	MC	1 As cast	50.0	0	11.2	0.8	0.8	3.3	0.3	15.6	1.9	14.6	1.5
		2 H/T 100h/1050°C	50.0	0	8.1	1.7	0.6	2.8	0.1	22.2	1.9	14.3	1.3
W41	γ'	1 As cast		18.5	0	4.0	7.8	64.1	0.07	0	0.7	4.4	0.5
		2 H/T 100h/1050°C		20.8	0	3.7	7.2	62.7	0.06	0	0.6	4.4	0.6
	MC	1 As cast	50.0	0	0	1.4	1.4	2.6	0.3	0	1.5	42.3	0.7
		2 H/T 100h/1050°C	50.0	0	0	1.2	1.2	3.3	0.3	0	0.8	42.1	1.1

TABLE 7 (cont'd)

Alloy	Phase		C	Al	Ti	Cr	Co	Ni	Zr	Nb	Mo	Ta	W
R6	γ'	1 As cast		20.2	1.1	3.2	7.2	63.2	0.06	2.1	0.6	1.9	0.5
		2 H/T 200h/1050°C		18.2	1.0	2.9	7.1	65.8	0.06	1.6	0.5	2.3	0.6
	MC	1 As cast	50.0	0	3.1	1.0	0.8	3.7	0.1	22.1	1.5	16.8	0.9
		2 H/T 200h/1050°C	50.0	0	3.5	0.3	0.4	2.1	0.2	27.7	1.4	13.8	0.6
R8	γ'	1 As cast		20.0	2.2	3.3	7.5	62.8	0.06	1.1	0.7	1.9	0.5
		2 H/T 200h/1050°C		18.5	2.0	3.5	7.5	64.2	0.06	1.0	0.7	2.0	0.6
	MC	1 As cast	50.0	0	10.7	0.8	0.9	3.5	0.2	14.5	2.3	15.6	1.5
		2 H/T 200h/1050°C	50.0	0	11.9	0.6	0.7	3.8	0.3	13.0	1.7	16.2	1.8

TABLE- 8

Measured and calculated lattice parameters of phases in nickel alloys (as-cast)

Alloy	Composition*					Phase	Measured Lattice Parameter (a) Å	Calculated Lattice Parameter (a) Å	Percentage difference between calculated and measured	
	Ti	Nb	Mo	Ta	W				Lattice Parameter	Cell Volume
W37	-	-	-	3	3	(1) Gamma	3.591	3.632	1.1	3.5
						(2) Gamma Prime	3.586	3.678	2.6	7.9
						(3) Carbide	4.439	4.315	2.8	8.2
W36	-	3	-	-	3	(1) Gamma	3.585	3.656	2.0	5.7
						(2) Gamma Prime	3.583	3.674	2.5	7.8
						(3) Carbide	4.443	3.398	1.0	5.9
W44	-	-	3	3	-	(1) Gamma	3.592	3.622	0.9	2.6
						(2) Gamma Prime	3.584	3.681	2.7	8.3
						(3) Carbide	4.427	4.480	1.2	3.6
W47	-	3	3	-	-	(1) Gamma	3.591	3.622	0.9	2.6
						(2) Gamma Prime	3.583	3.669	2.4	7.4
						(3) Carbide	4.451	4.451	0	0
R1	3	-	3	-	-	(1) Gamma	3.585	3.590	0.1	0.4
						(2) Gamma Prime	3.577	3.675	2.7	8.4
						(3) Carbide	4.319	4.278	0.9	2.8
W49	3	-	-	-	3	(1) Gamma	3.584	3.587	0.1	0.3
						(2) Gamma Prime	3.581	3.523	1.6	5.0
						(3) Carbide	4.319	4.333	0.3	1.0
W34	-	1.5	-	1.5	3	(1) Gamma	3.588	3.527	1.7	5.0
						(2) Gamma Prime	3.586	3.684	2.8	8.4
						(3) Carbide	4.441	4.440	0	0.1
W50	1.5	-	-	1.5	3	(1) Gamma	3.587	3.619	0.9	2.7
						(2) Gamma Prime	3.579	3.620	1.1	3.5
						(3) Carbide	4.389	4.440	1.2	3.4

TABLE 8 (cont'd)

Alloy	Composition*					Phase	Measured Lattice Parameter (a) Å	Calculated Lattice Parameter (a) Å	Percentage difference between calculated and measured	
	Ti	Nb	Mo	Ta	W				Lattice Parameter	Cell Volume
R13	1.5	1.5	-	-	3	(1) Gamma (2) Gamma Prime (3) Carbide	3.593 3.582 4.416	3.529 3.674 4.406	1.8 2.5 0.2	5.2 7.8 0.9
R2	1.5	-	3	1.5	-	(1) Gamma (2) Gamma Prime (3) Carbide	3.588 3.582 4.392	3.596 3.670 4.339	0.2 2.4 1.2	0.7 7.5 3.6
R14	1.5	1.5	3	-	-	(1) Gamma (2) Gamma Prime (3) Carbide	3.592 3.581 4.416	3.594 3.692 4.403	0.1 3.1 0.3	0.2 9.6 0.9
R15	-	1.5	3	1.5	-	(1) Gamma (2) Gamma Prime (3) Carbide	3.593 3.584 4.438	3.570 3.680 4.412	0.6 2.7 0.6	1.9 8.3 1.8
W43	-	1.5	1.5	1.5	1.5	(1) Gamma (2) Gamma Prime (3) Carbide	3.583 3.583 4.445	3.626 3.678 4.469	1.2 2.7 0.4	3.6 8.2 1.6
R3	1.0	1.0	1.5	1.0	1.5	(1) Gamma (2) Gamma Prime (3) Carbide	3.595 3.583 4.413(S)/ 4.460 (vw)	3.636 3.584 4.466	1.1 0 1.2	3.4 0 4.8
W41	-	-	1.5	3	1.5	(1) Gamma (2) Gamma Prime (3) Carbide	3.585 3.585 4.431	3.623 3.671 4.393	1.1 2.4 0.9	3.2 7.4 2.6
R4	1.0	1.0	2.0	1.0	1.0	(1) Gamma (2) Gamma Prime (3) Carbide	3.592 3.582 4.421	3.636 3.653 4.481	1.2 2.0 1.4	3.6 6.0 4.3

TABLE 8 (cont'd)

Alloy	Composition*					Phase	Measured Lattice Parameter (a) Å	Calculated Lattice Parameter (a) Å	Percentage difference between calculated and measured	
	Ti	Nb	Mo	Ta	W				Lattice Parameter	Cell Volume
R5	1.0	1.0	1.0	1.0	2.0	(1) Gamma (2) Gamma Prime (3) Carbide	3.590 3.584 4.416	3.636 3.681 4.438	1.3 2.7 0.5	3.9 8.3 1.5
R6	0.5	1.25	1.5	1.25	1.5	(1) Gamma (2) Gamma Prime (3) Carbide	3.595 3.585 4.435	3.650 3.673 4.522	1.5 2.4 2.0	4.6 7.5 6.0
R7	1.25	1.25	1.5	0.5	1.5	(1) Gamma (2) Gamma Prime (3) Carbide	3.593 3.583 4.420	3.663 3.690 4.512	1.9 3.0 2.1	5.9 9.2 6.3
R8	1.25	0.5	1.5	1.25	1.5	(1) Gamma (2) Gamma Prime (3) Carbide	3.593 3.583 4.417	3.630 3.677 4.453	1.0 2.6 0.8	3.0 7.8 2.4
R9	2.0	0.5	1.5	0.5	1.5	(1) Gamma (2) Gamma Prime (3) Carbide	3.594 3.581 4.400	3.641 3.671 4.441	1.3 2.5 0.9	4.0 7.6 2.8
R10	2.0	0.5	1.0	0.5	2.0	(1) Gamma (2) Gamma Prime (3) Carbide	3.591 3.581 4.378	3.642 3.677 4.363	1.4 2.6 0.3	4.2 8.2 1.0
R11	2.0	0.5	2.0	0.5	1.0	(1) Gamma (2) Gamma Prime (3) Carbide	3.590 3.580 4.378	3.636 3.655 4.405	1.3 2.1 0.6	4.0 7.2 1.9
R12	-	-	-	-	-	(1) Gamma (2) Gamma Prime (3) Carbide	3.567 3.564 Complex M_7C_3	3.616 3.670 -	1.4 3.0 -	4.2 9.1 -

TABLE 8 (cont'd)

NOTE:

(1) All phases (except for the carbide in R12) were cubic.

(2) Lattice parameters (a) calculated from the mean of the chemical and electron probe micro-analysis data in Tables and assumes atoms adopt face-centred-cubic structure. Thus closest distance of approach between atom centres $= \frac{a\sqrt{2}}{2}$ and $a = \frac{4r}{\sqrt{2}}$ where r is the Goldschmidt atomic radius. Values of r were taken from Reference 82. Thus calculated lattice parameter $\bar{a} = \sum_{i=1}^{n} C_i \cdot a_i$ where n = number of elements, c_i = atomic fraction of particular element and a_i = lattice parameter of particular element.

(3) For stoichiometric Ni_3Al the lattice parameter is 3.567 Å; the differences obtained between this value and that calculated from (2) is 2.7 per cent for lattice parameter (a) and 8 per cent for cell volume (a^3).

(4) Small concentrations of Ni and Co in MC phases ignored. Mixture law relationships calculated of of the form $\bar{a} = \sum_{i=1}^{n} C_i\ a_i$ where a_i is the lattice parameter value for stoichiometric: TiC, NbC, TaC given in Reference 72. Chromium assumed to be combined as cubic $Cr_{23}C_6$ phase.

* Composition includes that of the "base": 0.11 B, 0.7 C, 13.0 Al, 7.0 Cr, 10 Co, 63.1 Ni, 0.07 Zr

TABLE 9

X-Ray diffraction (lattice parameter) data for phases in as-cast and heat-treated alloys

Alloy	Phase	Lattice Parameter (a) Å			Change in lattice parameter with exposure Å		Percentage mismatch in lattice parameter between matrix and gamma prime			Lattice Parameter of other phases detected	
		As-cast	H/T 2000 h at 850°C	H/T 200 h at 1050°C	H/T 850°C	H/T 1050°C	As-cast	H/T 850°C	H/T 1050°C	Å	Intensity
W37	(1) Gamma	3.591	3.585	3.586	-0.006	-0.005	0.02	-0.003	-0.006	-	
	(2) Gamma Prime	3.586 (W)	3.586 (W)	3.588 (W)	0	0.002				-	
	(3) Carbide	4.439	4.435	4.452	-0.004	0.013				10.97/11.21	(VW)
W36	(1) Gamma	3.585	3.586	3.588	0.001	0.003	0.006	0	0.003	-	
	(2) Gamma Prime	3.583 (NV)	3.586 (NV)	3.587 (VW)	0.003	0.004				-	
	(3) Carbide	4.443	4.456	4.462	0.013	0.019				-	
W44	(1) Gamma	3.592	3.585	3.587	-0.007	-0.005	0.22	0	-0.003	-	
	(2) Gamma Prime	3.584 (NV)	3.585 (VW)	3.588 (W)	0.001	0.004				-	
	(3) Carbide	4.427	4.422	4.452	-0.005	0.025				11.02/11.20	(VW)
W47	(1) Gamma	3.591	ND	ND	ND	ND	0.22	ND	ND	-	
	(2) Gamma Prime	3.583 (W)	3.584 (S)	3.585 (VW)	0.001	0.002				-	
	(3) Carbide	4.451	4.445	4.468	-0.006	0.017				Hexagonal Ta_2C	
R1	(1) Gamma	3.585	3.577	3.579	-0.008	-0.006	0.22	0.003	0.003	-	
	(2) Gamma Prime	3.577 (S)	3.576 (S)	3.578 (M)	-0.001	0.001				-	
	(3) Carbide	4.319	4.319	4.312	0	-0.007				11.03	(VW)
W49	(1) Gamma	3.584	3.578	ND	-0.006	ND	0.008	0	ND	-	
	(2) Gamma Prime	3.581 (VW)	3.578 (NV)	3.580 (NV)	-0.003	-0.001				-	
	(3) Carbide	4.319	4.325	4.312	0.006	-0.007				-	
W34	(1) Gamma	3.588	ND	ND	ND	ND	0.006	ND	ND	-	
	(2) Gamma Prime	3.586 (NV)	3.588 (NV)	3.588 (NV)	0.002	0.002				-	
	(3) Carbide	4.441	4.447	4.459	0.006	0.018				-	

TABLE 9 (cont'd)

Alloy	Phase	Lattice Parameter a Å			Change in lattice parameter with exposure Å		Percentage mismatch in lattice parameter between matrix and gamma prime			Lattice Parameter of other phases detected	
		As-cast	H/T 2000 h at 850°C	H/T 200 h at 1050°C	H/T 850°C	H/T 1050°C	As-cast	H/T 850°C	H/T 1050°C	Å	Intensity
W50	(1) Gamma	3.587	ND	ND	ND	ND	0.03	ND	ND	-	
	(2) Gamma Prime	3.579 (NV)	3.583 (VW)	3.584 (VW)	0.004	0.005				-	
	(3) Carbide	4.389	4.380	4.382	-0.009	-0.007				-	
R13	(1) Gamma	3.593	ND	ND	ND	ND	0.03	ND	ND	-	
	(2) Gamma Prime	3.582 (VW)	3.585 (VW)	3.584 (NV)	0.003	0.002				-	
	(3) Carbide	4.416	4.411	4.438	-0.005	0.022				-	
R2	(1) Gamma	3.588	3.581	3.582	-0.007	-0.006	0.02	0.003	-0.003		
	(2) Gamma Prime	3.582 (VW)	3.580 (VW)	3.583 (VW)	-0.002	0.001					
	(3) Carbide	4.392	4.389	4.369	-0.003	-0.023					
R14	(1) Gamma	3.592	ND	ND	ND	ND	0.008	ND	ND	-	
	(2) Gamma Prime	3.581 (S)	3.583 (S)	3.583 (W)	0.002	0.002				-	
	(3) Carbide	4.416	4.410	4.435	-0.006	0.019				11.10 (VW)	
R15	(1) Gamma	3.593	ND	ND	ND	ND	0.03	ND	ND		
	(2) Gamma Prime	3.584 (VW)	3.587 (VW)	3.589 (VW)	0.003	0.005					
	(3) Carbide	4.438	4.445	4.453	0.007	0.015				11.05 (VW)	
W43	(1) Gamma	3.583	ND	ND	ND	ND	0	ND	ND	-	
	(2) Gamma Prime	3.583 (NV)	3.582 (VW)	3.585 (VW)	-0.001	0.002				-	
	(3) Carbide	4.445	4.443	4.456	-0.002	0.001				Hexagonal Nb_2C	
R3	(1) Gamma	3.595	3.583	3.585	-0.012	-0.010	0.22	0.003	0.008	-	
	(2) Gamma Prime	3.583 (VW)	3.582 (VW)	3.582 (VW)	-0.001	-0.001				-	
	(3) Carbide	4.413	4.412	4.396/ 4.460	-0.001	-0.017				-	
W41	(1) Gamma	3.585	3.585	3.587	0	0.002	0	0	0.006		
	(2) Gamma Prime	3.585 (NV)	3.585 (NV)	3.585 (NV)	0	0					
	(3) Carbide	4.431	4.445	4.440	0.014	0.009				11.11 (VW)	

TABLE 9 (cont'd)

Alloy	Phase	Lattice Parameter a Å			Change in lattice parameter with exposure Å		Percentage mismatch in lattice parameter between matrix and gamma prime			Lattice Parameter of other phases detected	
		As-cast	H/T 2000 h at 850°C	H/T 200 h at 1050°C	H/T 850°C	H/T 1050°C	As-cast	H/T 850°C	H/T 1050°C	Å	Intensity
R4	(1) Gamma	3.592	ND	ND	ND	ND	0.03	ND	ND	-	
	(2) Gamma Prime	3.582 (VW)	ND	ND	ND	ND				-	
	(3) Carbide	4.421	ND	ND	ND	ND				-	
R5	(1) Gamma	3.590	ND	ND	ND	ND	0.02	ND	ND	-	
	(2) Gamma Prime	3.584 (NV)	ND	ND	ND	ND				-	
	(3) Carbide	4.416	ND	ND	ND	ND				-	
R6	(1) Gamma	3.595	3.583	ND	-0.006	ND	0.03	0	ND	-	
	(2) Gamma Prime	3.585 (NV)	3.583 (NV)	3.586 (NV)	-0.002	0.001				-	
	(3) Carbide	4.435	4.415	4.430	-0.020	-0.005				-	
R7	(1) Gamma	3.593	ND	ND	ND	ND	0.03	ND	ND	-	
	(2) Gamma Prime	3.583 (NV)	ND	ND	ND	ND				-	
	(3) Carbide	4.420	ND	ND	ND	ND				-	
R8	(1) Gamma	3.593	3.583	ND	-0.010	ND	0.03	-0.003	ND	-	
	(2) Gamma Prime	3.583 (W)	3.584 (NV)	3.585 (NV)	0.001	0.002				-	
	(3) Carbide	4.417	4.410	4.410	-0.007	-0.007				-	
R9	(1) Gamma	3.594	ND	ND	ND	ND	0.04	ND	ND	-	
	(2) Gamma Prime	3.581 (W)	ND	ND	ND	ND				-	
	(3) Carbide	4.400	ND	ND	ND	ND				-	
R10	(1) Gamma	3.591	ND	ND	ND	ND	0.03	ND	ND	-	
	(2) Gamma Prime	3.581 (W)	ND	ND	ND	ND				-	
	(3) Carbide	4.378	ND	ND	ND	ND				-	
R11	(1) Gamma	3.590	ND	ND	ND	ND	0.03	ND	ND	-	
	(2) Gamma Prime	3.580 (S)	ND	ND	ND	ND				-	
	(3) Carbide	4.378	ND	ND	ND	ND				-	

TABLE 9 (cont'd)

Alloy	Phase	Lattice Parameter a Å			Change in lattice parameter with exposure Å		Percentage mismatch in lattice parameter between matrix and gamma prime			Lattice Parameter of other phases detected	
		As-cast	H/T 2000 h at 850°C	H/T 200 h at 1050°C	H/T 850°C	H/T 1050°C	As-cast	H/T 850°C	H/T 1050°C	Å	Intensity
R12	(1) Gamma	3.567	ND	ND	ND	ND	0.008	ND	ND	-	
	(2) Gamma Prime	3.564 (S)	ND	ND	ND	ND				-	
	(3) Carbide	Complex M_7C_3	ND	ND	ND	ND				-	

NOTE:

(W) = weak intensity of superlattice reflections
(VW) = very weak intensity of superlattice reflections
(M) = medium intensity of superlattice reflections
(S) = strong " " " "
(NV) = not visible
ND = not determined

TABLE 10

Comparison of measured and calculated densities of cast alloys

Alloy Code	Measured density $kg/m^3 \times 10^3$	Calculated density* for given vol.%	γ'/γ
W37	8.85	8.72 8.70	(1) 60/40 (2) 65/35
W36	8.40	8.44 8.41	(1) 60/40 (2) 65/35
W44	8.45	8.43 8.43	(1) 60/40 (2) 65/35
W47	8.10	8.12 8.10	(1) 60/40 (2) 65/35
R1	8.00	7.92 7.89	(1) 60/40 (2) 65/35
W49	8.30	8.27 8.22	(1) 60/40 (2) 65/35
W34	8.65	8.67 8.64	(1) 60/40 (2) 65/35
W50	8.50	8.44 8.41	(1) 60/40 (2) 65/35
R13	8.21	8.31 8.29	(1) 60/40 (2) 65/35
R2	8.26	8.08 8.06	(1) 60/40 (2) 65/35
R14	7.93	8.05 8.03	(1) 60/40 (2) 65/35
R15	8.22	8.33 8.31	(1) 60/40 (2) 65/35
W43	8.40	8.40 8.37	(1) 60/40 (2) 65/35
R3	8.45	8.25 8.22	(1) 60/40 (1) 65/35
W41	8.60	8.62 8.60	(1) 60/40 (2) 65/35

TABLE 10 (cont'd)

Alloy Code	Measured density $kg/m^3 \times 10^3$	Calculated density* for given vol.%	γ'/γ
R4	8.32	8.38 8.17	(1) 60/40 (2) 65/35
R5	8.55	8.37 8.34	(1) 60/40 (2) 65/35
R6	8.52	8.31 8.28	(1) 60/40 (2) 65/35
R7	8.35	8.23 8.20	(1) 60/40 (2) 65/35
R8	8.54	8.26 8.24	(1) 60/40 (2) 65/35
R9	8.29	8.23 8.21	(1) 60/40 (2) 65/35
R10	8.22	8.26 8.23	(1) 60/40 (2) 65/35
R11	8.23	8.20 8.17	(1) 60/40 (2) 65/35
R12	7.61	7.66 7.63	(1) 60/40 (2) 65/35

NOTE:

I * Density $\rho = \frac{n\overline{A}}{VN}$ where n = number of atoms per unit cell

$\overline{A}$ = mean atomic weight

V = cell volume

N = Avagadros's Number = 6.023×10^{23}/ mole.

II Based on γ compositions from Table 4 and the mean of chemical and electron probe micro-analysis data for γ', from Table 5.

TABLE 11

Linear regression equations for constitution of gamma matrices, eutectic gamma-prime and monocarbide phases in relation to the parent alloy composition (as-cast)

Atomic percentage of element present in phase = f (parent alloy composition)

Element	Maximum residual atomic %	Phase	
Aluminium	2.31	(1)	Al = 2.27 Mo - 0.77 Ta + 1.97 W
	2.16	(2)	Al = 0.31 Nb + 5.83 Mo + 0.85 Ta + 6.17 W
	-	(3)	Al = NIL
Titanium	0.39	(1)	Ti = 0.31 Ti
	0.49	(2)	Ti = 1.82 Ti + 0.06 Nb + 0.18 Mo - 0.09 Ta
	2.38	(3)	Ti = 10.86 Ti - 2.49 Nb + 1.25 Ta
Chromium	1.98	(1)	Cr = 4.39 Mo + 4.18 W
	1.08	(2)	Cr = -0.04 Nb + 1.03 Mo + 0.06 Ta + 1.28 W
	2.94	(3)	Cr = 0.34 Nb + 0.34 Ta + 0.28 W
Cobalt	2.42	(1)	Co = 5.08 Mo + 4.50 W
	0.75	(2)	Co = -0.14 Nb + 2.41 Mo - 0.04 Ta + 2.55 W
	-	(3)	Co = NIL
Nickel	6.04	(1)	Ni = 19.80 Mo + 21.35 W
	1.42	(2)	Ni = 21.76 Mo - 0.56 Ta + 21.24 W
	-	(3)	Ni = NIL
Niobium	0.44	(1)	Nb = 0.43 Nb - 0.02 Mo + 0.09 Ta + 0.07 W
	0.36	(2)	Nb = 1.26 Nb + 0.22 Mo - 0.11 Ta + 0.01 W
	7.06	(3)	Nb = 13.82 Nb + 2.41 Mo + 2.07 W
Molybdenum	0.28	(1)	Mo = -0.06 Nb + 1.62 Mo + 0.01 Ta + 0.18 W
	0.52	(2)	Mo = 0.41 Mo
	4.88	(3)	Mo = -3.11 Nb + 3.64 Mo - 2.32 Ta + 1.25 W
Tantalum	0.26	(1)	Ta = 0.11 Nb - 0.07 Mo + 0.38 Ta
	0.71	(2)	Ta = 0.11 Mo + 1.45 Ta - 0.09 W
	6.34	(3)	Ta = -5.58 Nb + 3.94 Mo + 10.00 Ta + 3.08W
Tungsten	0.57	(1)	W = 0.15 Mo + 1.10 W
	0.33	(2)	W = 0.18 Nb - 0.23 Mo + 0.13 Ta + 0.36 W
	5.59	(3)	W = -2.78 Nb - 0.20 Ta + 3.11 W

NB

(1) Gamma matrix
(2) Eutectic gamma-prime
(3) Monocarbide
(4) Small amounts of Ni, Co etc. in MC ignored

TABLE 12

Mean electron vacancy number of alloys

Alloy	W37	W36	W44	W47	R1	W49	W34	W50	R13	R2	R14	R15	W43
$\bar{N}_{V1}$ alloy	1.965	1.965	1.965	1.965	1.965	1.965	1.965	1.965	1.965	1.965	1.965	1.965	1.965
$\bar{N}_{V2}$ alloy	1.950	1.950	1.950	1.950	1.950	1.950	1.950	1.950	1.950	1.950	1.950	1.950	1.950
$\bar{N}_{V1}$ gamma 1	1.858	1.889	1.816	1.804	2.026	1.640	1.697	1.700	2.127	2.054	2.112	1.997	1.859
" 2	1.831	1.885	1.824	1.905	2.020	1.677	1.759	1.874	2.035	2.093	1.991	2.099	1.806
" 3	1.816	1.893	1.790	1.905	2.056	1.723	1.837	1.911	2.146	2.158	2.073	2.149	1.818
$\bar{N}_{V2}$ gamma 1	1.851	1.882	1.808	1.797	2.019	1.634	1.943	1.693	2.120	2.047	2.106	1.990	1.852
" 2	1.825	1.879	1.817	1.799	2.015	1.673	1.752	1.869	2.030	2.087	1.986	2.093	1.800
" 3	1.810	1.887	1.783	1.900	2.051	1.719	1.831	1.906	2.141	2.153	2.068	2.144	1.812
$\bar{N}_{V1}$ γ'	2.430	2.280	2.487	2.048	2.496	2.475	2.303	2.414	2.462	2.517	2.427	2.515	2.244
$\bar{N}_{V2}$ γ'	2.426	2.277	2.483	2.044	2.492	2.471	2.299	2.410	2.458	2.513	2.423	2.511	2.240

Alloy	R3	W41	R6	R8	N115 Blades	B1900	713C	IN100	MM200	N115	TRW1900	U500	U700
$\bar{N}_{V1}$ alloy	1.965	1.965	1.965	1.965	$\frac{2.84}{2.73}$	2.069	2.506	2.785	1.950	2.616	2.627	2.501	2.742
$\bar{N}_{V2}$ alloy	1.950	1.950	1.950	1.950	$\frac{2.81}{2.71}$	2.058	2.506	2.756	1.939	2.596	2.610	2.484	2.721
$\bar{N}_{V1}$ gamma 1	2.084	1.853	2.159	2.039							2.461		
2	2.072	1.861	1.782	1.705	(2.20)	2.139	2.361	2.352	2.001	2.400		2.383	2.497
3	2.167	1.902	1.803	1.830	ND								

TABLE 12 (cont'd)

Alloy		R3	W41	R6	R8	N115 Blades	B1900	713C	IN100	MM200	N115	TRW1900	U500	U700
$\bar{N}_{V2}$ gamma	1	2.074	1.846	2.151	2.031									
	2	2.066	1.854	1.774	1.699	2.10	2.131	2.361	2.340	1.99	2.390	2.453	2.370	2.485
	3	2.162	1.895	1.795	1.823	ND								
$\bar{N}_{V_1}$ γ'		2.483	2.404	2.475	2.498	ND	2.343	2.341	2.473	2.327	2.441	2.357	2.288	2.354
$\bar{N}_{V2}$ γ'		2.479	2.400	2.471	2.454	ND	2.340	2.341	2.468	2.323	2.437	2.354	2.285	2.350

NOTE:

(1) $\bar{N}_{V1}$ = Woodyat and Beattie method using 1.71 (Co), 0.66 (Ni) and 10.66 - GN for remaining elements

(2) $\bar{N}_{V2}$ = Method using 10.66 - GN for all elements

(3) $\bar{N}_{V1}$ gamma 1,2,3 = Method as in (1) based on data from Table 6, i.e. 1, as cast; 2, HT 850°C; 3, HT 1050°C

(4) $\bar{N}_{V2}$ gamma 1,2,3 = Method as in (2) based on data from Table 6

(5) $\bar{N}_{V1}$ γ' = Method as in (1) based on the mean of chemical and microprobe analysis data from Table 5

(6) $\bar{N}_{V2}$ γ' = Method as in (2) based on the mean of chemical and microprobe analysis data from Table 5

(7) The data for the Nimonic 115 alloy blades are from the present work, those for B1900 ff were from the analyses by Kreige and Baris

(8) ND = Not determined

TABLE 13

Results of gamma-prime solvus temperature measurement by differential thermal analysis

Alloy	W41	W37,W44	R6,W50	W34,W43,R13,R8,R9	R2,R3	R11,R15	W49,R4,R5,R10,R14	R7
Temperature °C	1242	1234	1220	1213	1210	1205	1198	1195
Alloy		W36	W47,R1	R12		Nimonic 115	Nimocast 713C	
Temperature °C		1190	1177	1155		1140	1148	

Alloy		IN100	MarM200	MarM246	MarM002	IN100	MarM200	MarM246
Temperature °C		1162	1140	1162	1191	1203/ 1207	1171/ 1182	1178/ 1188
						(Reference 86)		

Note that these solvus temperatures were recorded during cooling of the testpieces from the liquid state. Those measured during reheating were not so sharp and as in Reference 86 were up to about 35 °C higher than those measured during cooling.

TABLE .14

Vickers hardness data (30 kg) for alloys (i) as-cast (ii) heat-treated 2000 h at 850°C and (iii) heat-treated 200 h at 1050°C

Alloy/Condition	As-cast		Heat-treated 2000 h at 850°C		Heat-treated 200 h at 1050°C	
	Range	Average ± σ	Range	Average ± σ	Range	Average ± σ
W37	405/429	415 ± 8	412/432	424 ± 8	367/396	381 ± 9
W36	383/401	390 ± 8	365/409	387 ± 14	371/379	375 ± 3
W44	354/391	378 ± 14	382/429	411 ± 15	358/381	369 ± 10
W47	371/387	382 ± 7	325/369	346 ± 16	335/362	349 ± 13
R1	325/357	340 ± 12	325/348	338 ± 10	301/321	307 ± 8
W49	325/366	340 ± 18	325/358	342 ± 13	321/351	341 ± 13
W34	399/417	407 ± 6	407/426	413 ± 7	362/399	381 ± 12
W50	360/426	386 ± 21	359/388	379 ± 11	345/386	369 ± 13
R13	365/376	369 ± 4	349/386	374 ± 13	353/371	363 ± 7
R2	354/373	364 ± 7	341/367	352 ± 10	321/362	342 ± 13
R14	335/358	344 ± 10	333/367	350 ± 16	333/362	347 ± 10
R15	371/386	378 ± 6	374/396	386 ± 8	358/381	369 ± 9
W43	381/390	386 ± 4	376/400	388 ± 9	356/388	371 ± 10
R3	351/383	370 ± 12	341/381	361 ± 13	329/367	349 ± 16
W41	391/442	413 ± 21	369/420	402 ± 20	363/388	375 ± 10
R4	358/376	366 ± 7	341/388	360 ± 19	324/347	339 ± 13
R5	374/388	380 ± 6	288/362	335 ± 28	341/367	357 ± 9
R6	374/401	389 ± 12	360/409	384 ± 15	358/374	366 ± 6
R7	357/383	374 ± 10	369/388	381 ± 10	300/358	327 ± 22
R8	369/405	389 ± 15	365/391	380 ± 9	351/360	357 ± 4
R9	353/366	360 ± 5	347/383	366 ± 13	315/339	328 ± 10
R10	381/401	392 ± 8	362/401	374 ± 13	335/379	356 ± 16
R11	341/370	356 ± 11	351/381	365 ± 13	321/349	335 ± 11
R12	218/249	237 ± 11	209/253	231 ± 19	180/212	203 ± 13

TABLE 14 (cont'd)

Alloy/Condition	As-cast		Heat-treated 2000 h at 850°C		Heat-treated 200 h at 1050°C	
	Range	Average ± σ	Range	Average ± σ	Range	Average ± σ
MarM246	387/409	394 ± 15	N D		349/386	371 ± 11
Nimonic 115 standard heat-treatment	Manufacturer's Spec. 370/440 HV Typical 379 ± 9 measured value at NGTE					
Nimonic 115 blades containing sigma phase	395 ± 15 HV* 408 ± 10 HV**					
As above plus ½ h exposure at 1000°C	317 ± 17 HV					
Nimonic 115 blade sigma-free	343 ± 13 HV					

ND = not determined
*N_v = 2.84
**$N_{\bar{v}}$ = 2.73

TABLE 15

Miniature charpy impact test results (ft lbf)

Alloy/ condition	Test Temp.	W37	W36	W44	W47	R1	W49	W34	W50	R13
As-cast	R/T	1.0,2.3	1.5,2.2	2.8,4.2	2.9,5.6	4.6,6.8,8.6	1.6,3.8,9.6†	2.6,5.0	2.1,3.6	2.0,2.4
H/T 2000 h 850°C	R/T	2.0,1.4	2.0,1.2	3.8,2.1	3.6	3.2,2.6,3.4	2.0,3.2	1.8,2.3	2.0,2.1	1.1,5.0
H/T 200 h 1050°C	R/T	2.8,3.8	2.8	3.1	7.4,9.4	1.0,2.3	5.6	2.6,3.0	1.4,0.8	4.5,5.4
Alloy/ condition		R2	R14	R15	W43	R3	W41	R4	R5	R6
As-cast	R/T	2.5,3.4,3.5	1.7,2.3	1.5,2.3	1.8,4.5	1.8,2.4,2.8	2.0,2.4	1.6,3.0	2.2,2.2	1.0,2.4
H/T 2000 h 850°C	R/T	2.4,2.2	3.1	1.7	3.2	1.5,1.6	3.1,3.2	3.2,3.8	2.6,3.2	2.6,2.6
H/T 200 h 1050°C	R/T	1.8,2.6	3.2,5.2	3.8	1.9	1.2	2.3,2.5	0.4,0.6	1.6,1.8	1.0,1.8
Alloy/ condition		R7	R8	R9	R10	R11	R12			
As-cast	R/T	1.9,2.6	1.8,1.8	1.6,2.4	1.0,3.4	2.4,2.6	5.6,7.8,8.6†			
H/T 2000 h 850°C	R/T	1.5,3.5	1.3,1.5	0.4,0.8	2.1	1.5,2.3	4.4,4.6			
H/T 200 h 1050°C	R/T	0.2,0.8	1.2,1.8	0.3,1.0	1.8	1.2,3.0	1.2,1.5			

TABLE 15 (cont'd)

Alloy/ condition	Test Temp.	MarM246	Nimonic 115 bar fully heat treated	Nimonic 115 blades* containing sigma	Nimonic 115 blade*** (sigma free)
As-cast	R/T	1.4,1.8,2.0,2.0	8.8,9.3,10†	0.1,0.1, 0.1	8.3,8.6
	750°C	1.0,1.5,1.6	3.6,3.8	0.1,0.1	
H/T 200 h at 1050°C	R/T	2.4,3.3,4.2 8.5		As above, but H/T ½ h at 1000°C** 3.5,4.6	

R/T = 20°C

† Testpiece not fractured

* Data refer to blades removed after 1360 h and 8000 h service in engines because of brittleness

** H/T for ½ h at 1000°C dissolves sigma phase and restores 'toughness'

*** Blade removed after 950 h in service at similar operating temperature

NB (1) To convert ft lbf to Joules multiply by 1.356

(2) $\bar{N}v$ of Nimonic 115 alloy blades containing sigma phase = 2.84 and 2.73 respectively

(3) $\bar{N}v$ of sigma-free Nimonic 115 alloy blade = 2.54

TABLE 16

Tensile test data for experimental cast superalloys

Alloy	Casting technique	Test temperature °C	0.2% Proof stress tsi	% Elongation	% RA	Fracture stress tsi
R6	Conventional	20	47.6	14.4	24.0	62.2
	"	20	47.9	10.5	18.0	63.4
	"	750	50.6	2.7	12.0	54.3
	UDS	20	56.5	25.3	27.0	70.3
	UDS + aluminised coated	20	51.8	11.0	10.0	63.3
	UDS	750	62.1	6.4	8.0	75.8
R8	Conventional	20	48.7	11.2	20.0	63.4
	"	750	51.1	3.8	13.0	57.8
	UDS	20	53.9	11.8	ND*	64.8
	"	750	58.2	10.0	10.0	63.5

NOTE:- (1) All alloys were polycrystalline
(2) UDS alloys solidified at 15 in. h^{-1} and nominal $\langle 100 \rangle$
(3) Strain rate 0.2 per cent min^{-1}
(4) ND* not determined as testpiece fractured near ridges machined at end of gauge length to accommodate extensometer

TABLE 17

Creep/rupture properties of conventionally-cast experimental alloys

Alloy	Test conditions	Time, h, to given creep strain				Secondary creep rate $\%h^{-1} \times 10^{-3}$	% primary creep strain	Duration, h, of secondary creep	% Elongation	Time to rupture h
		0.1%	0.2%	0.5%	1.0%					
W37	(1) 30 tsi/850°C	2.0 1.0	8.0 18.0	32 50.0	81.0 72.0	4.0 7.0	0.4 0.15	60.0 23.0	5.0 2.0	206.0 97.0
	(2) 10 tsi/1000°C	18.0 3.0	35.0 8.0	143.0 60.0	202.0 162.0	4.0 4.0	0.20 0.30	90.0 94.0	5.0 3.5	264.0 251.0
	(3) 7 tsi/1040°C	35.0 35.0	80.0 80.0	145.0 162.0	174.0 156.0	2.5 2.5	0.15 0.15	115.0 120.0	2.5 5.1	248.0 164.0
W36	(1) 30 tsi/850°C	1.0 0.5	2.0 1.0	5.0 3.0	10.0 9.0	79.0 130.0	0.5 0.5	8.0 10.0	2.5 5.1	19.0 30.0
	(2) 10 tsi/1000°C	2.0 0.1	4.0 0.5	12.0 2.0	19.0 7.0	32.0 134.0	0.2 0.2	21.0 8.0	8.6 12.5	42.0 40.0
	(3) 7 tsi/1040°C	7.0 4.0	13.0 8.0	22.0 18.0	30.0 27.0	25.0 28.0	0.25 0.05	10.0 20.0	8.3 7.4	44.0 39.0
W44	(1) 30 tsi/850°C	3.0 2.0	5.0 5.0	14.0 13.0	28.0 25.0	34.0 37.0	0.30 0.30	10.0 14.0	4.8 3.0	67.0 44.0
	(2) 10 tsi/1000°C	2.0 15.0	5.0 36.0	30.0 68.0	58.0 91.0	12.0 6.0	0.20 0.10	37.0 33.0	5.9 5.0	101.0 127.0
	(3) 7 tsi/1040°C	3.0 5.0	10.0 40.0	48.0 125.0	101.0 158.0	8.5 2.0	0.30 0.15	95.0 100.0	6.5 4.6	157.0 188.0

TABLE 17 (cont'd)

Alloy	Test conditions	Time, h, to given creep strain				Secondary creep rate $\%h^{-1} \times 10^{-3}$	% primary creep strain	Duration, h of secondary creep	% Elongation	Time to rupture h
		0.1%	0.2%	0.5%	1.0%					
W47	(1) 30 tsi/850°C	1.0 1.0	2.0 3.0	4.0 8.0	9.0 13.0	110.0 66.0	0.3 0.25	10.0 11.0	5.0 6.0	20.0 28.0
	(2) 10 tsi/1000°C	12.0 3.0	23.0 5.0	30.0 11.0	36.0 18.0	25.0 40.0	0.05 0.10	12.0 7.0	7.0 7.1	52.0 44.0
	(3) 7 tsi/1040°C	7.0	16.0	29.0	43.0	11.0	0.10	25.0	4.6	53.0
R1	(1) 30 tsi/850°C	1.0 1.0	2.0 4.5	5.5 9.0	11.0 13.5	90.0 58.0	0.05 0.08	13.0 8.0	4.4 2.4	31.0 15.0
	(2) 10 tsi/1000°C	5.0 3.0	12.0 5.0	28.0 8.0	38.0 15.0	14.0 60.0	0.05 0.10	21.0 8.0	6.1 7.3	44.0 38.0
	(3) 7 tsi/1040°C	2.0 3.0	3.0 10.0	10.0 35.0	62.0 63.0	20.0 13.0	0.70 0.10	26.0 50.0	3.1 6.0	65.0 89.0
W49	(1) 30 tsi/850°C	5.0 2.0	9.0 3.0	15.0 9.0	18.0 28.0	11.0 23.0	0.05 0.5	7.0 16.0	1.4 2.8	19.0 50.0
	(2) 10 tsi/1000°C	9.0 2.0	20.0 6.0	28.0 24.0	30.0 40.0	9.0 15.0	0.10 0.10	20.0 20.0	1.3 2.4	30.0 45.0
	(3) 7 tsi/1040°C	4.0 1.5	10.0 2.0	50.0 13.0	76.0 46.0	6.0 17.0	0.20 0.25	21.0 35.0	5.6	107.0 79.0

TABLE 17 (cont'd)

Alloy	Test conditions	Time, h, to given creep strain				Secondary creep rate $\%h^{-1} \times 10^{-3}$	% primary creep strain	Duration, h of secondary creep	% Elongation	Time to rupture h
		0.1%	0.2%	0.5%	1.0%					
W34	(1) 30 tsi/850°C	4.0 3.0	6.0 5.0	34.0 40.0	66.0 74.0	13.0 15.0	0..2 0.2	42.0 70.0	5.4 3.5	170.0 135.0
	(2) 10 tsi/1000°C	10.0 15.0	40.0 60.0	100.0 99.0	140.0 120.0	3.0 4.0	0.10 0.05	64.0 50.0	3.6 4.5	166.0 126.0
	(3) 7 tsi/1040°C	5.0 7.0	10.0 13.0	45.0 78.0	104.0 134.0	7.0 4.0	0.25 0.35	85.0 115.0	5.5 4.6	145.0 150.0
W50	(1) 30 tsi/850°C	2.0 5.0	8.0 17.0	40.0 44.0	56.0 56.0	8.0 9.0	0.2 0.2	30.0 20.0	2.1 2.6	65.0 94.0
	(2) 10 tsi/1000°C	3.0 5.0	8.0 12.0	39.0 44.0	70.0 76.0	11.0 12.0	0.20 0.15	40.0 50.0	3.1 3.9	116.0 111.0
	(3) 7 tsi/1040°C	7.0 2.0	40.0 4.0	90.0 20.0	151.0 70.0	4.0 8.3	0.10 0.35	72.0 70.0	6.3 4.4	180.0 170.0
R13	(1) 30 tsi/850°C	10.0	27.0	46.0	65.0	6.0	0.05	28.0	8.4	141.0
	(2) 10 tsi/1000°C	13.0 22.0	30.0 34.0	57.0 54.0	80.0 71.0	6.0 5.0	0.10 0.05	46.0 34.0	7.5 3.4	139.0 92.0
	(3) 7 tsi/1040°C	12.0 9.0	25.0 23.0	76.0 48.0	122.0 96.0	6.0 8.0	0.15 0.15	80.0 40.0	5.2 6.1	166.0 162.0

TABLE 17 (cont'd)

Alloy	Test conditions	Time, h, to given creep strain				Secondary creep rate $\%h^{-1} \times 10^{-3}$	% primary creep strain	Duration, h, of secondary creep	% Elongation	Time to rupture h
		0.1%	0.2%	0.5%	1.0%					
R2	(1) 30 tsi/850°C	1.0	2.0	7.0	15.0	60.0	0.10	14.0	2.1	22.0
	(2) 10 tsi/1000°C	4.0	8.0	16.0	17.0	28.0	0,10	16.0	1.3	17.0
		4.0	9.0	20.0	37.0	25.0	0.05	21.0	5.1	68.0
	(3) 7 tsi/1040°C	9.0	24.0	65.0	89.0	7.0	0.05	55.0	4.5	112.0
		2.0	5.0	19.0	42.0	16.0	0.30	28.0	2.8	55.0
R14	(1) 30 tsi/850°C	10.0	15.0	21.0	28.0	10.0	0.05	12.0	6.4	44.0
		3.0	6.0	17.0	30.0	28.0	0.25	20.0	3.9	54.0
	(2) 10 tsi/1000°C	8.0	15.0	29.0	44.0	13.0	0.10	13.0	9.4	79.0
		10.0	20.0	45.0	55.0	8.0	0.05	23.0	8.0	83.0
	(3) 7 tsi/1040°C	3.0	8.0	25.0	58.0	14.0	0.25	48.0	5.8	97.0
		2.0	5.0	27.0	78.0	10.0	0.30	70.0	6.4	144.0
R15	(1) 30 tsi/850°C	3.0	7.0	11.0	15.0	34.0	0.10	6.0	2.3	20.0
		0.05	2.0	5.0	10.0	65.0	0.15	8.0	5.0	27.0
	(2) 10 tsi/1000°C	5.0	22.0	46.0	69.0	8.0	0.10	30.0	7.5	118.0
		1.0	5.0	15.0	22.0	18.0	0.15	8.0	24.8	25.0
	(3) 7 tsi/1040°C	34.0	54.0	77.0	91.0	4.0	0.10	58.0	4.4	109.0
		24.0	42.0	78.0	119.0	4.0	0.08	50.0	7.2	141.0

TABLE 17 (cont'd)

Alloy	Test conditions	Time, h, to given creep strain				Secondary creep rate $\%h^{-1} \times 10^{-3}$	% primary creep strain	Duration, h, of secondary creep	% Elongation	Time to rupture h
		0.1%	0.2%	0.5%	1.0%					
W43	(1) 30 tsi/850°C	4.0	9.0	13.0	20.0(e)	24.0	0.10	6.0	1.6	17.0
		15.0	22.0	27.0	35.0	4.0	0.10	15.0	5.0	46.0
	(2) 10 tsi/1000°C	5.0	10.0	27.0	53.0	17.0	0.10	20.0	6.3	96.0
		2.0	8.0	44.0	66.0	7.0	0.20	30.0	7.5	117.0
	(3) 7 tsi/1040°C	2.0	4.0	18.0	52.0	11.5	0.40	35.0	4.6	67.0
		12.0	30.0	57.0	78.0	5.0	0.10	35.0	4.0	90.0
R3	(1) 30 tsi/850°C	3.0	10.0	30.0	43.0	14.0	0.05	23.0	3.5	55.0
		2.0	5.0	21.0	45.0	20.0	0.10	30.0	2.9	84.0
	(2) 10 tsi/1000°C	5.0	15.0	42.0	73.0	9.0	0.10	25.0	7.5	142.0
		10.0	20.0	45.0	67.0	10.0	0.10	31.0	2.2	78.0
	(3) 7 tsi/1040°C	8.0	18.0	45.0	90.0	11.0	0.05	100.0	10.0	191.0
		7.0	28.0	54.0	103.0	8.0	0.10	100.0	7.3	184.0
W41	(1) 30 tsi/850°C	5.0	14.0	36.0	75.0	13.0	0.10	52.0	5.9	136.0
		27.0	34.0	50.0	70.0	5.0	0.05	30.0	3.8	101.0
	(2) 10 tsi/1000°C	20.0	60.0	140.0	220.0	3.0	0.05	128.0	4.0	287.0
		3.0	14.0	63.0	96.0	6.0	0.10	58.0	7.0	127.0
	(3) 7 tsi/1040°C	30.0	70.0	155.0	193.0	2.5	0.15	125.0	8.9	232.0
		5.0	11.0	90.0	157.0	2.5	0.30	110.0	8.8	235.0

TABLE 17 (cont'd)

Alloy	Test conditions	Time, h, to given creep strain				Secondary creep rate $\%h^{-1} \times 10^{-3}$	% primary creep strain	Duration, h, of secondary creep	% Elongation	Time to rupture h
		0.1%	0.2%	0.5%	1.0%					
R4	(1) 30 tsi/850°C	3.0 1.5	5.0 3.5	13.0 11.0	24.0 21.0	37.0 42.0	0.05 0.10	15.0 15.0	3.5 2.5	40.0 30.0
	(2) 10 tsi/1000°C	1.0 2.0	4.0 5.0	17.0 18.0	42.0 43.0	21.0 20.0	0.20 0.10	38.0 34.0	6.3 9.0	89.0 101.0
	(3) 7 tsi/1040°C	2.0 10.0	5.0 30.0	25.0 68.0	68.0 93.0	11.5 6.0	0.30 0.10	75.0 60.0	6.5 6.1	129.0 117.0
R5	(1) 30 tsi/850°C	5.0 4.0	12.0 10.0	28.0 24.0	46.0 41.0	17.0 23.0	0.15 0.05	28.0 26.0	5.6 4.5	96.0 92.0
	(2) 10 tsi/1000°C	35.0 3.0	50.0 8.0	69.0 32.0	88.0 77.0	3.0 11.0	0.05 0.30	36.0 75.0	5.7 7.0	113.0 159.0
	(3) 7 tsi/1040°C	3.0 8.0	10.0 22.0	45.0 64.0	112.0 98.0	7.0 6.5	0.30 0.10	70.0 65.0	8.1 7.1	170.0 142.0
R6	(1) 30 tsi/850°C	4.0	30.0	73.0	111.0	5.0	0.10	50.0	3.3	125.0
	(2) 10 tsi/1000°C	7.0 5.0	15.0 10.0	49.0 35.0	74.0 85.0	10.0 13.0	0.15 0.20	50.0 45.0	8.0 5.1	149.0 101.0
	(3) 7 tsi/1040°C	9.0 3.0	20.0 10.0	65.0 45.0	111.0 110.0	7.0 8.0	0.20 0.20	100.0 60.0	8.9 10.1	176.0 201.0

TABLE 17 (cont'd)

Alloy	Test conditions	Time, h, to given creep strain				Secondary creep rate $\%h^{-1} \times 10^{-3}$	% primary creep strain	Duration, h, of secondary creep	% Elongation	Time to rupture h
		0.1%	0.2%	0.5%	1.0%					
R7	(1) 30 tsi/850°C	1.5	3.0	10.0	17.5	40.0	0.10	14.0	1.6	20.0
	(2) 10 tsi/1000°C	24.0	38.0	65.0	88.0	6.0	0.05	35.0	4.0	128.0
		4.0	10.0	38.0	62.0	11.0	0.20	40.0	6.0	99.0
	(3) 7 tsi/1040°C	14.0	34.0	80.0	105.0	5.5	0.10	70.0	4.6	137.0
		10.0	30.0	78.0	116.0	4.5	0.10	65.0	2.9	119.0
R8	(1) 30 tsi/850°C	4.0	12.0	30.0	53.0	16.0	0.10	30.0	3.6	97.0
		2.0	8.0	28.0	52.0	16.0	0.15	28.0	4.0	85.0
	(2) 10 tsi/1000°C	9.0	20.0	50.0	83.0	10.0	0.10	58.0	3.0	119.0
		8.0	25.0	70.0	104.0	6.0	0.10	60.0	6.8	167.0
	(3) 7 tsi/1040°C	5.0	14.0	49.0	103.0	1.0	0.20	120.0	6.5	186.0
		4.0	12.0	55.0	105.0	7.0	0.10	85.0	6.4	169.0
R9	(1) 30 tsi/850°C	4.0	10.0	23.0	40.0	21.0	0.10	22.0	2.5	58.0
		5.0	11.0	21.0	29.0	19.0	0.05	12.0	3.0	34.0
	(2) 10 tsi/1000°C	1.5	3.0	13.0	35.0	23.0	0.40	40.0	5.0	50.0
		5.0	15.0	39.0	51.0	10.0	0.10	30.0	3.0	55.0
	(3) 7 tsi/1040°C	1.5	8.0	30.0	71.0	12.0	0.20	64.0	2.5	101.0
		2.0	6.0	30.0	72.0	11.0	0.25	64.0	4.0	94.0

TABLE 17 (cont'd)

Alloy	Test conditions	Time, h, to given creep strain				Secondary creep rate $\%h^{-1} \times 10^{-3}$	% primary creep strain	Duration, h, of secondary creep	% Elongation	Time to rupture h
		0.1%	0.2%	0.5%	1.0%					
R10	(1) 30 tsi/850°C	5.0 4.0	13.0 9.0	31.0 23.0	49.0 37.0	14.0 21.0	0.05 0.05	26.0 28.0	2.6 2.5	67.0 51.0
	(2) 10 tsi/1000°C	5.0 10.0	18.0 28.0	55.0 67.0	81.0 96.0	8.0 7.0	0.10 0.05	60.0 50.0	8.9 5.1	142.0 130.0
	(3) 7 tsi/1040°C	8.0 8.0	25.0 30.0	69.0 74.0	111.0 111.0	6.0 5.0	0.05 0.05	60.0 70.0	4.0 13.8	148.0 180.0
R11	(1) 30 tsi/850°C	1.0 4.0	3.0 9.0	15.0 19.0	29.0 31.0	29.0 21.0	0.15 0.05	18.0 8.0	4.1 2.4	64.0 39.0
	(2) 10 tsi/1000°C	16.0 4.0	30.0 14.0	53.0 33.0	70.0 53.0	6.0 13.0	0.10 0.10	35.0 25.0	4.6 6.8	105.0 101.0
	(3) 7 tsi/1040°C	8.0 11.0	22.0 25.0	86.0 73.0	125.0 91.0	4.5 6.0	0.10 0.10	90.0 70.0	6.6 2.3	135.0 98.0
R12	850°C	Testpiece fractured on loading at 16 tsi								<0.1
	10 tsi 1000°C 3 tsi	Testpiece fractured on loading at 3 tsi							1.0 1.0	0 200.0 (D)
	3 tsi 1040°C	12.0	20.0	35.0 1.0	49.0	0.10	0.10	10.0	4.1 0.9	54.0 1.3

NOTE:

*All tests done on uncoated testpieces in air
e = extrapolated
D = discontinued

TABLE 18.

Linear regression equations for creep-rupture tests on conventionally-cast alloys at 850°C, 1000°C and 1040°C

The equations are of the form: $y = A + Bx$

where A and B are coefficients, y is the time to produce prescribed levels of creep strain, and the variable x is either γ' solvus temperature (°C) or mean level of 'as-cast' hardness.

Test condition 1 - 30 tsi/850°C

(a) x = as-cast hardness

y (hours)	A	B	Significance	Standard deviation (hours)
0.5% strain	-126.6	0.3990	95%	15.1
1.0% strain	-225.9	0.7039	99%	22.2
time-to-rupture	-411.6	1.2677	99%	36.5

(b) x = γ' solvus temperature (°C)

y (hours)	A	B	Significance	Standard deviation (hours)
0.1% strain	-116.8	0.1001	95%	3.3
0.5% strain	-696.8	0.5969	99%	14.0
1.0% strain	-1152.1	0.9869	99%	20.9
time-to-rupture	-1893.6	1.6233	99%	36.0

TABLE 18 (cont'd)

Test condition 2 - 10 tsi/1000°C

(a) x = as-cast hardness

y (hours)	A	B	Significance	Standard deviation (hours)
0.5% strain	-287.2	0.8815	99.9%	19.6
1.0% strain	-482.5	1.4663	99.9%	28.8
time-to-rupture	-619.8	1.9257	99.9%	37.0

(b) x = γ' solvus temperature (°C)

y (hours)	A	B	Significance	Standard deviation (hours)
0.5% strain	-1152.0	0.9915	99%	21.2
1.0% strain	-1994.8	1.7103	99.9%	30.9
time-to-rupture	-2487.9	2.1484	99.9%	41.3

TABLE 18 (cont'd)

Test condition 3 - 7 tsi/1040°C

(a) x = as-cast hardness

y (hours)	A	B	Significance	Standard deviation (hours)
0.1% strain	-65.0	0.1956	95%	7.3
0.5% strain	-299.5	0.9498	99%	25.8
1.0% strain	-280.2	0.9919	99%	28.4
time-to-rupture	-339.5	1.2595	95%	44.2

(b) x = γ' solvus temperature (°C)

y (hours)	A	B	Significance	Standard deviation (hours)
0.5% strain	-1501.9	1.2924	99.9%	24.3
1.0% strain	-1554.4	1.3650	99.9%	26.7
time-to-rupture	-2515.5	2.1956	99.9%	35.8

TABLE 19

Creep-rupture properties of conventionally-cast and UDS alloys

Alloy	Condition	Creep test conditions	Time, h, to given creep strain				Secondary creep rate $\%h^{-1} \times 10^{-3}$	% primary creep strain	Duration, h, of secondary creep	% Elongation	Time to rupture, h
			0.1%	0.2%	0.5%	1.0%					
R6	CC	30 tsi/850°C	4.0	30.0	73.0	111.0	5.0	0.1	50.0	3.3	125
	UDS		1.0	3.0	10.0	24.0	39.0	0.2	19.0	30.0	158
	UDS + Aluminised		1.5	2.0	3.0	7.0	36.0	1.2	20.0	29.0	140
R6LC	UDS		1.0	4.0	13.0	25.0	36.0	0.2	19.0	35.0	140
R8	CC	30 tsi/850°C	4.0	12.0	30.0	53.0	16.0	0.10	30.0	3.6	97
	"		2.0	8.0	28.0	52.0	16.0	0.15	28.0	4.0	85
	UDS		1.0	3.0	20.0	47.0	23.0	0.40	25.0	21.5	211
	"		7.0	12.0	27.0	49.0	20.0	0.10	34.0	18.4	187
R6	CC	10 tsi/1000°C	7.0	15.0	49.0	74.0	10.0	0.15	50.0	8.0	149
	"		5.0	10.0	35.0	85.0	13.0	0.20	45.0	5.1	101
	UDS		25.0	35.0	60.0	81.0	5.0	0.10	32.0	41.0	218
	UDS + Aluminised		2.0	4.0	19.0	36.0	22.0	0.20	23.0	44.0	138
R6LC	UDS		20.0	35.0	58.0	78.0	8.0	0.10	25.0	50.0	161
	"		8.0	15.0	32.0	60.0	17.0	0.10	45.0	43.0	158
R8	CC	10 tsi/1000°C	9.0	20.0	50.0	83.0	10.0	0.10	58.0	3.0	119
	"		8.0	25.0	70.0	104.0	6.0	0.10	60.0	6.8	167
	UDS		6.0	22.0	64.0	85.0	6.0	0.15	35.0	39.0	168
R6	CC	7 tsi/1040°C	9.0	20.0	65.0	111.0	7.0	0.20	100.0	8.9	176
	"		3.0	10.0	45.0	110.0	8.0	0.20	60.0	10.1	201
	UDS		35.0	55.0	88.0	114.0	2.0	0.10	40.0	34.0	204
	UDS + Aluminised		2.0	5.0	17.0	56.0	1.0	0.50	65.0	38.0	223
R6LC	UDS		125.0	146.0	153.0	159.0	1.0	0.03	100.0	27.3	175
R8	CC	7 tsi/1040°C	5.0	14.0	49.0	103.0	1.0	0.20	120.0	6.5	186
	"		4.0	12.0	55.0	105.0	7.0	0.10	85.0	6.4	169
	UDS		85.0	123.0	156.0	188.0	1.0	0.01	100.0	40.0	277
	"		82.0	150.0	172.0	196.0	1.0	0.01	100.0	24.0	300

TABLE 19 (cont'd)

Alloy	Condition	Creep test conditions	Time, h, to given creep strain				Secondary creep rate $\%h^{-1} \times 10^{-3}$	% primary creep strain	Duration, h, of secondary creep	% Elongation	Time to rupture, h
			0.1%	0.2%	0.5%	1.0%					
R6	CC	4 tsi/1100°C	1.0	3.0	11.0	28.0	28.0	0.5	71.0	4.8	143
R6LC	UDS		2.0	6.0	40.0	215.0	2.0	0.6	150.0	16.4	376
R8	CC	4 tsi/1100°C	0.2	0.4	0.8	2.3	12.5	6.0	71.0	7.4	156
	UDS		0.2	0.4	1.0	3.3	1.7	5.6	350.0	15.2	720
	"		0.5	1.0	15.0	200.0	8.9	0.8	320.0	>16.3	693(D)
R6	CC	45 tsi/760°C	0.5	1.0	1.5	3.0	160.0	1.2	6.0	3.0	13
	"	"	0.5	1.0	2.0	9.0	38.0	1.1	20.0	2.6	40
	"	"	0.5	1.0	2.0	4.0	160.0	1.2	6.0	4.3	14
	UDS	"	0.1	0.4	1.0	1.2	57.0	6.1	33.0	29.0	175
	"	42 tsi/750°C									
	"	"	1.0	1.5	2.0	3.0	15.0	5.0	330.0	17.3	592
	UDS + Aluminised	"	1.0	1.2	2.0	3.0	11.0	3.4	350.0	23.1	763
	prestressed 30 tsi/301 h	"	0.5	1.0	2.0	5.0	8.0	1.8	730.0	16.5	1050
R6LC	UDS	"	2.0	3.0	3.5	4.0	19.0	4.3	125.0	21.8	451
R8	CC	45 tsi/760°C	0.5	1.0	1.5	2.5	182.0	1.4	7.0	4.9	14
	"		0.5	1.0	2.5	4.5	110.0	0.6	3.0	3.0	7
	UDS		0.1	0.2	0.8	1.2	32.0	5.4	58.0	12.0	133
	UDS + H/T 16 h at 870°C		0.1	0.2	0.5	1.0	31.0	3.8	80.0	13.6	200
	UDS + 0.2% tensile strain at 760°C		0.1	0.3	0.6	1.0	62.0	8.5	18.0	11.9	44

NOTE: 1. All alloys were polycrystalline
2. CC = conventionally cast
3. UDS = unidirectionally solidified at 15 in. h^{-1} and nominal <100>
4. D = discontinued because of furnace failure

TABLE 20

Typical creep-rupture properties of selected experimental alloys in comparison to some commercial superalloys (IN100 and MarM246) tested at NGTE

Alloy designation	Casting method	Test conditions	Time, h, to % creep strain		Secondary creep rate $\%h^{-1} \times 10^{-3}$	% Elongation at fracture	Mean time, h, to rupture
			0.5	1.0			
W37/HRA 376	Conventional	30 tsi/850°C	41	77	5.5	3.5	152.0
R6	Conventional	"	73	111	5.0	3.1	125.0
	UDS	"	10	24	39.0	30.0	158.0
R8	Conventional	"	29	53	16.0	3.8	91.0
	UDS	"	24	48	22.5	20.0	199.0
IN100	Conventional	"	3	10	60	3.8	43.0
	UDS	"	10	23	35	15.2	80.0
MarM246	Conventional	"	9	25	30	3.5	62.0
	UDS	"	10	36	20	15.1	182.0
W37/HRA 376	Conventional	7 tsi/1040°C	154	165	2.5	3.8	206.0
R6	Conventional	"	55	111	7.5	8.5	188.0
	UDS	"	88	114	2.0	34.0	204.0

TABLE 20 (cont'd)

Alloy designation	Casting method	Test conditions	Time, h, to % creep strain		Secondary creep rate $\%h^{-1} \times 10^{-3}$	% Elongation at fracture	Mean time, h, to rupture
			0.5	1.0			
R8	Conventional	7 tsi/1040°C	52	104	4.0	6.4	178.0
	UDS	"	156	188	1.0	40.0	277.0
IN100	Conventional	"	32	59	11.0	8.6	85.0
	UDS	"	6	20	33.0	19.4	105.0
MarM246	Conventional	"	3	21	11.0	5.1	129.0
	UDS	"	29	86	7.1	19.0	253.0
R6	Conventional	4 tsi/1100°C	11	28	28.0	4.8	143.0
R6LC	UDS	"	40	215	2.0	16.4	376.0
R8	Conventional	"	0.8	2.3	12.5	7.4	156.0
	UDS	"	8	201	5.3	>15.8	>707.0
IN100	Conventional	"	<1	<1	Not determined	61.7	2.0
MarM246	Conventional	"	3	11	31.0	3.9	57.0
	UDS (3)		1	5	20.0	17.9	142.0
	UDS (4)		1	4	31.0	17.5	90.0

NOTE:- 1. All alloys were polycrystalline
2. UDS alloys solidified at 15 in. h^{-1} and nominal <100>
3. MarM246 composition with 0.1W/o C
4. MarM246 composition with 0.15W/o C
5. Data are generally the mean of at least two tests

TABLE 21

Temperature, °C, to produce rupture in 100 h at given stress level for conventionally-cast and UDS alloys[1]

Stress tsi / Alloy		MarM246	IN100	W37	W41	R6	R8	R10
30	2	839	831	859	854	855	848	838
	3	839	875	851	850	855	848	843
	4	863	845	ND	ND	860	865	ND
7	2	1046	1036	1059	1062	1056	1055	1053
	3	1046	1054	1054	1060	1056	1055	1059
	4	1064	1041	ND	ND	1058	1066	ND
4	2	1085	NA	ND	ND	1110	1112	ND
	3	1085	NA	ND	ND	1110	1112	ND
	4	1101	ND	ND	ND	1136	1147	ND

1. Based on Larson-Miller parameter $P = T\left[20 + \log t\right]$ where T = temperature K, t = time h and mean time-to-rupture from Table 19
2. For conventionally cast alloys
3. For conventionally cast alloys corrected to density of MarM246 alloy
4. For UDS alloys, uncorrected for density

NA = rupture duration too short (2 h) for meaningful extrapolation

ND = not determined

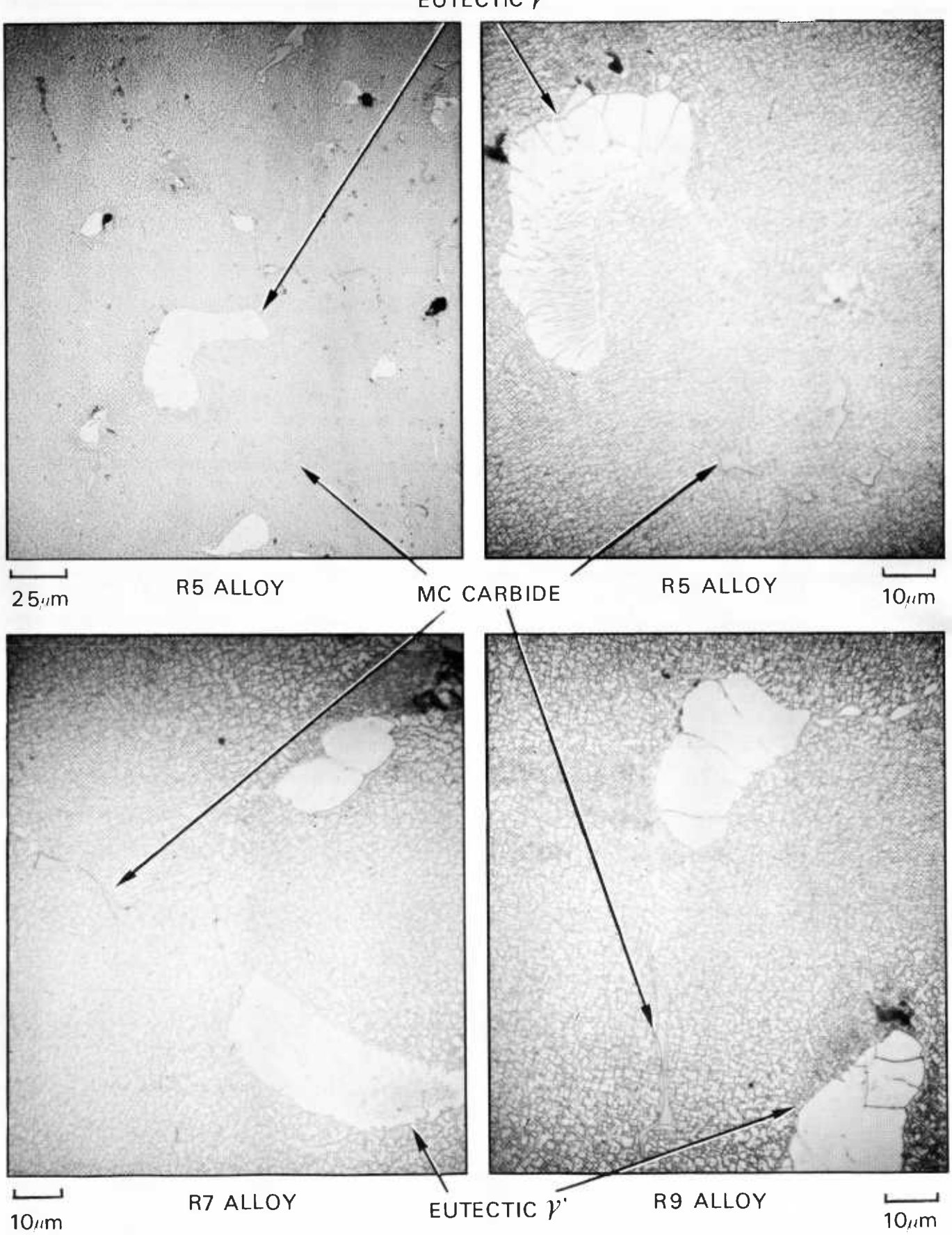
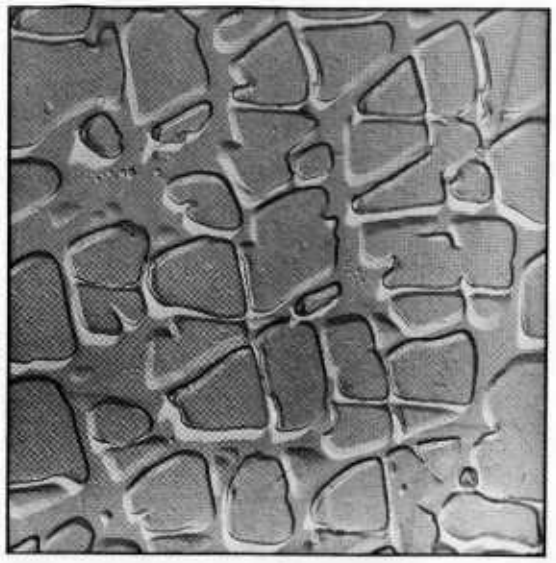


FIG.1 TYPICAL OPTICAL MICROGRAPHS OF THE STRUCTURE OF THE EXPERIMENTAL SUPERALLOYS (AS CAST)



CUBOIDAL γ′

3 μm



EUTECTIC γ′

20 μm



EUTECTIC γ′

20 μm

FIG.2 ELECTRON MICROGRAPHS (REPLICAS) SHOWING TYPICAL 'AS-CAST' STRUCTURES

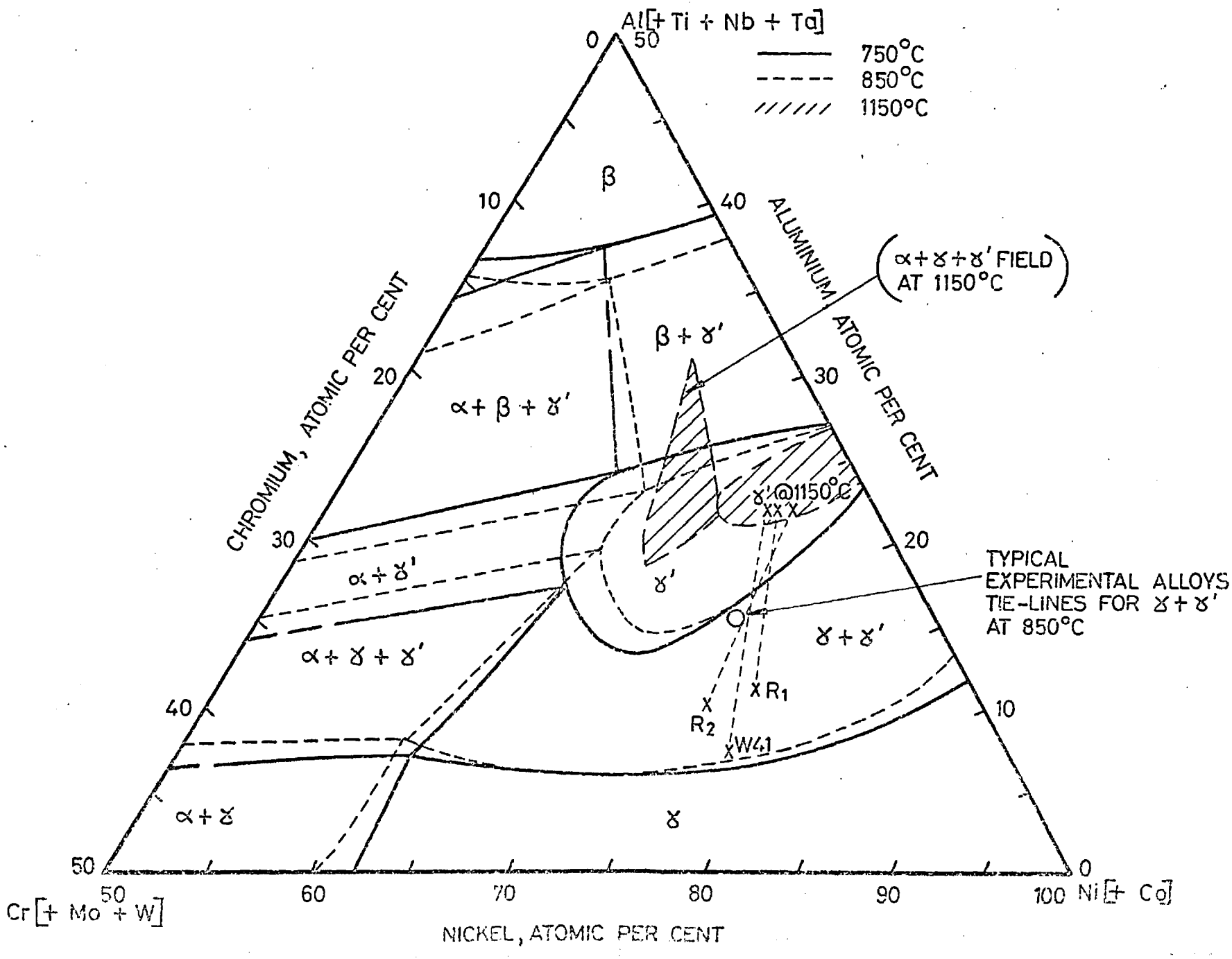


FIG. 3 THE NICKEL – CHROMIUM – ALUMINIUM PHASE DIAGRAM: ISOTHERMAL SECTIONS FOR 750°C, 850°C AND 1150°C

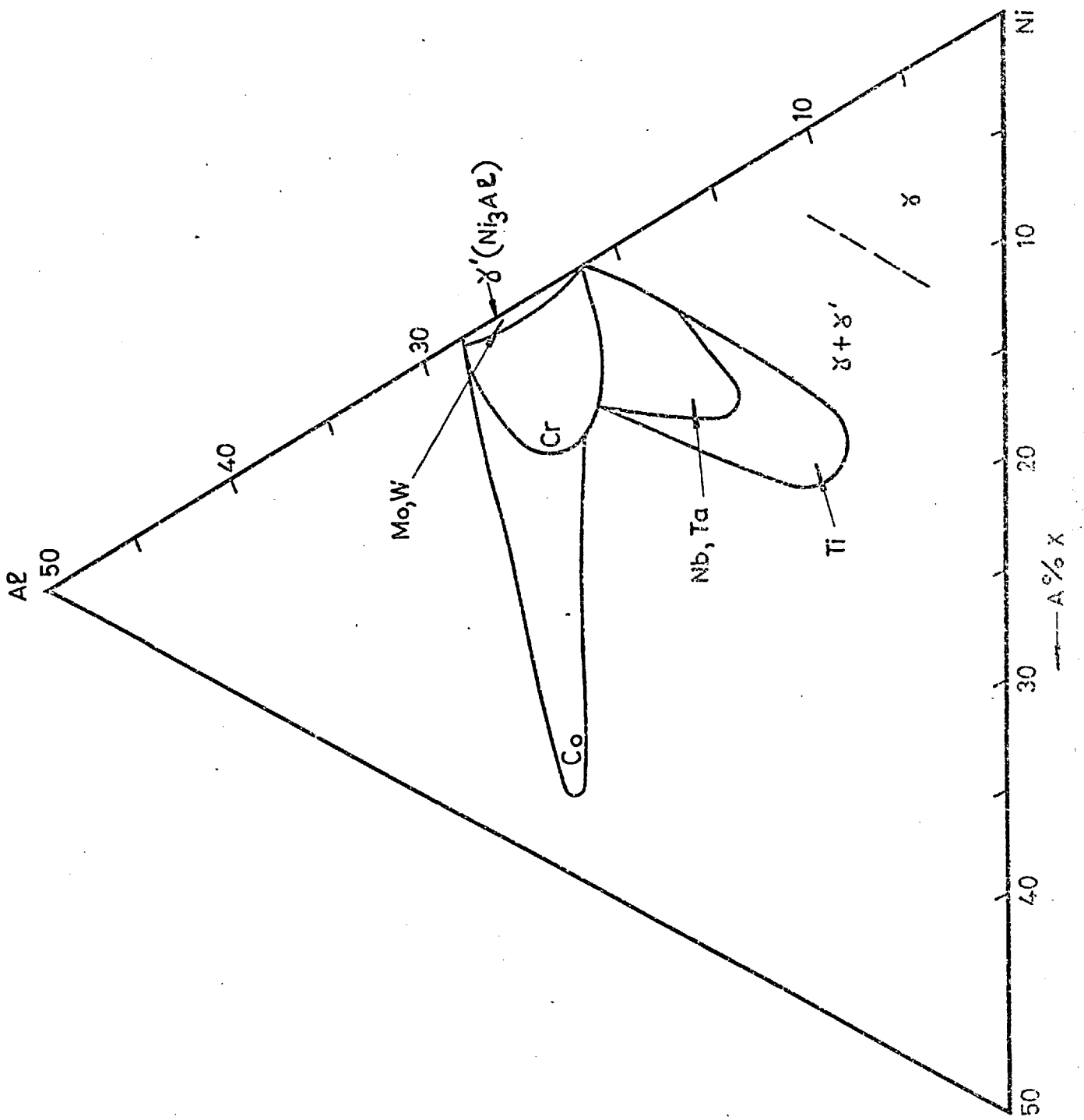
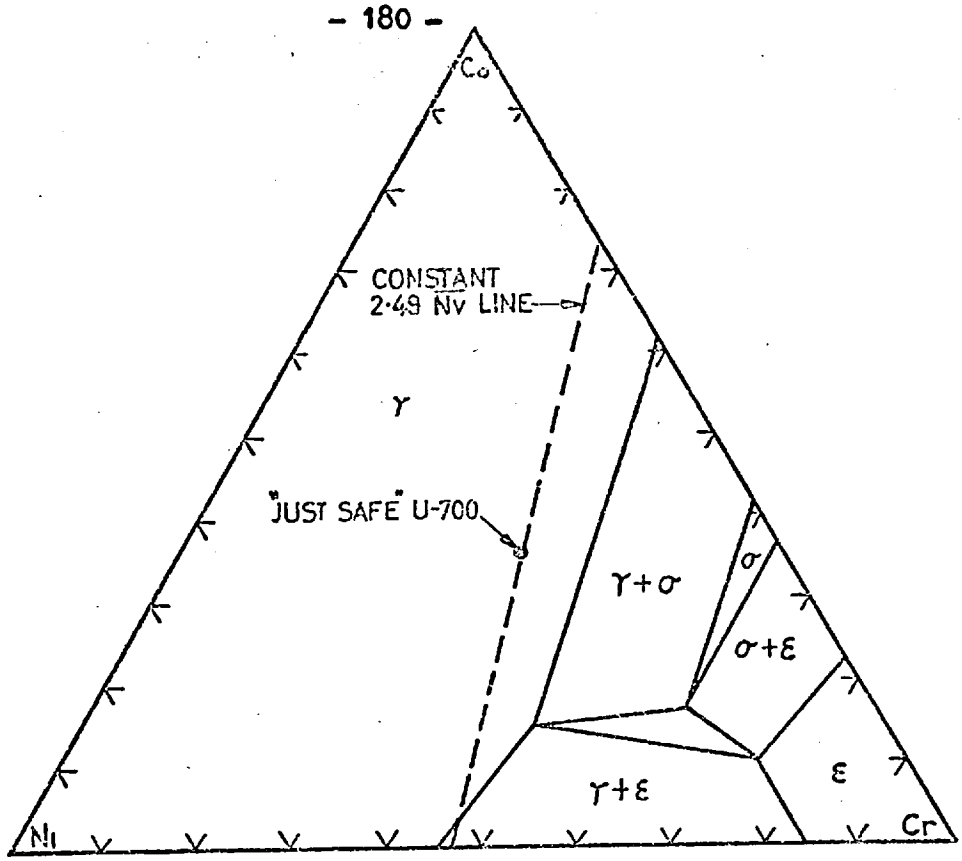
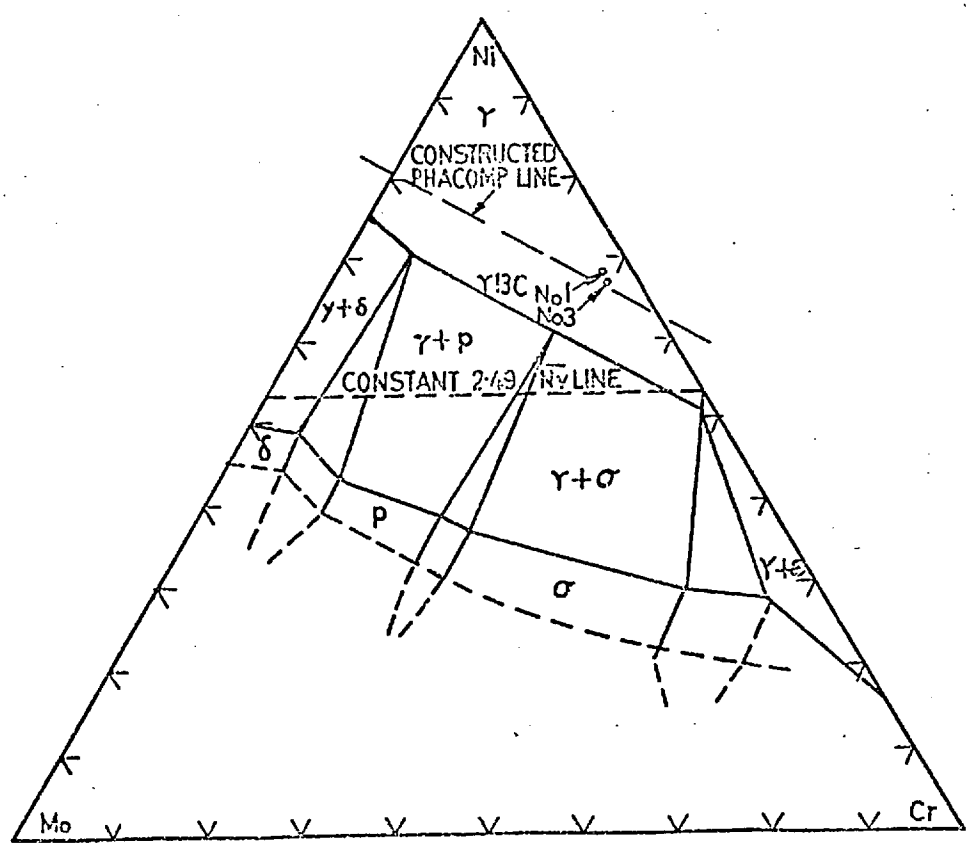


FIG.4 Ni_3Al SOLID SOLUTION FIELD AT APPROXIMATELY 2100°F (1150°C) FOR VARIOUS TERNARY ALLOYS

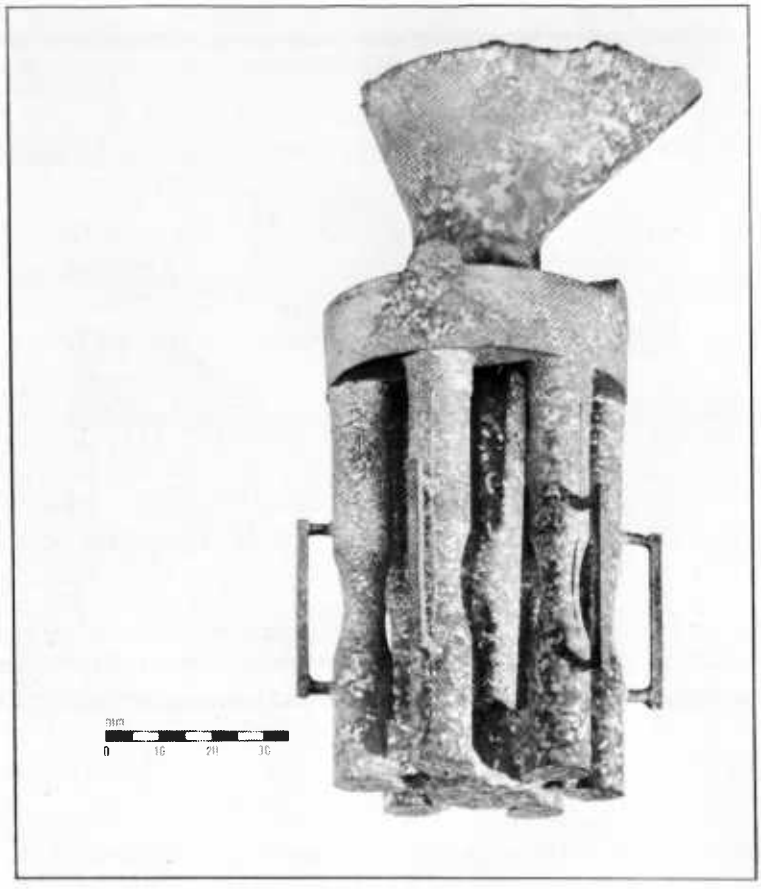


(a) Ni Co Cr TERNARY AT 1204°C

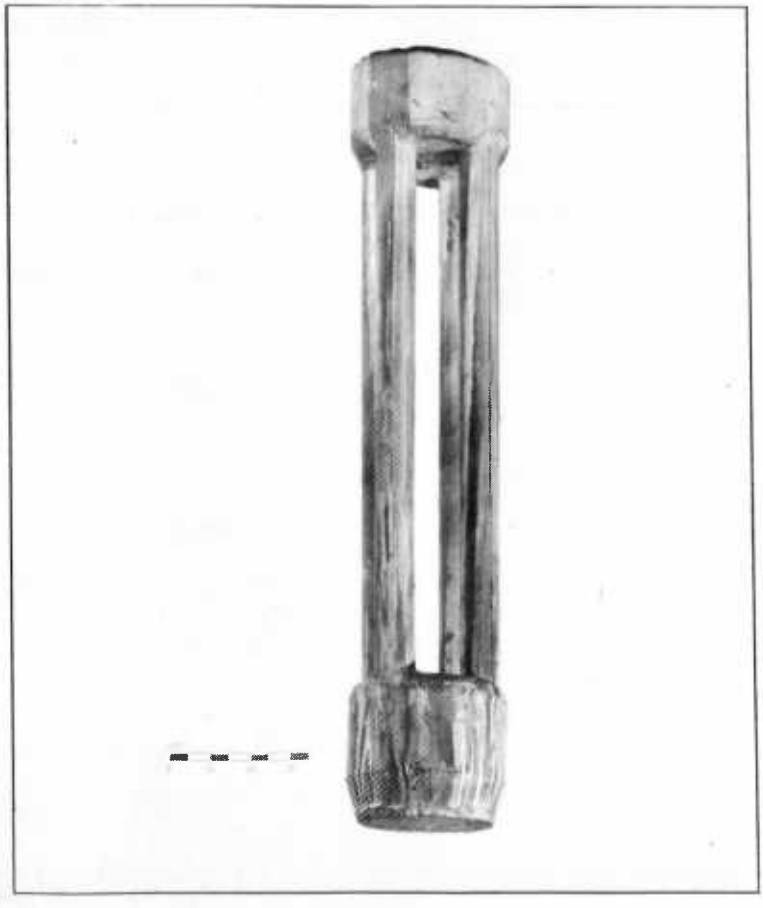


(b) Ni Cr Mo TERNARY AT 1204°C

FIG.5 PHACOMP PREDICTION OF MATRIX COMPOSITIONS OF U700 & IN713C IN THE Ni Co Cr & Ni Cr Mo SYSTEMS[14]

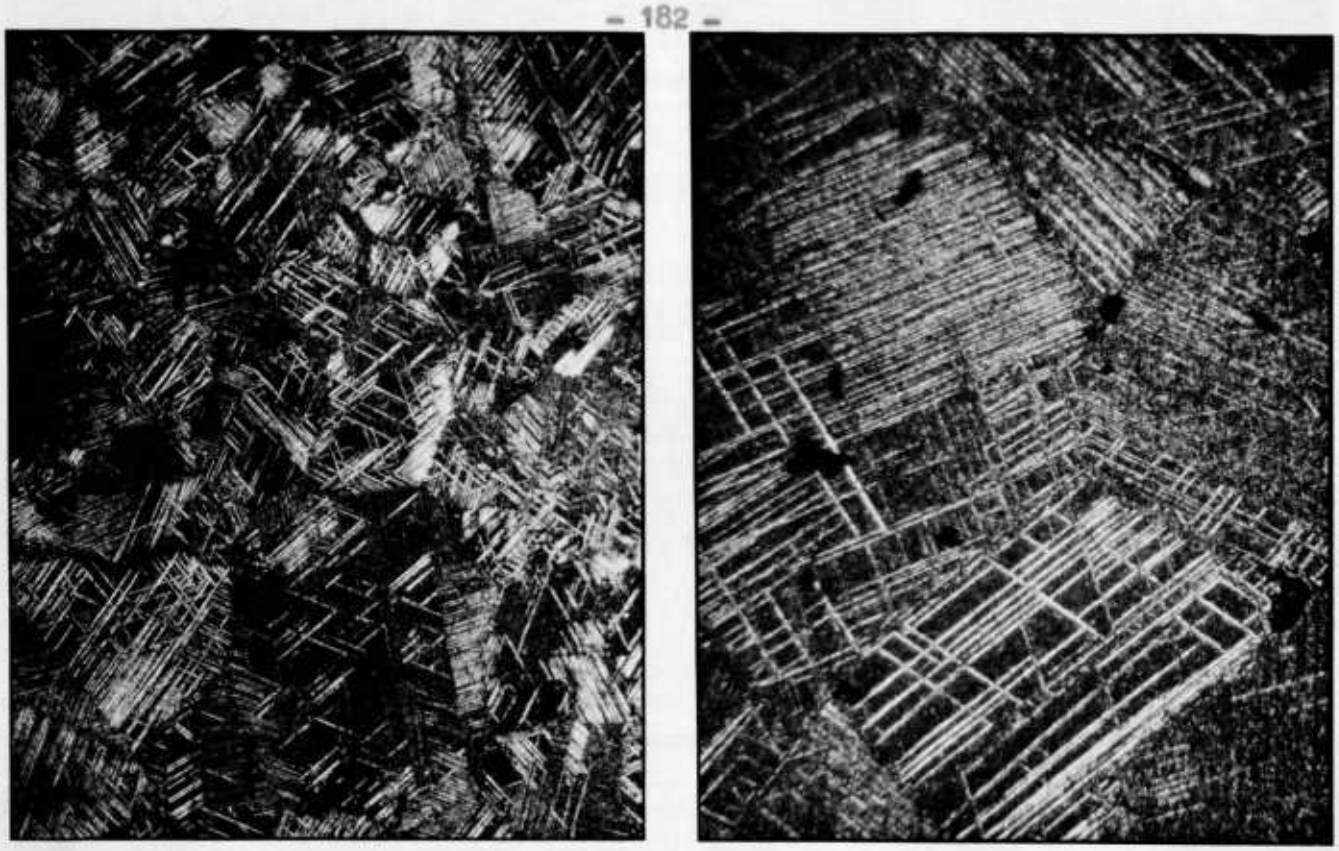


(a) CONVENTIONALLY CAST ALLOY



(b) UNIDIRECTIONALLY SOLIDIFIED ALLOY

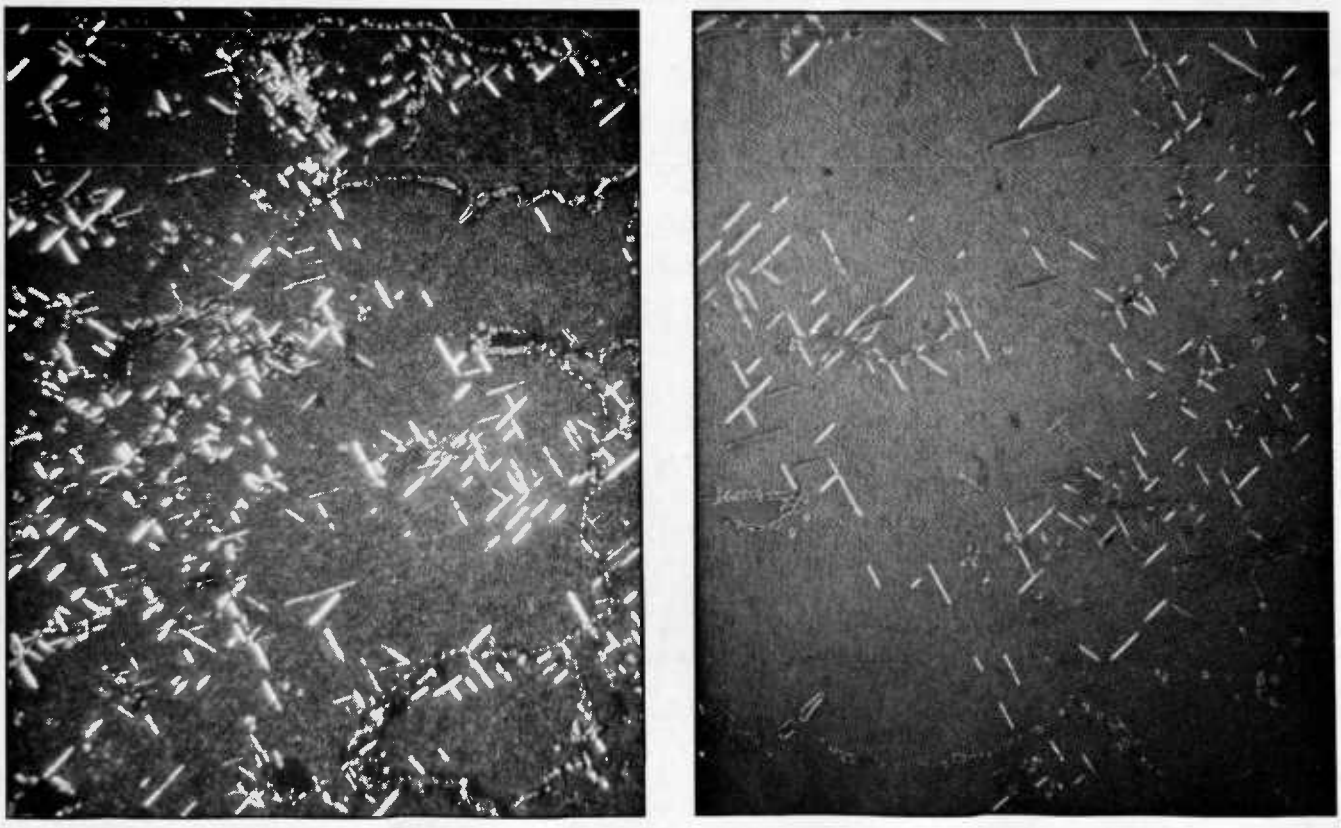
FIG.6 TYPICAL MOULD ASSEMBLIES



100μm

SIGMA PHASE IN NIMONIC 115 ALLOY

25μm



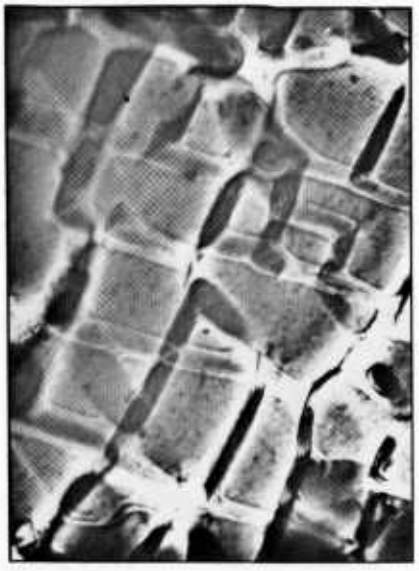
25μm

ACICULAR M_6C PHASE IN MM246 ALLOY

15μm

(POLARISED LIGHT)

FIG.7 OPTICAL MICROSTRUCTURES OF NIMONIC 115 ALLOY BLADE AND MM246 ALLOY CREEP TESTPIECE



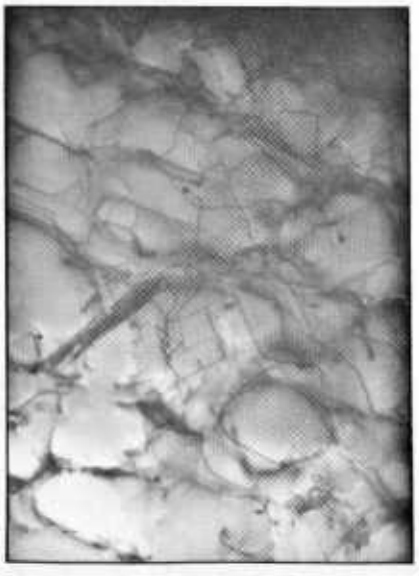
BRIGHT FIELD

1 μm



BRIGHT FIELD

1 μm



BRIGHT FIELD

1 μm

FIG.8 TYPICAL STRUCTURES OF AS-CAST ALLOYS FROM TRANSMISSION ELECTRON MICROSCOPY (1 MeV)



BRIGHT FIELD

0.5μm



BRIGHT FIELD

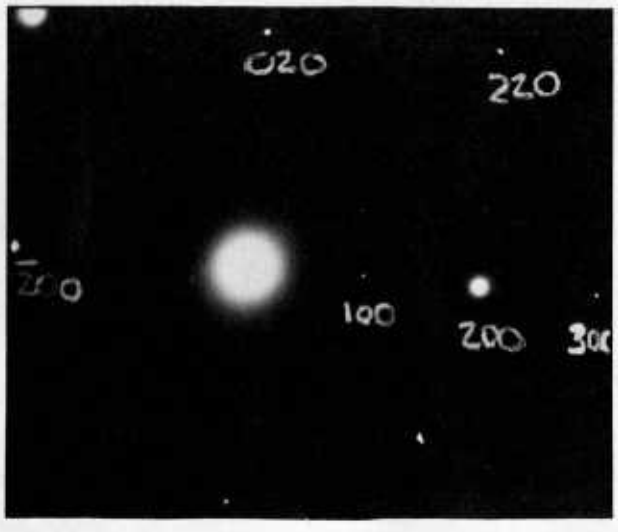
0.25μm



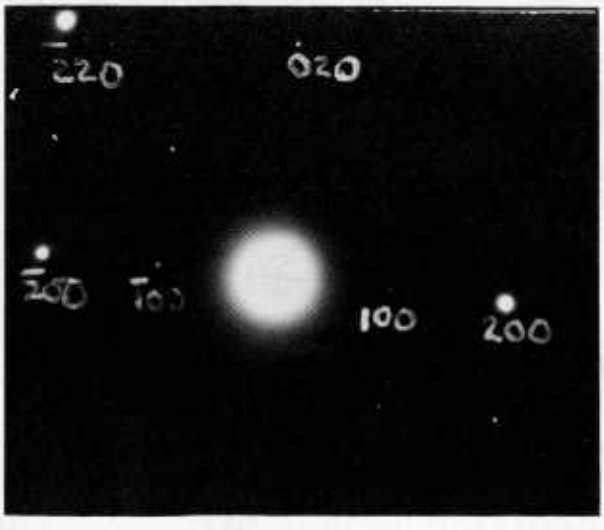
DARK FIELD



DARK FIELD

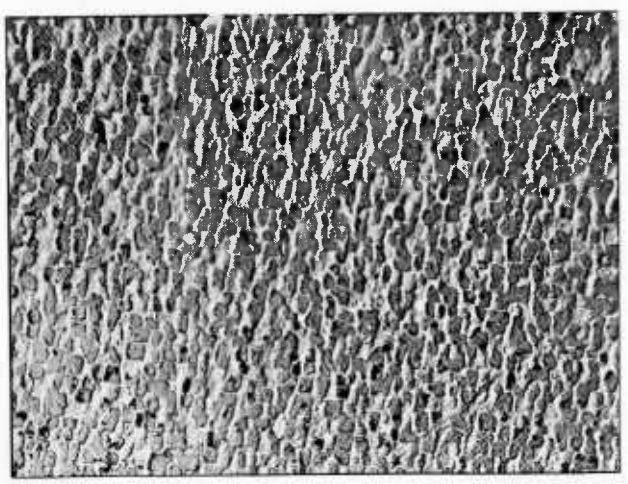


S.A.D.P. $[00\bar{1}]$



S.A.D.P. $[00\bar{1}]$

FIG.9 TYPICAL THIN FOIL MICROSTRUCTURES OF AS-CAST ALLOYS USING 100keV ELECTRON MICROSCOPE

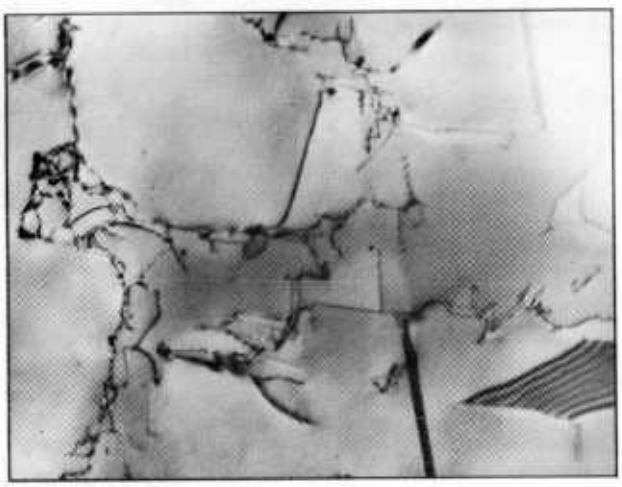


6μm

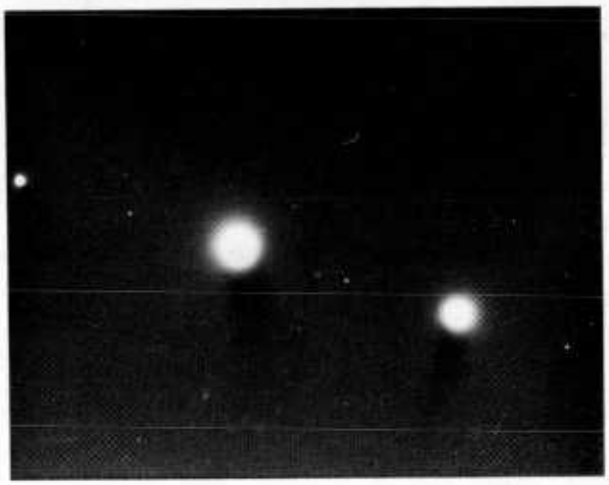


0.5μm

REPLICAS OF R12 ALLOY

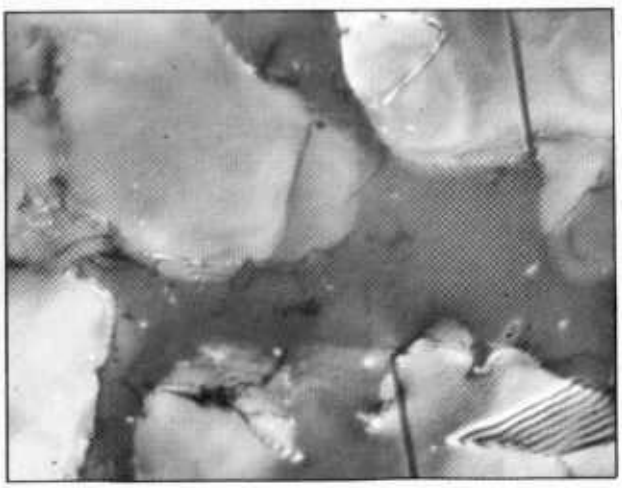


BRIGHT FIELD



S.A.D.P.

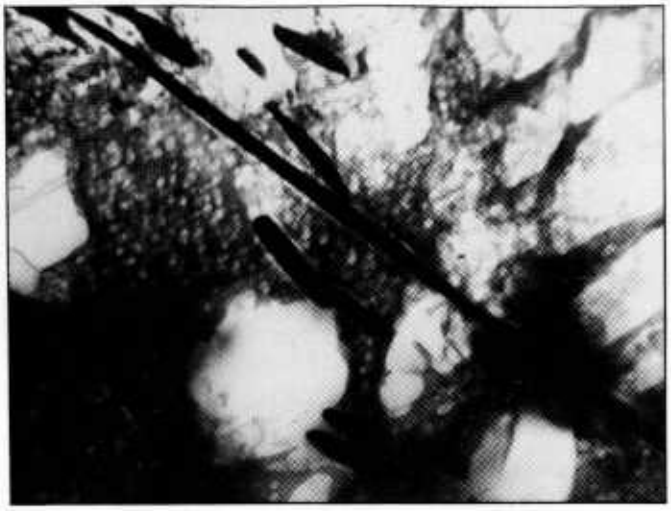
THIN FOIL W47 ALLOY



DARK FIELD

0.5μm

FIG.10 TYPICAL ELECTRON MICROGRAPHS OF THE STRUCTURES OF EXPERIMENTAL ALLOYS AFTER HEAT-TREATMENT FOR 2000h AT 850°C



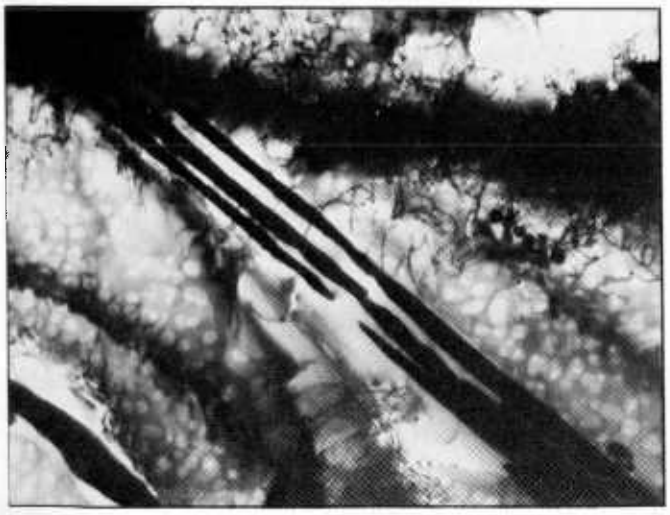
1μm

DARK ACICULAR PHASE IS SIGMA



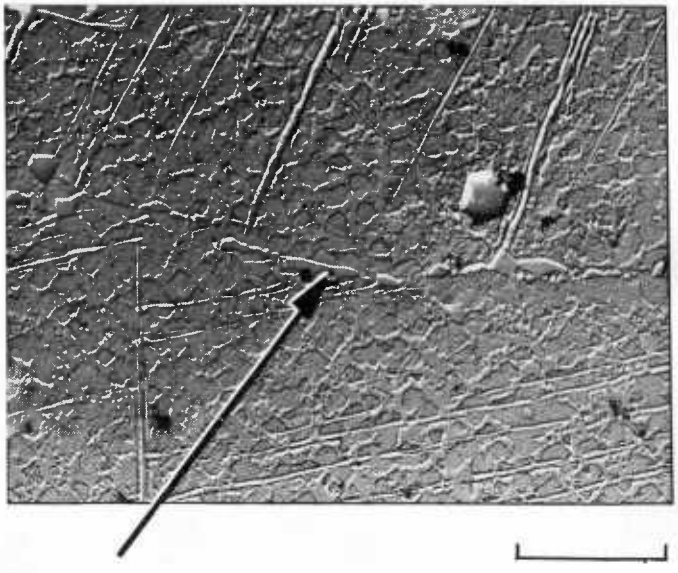
1μm

LIGHT SPEROIDAL AND CUBIC PHASES ARE GAMMA-PRIME



1μm

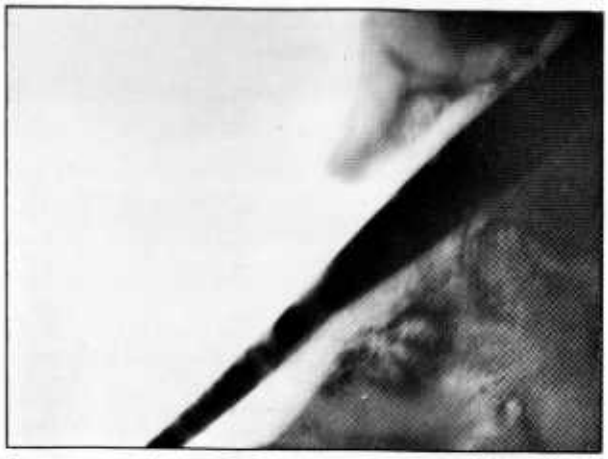
AS ABOVE



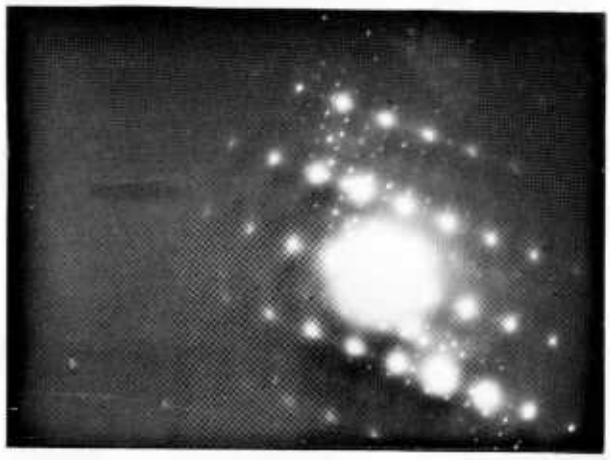
6μm

GRAIN BOUNDARY

FIG.11 TYPICAL ELECTRON MICROGRAPHS SHOWING THE MICROSTRUCTURE OF THE NIMONIC 115 ALLOY BLADE (100keV)



BRIGHTFIELD SIGMA PLATELET 0.3μm



S.A.D.P. [112]



DARKFIELD SIGMA PLATELET 0.3μm



BRIGHT FIELD 2μm



BRIGHT FIELD 1μm



BRIGHT FIELD 0.7μm

FIG.12 NIMONIC 115 ALLOY BLADE STRUCTURE (THIN FOIL) USING 1 MeV MICROSCOPE

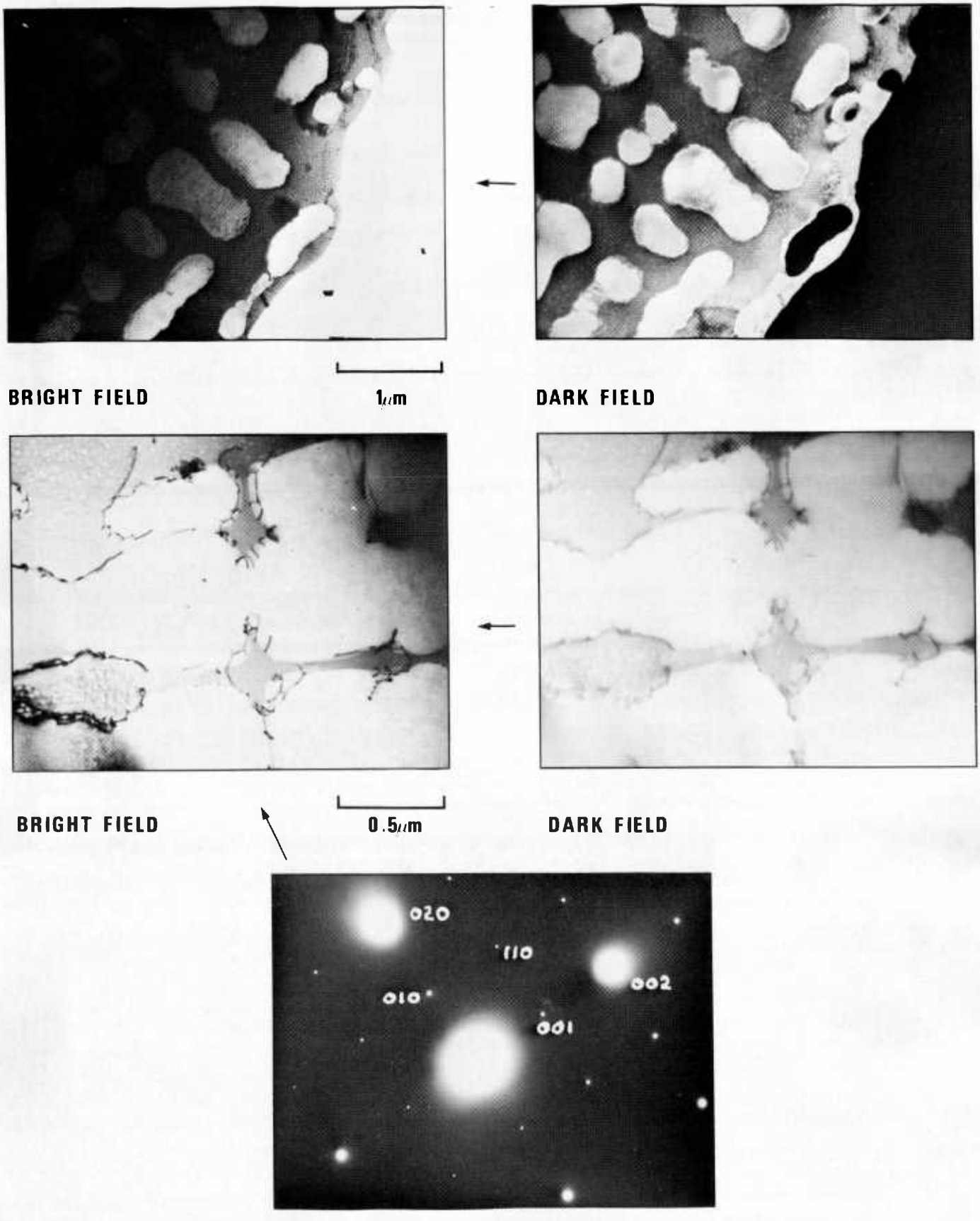
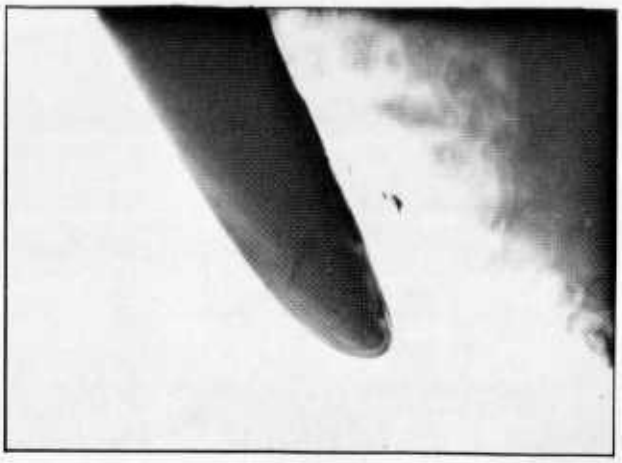


FIG.13 THIN FOIL MICROSTRUCTURE OF MM246 ALLOY TESTPIECE. WATER-QUENCHED AFTER 200h EXPOSURE AT 1050°C



TWO STAGE REPLICA

10μm



BRIGHT FIELD

0.25μm



EXTRACTION REPLICA

3μm



DARK FIELD



THIN FOIL

1μm



S.A.D.P.

$[00\bar{1}]$

FIG.14 ELECTRON MICROGRAPHS OF MM246 SINGLE CRYSTAL AFTER CREEP/RUPTURE TESTING AT 1050°C

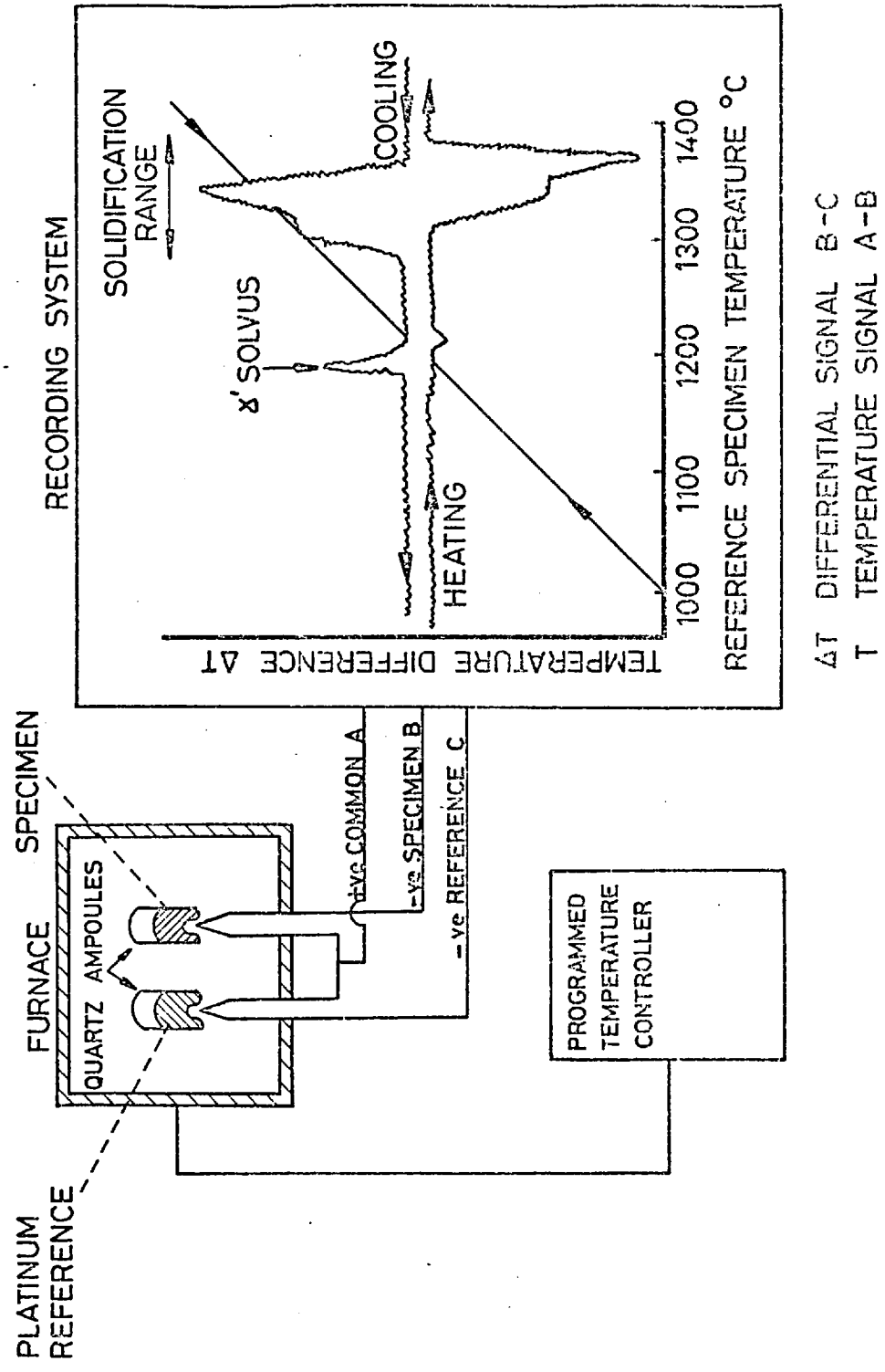


FIG.15 SCHEMATIC DIFFERENTIAL THERMAL ANALYSIS OF A CAST NICKEL SUPERALLOY

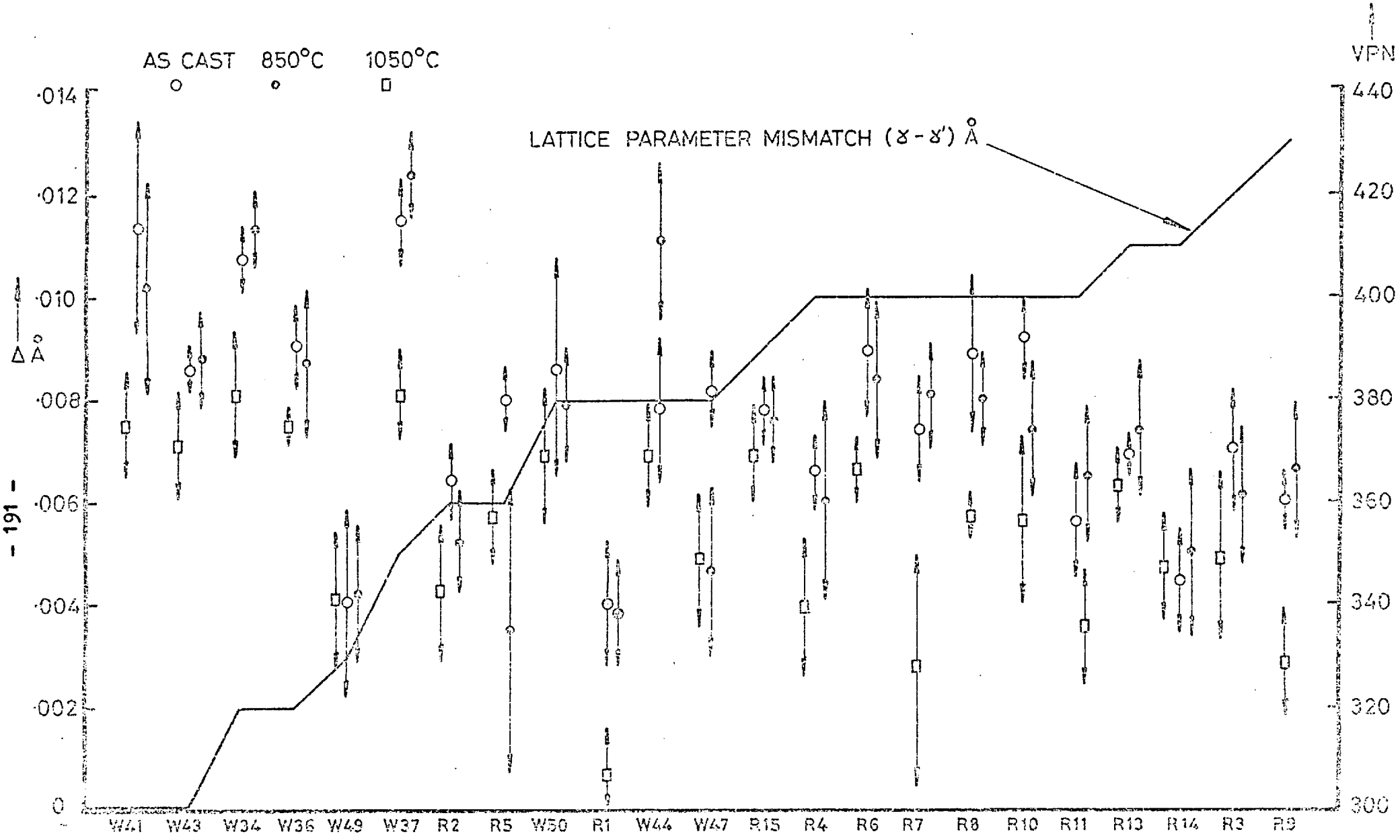


FIG.16 VPN DATA vs LATTICE CONSTANT MISMATCH (γ - γ') Å FOR INDIVIDUAL ALLOYS

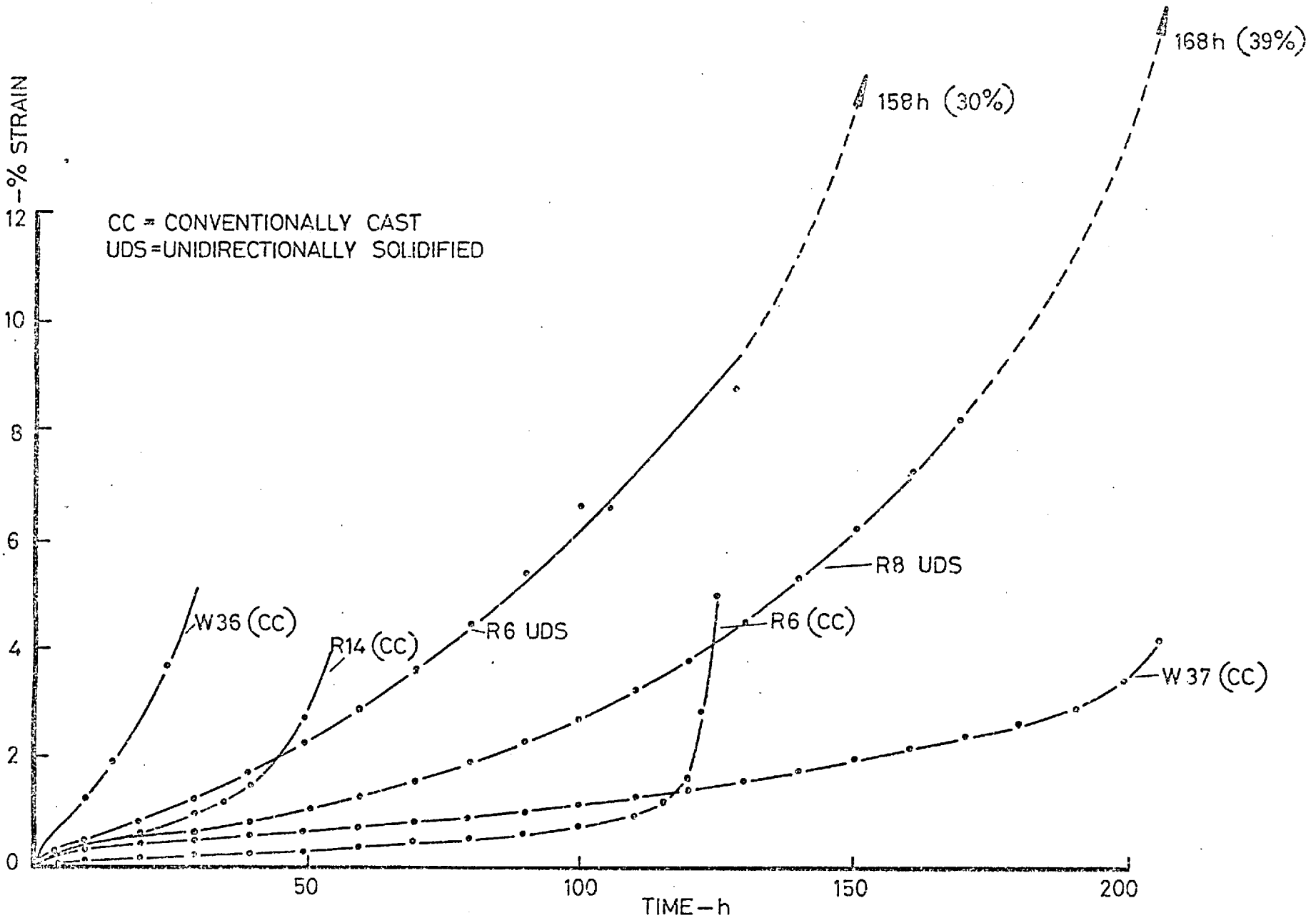


FIG.17 TYPICAL CREEP-RUPTURE CURVES AT 30 tsi / 850 °C

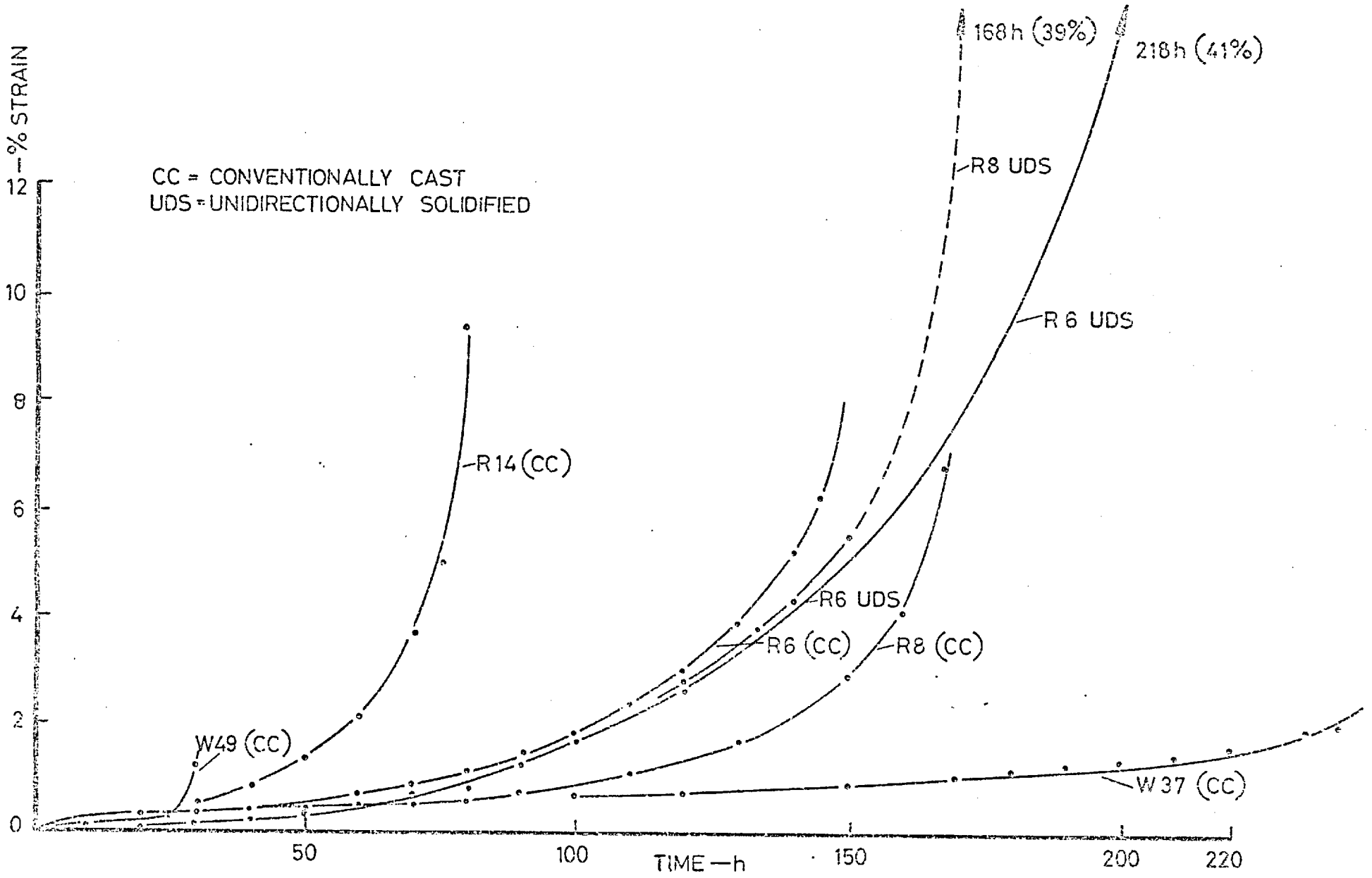


FIG.18 TYPICAL CREEP-RUPTURE CURVES AT 10 tsi / 1000°C

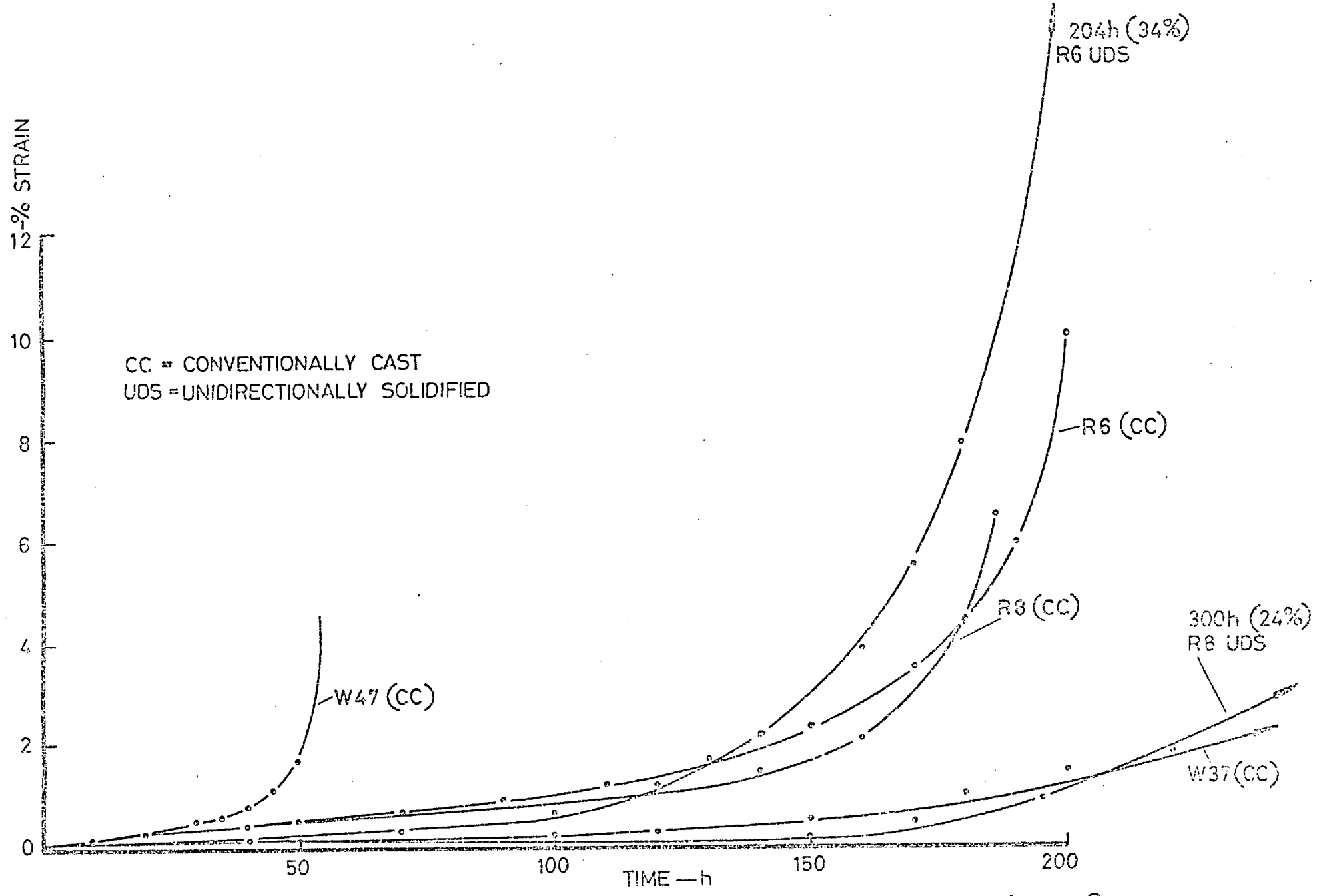


FIG.19 TYPICAL CREEP-RUPTURE CURVES AT 7 tsi /1040°C

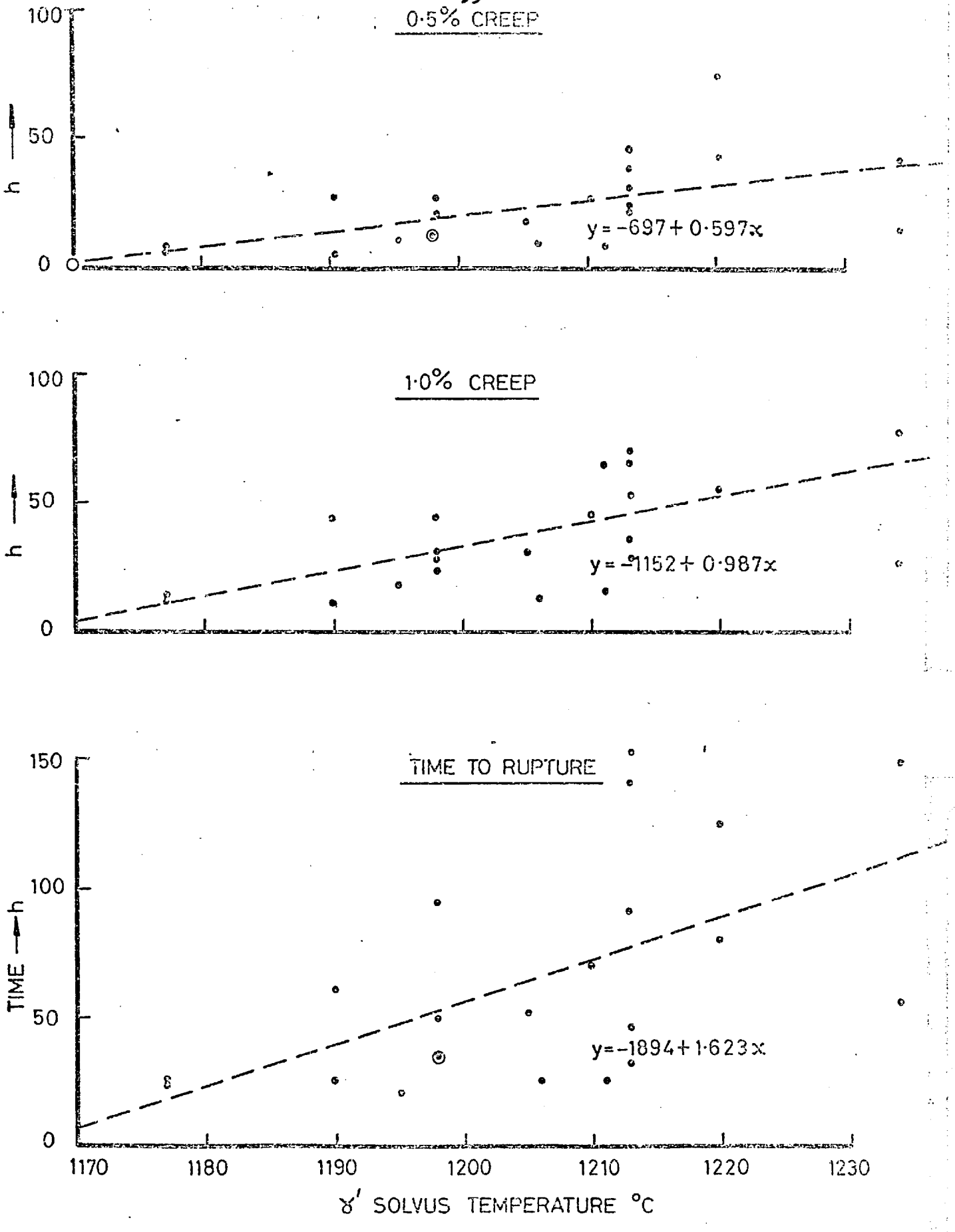


FIG.20 RELATIONSHIP BETWEEN TIMES TO 0·5%, 1% CREEP STRAIN AND TIME TO PRODUCE RUPTURE VERSUS γ' SOLVUS TEMPERATURE AT 30 tsi/850°C

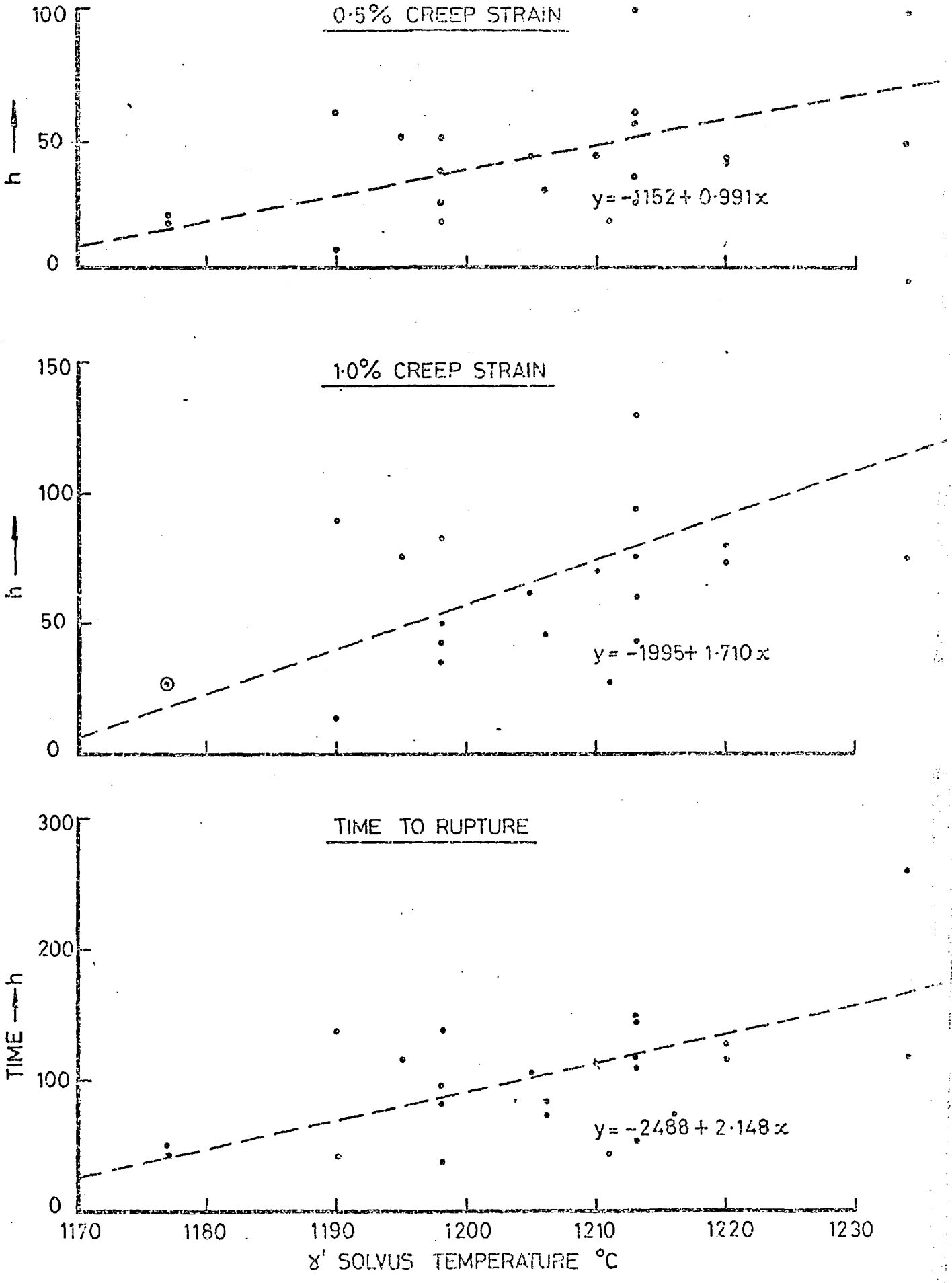


FIG.21 RELATIONSHIP BETWEEN TIMES TO 0·5%, 1% CREEP STRAIN AND TIME TO PRODUCE RUPTURE VERSUS γ' SOLVUS TEMPERATURE AT 10 tsi/1000 °C

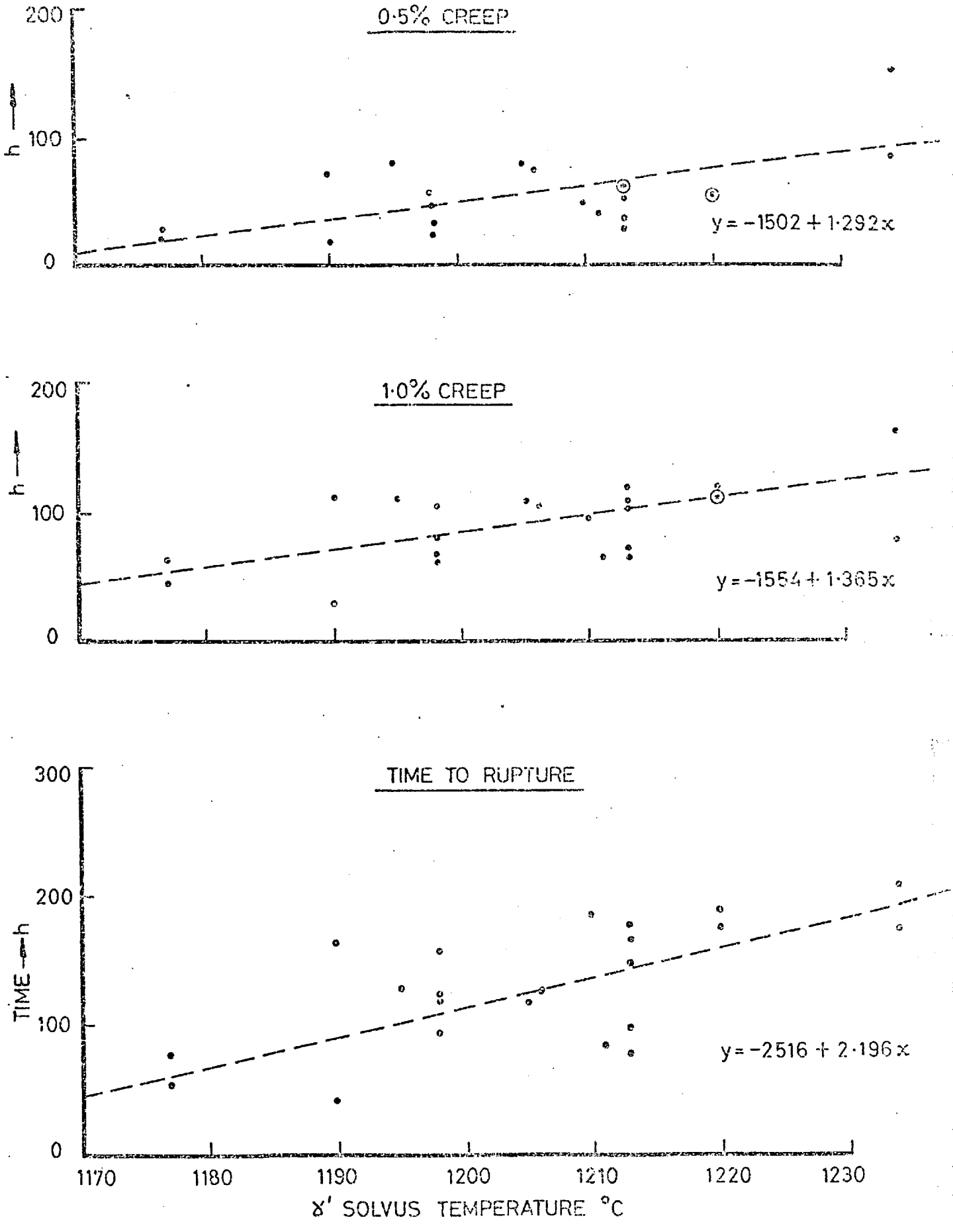


FIG.22 RELATIONSHIP BETWEEN TIMES TO 0·5%, 1% CREEP STRAIN AND TIME TO PRODUCE RUPTURE VERSUS γ′ SOLVUS TEMPERATURE AT 7 tsi/1040°C

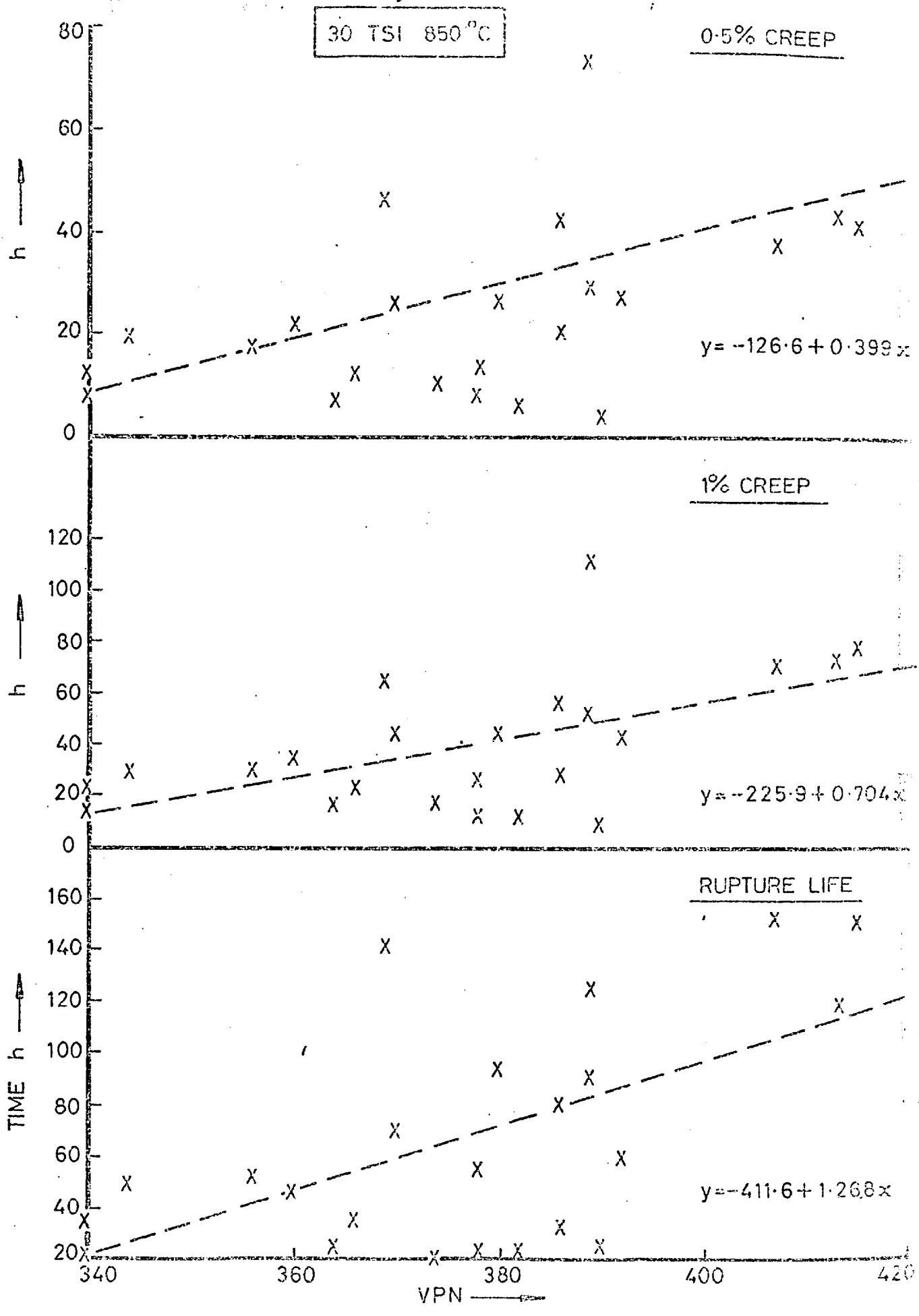


FIG.23 RELATIONSHIP BETWEEN TIME TO PRODUCE 0·5%,1% CREEP STRAIN AND RUPTURE AT 850°C VERSUS 'AS-CAST' HARDNESS

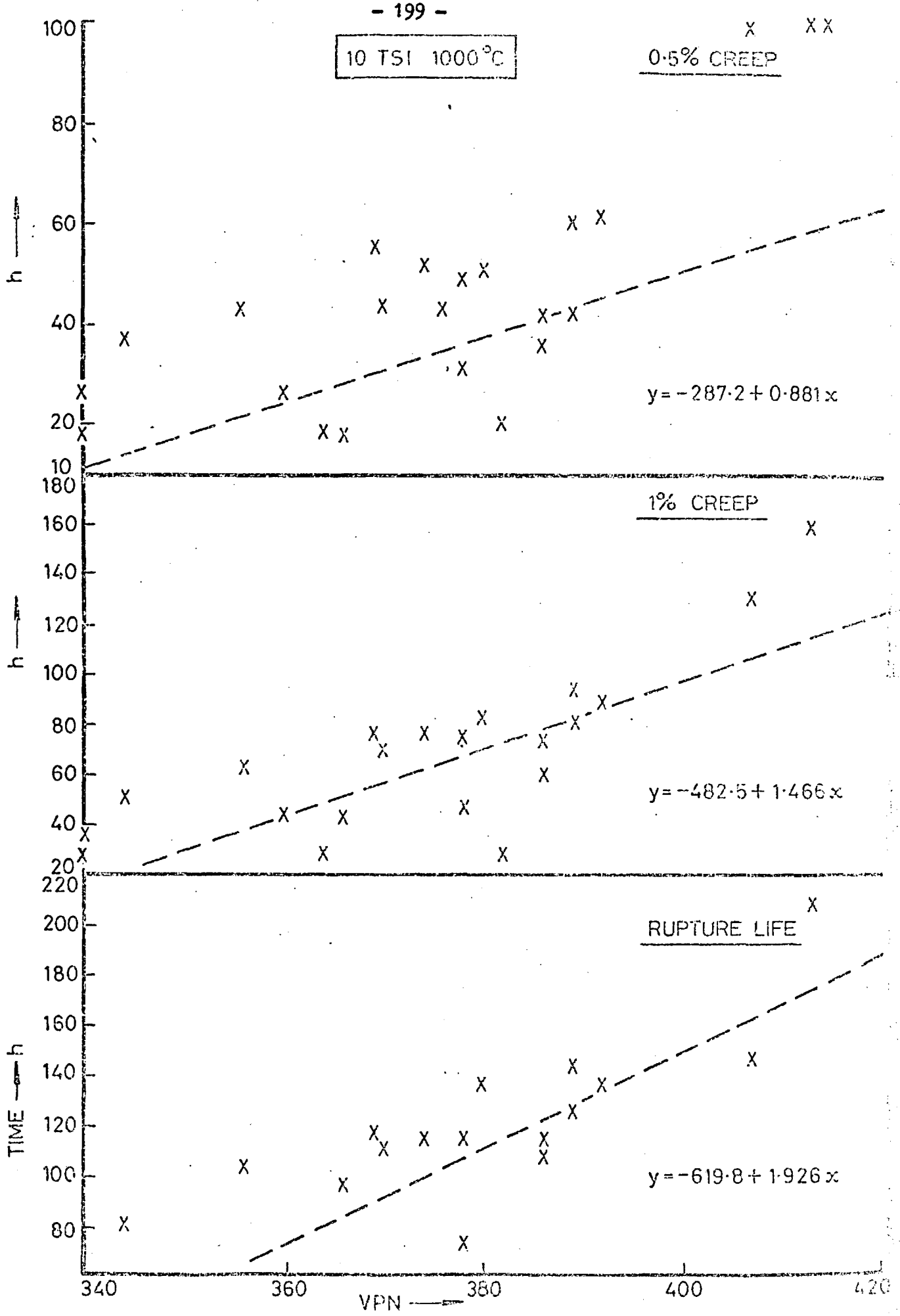


FIG.24 RELATIONSHIP BETWEEN TIME TO PRODUCE 0·5%, 1% CREEP STRAIN AND RUPTURE AT 1000°C VERSUS 'AS-CAST' HARDNESS

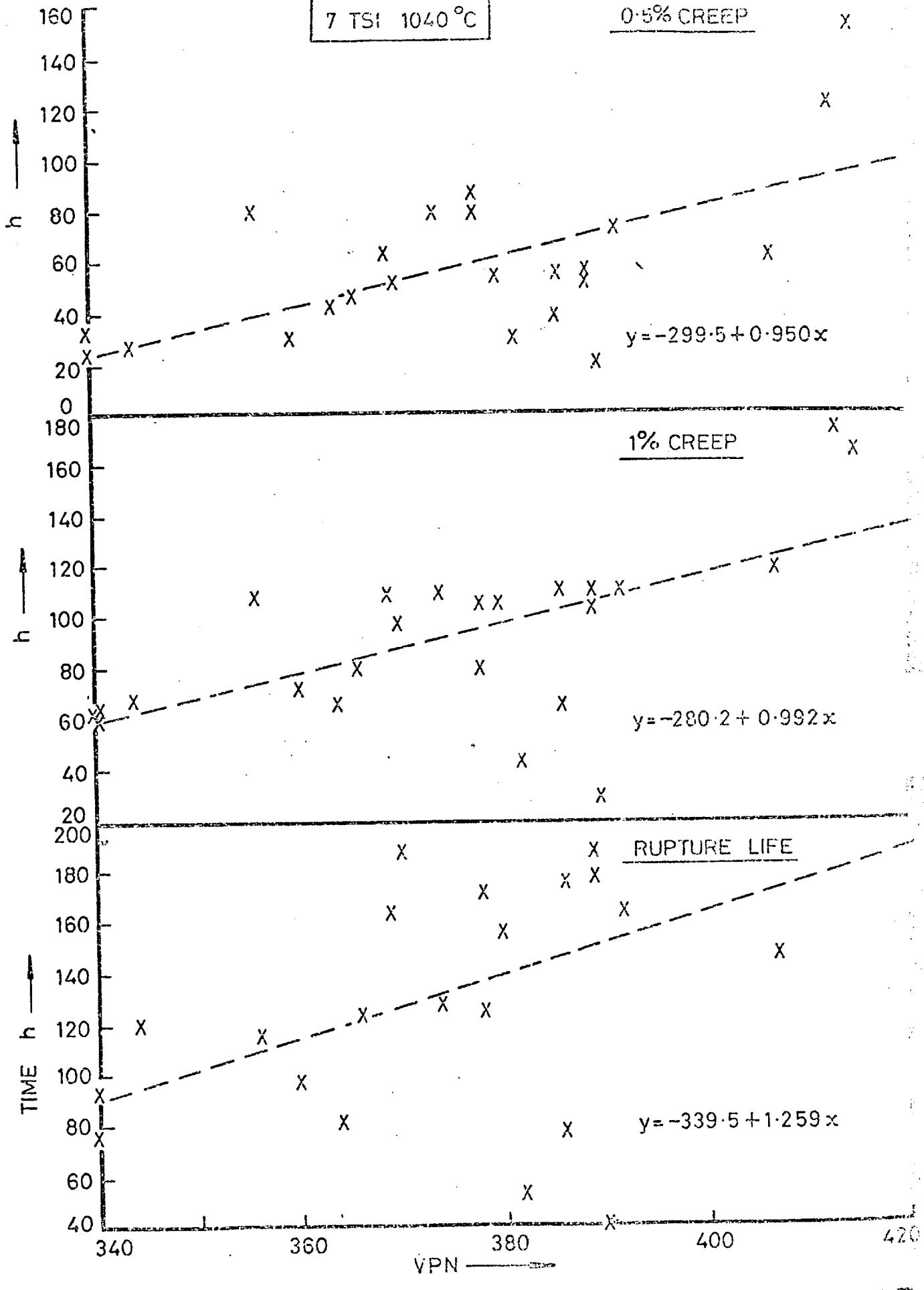


FIG.25 RELATIONSHIP BETWEEN TIME TO PRODUCE 0·5%, 1% CREEP STRAIN AND RUPTURE AT 1040°C VERSUS 'AS-CAST' HARDNESS



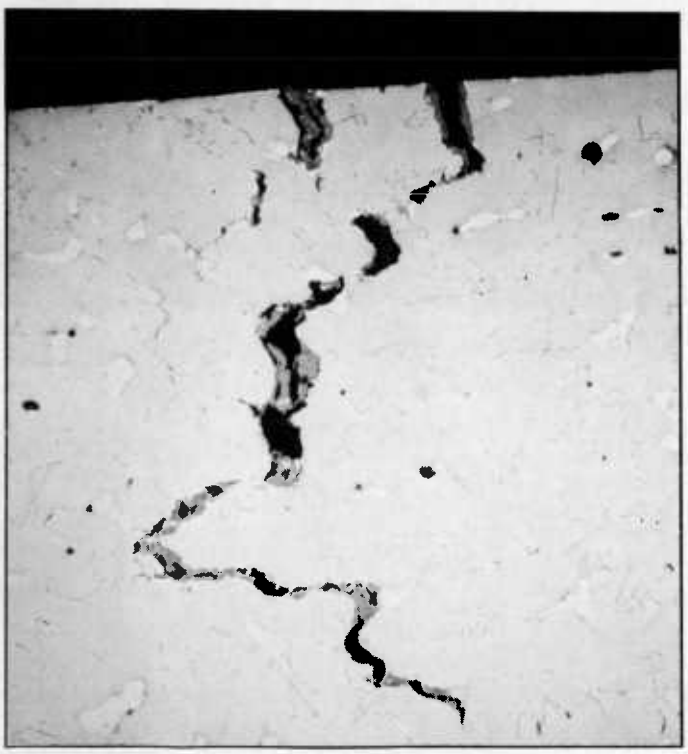
R10 ALLOY

50μm



R15 ALLOY

50μm



W50 ALLOY

100μm



W44 ALLOY

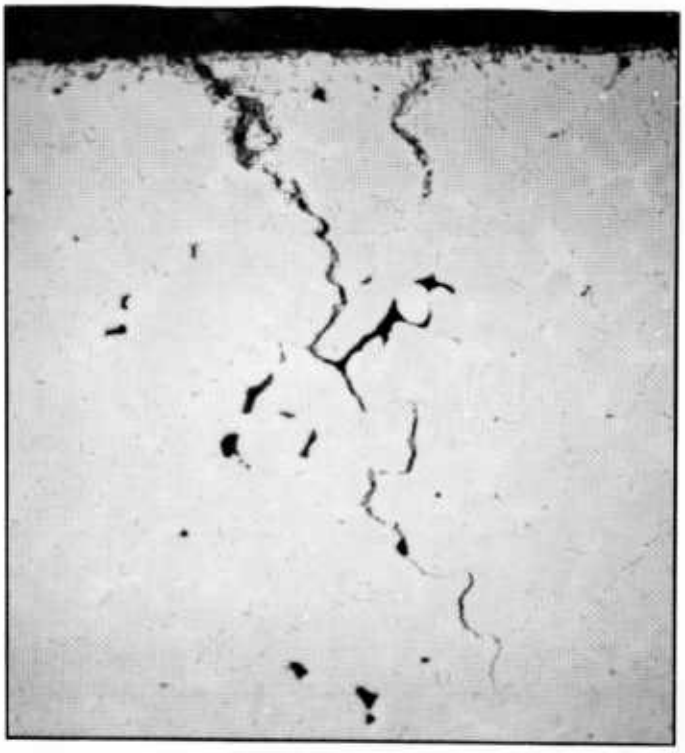
50μm

FIG.26 TYPICAL OPTICAL MICROGRAPHS SHOWING MICROCRACKS IN CONVENTIONALLY-CAST ALLOYS AFTER CREEP-RUPTURE TESTING AT 30tsi/850°C



W37 ALLOY

100μm



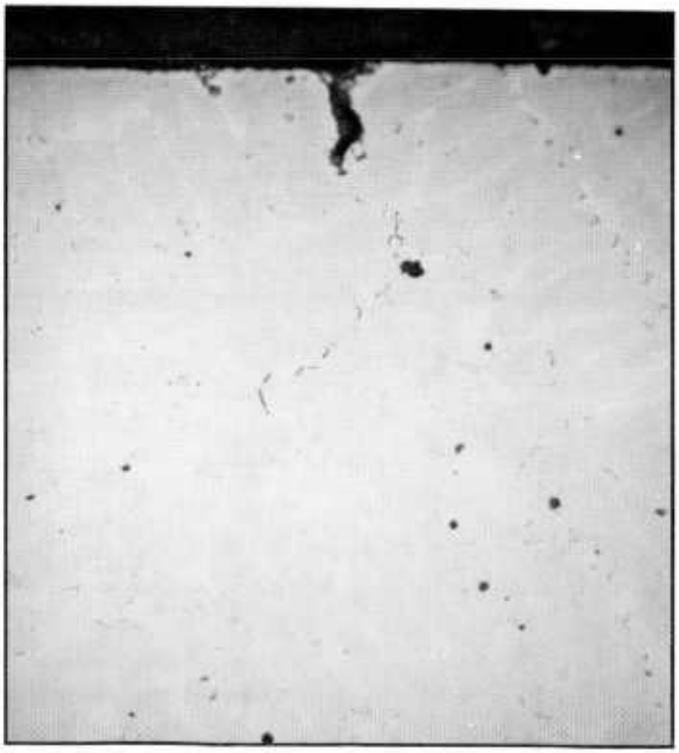
W50 ALLOY

100μm



R7 ALLOY

100μm



R13 ALLOY

50μm

FIG.27 TYPICAL MICROGRAPHS SHOWING MICROCRACKS IN CONVENTIONALLY-CAST ALLOYS AFTER CREEP-RUPTURE TESTING AT 10tsi/1000°C



W37 ALLOY

50μm



W47 ALLOY

100μm



W44 ALLOY

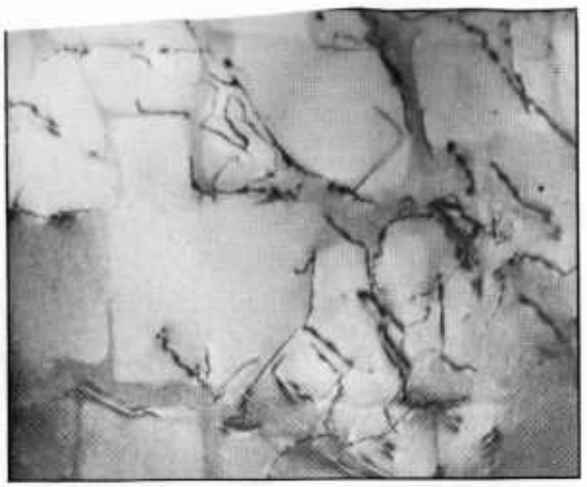
100μm



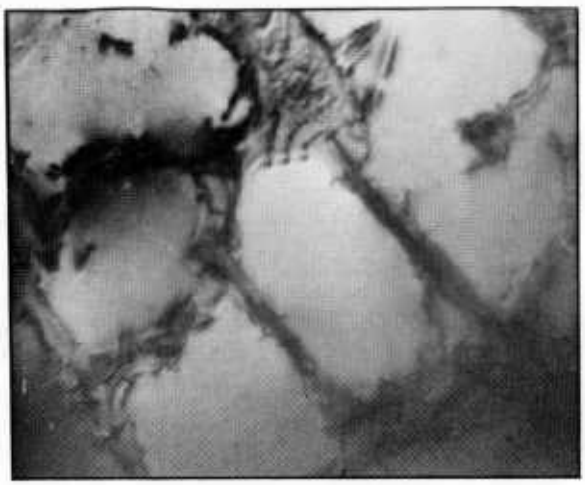
R8 ALLOY

100μm

FIG.28 TYPICAL OPTICAL MICROGRAPHS SHOWING MICROCRACKS IN CONVENTIONALLY-CAST ALLOYS AFTER CREEP-RUPTURE TESTING AT 7tsi/1040°C



B/F 1μm



B/F 0.5μm

(a) DEFORMED 0.2%



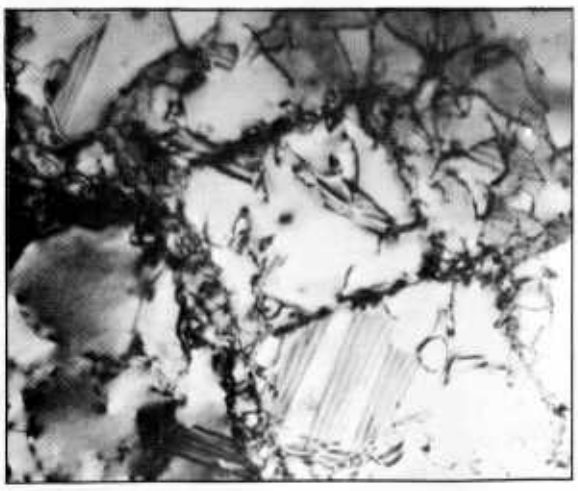
B/F 0.5μm



B/F 0.5μm

(b) FRACTURED

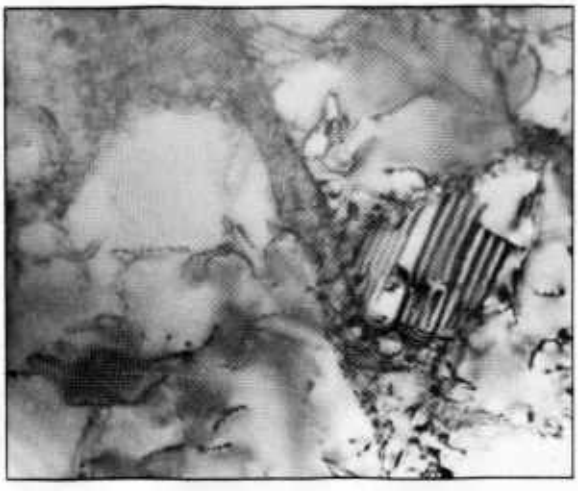
FIG.29 THIN FOIL MICROSTRUCTURES OF R8 ALLOY TENSILE TESTED AT ROOM TEMPERATURE



B/F

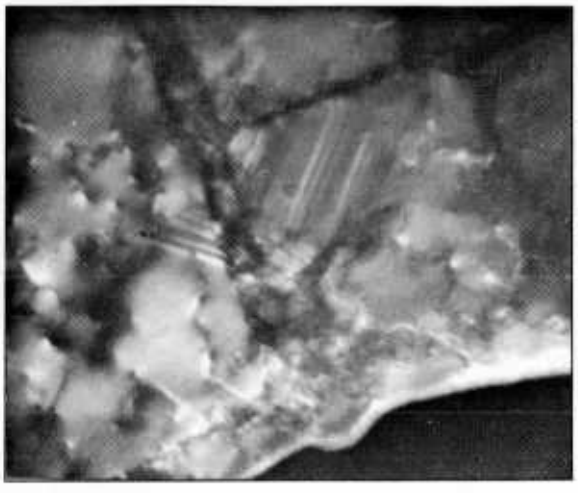
0.25μm

TILT
14°



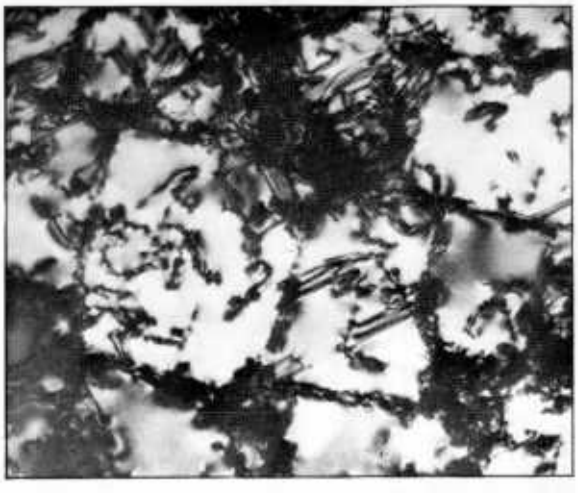
B/F

0.25μm



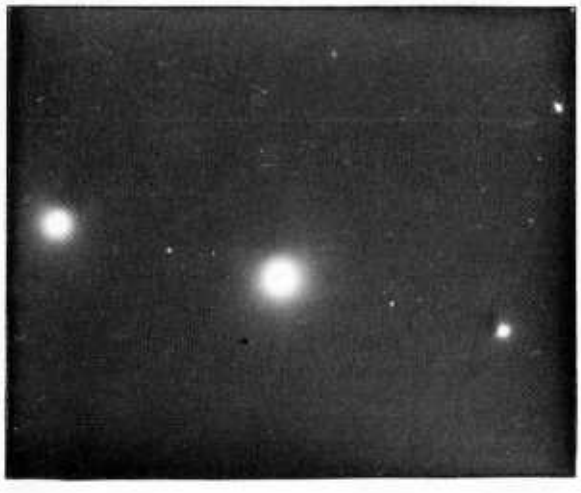
D/F

0.25μm



B/F

0.5μm



SADP

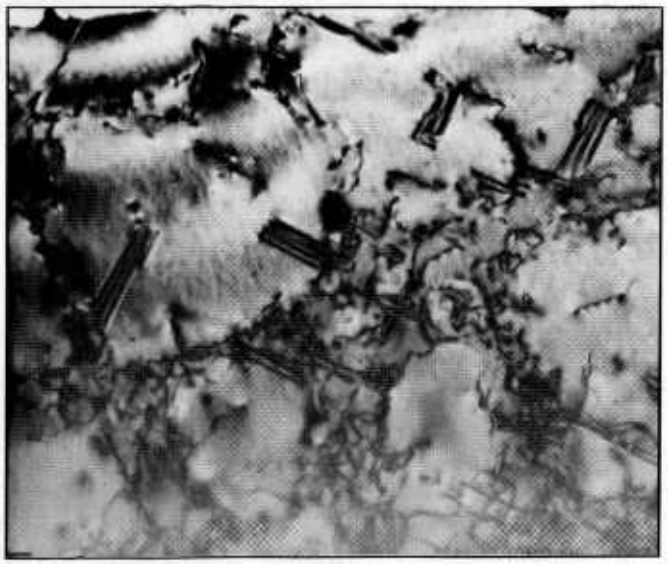
[00$\bar{1}$]



SADP

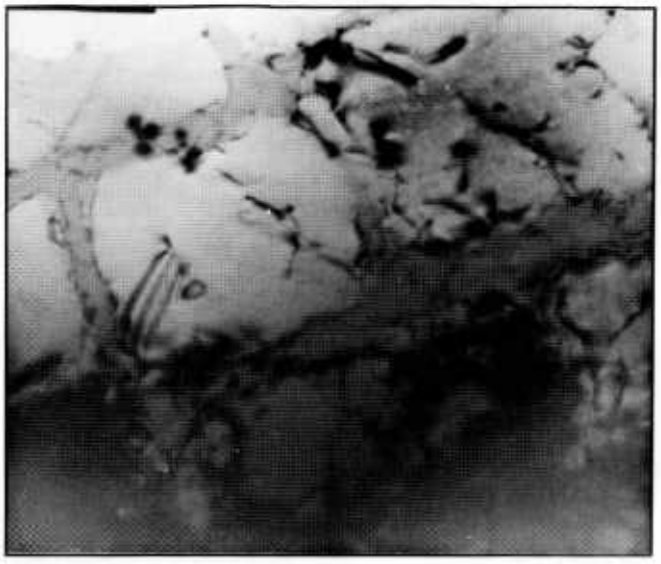
[$\bar{1}$10]

FIG.30 THIN FOIL MICROSTRUCTURES OF R6 ALLOY FRACTURED IN A TENSILE TEST AT 750°C



B/F

0.25μm



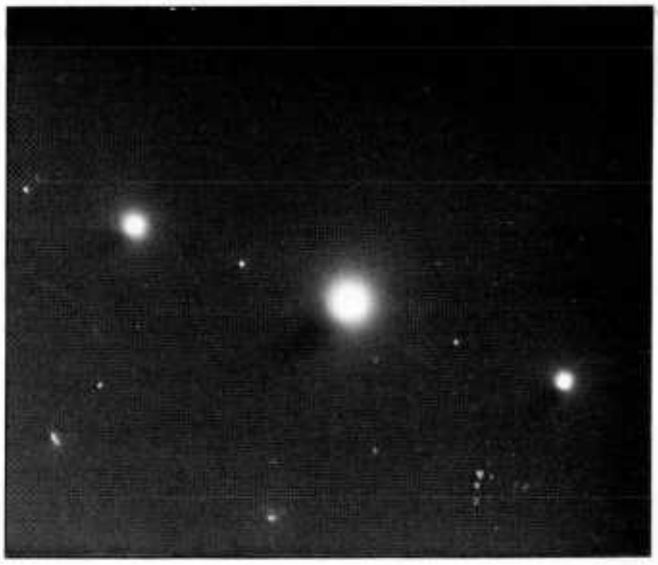
D/F

0.25μm



B/F

0.25μm



SADP

[00$\bar{1}$]

FIG.31 THIN FOIL MICROSTRUCTURES OF R6 ALLOY FRACTURED AFTER CREEP TESTING AT 760°C



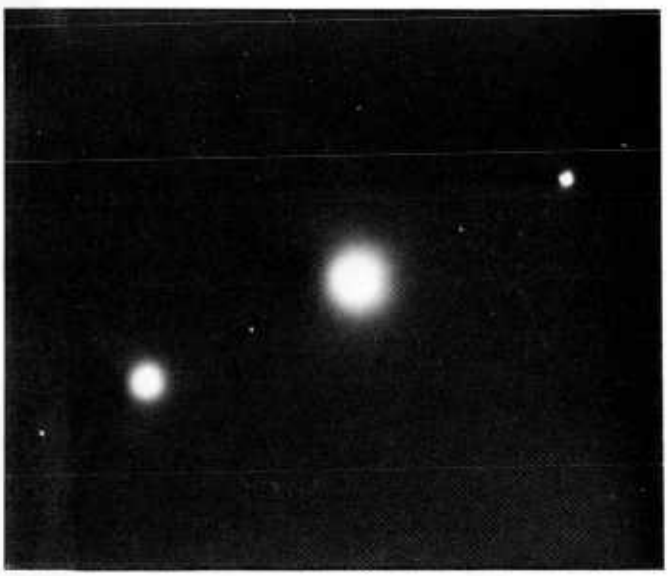
B/F

0.5μm



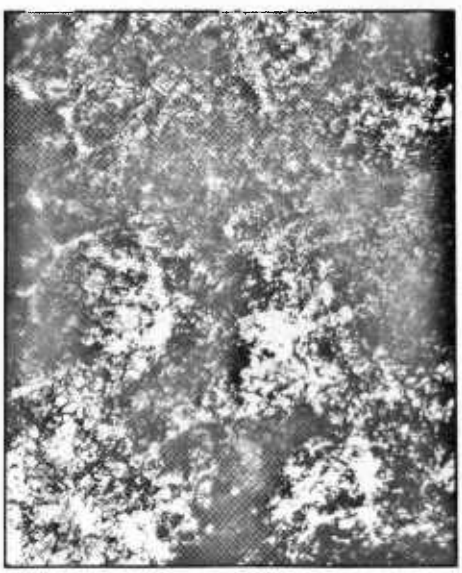
D/F

0.5μm



SADP

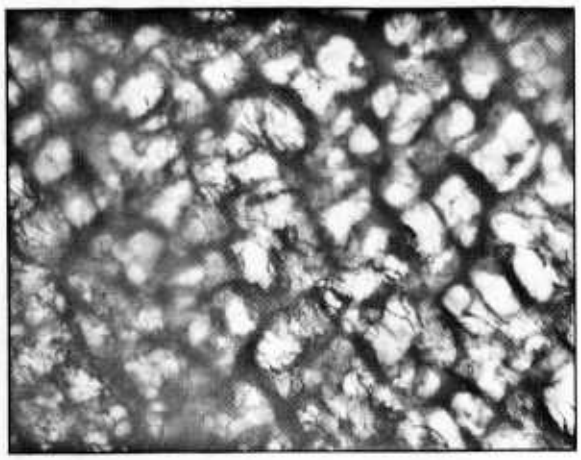
[$\bar{1}$10]



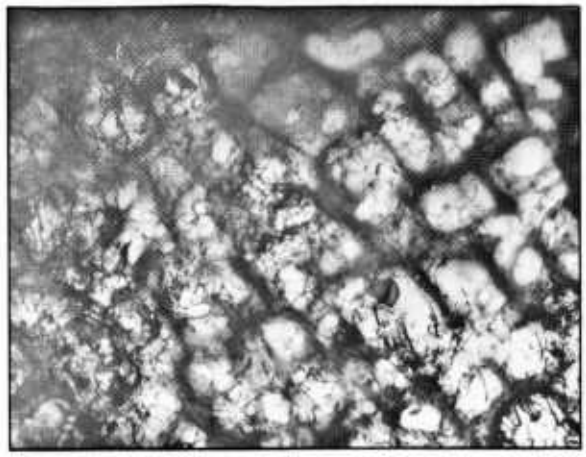
B/F

1μm

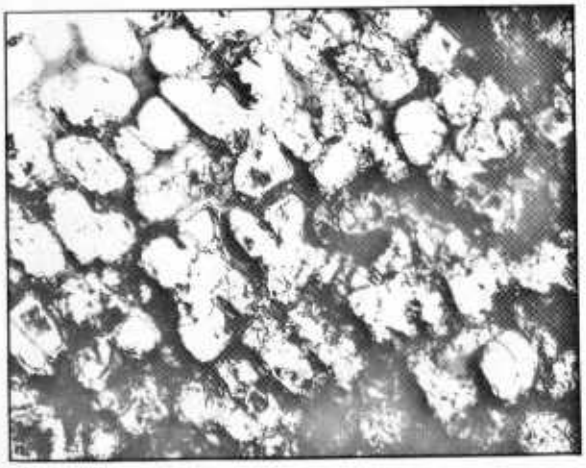
FIG.32 THIN FOIL MICROSTRUCTURES OF R8 ALLOY FRACTURED IN A CREEP-RUPTURE TEST AT 760°C



B/F 2μm



B/F 2μm



B/F 2μm



SADP [$\bar{1}$10]

FIG.33 THIN FOIL MICROSTRUCTURES OF W36 ALLOY CREEP-RUPTURE TESTED AT 850°C

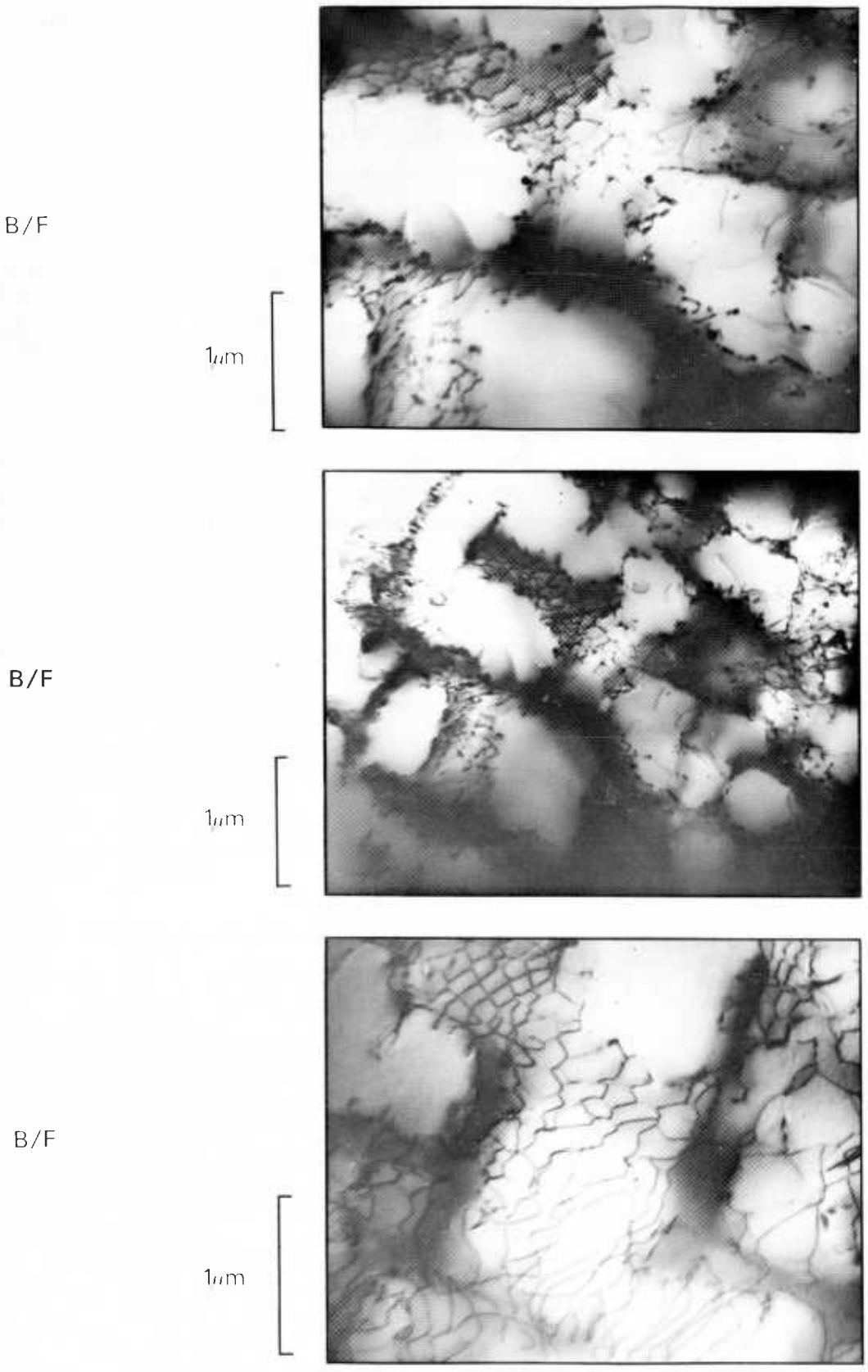


FIG.34 THIN FOIL MICROSTRUCTURES OF R8 ALLOY DEFORMED 0.3% IN A CREEP TEST AT 1000°C

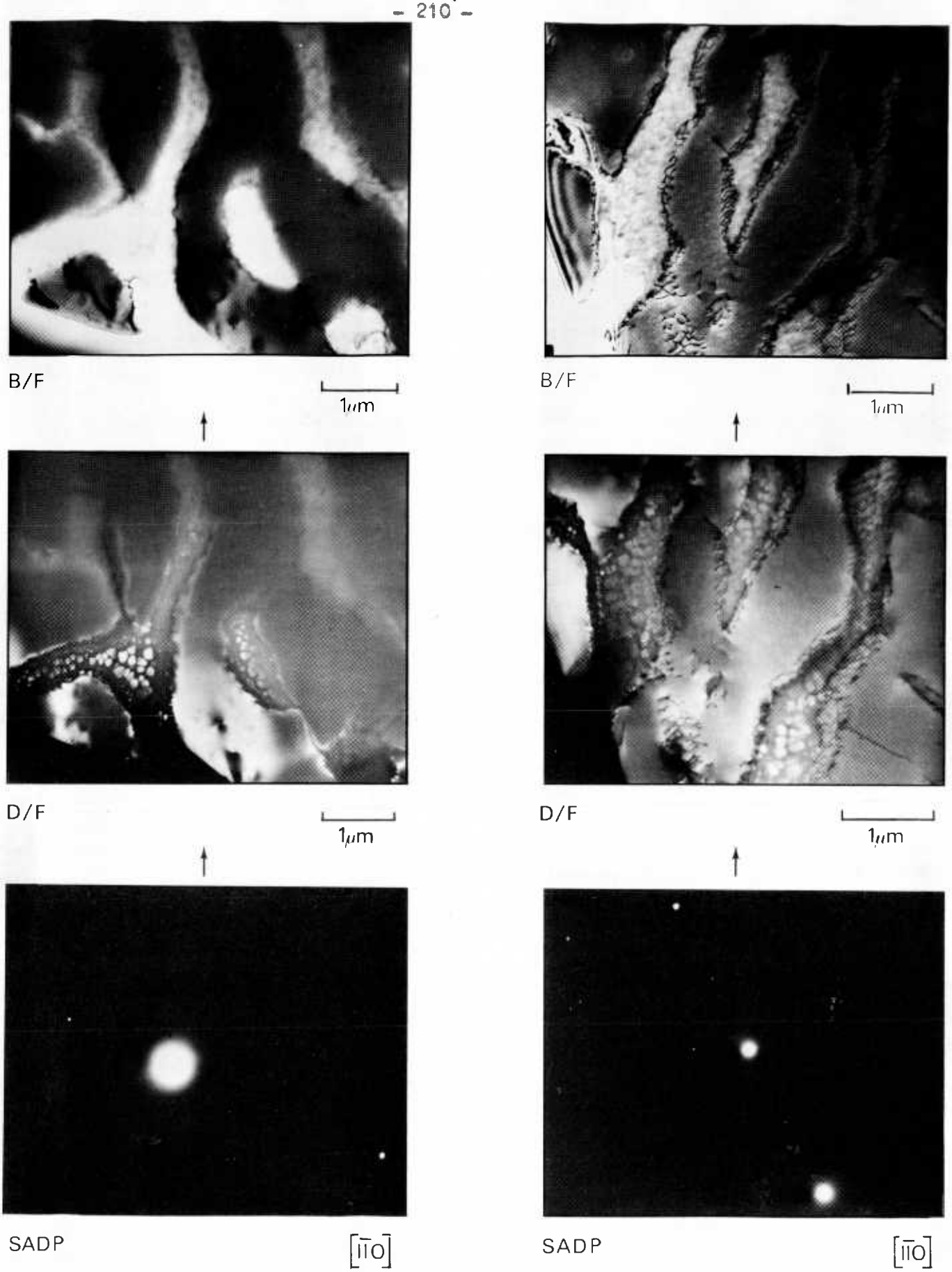
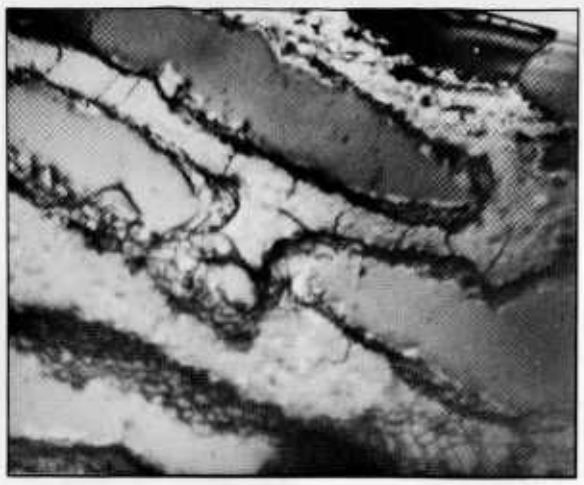
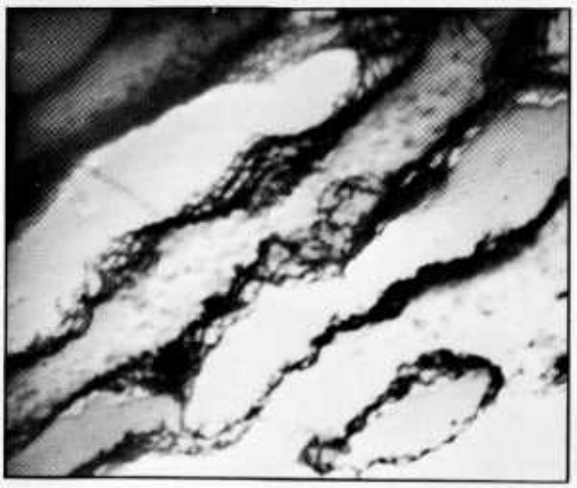


FIG.35 THIN FOIL MICROSTRUCTURES OF R6 ALLOY CREEP TESTED AT 1040°C(LONGITUDINAL SECTIONS FROM GAUGE LENGTH)



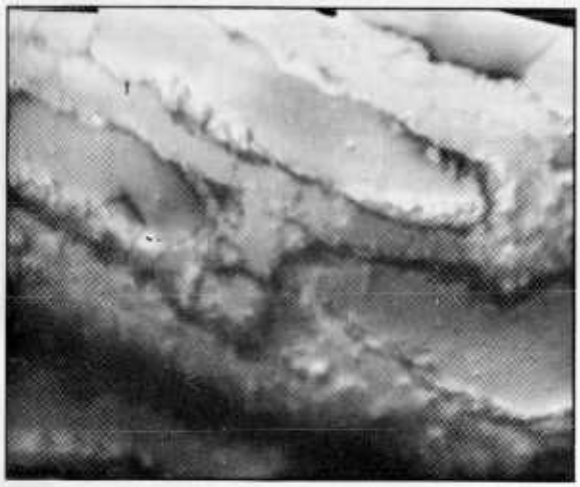
B/F

0.5μm



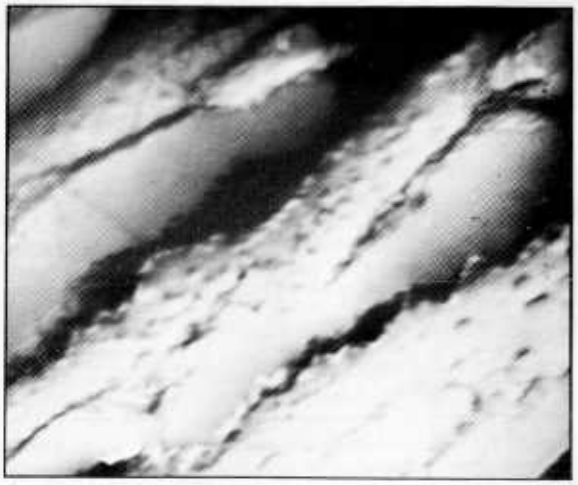
B/F

0.5μm



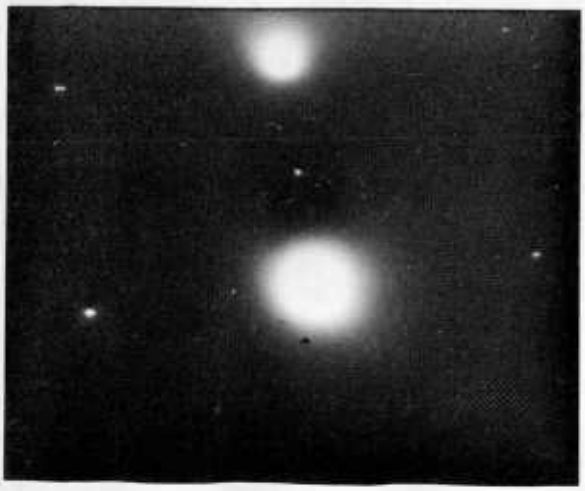
D/F

0.5μm



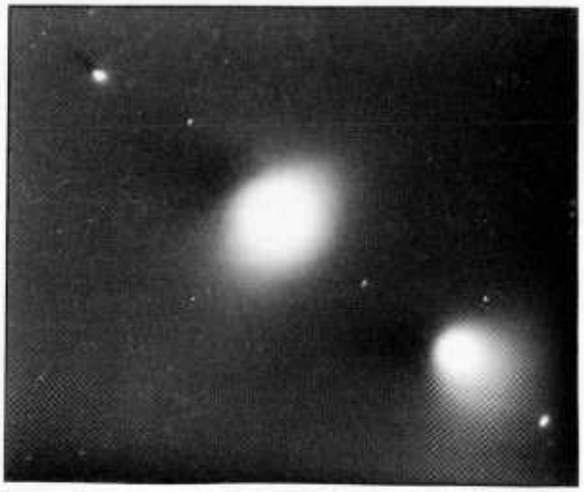
D/F

0.5μm



SADP

$[00\bar{1}]$



SADP

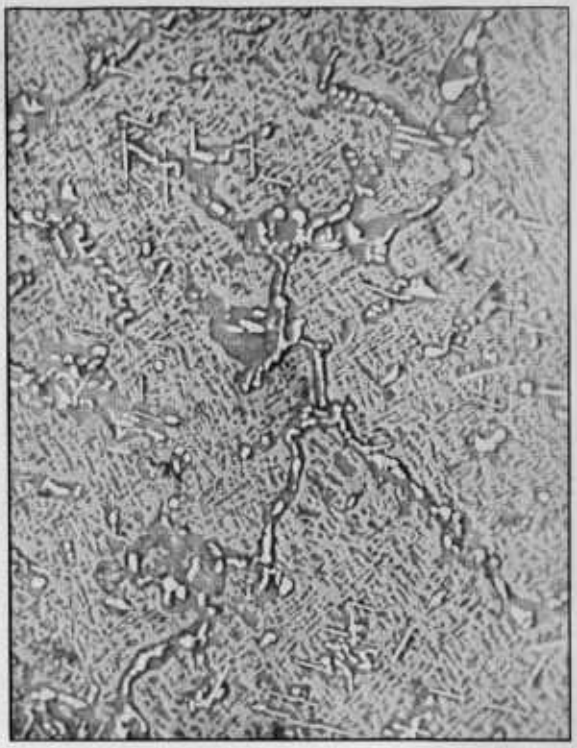
$[1\bar{1}0]$

FIG.36 THIN FOIL MICROSTRUCTURES OF MM246 ALLOY SINGLE CRYSTAL CREEP-RUPTURE TESTED AT 1040°C (LONGITUDINAL SECTIONS)



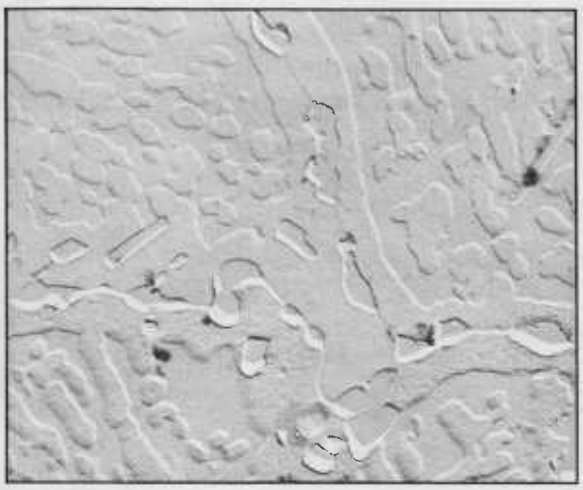
REPLICA

5μm



SEM

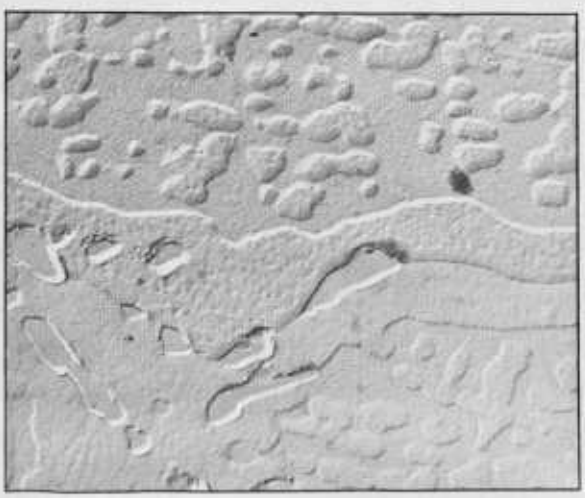
15μm



REPLICA

5μm





REPLICA

2.5μm

10μm

FIG.37 TYPICAL GRAIN BOUNDARY REGIONS OF MM246 ALLOY AFTER 200h HEAT-TREATMENT AT 1050°C

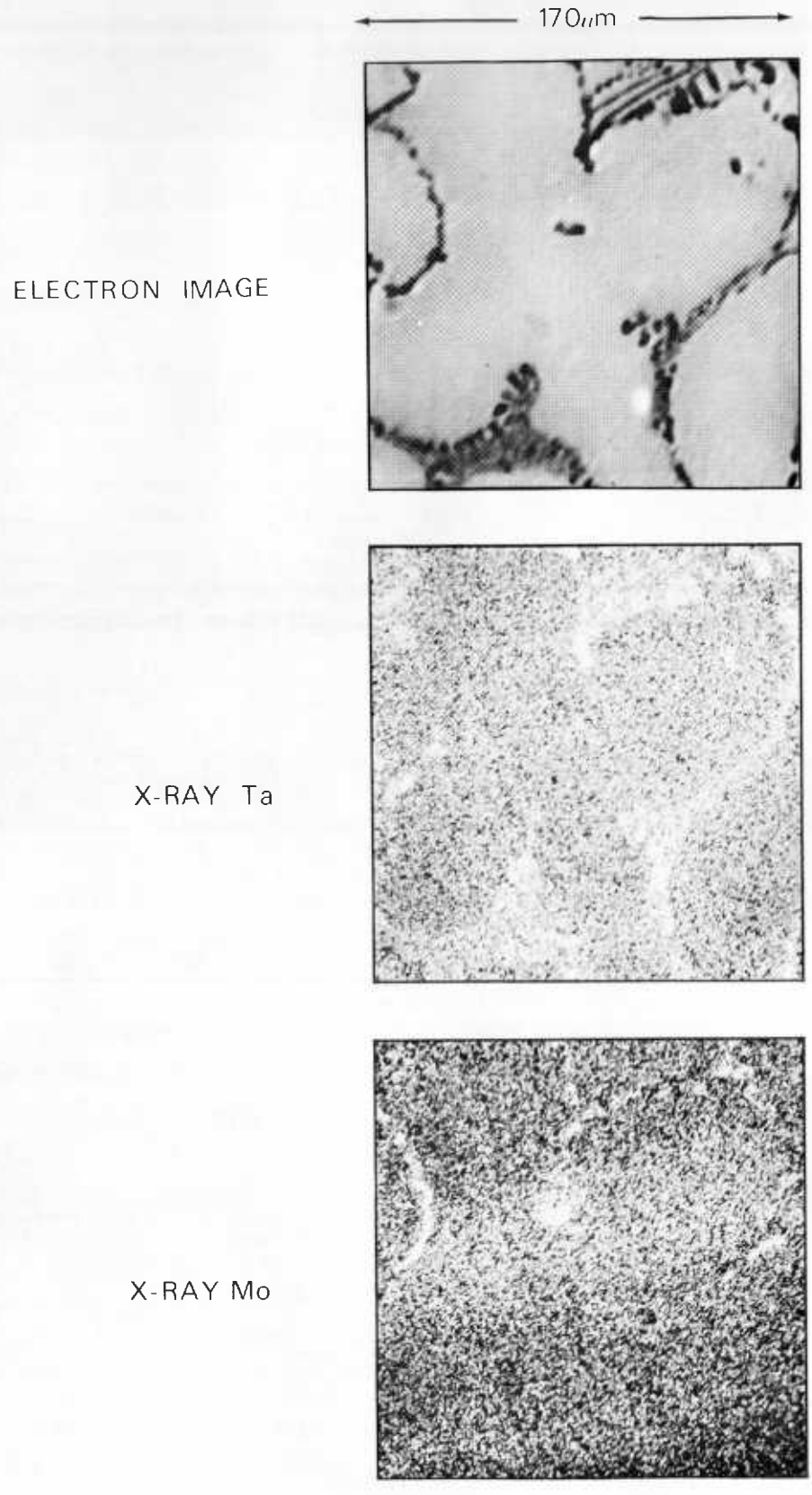


FIG.38 TYPICAL APPEARANCE OF DENDRITIC REGION OF W44 ALLOY CREEP-RUPTURE TESTED AT 1000°C AS REVEALED BY E.P.M.A.

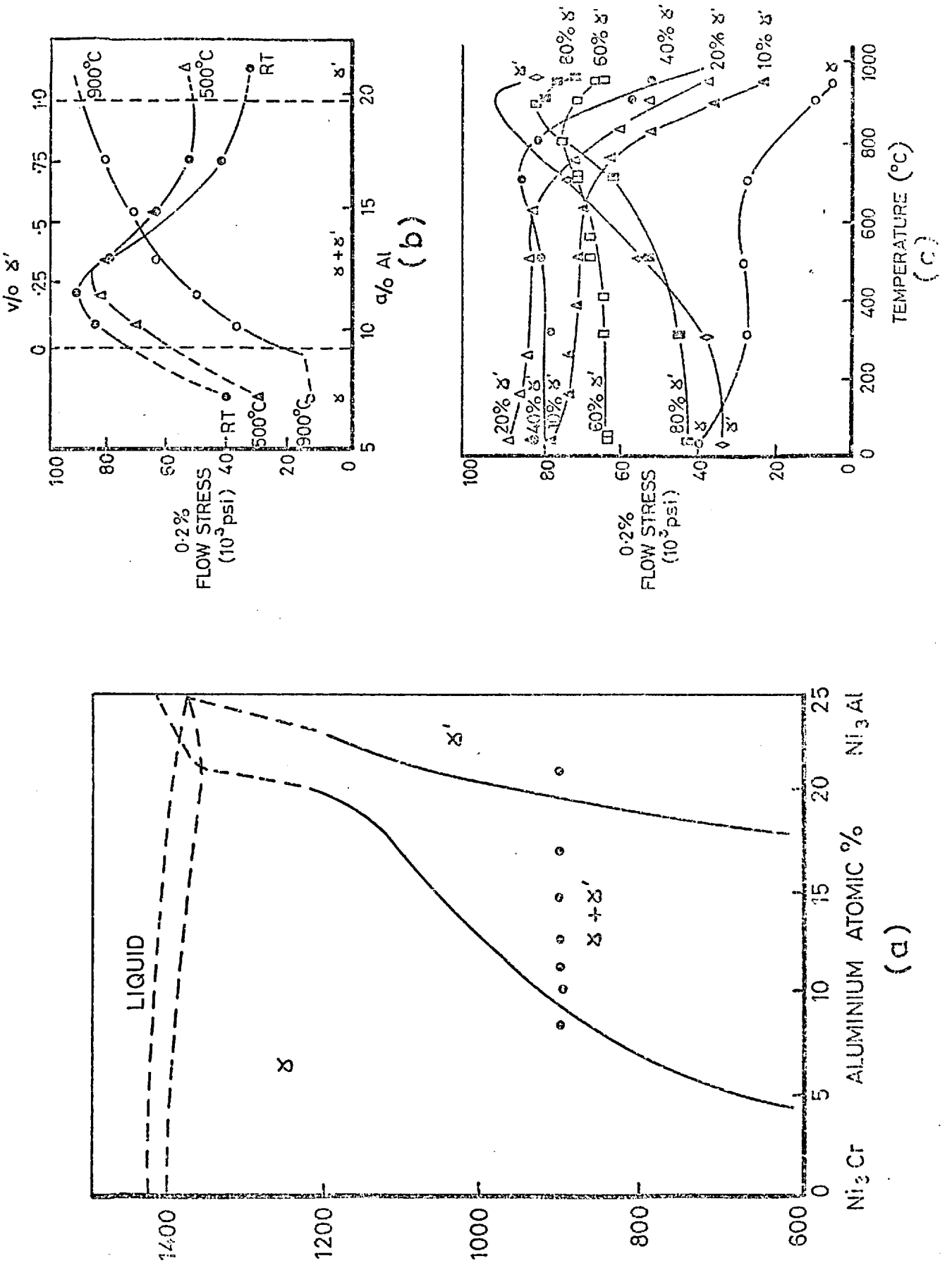


FIG. 39 (a) SECTION THROUGH Ni-Cr-Al TERNARY AT 75 a/o Ni ILLUSTRATING ALLOYS INVESTIGATED (REFERENCE 110). (b) AND (c) EFFECTS OF V/o γ' AND TEMPERATURE ON FLOW STRESS.

A

Constitution and microstructure of certain cast nickel superalloys: Part I

by J. E. Restall and E. C. Toulson

Progress in the design of modern aero engines has become increasingly dependent on the development of reliable cast nickel superalloys, which are steadily replacing wrought nickel alloy components.

The operating temperature, life, and time-between-overhaul of civil aircraft gas turbine engines have steadily been increasing for a number of years. These improvements have been achieved by engineering design, the continuing development of cooling techniques, and improvements in materials to withstand the service environment. Wrought nickel superalloys have formed the backbone of high-temperature turbine materials which have enabled engine lifetimes of up to 50 000 hours to be realised. The reliability of components has been guaranteed by close control of processing, a deep understanding of the physical metallurgy, and establishment of the relationship of structure to properties, of these materials.

More recently, wrought nickel alloys have been partly replaced by cast components in certain engines (for example, the use of IN100 alloy both in the *Olympus* engine for *Concorde* and the *Pegasus* engine for the *Harrier*) because of the higher temperature capability of the cast materials and economies in production associated with investment casting. Less is known about some characteristics of casting alloys at present, as most of the early materials were developed with the immediate engineering objective of the attainment of the best creep-rupture strength at the highest possible temperature. However, improvements in process control and closer collaboration between manufacturers and users have underlined the need to consider other property requirements of casting alloys which are now being more readily accepted for use in aircraft engines.

The phase chemistry of cast nickel alloys is particularly complex, as these materials may contain up to 12 elements, each of which serves a particular purpose. In order to control undesirable structural modifications that may occur during long-term exposure in service resulting in embrittlement and loss of strength of a component, and in order to use expensive and sometimes dense alloying elements, such as W and Ta, to their best advantage, the way in which they are partitioned between the different phases that are present in alloys should be known.

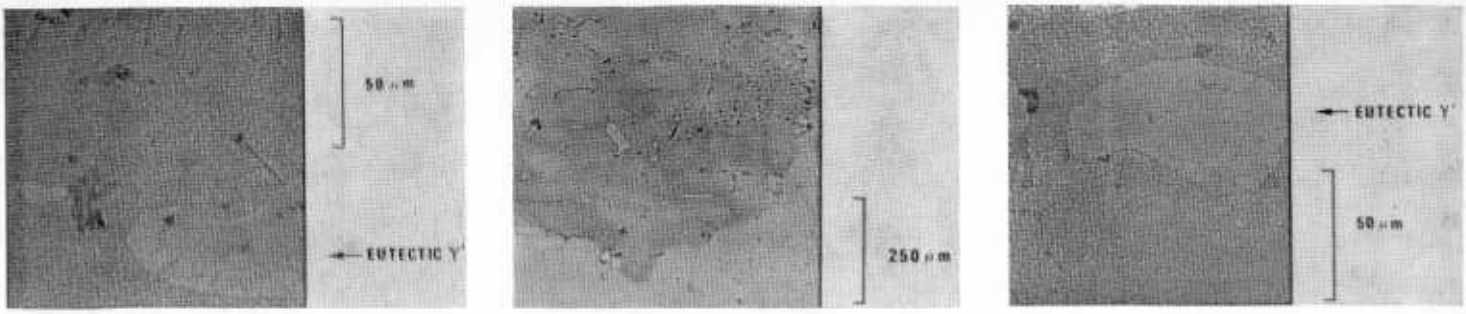
The work reported here is part of a continuing programme on the characterisation of phases in high-temperature nickel alloys, an understanding of which may help in the development of cheaper and better materials. A series of experimental and commercial nickel alloys has been examined using a combination of electron probe, spectrographic, and wet chemical techniques for analysis of the constituent phases. This was supported in part by X-ray diffraction analyses of their structures. Relationships between the composition of the phases and the composition of the parent alloys were tentatively established.

Materials and experimental work

The materials examined may conveniently be divided into three groups (Table I). The first group was based on HRA-376 alloy which is one of the strongest nickel alloys developed for creep strength at high temperatures. HRA-376 alloy (designated A33 in Table I) nominally contains 3 atomic-% each of tantalum and tungsten, in addition to nickel, chromium, cobalt, and the other elements listed. The remainder of the alloys in group 1 were designed by substituting combinations of niobium, titanium, and molybdenum partly or wholly for the tantalum and tungsten in the HRA-376 alloy. Most of the work reported here has been carried out on this group of materials. The second group of alloys in Table I was based on the commercial, high strength MM246 alloy, but with five elements removed in succession, according to what is believed to be their function in the alloy. Mo and W were removed first; these are believed to strengthen the nickel-base matrix (gamma). Co, which raises the solvus temperature of the age-hardening precipitate (gamma-prime), was next removed. Finally, Ti and Ta were removed: these appear to be generally distributed between the gamma-prime and carbide phases. This group of materials is the subject of current further research. The third group of materials contained the readily available commercial nickel alloys IN100, MM200, and *Nimocast* 713C. All materials were vacuum melted and conventionally cast into ceramic shell moulds to give 0·5 in diameter bar stock from which the specimens for examination were prepared.

The testpieces for optical microscopic examinations were prepared by conventional grinding through successive grades of silicon carbide paper with final polishing using 0·25 μm diamond paste. Etching was done using 'glyceregia' (2 : 1 HCl : HNO_3 + 3 glycerol, vol-%) or Kalling's reagent (50 ml litre HCl + 50 ml litre methanol + 2·5 g $CuCl_2$, diluted to 50% with alcohol). Specimens for electron microprobe analysis of phases *in situ* were prepared similarly, with the exception of etching. In certain cases extraction residues of the gamma-prime phase were rapidly melted in a small quartz capsule using RF induction heating, and the fused material after metallographic preparation was subjected to microprobe analysis. Specimens for electron microscopy were largely negative replicas or extraction replicas of the alloys, although some thin foils were examined. The negative replicas made by the standard two-stage technique (*i.e.* plastic replicas), shadowed with Au : Pd alloy and carbon backed, were taken from surfaces electro-polished with a solution of 15% H_2SO_4 in methanol, and etched in glyceregia. Extraction replicas were pre-

The authors are both with the Materials Science Department, the National Gas Turbine Establishment, Pyestock, Farnborough, Hants.



1 Typical features of cast nickel base alloys revealed by optical microscopy

pared by coating the specimens with a layer of carbon, followed by electrolysis in methanol-HCl solution. The thin foil specimens were prepared by a jet-thinning technique, followed by final polishing in a perchloric/acetic acid mixture.

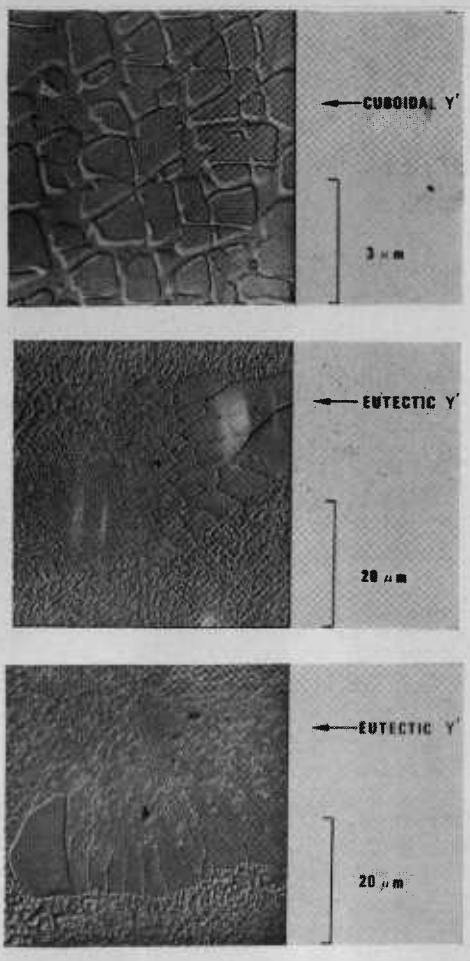
X-ray diffraction studies on the HRA-376 alloy group, carried out both at Fulmer Research Institute Ltd. and RAE, were based on carbide residues extracted from a 10% HCl-methanol solution containing 5% tartaric acid, and gamma-prime residues prepared by standard electrolytic separation in a 20% orthophosphoric acid solution in water. The residues were separated from the electrolytes using 'Millipore' filters. The diffraction photographs at Fulmer Research Institute were obtained using a Philips 11·46 cm diameter camera, and the specimens, in powder form, were enclosed in 0·3 mm silica quills. Each was exposed to cobalt Kα radiation for a period of 24 hours. In general the photographs obtained from gamma-prime extracts were of much higher quality than those obtained from the carbides. The accuracy with which their lattice parameters may be given is consequently much greater. Attempts were made to measure the lattice parameter of the matrix (gamma) phase using a flat plate camera by obtaining diffraction patterns from the polished surface of bulk-alloy specimens. The diffraction patterns were poor because of the worked surface layer caused during preparation. Attempts to remove this layer by various etchants produced little improvement. Eventually, filings were obtained from each specimen and photographed in a powder camera. Although the filing process itself caused lattice strain resulting in rather broad diffractions, the quality was superior to that obtained in the flat plate camera. The lattice parameters of the gamma matrices cannot be given with the same degree of accuracy as the gamma-prime results. Some checks were made using equipment at RAE.

Chemical analyses of the parent alloys of the HRA-376 alloy group in bulk form, and of the extracted gamma-prime and MC carbide phases, and the gamma phases (nickel solid solutions) in the form of liquids separated from solid residues were

TABLE I. Chemical composition of alloys

Material		B	C	Al	Ti	Cr	Co	Ni	Zr	Nb	Mo	Ta	W
HRA 376 alloy group A33	(1)	0·02	0·15	5·7	—	5·9	9·6	60·6	0·10	—	—	8·9	9·0
	(2)	0·02	0·14	5·9	—	5·9	9·6	60·0	0·11	—	—	9·0	9·3
	(3)	0·11	0·7	13·0	—	7·0	10·0	63·1	0·07	—	—	3·0	3·0
A39	(1)	0·02	0·15	5·9	—	6·1	9·8	61·9	0·10	2·3	—	4·5	9·2
	(2)	0·02	0·12	5·8	—	5·9	10·0	61·6	0·10	2·7	—	4·6	9·1
	(3)	0·11	0·7	13·0	—	7·0	10·0	63·1	0·07	1·5	—	1·5	3·0
A40	(1)	0·02	0·15	6·0	—	6·2	10·1	63·2	0·10	4·8	—	—	9·4
	(2)	0·02	0·14	6·1	—	6·1	10·3	62·9	0·10	5·4	—	—	8·9
	(3)	0·11	0·7	13·0	—	7·0	10·0	63·1	0·07	3·0	—	—	3·0
A54	(1)	0·02	0·15	5·9	—	6·1	9·8	61·8	0·10	—	2·4	9·1	4·6
	(2)	0·02	0·13	6·2	—	6·0	9·9	61·4	0·09	—	2·4	9·1	4·7
	(3)	0·11	0·7	13·0	—	7·0	10·0	63·1	0·07	—	1·5	3·0	1·5
A53	(1)	0·02	0·15	6·0	—	6·2	10·1	63·1	0·10	—	5·0	9·3	—
	(2)	0·03	0·13	6·1		6·0	10·3	63·3	0·10	—	4·9	9·1	—
	(3)	0·11	0·7	13·0		7·0	10·0	63·1	0·07	—	3·0	3·0	—
A44	(1)	0·02	0·15	6·0	—	6·2	10·1	64·4	0·10	2·4	2·5	4·6	3·5
	(2)	0·02	0·14	6·2	—	6·1	10·3	64·3	0·10	2·6	2·5	4·6	3·1
	(3)	0·11	0·7	13·0	—	7·0	10·0	63·1	0·07	1·5	1·5	1·5	1·5
A60	(1)	0·02	0·15	6·2	—	6·5	10·5	66·2	0·10	5·1	5·2	—	—
	(2)	0·02	0·12	6·2	—	6·6	10·9	65·3	0·10	5·6	5·1	—	—
	(3)	0·11	0·7	13·0	—	7·0	10·0	63·1	0·07	3·0	3·0	—	—
A52	(1)	0·02	0·15	5·9	1·2	6·1	10·0	62·6	0·10	—	—	4·6	9·3
	(2)	0·02	0·13	6·0	1·1	6·2	10·2	63·0	0·10	—	—	4·5	8·7
	(3)	0·11	0·7	13·0	1·5	7·0	10·0	63·1	0·07	—	—	1·5	3·0
A51	(1)	0·02	0·15	6·1	2·5	6·4	10·3	64·8	0·10	—	—	—	9·6
	(2)	0·02	0·14	6·1	2·4	6·4	10·3	65·4	0·12	—	—	—	9·1
	(3)	0·11	0·7	13·0	3·0	7·0	10·0	63·1	0·07	—	—	—	3·0
MM246 alloy group A101	(1)	0·02	0·15	5·5	1·5	9·0	10·0	59·8	0·05	—	2·5	1·5	10·0
	(2)	0·02	0·14	5·7	1·7	9·2	9·9	59·3	0·09	—	2·6	1·7	9·7
	(3)	0·11	0·7	12·4	2·1	10·3	9·8	59·1	0·06		1·6	0·5	3·1
A102	(1)	0·02	0·15	5·6	1·5	9·1	10·1	61·9	0·05	—	—	1·6	10·1
	(2)	0·02	0·14	5·7	1·8	9·3	9·8	71·7	0·08	—	—	1·7	9·7
	(3)	0·13	0·7	12·4	2·1	10·4	9·6	61·2	0·05	—	—	0·5	3·0
A103	(1)	0·02	0·17	6·0	1·6	9·9	10·9	59·9	0·05	—	—	1·7	—
	(2)	0·02	0·16	5·9	1·8	10·0	10·7	69·4	0·07	—	—	1·9	—
	(3)	0·12	0·7	11·9	2·1	10·4	9·9	64·3	0·04	—	—	0·6	—
A104	(1)	0·02	0·17	6·0	1·6	9·8	—	80·6	0·05	—	—	1·7	—
	(2)	0·03	0·13	5·9	1·8	10·1	—	80·3	0·07	—	—	1·6	—
	(3)	0·12	0·7	11·9	2·0	10·5	—	74·2	0·04	—	—	0·5	—
A105	(1)	0·02	0·17	6·0	1·7	9·9	—	82·1	0·05	—	—	—	—
	(2)	0·02	0·16	6·0	2·0	10·3	—	81·4	0·08	—	—	—	—
	(3)	0·11	0·7	12·1	2·3	9·5	—	75·3	0·05	—	—	—	—
A106	(1)	0·02	0·17	6·0	—	9·9	—	83·8	0·05	—	—	—	—
	(2)	0·02	0·15	6·0	—	10·1	—	83·6	0·08	—	—	—	—
	(3)	0·11	0·7	11·9	—	10·5	—	76·8	0·05	—	—	—	—
Nimocast 713C alloy A21	(1)	0·01	0·12	6·1	0·7	12·5	—	73·9	0·1	2·0	4·5	—	—
	(3)	0·06	0·6	12·4	0·8	13·2	—	69·1	0·06	1·2	2·6	—	—
In100 alloy A92	(1)	0·01	0·18	5·5	4·7	10·0	15·0	61·5	0·06	—	3·0	—	—
	(3)	0·07	0·7	11·1	5·8	10·3	13·7	56·3	0·07	—	1·8	—	—
MM200 alloy A84	(1)	0·01	0·15	5·0	2·0	9·0	10·0	60·2	0·05	1·0	—	—	12·5
	(3)	0·11	0·76	11·4	2·6	10·6	10·4	63·0	0·03	0·7	—	—	4·5

(1) Nominal wt.-%. (2) Actual wt.-%. (3) Nominal atomic-%.



2 Electron micrographs of 'Cuboidal' and eutectic gamma-prime

carried out by the Chemical Inspectorate (Royal Arsenal, Woolwich and Bragg Laboratory, Sheffield). These anlayses involved the use of conventional wet-chemical, X-ray fluorescence, and atomic absorption techniques. Fulmer Research Institute supplied spectrographic analysis results for nine samples of gamma-prime extracted from the as-cast alloys.

Results

General features of cast superalloys

Before presenting the results dealing with the chemistry of the three principal phases in the cast nickel alloys, reference is made to pertinent features of their microstructure. Figure 1 shows the optical microstructure of a typical as-cast, high strength nickel alloy. The phases that are resolvable include primary dendrites of gamma (nickel-base matrix) solid solution with interdendritic regions of MC carbide, and areas of 'white-etching', kidney-shaped gamma-prime (Ni_3Al-type compound) which result from eutectic solidification. MC carbide particles are present at grain-

TABLE II. Quantitative electron microprobe analysis data for the dendrite, eutectic gamma-prime and MC carbides compared with parent-alloy compositions (atomic %)

Alloy Phase	B	C	Al	Ti	Cr	Co	Ni	Zr	Nb	Mo	Ta	W
A33	0·11	0·7	13·0	—	7·0	10·0	63·12	0·07	—	—	3·0	3·0
Dendrite	—	—	12·4	—	7	9·6	66·2	—	—	—	2·4	2·8
γ′	—	—	19·9	—	5·1	7·9	61·9	—	—	—	3·5	1·8
MC	—	50·0	—	—	2·1	1·6	2·6	0·3	—	—	30·3	13·5
A39	0·11	0·7	13·0	—	7·0	10·0	63·12	0·07	1·5	—	1·5	3
Dendrite	—	—	14·7	—	8·1	9·8	63·2	—	0·7	—	0·7	2·7
γ′	—	—	19·9	—	3·6	7·0	64·3	—	1·5	—	2·1	1·6
MC	—	50·0	—	—	0·1	0·1	1·0	0·2	32·1	—	16·0	1·4
A40	0·11	0·7	13·0	—	7·0	10·0	63·12	0·07	3·0	—	—	3·0
Dendrite	—	—	12·9	—	8·9	9·3	65·2	—	2·0	—	—	1·8
γ′	—	—	19·2	—	4·2	7·1	64·5	—	3·5	—	—	1·7
MC	—	50·0	—	—	4·3	1·8	3·0	0·5	38·5	—	—	1·9
A54	0·11	0·7	13·0	—	7·0	10·0	63·12	0·07	—	1·5	3·0	1·5
Dendrite	—	—	13·6	—	6·8	9·8	63·2	—	—	1·1	3·2	1·6
γ′	—	—	18·5	—	4·0	12·0	60·0	—	—	0·7	4·4	0·5
MC	—	50·0	—	—	1·4	1·4	2·6	0·3	—	1·5	42·3	0·7
A53	0·11	0·7	13·0	—	7·0	10·0	63·12	0·07	—	3·0	3·0	—
Dendrite	—	—	13·9	—	7·7	11·4	61·6	—	—	2·6	2·7	—
γ′	—	—	21·1	—	2·8	6·5	63·2	—	—	1·0	5·4	—
MC	—	50·0	—	—	1·7	0·8	2·5	0·3	—	2·9	43·0	—
A44	0·11	0·7	13·0	—	7·0	10·0	63·12	0·07	1·5	1·5	1·5	1·5
Dendrite	—	—	12·5	—	6·5	9·8	64·7	—	1·0	1·1	0·5	1·2
γ′	—	—	21·9	—	3·1	6·4	62·9	—	2·2	0·6	2·5	0·4
MC	—	50·0	—	—	0·6	0·5	2·5	0·2	24·3	1·3	14·6	5·8
A60	0·11	0·7	13·0	—	7·0	10·0	63·12	0·07	3·0	3·0	—	—
Dendrite	—	—	12·8	—	8·4	11·2	63·0	—	2·0	2·6	—	—
γ′	—	—	18·7	—	3·2	6·8	65·4	—	4·8	1·1	—	—
MC	—	50·0	—	—	0·3	0·4	2·6	0·2	45·2	1·6	—	—
A52	0·11	0·7	13·0	1·5	7·0	10·0	63·12	0·07	—	—	1·5	3·0
Dendrite	—	—	14·5	1·0	8·2	11·1	61·4	—	—	—	1·3	2·6
γ′	—	—	21·8	2·1	3·6	7·6	61·3	—	—	—	2·0	1·4
MC	—	50·0	—	16·6	1·0	0·5	2·2	0·2	—	—	24·9	4·6
A51	0·11	0·7	13·0	3·0	7·0	10·0	63·12	0·07	—	—	—	3·0
Dendrite	—	—	12·5	2·0	8·1	10·3	63·4	—	—	—	—	3·8
γ′	—	—	18·5	5·6	4·0	7·4	63·5	—	—	—	—	1·0
MC	—	50·0	—	32·1	1·2	0·4	2·3	0·2	—	—	—	13·9
A101	0·11	0·7	12·4	2·1	10·3	9·8	59·1	0·06	—	1·6	0·5	3·1
Dendrite	—	—	11·9	1·4	10·9	9·5	61·9	—	—	1·5	0·5	2·5
γ′	—	—	17·6	5·4	4·5	7·2	64·0	—	—	0·5	0·4	0·4
MC	—	50·0	—	29·2	1·5	0·6	2·7	0·2	—	3·2	8·5	4·4
A102	0·13	0·7	12·3	2·1	10·4	9·6	61·2	0·05	—	—	0·5	3·0
Dendrite	—	—	12·3	1·3	10·5	10·4	62·8	—	—	—	0·4	2·3
γ′	—	—	18·5	5·2	4·8	6·6	63·7	—	—	—	0·6	0·5
MC	—	50·0	—	29·7	1·9	0·8	2·5	0·2	—	—	11·0	4·3
A103	0·12	0·7	11·9	2·1	10·4	9·9	64·3	0·04	—	—	0·6	—
Dendrite	—	—	12·3	2·1	11·2	10·2	63·7	—	—	—	0·5	—
γ′	—	—	17·1	5·9	4·8	6·2	64·6	—	—	—	1·5	—
MC	—	50·0	—	29·3	1·4	0·1	1·9	0·2	—	—	17·3	—
A104	0·12	0·7	11·9	2·0	10·5	—	74·2	0·04	—	—	0·5	—
Dendrite	—	—	12·6	1·4	11·9	—	73·6	—	—	—	0·5	—
γ′	—	—	—	—	—	—	—	—	—	—	—	—
MC	—	50·0	—	34·7	3·6	—	2·2	0·2	—	—	9·3	—
A105	0·11	0·7	12·1	2·3	9·5	—	75·3	0·05	—	—	—	—
Dendrite	—	—	12·4	1·8	10·7	—	75·1	—	—	—	—	—
γ′	—	—	—	—	—	—	—	—	—	—	—	—
MC	—	50·0	—	39·8	7·5	—	2·2	0·3	—	—	—	—
A106	0·11	0·7	11·9	—	10·5	—	76·8	0·05	—	—	—	—
Dendrite	—	—	12·5	—	10·6	—	77·0	—	—	—	—	—
γ′	—	—	—	—	—	—	—	—	—	—	—	—
MC	—	50·0	—	—	44·2	—	5·3	—	—	—	—	—
Nimocast 713C A21	0·05	0·5	12·2	0·7	13·2	—	69·7	0·05	1·2	2·5	—	—
Dendrite	—	—	12·6	0·6	13·7	—	70·2	—	0·6	2·3	—	—
γ′	—	—	18·9	2·1	4·0	—	71·9	—	2·0	1·1	—	—
MC	—	50·0	—	27·3	1·4	—	1·6	0·1	18·1	3·8	—	—
IN100 A92	0·07	0·7	11·1	5·8	10·3	13·7	56·3	0·07	—	1·8	—	—
Dendrite	—	—	—	—	—	—	—	—	—	—	—	—
γ′	—	—	13·7	10·7	4·0	10·7	61·7	—	—	0·05	—	—
MC	—	50·0	—	39·8	0·7	0·3	2·0	0·2	—	7·1	—	—
MM200 A84	0·11	0·76	11·4	2·6	10·6	10·4	63·0	0·03	0·7	—	—	4·5
Dendrite	—	—	11·5	2·1	10·6	11·0	59·9	—	0·2	—	—	4·5
γ′	—	—	16·3	5·5	5·7	7·0	63·6	—	0·6	—	—	1·4
MC	—	50·0	—	27·3	0·8	0·1	1·3	0·2	11·7	—	—	8·6

Note: the dendrite analysis refers to mean composition of the matrix, and includes the 60 vol-% of the cuboidal-type gamma-prime precipitate. γ′-composition refers to the eutectic gamma-prime.

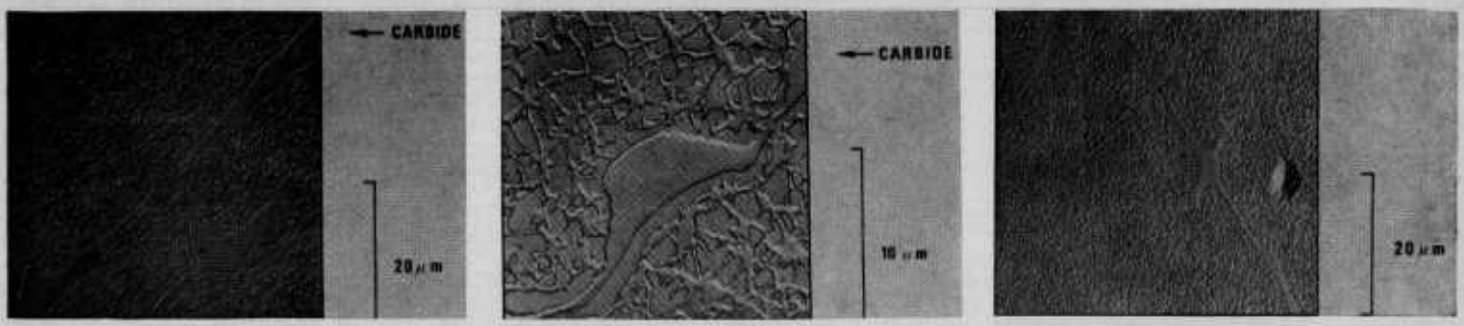
TABLE III. Comparative analyses of γ′ phases in nickel alloys (wt-%)

Alloy	Phase	Elements	B	C	Al	Ti	Cr	Co	Ni	Zr	Nb	Mo	Ta	W
	(1)	Eutectic			9·4		4·6	8·2	61·9	0·1	—	—	10·0	5·8
A33	(2)	Re-fused			8·4		2·4	7·5	65·5	ND			10·0	6·2
	(3)	Spectrographic			8·6		2·1	7·5	64·9	—			8·9	8·9
W37	(4)	Calculated			8·9		3·0	7·6	62·6	—			10·8	7·1
	(1)	Eutectic			9·3	—	3·2	7·1	66·3	0·1	2·4	—	6·5	5·2
A39	(2)	Re-fused			8·5		2·5	7·6	65·4	ND	2·6		6·7	6·7
	(3)	Spectrographic			7·6		2·2	7·4	66·3	—	2·8		5·9	7·8
W34	(4)	Calculated			8·9		3·9	8·6	62·4	—	2·4		5·5	8·2
	(1)	Eutectic			9·2	—	3·9	7·1	68·0	0·1	5·7	—	—	6·0
A40	(2)	Re-fused			8·4		3·2	8·7	66·2	ND	5·6			7·9
	(3)	Spectrographic			8·1		2·3	6·5	70·3	—	4·7			8·1
W36	(4)	Calculated			8·9		3·4	8·7	65·1	—	5·8			8·2
	(1)	Eutectic			9·1	—	3·8	7·9	61·7	0·1	—	1·2	14·5	1·7
A54	(2)	Re-fused			8·7		2·2	7·3	67·0	ND		0·9	10·9	3·0
	(3)	Spectrographic			8·6		2·4	7·6	65·9	—		1·3	9·6	4·6
W41	(4)	Calculated			9·4		2·2	7·0	65·1	—		1·4	10·4	4·3
	(1)	Eutectic			9·8	—	2·5	6·6	62·6	0·1	—	1·6	16·8	—
A53	(2)	Re-fused			8·7		2·0	6·4	68·7	ND		2·2	12·0	
	(3)	Spectrographic			9·6		1·9	7·3	67·2			2·8	11·2	
W44	(4)	Calculated			9·5		2·4	7·1	67·1	—		2·8	10·9	
	(1)	Eutectic			10·6	—	2·9	6·6	68·9	0·1	3·6	1·0	8·0	1·3
A44	(2)	Re-fused			8·8		3·0	7·2	68·5	ND	2·5	1·5	5·3	3·2
	(3)	Spectrographic			8·2		2·0	6·7	72·0	—	2·2	1·4	4·8	2·7
W43	(4)	Calculated			9·9		1·6	7·0	69·0	—	2·7	1·8	5·7	2·3
	(1)	Eutectic			9·3	—	3·0	8·1	69·4	0·1	8·2	1·9	—	—
A60	(2)	Re-fused			9·2		3·4	8·0	69·5	ND	6·8	3·1		
	(3)	Spectrographic			7·1		1·8	6·2	76·6	—	5·6	2·7		
W47	(4)	Calculated			9·2		4·4	9·5	66·2	—	7·1	3·7		
	(1)	Eutectic			9·0	2·1	3·5	8·2	66·1	0·1			6·3	4·7
A52	(2)	Re-fused			8·8	1·2	2·4	8·0	67·1	ND			4·7	7·8
	(3)	Spectrographic			8·9	1·2	2·0	6·9	67·9	—			4·2	8·9
W50	(4)	Calculated			9·0	1·4	4·0	9·0	62·8	—			5·0	8·7
	(1)	Eutectic			9·6	5·1	4·0	8·4	69·1	0·1				3·7
A51	(2)	Re-fused			9·0	2·6	3·2	8·4	69·5	ND				7·3
	(3)	Spectrographic			8·6	3·2	2·6	7·8	68·8	—				9·1
W49	(4)	Calculated			9·3	3·0	4·4	10·0	65·3	—				8·0

Comparative analyses of γ′-phases in nickel alloys (atomic-%)

	(1)	Eutectic			19·9	—	5·1	7·9	61·9	0·07	—	—	3·5	1·8
A33	(2)	Re-fused			18·4		2·7	7·5	66·1	ND			3·3	2·0
	(3)	Spectrographic			19·0		2·4	7·6	65·2	,,			2·9	2·9
W37	(4)	Calculated			19·6		3·5	7·7	63·4	,,			3·6	2·3
	(1)	Eutectic			19·9	—	3·6	7·0	64·3	0·07	1·5	—	2·1	1·6
A39	(2)	Re-fused			18·4		2·8	7·6	65·3	ND	1·6		2·2	2·1
	(3)	Spectrographic			16·7		2·5	7·4	67·1	,,	1·8		2·0	2·5
W34	(4)	Calculated			19·2		4·4	8·5	62·0	,,	1·5		1·8	2·6
	(1)	Eutectic			19·2	—	4·2	7·1	64·5	0·07	3·5	—	—	1·7
A40	(2)	Re-fused			17·8		3·5	8·5	64·4	ND	3·4			2·5
	(3)	Spectrographic			17·2		2·5	6·3	68·6	,,	2·9			2·5
W36	(4)	Calculated			18·8		3·7	8·4	63·1	,,	3·5			2·5
	(1)	Eutectic			18·5	—	4·0	7·8	64·1	0·07	—	0·7	4·4	0·5
A54	(2)	Re-fused			18·8		2·5	7·2	66·6	ND		0·5	3·5	0·9
	(3)	Spectrographic			18·7		2·7	7·2	66·0	,,		0·8	3·1	1·5
W41	(4)	Calculated			20·3		2·5	7·0	64·7	,,		0·9	3·3	1·3
	(1)	Eutectic			21·1	—	2·8	6·5	63·2	0·07	—	1·0	5·4	—
A53	(2)	Re-fused			18·6		2·3	6·3	67·7	ND		1·3	3·8	
	(3)	Spectrographic			20·3		2·1	7·1	65·3	,,		1·7	3·5	
W44	(4)	Calculated			20·1		2·6	6·9	65·3	,,		1·5	3·4	
	(1)	Eutectic			21·9		3·1	6·4	62·9	0·07	2·2	0·6	2·5	0·4
A44	(2)	Re-fused			18·5		3·3	6·9	66·2	ND	1·5	0·9	1·6	1·0
	(3)	Spectrographic			17·2		2·2	6·5	69·5	,,	1·4	0·9	1·5	0·9
W43	(4)	Calculated			20·5		1·7	6·6	65·5	,,	1·6	1·1	1·8	0·7
	(1)	Eutectic			18·7		3·2	6·8	65·4	0·07	4·8	1·1	—	—
A60	(2)	Re-fused			18·6		3·6	7·4	64·7	ND	4·0	1·8		
	(3)	Spectrographic			14·6		1·9	5·8	72·7	,,	3·3	1·6		
W47	(4)	Calculated			18·6		4·7	8·8	61·6	,,	4·2	2·1		
	(1)	Eutectic			21·8	2·1	3·6	7·6	61·3	0·07	—	—	2·0	1·0
A52	(2)	Re-fused			18·7	1·4	2·6	7·8	65·5	ND			1·5	2·4
	(3)	Spectrographic			19·0	1·4	2·2	6·7	66·5	,,			1·3	2·8
W50	(4)	Calculated			19·2	1·7	4·4	8·8	61·6	,,			1·6	2·7
	(1)	Eutectic			18·5	5·6	4·0	7·4	63·5	0·07	—	—	—	1·0
A51	(2)	Re-fused			18·3	3·0	3·4	6·9	65·2	ND				2·2
	(3)	Spectrographic			17·8	3·7	2·8	7·4	65·5	,,				2·8
W49	(4)	Calculated			19·0	3·5	4·6	9·3	61·2	,,				2·4

(1) Eutectic (2) Re-fused (3) Spectrographic (4) Calculated on basis of Chemical Inspectorate results for gamma phase and assumes 60 vol-% γ′/40 vol-% gamma ND—not determined

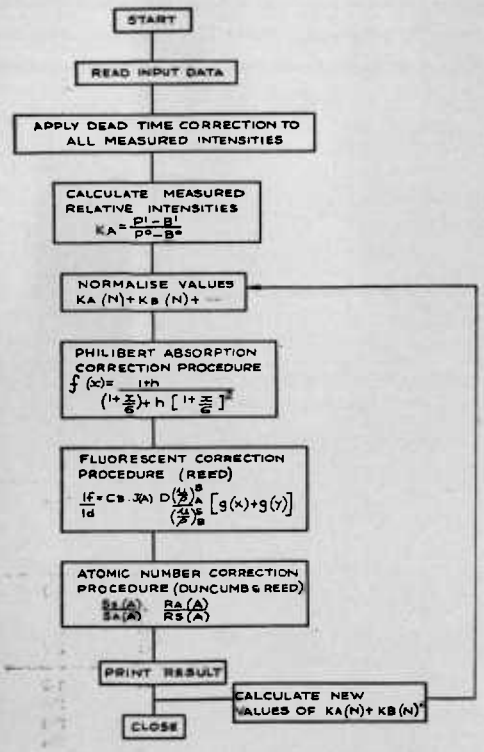


3 Electron micrographs of MC(carbide) phase

boundary regions. Lesser amounts of nitrides, borides, and sulphides are also generally present. The matrix gamma has the austenitic face centred/cubic structure, gamma-prime is the precipitation hardening, ordered-face centred/cubic structure phase, and the simple MC carbides generally have the face centred/cubic structure. Examination of the gamma dendrites using higher resolution electron microscope techniques shows the presence of gamma-prime which may appear in the form of cuboids (see Fig. 2) 0·2–0·8 μm in size or finer, depending on the cooling rate. The distinction should be noted between the types of gamma-prime found in the cast alloys. There is the eutectic gamma-prime, formed from the super-saturated liquid phase, and there is a finer, cuboidal or spheroidal gamma-prime formed from the solid material that is super-saturated with gamma-prime-forming elements (Al, Ti, Nb, Ta, etc.). Figure 2 shows electron micrographs of eutectic gamma-prime, composed of massive particles of gamma-prime separated by thin lamellae of gamma (nickel solid solution). The eutectic gamma-prime grows coherently with the surrounding matrix, frequently on a dendrite tip. Figure 3 shows typical electron micrographs of MC carbide. Note the differing morphologies and sizes adopted by this phase.

Chemical and electron microprobe analyses

The initial electron microprobe analysis investigations were concerned with the eutectic gamma-prime and MC carbide *in situ*, with checks being made on the cuboidal gamma-prime and matrix phases that were individually below microprobe resolution (< 1 μm). The gamma prime analysed by Chemical Inspectorate, and



4 Flow diagram of computer correction procedure for electron-probe microanalysis

TABLE IV. Composition of gamma phases in nickel alloys (chemical inspectorate)

Alloy	Gamma phase	Al	Ti	Cr	Co	Ni	Zr	Nb	Mo	Ta	W
A33	(1)	2·0		10·5	12·8	59·8				3·6	11·3
	(2)	4·7		12·7	13·6	64·0				1·3	3·8
A39	(1)	1·5		8·9	12·4	63·1		1·4		2·0	10·7
	(2)	3·5		10·7	13·2	67·4		0·9		0·7	3·6
A40	(1)	2·2		10·2	13·1	61·9		2·7			9·9
	(2)	5·0		12·9	13·4	63·7		1·8			3·3
A54	(1)	1·6		11·8	14·6	59·5			4·1	2·9	5·5
	(2)	3·6		13·9	15·1	61·9			2·6	1·0	1·8
A53	(1)	1·5		11·4	15·6	61·1			7·9	2·5	
	(2)	3·3		13·1	15·8	62·1			4·9	0·8	
A44	(1)	1·4		12·8	16·0	59·2		1·2	3·8	1·8	3·8
	(2)	3·1		14·8	16·4	60·6		0·8	2·4	0·6	1·3
A60	(1)	2·2		10·0	13·4	65·7		1·3	7·4		
	(2)	4·8		11·2	13·3	65·4		0·8	4·5		
A52	(1)	1·9	0·2	9·6	12·4	65·8				1·5	8·6
	(2)	4·3	0·2	11·3	12·8	68·1				0·5	2·9
A51	(1)	1·6	0·5	9·6	11·1	67·9					9·4
	(2)	3·6	0·6	11·2	11·4	70·1					3·1

(1) wt-%. (2) atomic-%.

TABLE V. Comparative analyses of phases in nickel alloys in relation to parent-alloy compositions

Alloy	Phase	B	C	Al	Ti	Cr	Co	Ni	Zr	Nb	Mo	Ta	W
	(1) Alloy	0·11	0·7	13·0	—	7·0	10·0	63·1	0·07	—	—	3·0	3·0
A33	(2) Matrix-gamma			4·7		12·7	13·6	64·0	ND			1·3	3·8
	(3) Gamma-prime			19·1		3·4	7·7	64·4	0·07			3·2	2·2
W37	(4) Carbide		50·0			2·3			0·4			32·8	14·5
	(1) Alloy	0·11	0·7	13·0	—	7·0	10·0	63·1	0·07	1·5	—	1·5	3·0
A39	(2) Matrix-gamma			3·5		10·7	13·2	67·4	ND	0·9		0·7	3·6
	(3) Gamma-prime			18·3		3·0	7·3	65·4	0·07	1·8		2·1	2·1
W34	(4) Carbide		50·0			0·1			0·2	32·2		16·1	1·4
	(1) Alloy	0·11	0·7	13·0	—	7·0	10·0	63·1	0·07	3·0	—	—	3·0
A40	(2) Matrix-gamma			5·0		12·9	13·4	63·7	ND	1·8			3·3
	(3) Gamma-prime			18·1		3·4	7·3	65·7	0·07	3·3			2·2
W36	(4) Carbide		50·0			4·8			0·4	42·6			2·0
	(1) Alloy	0·11	0·7	13·0	—	7·0	10·0	63·1	0·07	—	1·5	3·0	1·5
A54	(2) Matrix-gamma			3·6		13·9	15·1	61·9	ND		2·6	1·0	1·8
	(3) Gamma-prime			18·7		3·1	7·4	65·3	0·07		0·7	3·7	1·1
W41	(4) Carbide		50·0			1·5			0·3		1·6	45·8	0·8
	(1) Alloy	0·11	0·7	13·0	—	7·0	10·0	63·1	0·07	—	3·0	3·0	—
A53	(2) Matrix-gamma			3·3		13·1	15·8	62·1	ND	—	4·9	0·8	
	(3) Gamma-prime			20·0		2·4	6·6	65·5	0·07		1·3	4·2	
W44	(4) Carbide		50·0			1·5			0·3		3·0	44·9	
	(1) Alloy	0·11	0·7	13·0	—	7·0	10·0	63·1	0·07	1·5	1·5	1·5	1·5
A44	(2) Matrix-gamma			3·1		14·8	16·4	60·6	ND	0·8	2·4	0·6	1·3
	(3) Gamma-prime			19·2		3·5	6·6	65·5	0·07	1·7	0·8	1·9	0·8
W43	(4) Carbide		50·0			0·6			0·2	26·0	1·4	15·6	6·2
	(1) Alloy	0·11	0·7	13·0	—	7·0	10·0	63·1	0·07	3·0	3·0	—	—
A60	(2) Matrix-gamma			4·8		11·2	13·3	65·4	ND	0·8	4·5		
	(3) Gamma-prime			17·3		2·9	6·7	67·6	0·07	4·0	1·5		
W47	(4) Carbide		50·0			0·2			0·2	48·0	1·6		
	(1) Alloy	0·11	0·7	13·0	1·5	7·0	10·0	63·1	0·07	—	—	1·5	3·0
A52	(2) Matrix-gamma			4·3	0·2	11·3	12·8	68·1	ND			0·5	2·9
	(3) Gamma-prime			19·8	1·6	2·8	7·4	64·7	0·07			1·6	2·1
W50	(4) Carbide		50·0		17·6	1·1			0·2			26·3	4·8
	(1) Alloy	0·11	0·7	13·0	3·0	7·0	10·0	63·1	0·07	—	—	—	3·0
A51	(2) Matrix-gamma			3·6	0·6	11·2	11·4	70·1	ND				3·1
	(3) Gamma-prime			18·2	4·1	3·4	7·6	64·7	0·07				2·0
W49	(4) Carbide		50·0		33·9	1·3			0·2				14·6

(1) Nominal composition (2) Chemical analysis of solution (3) Mean of microprobe and 'spectro' results (4) Microprobe

the extractions subsequently re-fused and subjected to microprobe and spectrographic analyses, were a mixture of eutectic, formed from the liquid, and cuboidal-type, formed by solid-state reaction. Some checks were made on the composition of carbide extraction residues using spectrographic analysis. The microprobe analysis data were processed by the previously developed computer correction procedure.[1] A flow diagram is shown in Fig. 4.

Table I lists the chemical analyses of the cast ingots from which the individual test-pieces were prepared. Comparison of nominal and actual bulk analysis data supplied by Chemical Inspectorate showed maximum differences of 0·02 wt.-% carbon, and 0·4 wt.-% of the metallic elements present. Table II lists the quantitative electron microprobe analysis data (EMPA) for the dendrites, eutectic gamma-prime, and MC carbides *in situ* in relation to the parent-alloy compositions. Note that the MC analyses include the small concentrations of nickel and cobalt (up to 3%) detected by microprobe analysis. The term 'dendrite' here refers to the mean dendrite composition, and includes both the matrix gamma and approximately 60 vol.-% of cuboidal-type gamma-prime precipitate. A comparison, for the HRA-376 group, between the compositions of the MC carbides and eutectic gamma-prime analysed *in situ* by the microprobe, and the extraction-residue gamma-prime, analysed elsewhere, and extracted gamma-prime re-fused and subsequently microprobe analysed is given in Table III. Note that the MC data here exclude the small amounts of nickel and cobalt detected by EMPA. The compositions of the nickel-base matrices from chemical analyses of the liquids separated from the gamma-prime by extraction procedures are given in Table IV. Table V compares (for the HRA-376 group of materials) the parent-alloy compositions with those of the 'true' matrix (*i.e.* containing no gamma-prime), the 'average' gamma-prime (cuboidal plus eutectic), and the MC carbides.

A comparison between the two types of analysis (microprobe and spectrographic) gave similar relative concentrations of the metallic elements in each MC phase, but there were some discrepancies in the nickel content. Spectrographic analysis data are subject to greater error, since the MC phase is present to a level of only approximately 2% in the alloys, and small levels of contamination of the extraction residues will markedly affect the accuracy of the analysis. The microprobe analyses are believed to give the more accurate data, and were used exclusively for denoting carbide compositions in this work.

References

1. J. E. Restall, *Metallurgia*, 1969, **80** No. 479, 121–125.

© 1973. Metals and Materials.

Part II will appear in the April issue of *Metals and Materials*.

Constitution and microstructure of certain cast nickel superalloys: Part II*

by J. E. Restall and E. C. Toulson

This work is part of the continuing programme in the characterisation of phases in cast nickel superalloys. In the previous article (Part I) general microstructural features and compositions of the three principal phases present in the microstructure were described.

The results of the X-ray diffraction analyses of the structure of the three principal phases present in each of the HRA-376 group and the MM246 group alloys are listed in Table VI. All phases were found to be cubic. The binary Ni_3Al phase exhibits superlattice reflections whilst many alloyed gamma-prime phases in this series did not. Table VII compares the measured densities of alloys in the HRA-376 group with those calculated from the relationship $\rho = n\bar{A}/VN$, where n = number of atoms per unit cell, $\bar{A}$ = mean atomic weight, V = cell volume, and N = Avogadro's number.

Using the microprobe analysis results for the three groups of alloys, a series of linear regression equations were established to express the atomic concentration of an element in both the eutectic gamma-prime and MC phases in terms of the composition of the parent alloy and, separately, in terms of the concentration of other elements present in the phase. Table VIII lists these relationships.

From optical microscopy of as-cast testpieces in the HRA-376 group alloys, the average volume fraction of eutectic gamma-prime was 4% $\pm \frac{1}{2}$%. From examination of a minimum of 6 replicas of testpieces in the same group of alloys, the volume fraction of cuboidal gamma-prime was 60% $\pm$ 2%. In order to determine whether any significant quantity of gamma-prime precipitate dissolved in the orthophosphoric acid electrolyte during extraction procedures, some of the gamma-prime extracts were examined directly by electron microscopy. The morphology of the precipitates tended to be cubic with no visible rounding of edges or corners. Following the work of Blok *et al*[2] for further checking of the possibility of preferential elutriation of one or more elements by the orthophosphoric acid electrolyte, a solution of 1% ammonium sulphate: 1% citric acid was used as an alternative. This second electrolyte was not as efficient in extracting gamma-prime (it extracted only one quarter of the amount of precipitate), and had little effect on the composition of the gamma-prime, although chemical analysis of one gamma solution showed a lower tungsten concentration (*i.e.* 5·9 wt.-% as compared to 9·9 wt.-% tungsten from orthophosphoric acid electrolyte.

Discussion of results

Distribution of elements measured by microprobe analysis

From examination of the microprobe-analysis data given in Part I (March issue) on HRA-376 alloy (A33), it is evident that tantalum significantly partitions itself between the gamma-prime and carbide (see Fig. 5), whereas the tungsten appears

* Part I appeared in the March issue of *Metals and Materials*.

The authors are both with the Materials Science Department, the National Gas Turbine Establishment, Pyestock, Farnborough, Hants.

as a weaker MC carbide former, but partitions significantly to the matrix. The addition of niobium in A39 displaces tungsten from the carbide (Fig. 6), and gamma-prime phases to the matrix, whilst both niobium and tantalum are strong carbide and gamma-prime supporters. Total replacement of tantalum by niobium (A40) leads largely to the formation of a NbC phase, whilst the tungsten partitions to the matrix. Part-substitution of molybdenum for tungsten (A54) in HRA-376 alloy shows that neither element is a particularly strong MC or gamma-prime supporter. A similar trend in alloying behaviour for molybdenum is observed in alloy A53. Figure 7 shows microprobe-analysis scans for tantalum and aluminium. The replacement of tantalum and tungsten respectively by niobium and molybdenum (A60) resulted in partitioning of niobium to the carbide and gamma-prime (see Fig. 8), and the molybdenum to the matrix. Alloy A52 shows that an equal atomic % of titanium and tantalum, in combination with tungsten in the alloy, results in preferential partitioning of the former two elements to both the MC carbide (see Fig. 9) and gamma-prime, and the tungsten to the matrix. The total replacement of tantalum by titanium in the alloy A51 leads to the formation of a complex titanium/tungsten carbide, the residual titanium being largely distributed in the gamma-prime (see Fig. 10), and the tungsten in the matrix. When the four refractory metal elements are present in equal proportions in the alloy (A44), the niobium and tantalum partition to the carbide and gamma-prime, whilst the tungsten and molybdenum alloy with the gamma matrix. An indication of the sequence of distribution of elements in phases in the HRA-376 alloy group is given in Table IX.

From the HRA-376 group alloys it is clear that niobium, tantalum, and titanium partition preferentially to the carbide and gamma-prime phases. Further distinction between the roles of these elements shows that in alloys containing both niobium and tantalum, niobium is the stronger carbide former. Tungsten and molybdenum tend to partition to the gamma-matrix in niobium—containing alloys, and those containing tantalum and titanium together. Tungsten is a significant carbide former in the single presence of tantalum or titanium in the alloys A33 and A51. Molybdenum is not a strong MC former in any alloy among this group. For 'equivalent' alloys where molybdenum is substituted partly or wholly for tungsten, the molybdenum partitions more readily to the gamma matrices.

The two groups of alloys based on HRA-376 and MM246 behaved similarly, such that one group of elements partitioned preferentially toward the MC and gamma-prime, whilst another preferentially alloyed with the matrix. The data in Table

TABLE VI. X-ray diffraction results

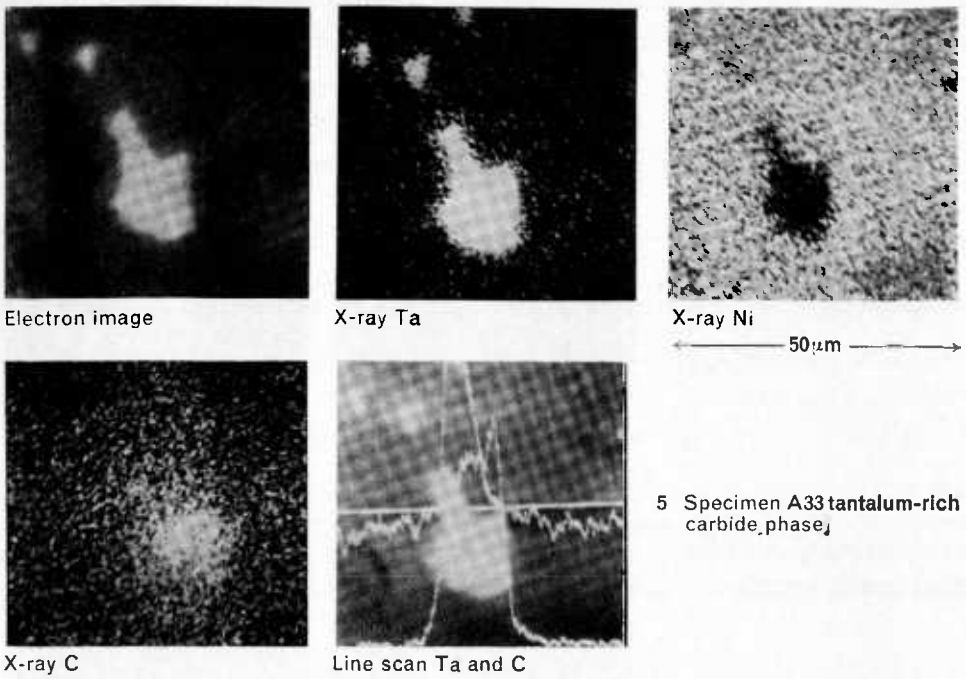
Alloy code	Phase	Lattice parameter (a) Å	Remarks	Calculated lattice parameter Å (a)	Percentage difference between calculated and measured lattice parameter	Percentage difference between calculated and measured cell volume
A33	(1) Matrix	3·591 ±0·002		3·632	1·1	3·5
	(2) Gamma-prime	3·586 0·001	Weak superlattice diffractions present	3·678	2·6	7·9
	(3) Carbide	4·439 0·003	carbide diffractions diffuse	4·315	2·8	8·2
A39	(1) Matrix	3·588 ±0·003		3·527	1·7	5·0
	(2) Gamma-prime	3·586 0·001	No superlattice diffractions detected	3·684	2·8	8·4
	(3) Carbide	4·441 0·002	carbide diffractions faint and spotty	4·440	0·02	0·07
A40	(1) Matrix	3·585 ±0·001		3·656	2·0	5·7
	(2) Gamma-prime	3·583 0·001	No superlattice diffractions detected	3·674	2·5	7·8
	(3) Carbide	4·443 0·003	carbide diffractions very spotty	4·398	1·0	5·9
A54	(1) Matrix	3·5850 ±0·0005		3·623	1·1	3·2
	(2) Gamma-prime	3·5850 0·0005	No superlattice diffractions detected	3·671	2·4	7·4
	(3) Carbide	4·431 0·003	carbide diffractions very broad and spotty	4·393	0·9	2·6
A53	(1) Matrix	3·592 ±0·003		3·622	0·9	2·6
	(2) Gamma-prime	3·5840 0·0005	No superlattice diffractions detected	3·681	2·7	8·3
	(3) Carbide	4·427 0·003	carbide diffractions strong but very broad	4·480	1·2	3·6
A44	(1) Matrix	3·583 ±0·002		3·626	1·2	3·6
	(2) Gamma-prime	3·583 0·0005	No superlattice diffractions detected,	3·678	2·7	8·2
	(3) Carbide	4·445 0·003	carbide diffractions very spotty	4·469	0·4	2·8
A60	(1) Matrix	3·591 ±0·003		3·622	0·9	2·6
	(2) Gamma-prime	3·583 0·0005	Weak superlattice diffractions, carbide	3·669	2·4	7·4
	(3) Carbide	4·451 0·002	diffractions weak and spotty	4·451	0	0
A52	(1) Matrix	3·587 ±0·003		3·619	0·9	2·7
	(2) Gamma-prime	3·5785 0·0005	No superlattice diffractions detected	3·620	1·1	3·5
	(3) Carbide	4·389 0·0015	carbide diffractions strong, broad and very spotty	4·440	1·16	3·4
A51	(1) Matrix	3·5835 ±0·0005		3·587	0·1	0·3
	(2) Gamma-prime	3·581 0·001	Very weak superlattice diffractions,	3·523	1·6	5·0
	(3) Carbide	4·319 0·001	carbide diffractions weak but very sharp	4·333	0·3	1·0
A101	(1) Matrix	3·595 ±0·002				
	(2) Gamma-prime	3·5825 0·0005	No superlattice diffractions detected,			
	(3) Carbide	4·344 0·001	lattice parameter close to that of TiC (4·33 Å)			
A102	(1) Matrix	3·583 ±0·002				
	(2) Gamma-prime	3·581 0·0005	No superlattice diffractions detected,			
	(3) Carbide	4·356 0·001	mixed titanium-tantalum carbide			
A103	(1) Matrix	3·567 ±0·002				
	(2) Gamma-prime	3·5725 0·0005	Strongest superlattice diffractions			
	(3) Carbide	4·375 0·001	detected, mixed titanium-tantalum carbide			
A104	(1) Matrix	3·566 ±0·002				
	(2) Gamma-prime	3·572 0·0005	Strong superlattice diffractions detected,			
	(3) Carbide	4·378 0·001	mixed titanium-tantalum carbide			
A105	(1) Matrix	3·563 ±0·002				
	(2) Gamma-prime	3·5705 0·0005	Strong superlattice diffractions detected,			
	(3) Carbide	4·307 0·001	mixed titanium-chromium carbide			
A106	(1) Matrix	3·561 ±0·002				
	(2) Gamma-prime	3·5665 0·0005	Strong superlattice diffractions			
	(3) Carbide	— —	detected, complex diffraction pattern (non-cubic): possibly M_7C_3			

Note: 1. All phases in both groups of alloys, except for the carbide in A106, were cubic.

2. Lattice parameters (a) calculated with reference to Table V, and assumes atoms adopt face centred cubic structure. Thus closest distance of approach between atom centres = $a\sqrt{2}/2$ and $a = 4r/\sqrt{2}$, where r is the Goldschmit atomic radius. Values of r were taken from reference 5, Thus, calculated lattice parameter $\bar{a} = \sum_{i=1}^{n} Ci.ai$, where n = number of elements, Ci = atomic fraction of particular element, and ai = lattice parameter of particular element.

3. For stoichiometric Ni_3Al, the lattice parameter is 3·567 Å. The differences obtained between this value and that calculated from (2) is 2·7% for lattice parameter (a), and 8% for cell volume (a^3).

4. Small concentrations of Ni and Co in MC phases ignored. Mixture-law relationships calculated of the form $\bar{a} = \sum_{i=1}^{n} Ci \cdot ai$, where ai is the lattice-parameter value for stoichiometric. TiC, NbC, TaC given in reference 9. Chromium assumed to be combined as cubic $Cr_{23}C_6$ phase.



5 Specimen A33 tantalum-rich carbide phase

II refer solely to quantitative electron-probe microanalysis and were not supported by spectrographic or other chemical analysis techniques. For MM246 alloy (A101) it is clear that the titanium and tantalum are good MC carbide formers. In addition titanium segregates significantly to the eutectic gamma-prime whilst the tungsten and molybdenum tend to alloy with the matrix. (Note that the dendrite composition reflects that of the matrix). Alloy A102 (molybdenum-free) shows that titanium and tantalum segregate towards the MC carbide and gamma-prime, while tungsten, chromium, and cobalt alloy with the matrix gamma. Removal of both tungsten and molybdenum from MM246 (*i.e.* A103) leads to a greater partitioning of tantalum to the MC and gamma-prime phases. Removal of cobalt (A104 alloy) resulted in a material containing no eutectic gamma-prime. However, titanium and tantalum showed characteristic carbide-forming tendencies. Alloy A105, tantalum-free, was also free of eutectic gamma-prime, and the MC was very rich in titanium. Alloy A106, free of all gamma-prime-forming elements except aluminium, and all carbide-forming elements except chromium, was free of eutectic gamma-prime. The carbide phase was chromium-rich.

The third group of materials includes *Nimocast* 713C, IN100, and MM200 alloy. The first alloy, 713C, shows differences relative to the other two materials by virtue of the absence of cobalt and the very small amounts ($< 0{\cdot}5\%$) of eutectic gamma-prime present in the microstructure. It is clear that, in common with many other alloys, titanium and niobium tend to segregate to the MC and gamma-prime phases. Chromium and molybdenum do not alloy so readily with the MC and gamma-prime. For the IN100 alloy, titanium predominates in the MC phase, which contains a significant quantity of molybdenum and approximately 12% vanadium. The gamma-prime phase also is titanium-rich. The general pattern for titanium and niobium to partition preferentially to MC and gamma-prime phases is exhibited by MM200 alloy. Chromium, cobalt and tungsten tend to alloy preferentially with the matrix in the latter material.

The elements exhibiting strong MC carbide-forming tendencies were also scavengers for the small amounts of sulphur present in the alloys (see Fig. 11). These metallic elements could also be detected in complex boride phases (Fig. 12).

Comparison between microprobe analysis data and those from other techniques

A comparison may be made by reference to Table III between the results of the various types of analysis applied to the gamma-prime phase in the HRA-376 alloy group. The 'calculated' analyses are based on the wet chemical (colorimetric) analysis of the gamma phase remaining after filtration of extraction residues, and assumes the alloy contains approximately 60 vol.-% of gamma-prime phase and 40% of the matrix gamma. In the various analyses, the data tabulated refer generally to a mean of at least two determinations. For microprobe analysis, a minimum of three sets of data were evaluated. Comparing aluminium contents in the series, with the exception of one or two low values from spectrographic analysis, there is agreement to within approximately 1·5 atomic-% of the average value for any alloy. For titanium in A52 and A51, apart from the higher concentration in the eutectic gamma-prime, there is acceptable agreement between the data. The chromium content of 're-fused' material is, with the exception of A60, in good agreement throughout the series. The eutectic gamma-prime tends on average to contain more chromium than the cuboidal gamma-prime phase. The cobalt contents of the gamma-prime phases are in good agree-

TABLE VII. Measured and calculated densities of alloys in HRA-376 group

Alloy code	Measured density kg/m³ × 10³	Calculated density for given vol-%	γ'/γ
A33	8·85	8·72	60/40
		8·70	65/35
A39	8·65	8·67	60/40
		8·64	65/35
A40	8·40	8·44	60/40
		8·41	65/35
A54	8·60	8·62	60/40
		8·60	65/35
A53	8·45	8·43	60/40
		8·43	65/35
A44	8·40	8·40	60/40
		8·37	65/35
A60	8·10	8·12	60/40
		8·10	65/35
A52	8·50	8·44	60/40
		8·41	65/35
A51	8·30	8·27	60/40
		8·22	65/35

Note: Compositions listed in Table V.

Density $\rho = n\bar{A}/VN$ where n = number of atoms per unit cell, $\bar{A}$ = mean atomic weight, V = cell volume, N = Avogadro's Number = $6{\cdot}023 \times 10^{23}$/mol.



6 Specimen A39 niobium-rich carbide phase

ment throughout the series, as are the niobium contents. Relative to the cuboidal gamma-prime phases, the eutectic on average appears to have a greater solubility for niobium. Similar results were obtained for tantalum throughout the series, and there was a tendency on average for the eutectic phase to contain more tantalum. There was fairly good agreement on molybdenum and tungsten (except for A54) contents throughout the series, though, in contrast to the effects of Nb and Ta, the eutectic gamma-prime phases tended to have lower tungsten and molybdenum contents than the cuboidal gamma-prime.

Phacomp and composition of matrix phases

The results of the chemical analyses of the various matrix phases (Table IV) showed that significant quantities of gamma-prime- and carbide-forming elements dissolve in the heavily alloyed nickel matrix. These data are at variance with the assumptions of the Phacomp procedure,[3] developed for predicting the phase relationships occurring in high-temperature materials during prolonged service exposure. In Phacomp it is assumed that none of these elements dissolve in the matrix phase. However, the gamma-prime powder residues examined in the electron microscope appeared unattacked by the electrolyte and, without a certain quantity of these elements dissolving in the matrix phase, the analyses of the gamma-prime and carbide phases were insufficient to give good correlation with the parent-alloy compositions. Although the Phacomp procedure, developed by Woodyatt *et al* for predicting the tendency for alloys to form TCP phases during prolonged exposure in service, contains many assumptions concerning the constitution and microstructure, the value of the critical factor (the average electron vacancy number, $\bar{N}v$) derived from these assumptions differs from the $\bar{N}v$ derived by a different route in the present work.



7 Specimen A53 tantalum-rich gamma-prime

Phacomp procedure

The method developed by Woodyatt *et al* for predicting the occurrence of a sigma-type phase from the composition in austenitic superalloys is simplified as follows:

1. The alloy composition is evaluated in atomic-%.
2. All of the boron combines to form a complex boride of the following general composition (Mo 0·5: Ti 0·15: Cr 0·25: Ni 0·10)$_3$ B$_2$
3. One half of the carbon forms monocarbides in the order of preference: TaC, NbC, ZrC, TiC, VC. The remaining carbon forms $M_{23}C_6$ [$Cr_{21}(MoW)_2C_6$, or $Cr_{23}C_6$ in absence of Mo and W] at Mo + W levels less than 6%. Above this level M_6C [$(Ni\ Co_2\ Mo_3)C$] forms in place of $M_{23}C_6$.
4. All of the aluminium plus niobium, and titanium available after carbide precipitation, and chromium equal to 10% of the parent-alloy composition combine with three times as much nickel to form gamma-prime [$Ni_3(Al . Ti . Nb)$].
5. The remaining amounts of the various elements after phase formation are scaled to 100 and are equal to the matrix atomic composition. The mean electron vacancy number Nv is calculated from the matrix composition as

$$\bar{N}v = \sum_{i=1}^{n} Mi\,(Nv)i$$

where $\bar{N}v$ = average electron-vacancy number, Mi = the atomic fraction of particular element, Nv = individual electron-vacancy number of particular element, and n = number of elements in matrix. Thus

$\bar{N}v$ = 4·66 (Cr + Mo) + 1·71 (Co) + 0·66 (Ni)

Alloys with $\bar{N}v$ less than 2·52 are unlikely to form sigma, those with $\bar{N}v$ greater than 2·52 have been reported to contain sigma. For cast alloys the Phacomp relationship is still found to apply, but less accurately than for wrought alloys. From reference 3, and assuming that W substitutes for Mo, and Nb or Ta substitutes for Ti in the boride phases, that half the carbon forms MC, and the remainder $Cr_{21}(Mo, W)_2C_6$, the mean electron vacancy number, $\bar{N}v$, obtained for the HRA-376 group of alloys was 1·97.

TABLE VIII. Linear regression equations for constitution of eutectic gamma-prime, monocarbide phases, and parent-alloy constitution for the three groups of alloys

Element	Confidence limit, atomic %	Phase	K±	Atomic-% of element present in phase = f (parent-alloy composition) = constant (K) + a.Al + b.Ti + c.Cr etc	Comments
Aluminium	1·0	Eutectic gamma-prime	30·3 ± 1·9	Al = 30·3 − 0·88 Ti − 1·06 Cr − 0·31 Co − 1·44 Nb − 0·81 Ta	Excludes *Nimocast* 713C (A21) and alloys A104, A105, and A106
Titanium	1·2	,,	26·3 ± 3·3	Ti = 26·3 − 0·85 Al − 1·08 Cr − 1·53 Nb − 1·16 Ta	
Chromium	0·65	,,	15·6 ± 3·7	Cr = 15·6 − 0·44 Al − 0·48 Ti − 0·85 Nb − 0·64 Ta	
Cobalt	1·72	,,	86·1 ± 12·3	Co = 86·1 − 0·33 Al − 1·15 Ni	
Nickel	1·25	,,	67·7 ± 0·9	Ni = 67·7 − 0·61 Co	
Niobium	0·52	,,	18·0 ± 2·4	Nb = 18·0 − 0·56 Al − 0·56 Ti − 0·70 Cr − 0·18 Co − 0·60 Ta	
Molybdenum	0·41	,,	0·9 ± 0·1	Mo = 0·9 − 0·09 Ti − 0·50 W	
Tantalum	0·87	,,	18·3 ± 4·3	Ta = 18·3 − 0·54 Al − 0·71 Ti − 0·88 Cr − 1·20 Nb	
Tungsten	0·77	,,	1·65 ± 0·17	W = 1·65 − 0·15 Ti − 1·5 Mo	
Titanium	1·29	MC	17·9 ± 5·5	Ti = 17·9 − 0·24 Ti + 1·43 Cr + 19·16 Zr − 12·29 Nb − 1·62 Mo − 12·15 Ta − 1·57 W	Excludes alloys A105 and A106
Zirconium	0·1	,,	0·2 ± 0·04	Zr = 0·2 + 0·05 Nb − 0·05 Mo + 0·05 Ta	
Chromium	1·67	,,	3·4 ± 1·6	Cr = 3·4 − 0·85 Mo − 0·45 W	
Niobium	2·39	,,	3·0 ± 2·2	Nb = 3·0 − 0·28 Cr + 15·58 Nb	
Molybdenum	1·17	,,	−1·0 ± 0·5	Mo = − 1·0 − 0·74 Ti + 1·36 Mo	
Tantalum	3·21	,,	2·6 ± 1·2	Ta = 2·6 − 1·75 Nb + 13·47 Ta	
Tungsten	3·86	,,	12·8 ± 10·3	W = 12·8 − 0·56 Cr − 118·0 Zr + 2·05 W	
				Atomic-% of element present in phase = f (phase composition) = constant (K) + a.Al + b.Ti + c.Cr etc	
Aluminium	2·3	Eutectic gamma-prime	20·8 ± 0·6	Al = 20·8 − 0·59 Ti − 0·35 Nb	Excludes A104, A105, A106 and Nimocast 713C
Titanium	1·5	,,	15·1 ± 1·5	Ti = 15·1 − 0·43 Al − 1·36 Nb − 1·20 Ta − 1·28 W	
Chromium	0·7	,,	13·5 ± 3·0	Cr = 13·5 − 0·36 Al − 0·40 Ti − 0·73 Nb − 0·56 Ta	
Cobalt	1·7	,,	86·3 ± 11·8	Co = 86·3 − 0·35 Al − 1·15 Ni	
Nickel	1·3	,,	72·8 ± 2·2	Ni = 72·8 − 0·25 Al − 0·69 Co	
Niobium	0·8	,,	14·3 ± 3·0	Nb = 14·3 − 0·39 Al − 0·56 Ti − 0·79 Cr − 0·75 Ta	
Molybdenum	0·4	,,	0·9 ± 0·1	Mo = 0·9 − 0·08 Ti − 0·49 W	
Tantalum	1·2	,,	4·8 ± 0·4	Ta = 4·8 − 0·56 Ti − 0·95 Nb − 0·98 W	
Tungsten	0·8	,,	1·6 ± 0·2	W = 1·6 − 0·15 Ti − 0·16 Mo	
Titanium	2·1	Monocarbide	47·2 ± 0·9	Ti = 47·2 − 0·65 Cr − 0·98 Nb − 0·70 Mo − 0·95 Ta − 0·75 W	Excludes A105 and A106
Chromium	1·8	,,	1·1 ± 0·7	Cr = 1·1 + 11·64 Zr − 0·06 Nb − 0·06 Ta −0·13 W	
Zirconium	0·2	,,	0·24 ± 0·03	Zr = 0·24 − 0·005 Ti − 0·04 Cr	
Niobium	2·1	,,	48·2 ± 0·8	Nb = 48·2 − 1·02 Ti − 0·69 Cr − 0·73 Mo − 0·97 Ta − 0·77 W	
Molybdenum	2·5	,,	40·4 ± 8·5	Mo = 40·4 − 0·82 Ti − 0·74 Cr − 0·82 Nb − 0·79 Ta − 0·70 W	
Tantalum	2·3	,,	49·6 ± 0·9	Ta = 49·6 − 1·05 Ti − 0·70 Cr − 1·03 Nb − 0·74 Mo − 0·79 W	
Tungsten	3·4	,,	57·3 ± 4·6	W = 57·3 − 1·20 Ti − 0·87 Cr − 1·18 Nb − 0·95 Mo − 1·14 Ta	

equations expressing the concentration of elements in the eutectic gamma-prime and MC carbide phases in terms of the other elements present, and the composition of the parent alloys. The equations were of the type

$$\%A = ax + by + cz + \ldots$$

where a, b, and c are coefficients and x, y, and z are atomic percentages of elements x, y, and z respectively. In terms of 'significant' elements in gamma-prime, three groups of elements could be separated, one containing Al, Ti, Cr, and Nb, the second showing the interdependence of Mo, W, and Ti, and the third the interdependence of Co and Ni. From the regression equations for the percentage of an element in the MC carbide, two anomolies were found. The zirconium content could be expressed as a function of titanium and chromium, and the chromium content was a linear function of zirconium, niobium and tantalum.

Comparison between analyses and those reported in the literature

A further observation arising from the present work was that, in contrast to the order of preference for MC formation given by Sims,[6] niobium is a much stronger monocarbide former than either

The work of Kreige and Baris[4] on commercial superalloys also showed that significant quantities of aluminium, with somewhat lesser amounts of titanium, niobium, and tantalum are present in the matrix phases. Their influence on the matrix electron vacancy number cannot be ignored.

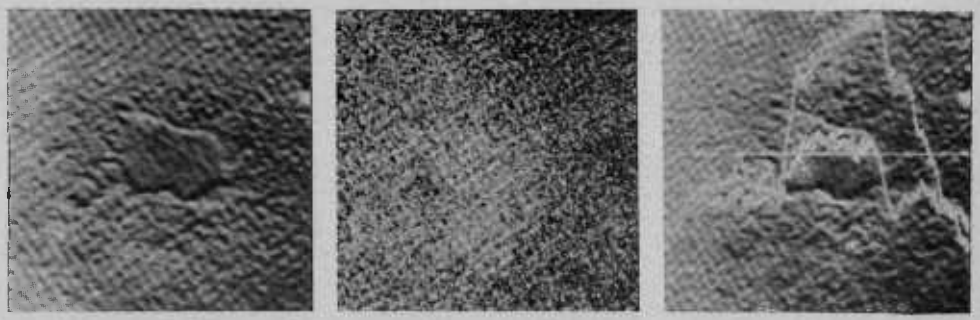
From the present work it was clear that niobium was a stronger MC former than tantalum, and that significant quantities of aluminium, titanium, niobium, and tantalum are soluble in the gamma matrix phases. Using the analyses of the various matrices from Table IV, the following mean electron vacancy numbers were obtained:

Alloy	A33	A39	A40	A54	A53	A44	A60	A52	A51
$\bar{N}v$	1·86	1·66	1·82	1·87	1·81	1·83	1·81	1·70	1·64

For the purpose of these calculations, except for Ni and Co the Nv was assumed to be 10·66 minus the group number of the element in the periodic table, and thus $NvAl = 7·66$. Note that the mean electron vacancy numbers of the alloys calculated here are somewhat lower than those derived from the Phacomp procedure described above. From the present work, the solubility of all elements present in the gamma matrices is accounted for in deriving the values of $\bar{N}v$, whereas other Phacomp procedures ignore the fact that Al, Ti, Nb, and Ta are present in the gamma phase of nickel-base superalloys. The revised procedure applied to true matrices analyses obtained by Kriege and Baris, gives an $\bar{N}v$ of 2·35 for IN100 alloy, and of 2·44 for *Nimocast* 713C alloy. From published Phacomp procedures, the Nv of IN100 and *Nimocast* 713C are in the region of 2·5. Unless the melt compositions are rigidly controlled, both IN100 and *Nimocast* 713C are sigma prone. There was no evidence of the formation of M_6C or sigma phase in test-pieces exposed for 2 000 h at 1123 K.

Correlation of composition with lattice parameter and density

Table V details the composition of the three principal phases for each alloy in the HRA-376 series, in relation to the individual parent-alloy composition. From these data it is evident that titanium, niobium, and tantalum tend to form carbides and to alloy with the gamma-prime phases in preference to alloying with the gamma matrices. With the exception of the alloys in which it forms pseudo-binary carbides with tantalum or titanium (there are always traces of other elements present), tungsten preferentially alloys with the gamma phases. Chromium, cobalt, and molybdenum preferentially alloy with the matrix phases. Zirconium is not present in large amounts in any of the alloys but can readily be detected in MC carbides and in the gamma-prime phases.



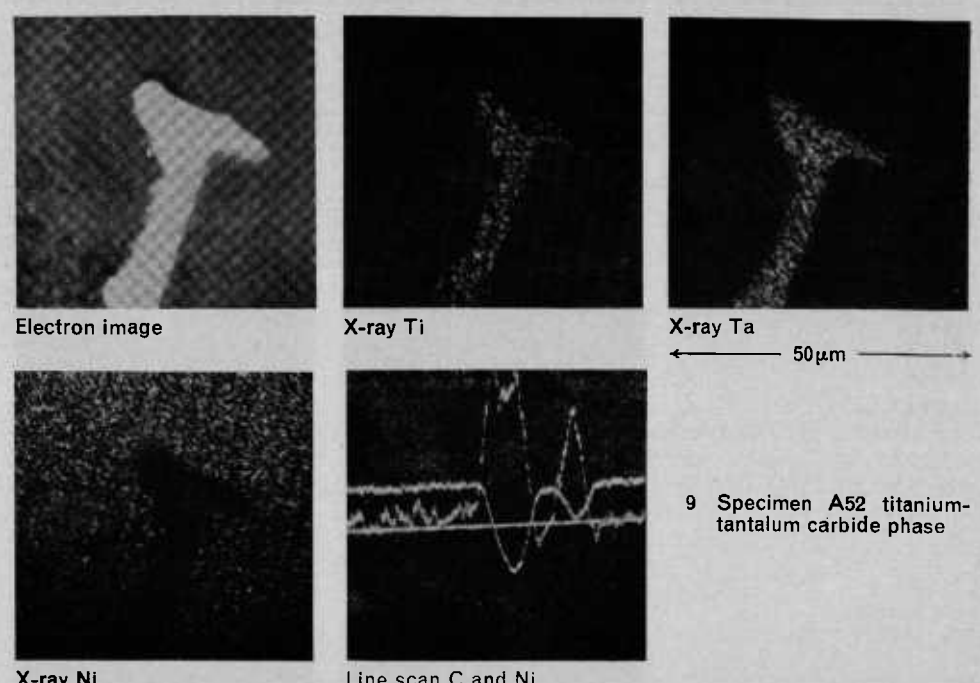
8 Specimen A60 niobium-rich gamma-prime

Table VI lists the lattice-parameter measurements for the phases in both the HRA-376 and MM246 series of alloys. It was noted that the lattice parameters of the matrix phases throughout both series of alloys were higher than the accepted value for pure Ni ($a_0 = 3·5240$ Å) and, with the exception of the gamma-prime phase in alloy A106 of the MM246 group, that the lattice parameters of the precipitation hardening phase were higher than that given for stoichiometric Ni_3Al ($a_0 = 3·5673$ Å). These data were used in conjunction with Table V to explore law-of-mixtures relationships with respect to the lattice parameter of the constituents. For calculation of the lattice parameter of the phases, a co-ordination number of twelve was assumed – that is, each atom was in contact with twelve nearest neighbours, the lattice was face centred cubic, and the Goldschmidt atomic radii were taken from reference 5. Very good agreement was obtained between the measured lattice parameters and those calculated from a simple law-of-mixtures relationship.

Further combined use of Tables V and VI and electron microscope observations of the volume of gamma-prime precipitate (approximately 60 vol-%) is illustrated in Table VII which lists the measured and calculated densities of alloys in the HRA-376 group, With the exception of the A33 alloy, where the difference is 1·7%, the measured and calculated values of alloy density are in very good agreement.

Constitution of phases and parent-alloy compositions

Table VIII lists the linear regression

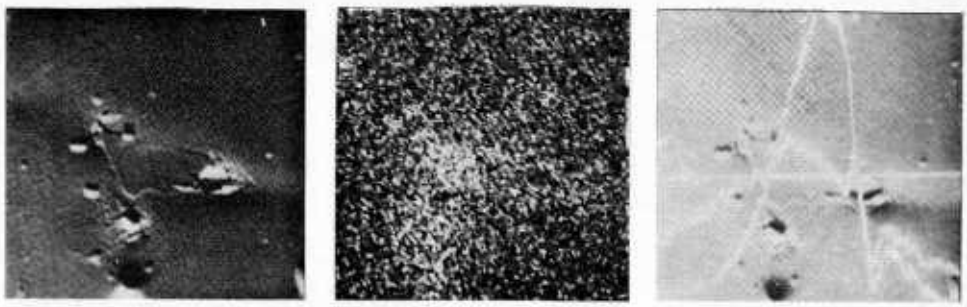


9 Specimen A52 titanium-tantalum carbide phase

tantalum or titanium in as-cast nickel superalloys. Tantalum is a stronger monocarbide former than titanium when these two elements are present in equi-atomic proportions in the cast superalloy designated A52. It is not clear whether Sims' observations were based on alloys containing equi-atomic proportions of the significant elements. A comparison of the data from the present study on the MM200 alloy with those published by Gregg and Piearcey[8] gave lower titanium, slightly higher chromium, and higher tungsten contents in the eutectic gamma-prime phase. The NGTE analyses of 'equiaxed-cast' MM200 alloy gave higher aluminium and niobium contents for the eutectic gamma-prime, and higher titanium and lower tungsten content of the carbide, than the data given in reference 8. The NGTE analyses of eutectic gamma-prime also gave higher aluminium and titanium contents than those listed by Sims for MM200 alloy. The results of a comparison of the NGTE microprobe analysis data for eutectic gamma-prime with data on wet chemical analysis of extracted gamma-prime residues cited by Kreige and Baris were as follows. The aluminium, titanium, and chromium contents of eutectic gamma-prime in the MM200 alloy were higher than the values from the residue analysis by 1·3 wt.-% Al, 1·8% Ti, and 2% Cr respectively. The Nb content was 0·7% lower, and the W content 8% lower than the values quoted by Kreige *et al.* Comparison of the NGTE data with those of Kreige for the IN100 alloy gave an agreement to within 1·0 wt.-% for all constituent elements (*e.g.* to within 0·7 wt.-% for aluminium), but the vanadium contents differed significantly (0·3 wt.-% V for eutectic gamma-prime compared to 1·3 wt.-% V from residue analysis). Good agreement was obtained between the microprobe analyses and wet chemical analyses of a bulk sample of gamma-prime, containing six elements and cast at NGTE.

Conclusions

The structure and composition of phases present in three groups of cast nickel alloys have been studied using a combination of optical and electron microscopy, electron microprobe analysis, wet chemical and spectrographic techniques, and X-ray diffraction. The initial objective was to determine the way in which the complex mixture of alloying elements partitioned between the three principal phases – gamma-prime, matrix, and carbide – present in the microstructure. Elements that tended to form monocarbide (MC) phases (*i.e.* niobium, tantalum, and titanium tended to alloy preferentially with the gamma-prime phases. Tungsten, molybdenum, chromium, and cobalt tended to alloy preferentially with the matrix phases. These general trends were observed

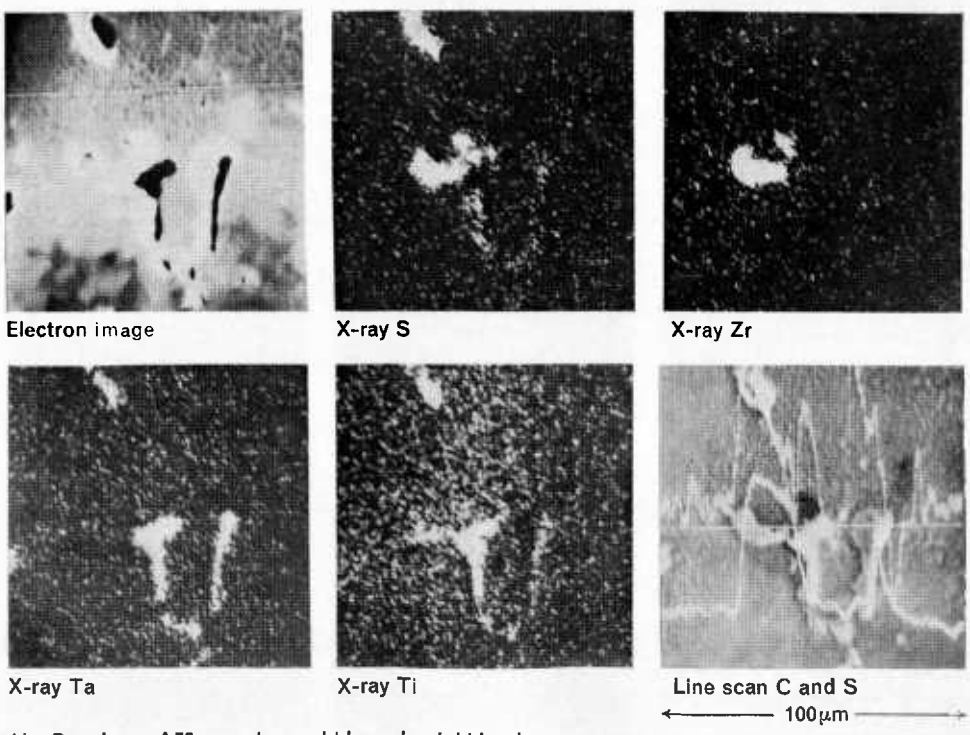


10 Specimen A51 titanium-rich gamma-prime

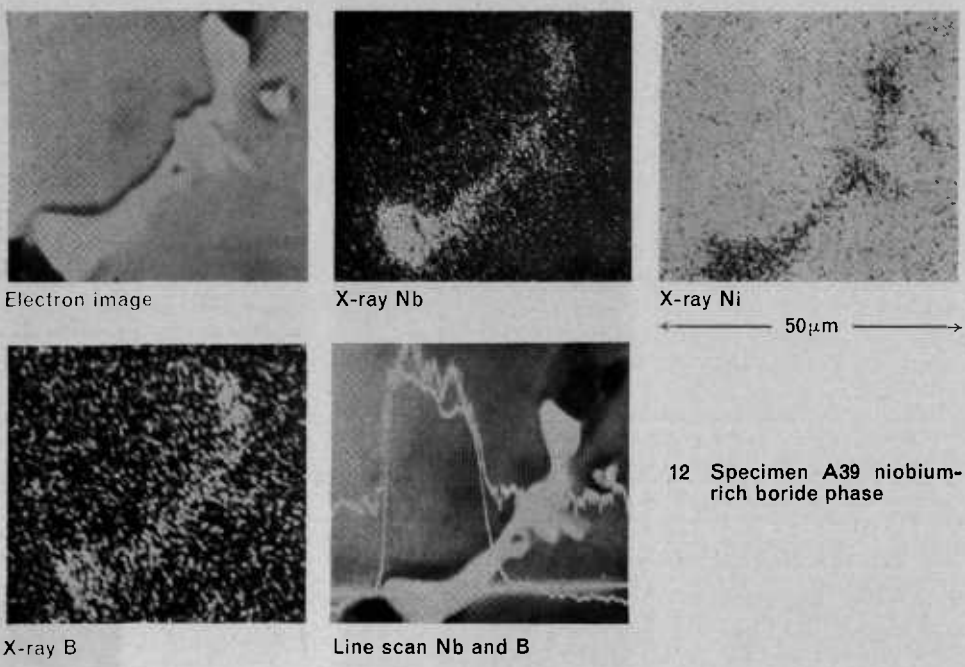
TABLE IX. Distribution tendency of alloying elements between matrix, gamma-prime and carbide phases in H.R.A.-376 alloy group

Alloy composition	Matrix	Gamma-prime	Carbide (MC)
3 Ta—3W	W	Ta	Ta W
3 Ta—3Mo	Mo	Ta	Ta
3 Ti—3W	W	Ti	Ti W
3 Ta—1½W—1½Mo	MoW	Ta	Ta
1½Ti—1½Ta—3W	W	Ti Ta	Ta Ti
3 Nb—3W	W	Nb	Nb
3 Nb—3 Mo	Mo	Nb	Nb
1½Nb 1½Ta—3W	W	Ta Nb	Nb Ta
1½Nb 1½Ta—1½W—1½Mo	MoW	Ta Nb	Nb Ta

throughout the three groups of materials. Generally good agreement was obtained between the microprobe, wet chemical, and spectrographic data for the gamma-prime phases analysed. Good correlation was obtained between the measured and calculated values of the lattice parameter of phases and density of the parent alloys in the HRA-376 group of alloys. A series of linear regression equations were developed to relate the composition of the phases and parent alloys. Some of the assumptions of the Phacomp procedure for predicting phase equilibria in cast superalloys were tentatively explored. Mean electron vacancy numbers were calculated for gamma



11 Specimen A52 complex carbide and sulphide phases



12 Specimen A39 niobium-rich boride phase

matrix phases containing Al, Ti, Nb, and Ta by a procedure slightly different from those published in the literature, which ignores the real presence of these elements in the gamma phase in commercial nickel superalloys. It is suggested that the present work may be used as a basis for modifying the Phacomp procedure.

Acknowledgements

The authors wish to acknowledge the assistance of Mr. R. Freeman, Fulmer Research Institute Ltd. with the X-ray diffraction analyses, and that of Mr. Cadwell, Mathematical Services Dept., RAE, for processing the linear regression equations.

References

2. N. I. Blok and A. I. Glazova, (trans. E. Haifer, 1968, AD 682767) 'Comparisons of Methods of Separating Phases in Nickel-Chromium Alloys. in 'Spectro and Chemical Methods of Analysing Materials', Izd-VO Metallurgiya, 1964, Moscow.

3. L. Woodyatt *et al*, *Trans. Met. Soc. AIME*, 1966, **236**, 519–527.

4. O. H. Kreige and J. M. Baris, *Trans. ASM Quarterly*, 1969, **62**, No. 1, 195–200.

5. A. Taylor, 'X-ray Metallography', 1961, John Wiley and Sons Inc.

6. C. T. Simms, 'The Role of Refractory Metals in Austenitic Superalloys', 1968, 6th Plansee Seminar.

7. R. A. Gregg and B. J. Piearcey, *Trans. Met. Soc. AIME*, 1964, Vol. **230**, 599–600.

8. B. J. Piearcey *et al. ASM Trans. Quart.*, 1967, **60**, 634–645.

9. H. J. Goldsmidt, 'Interstitial Alloys', 1967, Butterworths.

© 1973. Metals and Materials.

LABORATORY METHODS
MECHANICAL : CHEMICAL : PHYSICAL : METALLOGRAPHIC
INSTRUMENTS AND MATERIALS

SEPTEMBER, 1969 Vol. LXXX, No. 479

An Examination of Correction Procedures for Quantitative Electron-Probe Microanalysis

By J. E. Restall

National Gas Turbine Establishment

Three computer programs, written in Mercury Autocode, have been prepared for the correction of electron-probe microanalysis data obtained from commercial alloys, carbides and other materials. The procedures include "dead-time" correction for the counters and electronic circuitry, and corrections for background "noise", X-ray absorption, fluorescence and atomic number effects. A comparison is made between results obtained from electron-probe microanalysis at 25 kV. of seven materials using two sets of mass absorption coefficients (Birks' and Heinrich's), and three types of iterative procedure for correction of the raw data measured by the probe. It is concluded that recent correction procedures selected from the literature, using Heinrich's mass absorption coefficients, a fluorescence correction by Reed and an atomic number correction developed by Duncumb and Reed give an acceptable accuracy of quantitative analysis for: molybdenum disilicide, binary nickel-aluminium compounds and an experimental niobium alloy. Comparative data are given for carbide phases in a nickel alloy.

At this time several articles describing correction procedures for electron-probe microanalysis have appeared in the literature and computer programs have been developed to overcome the otherwise tedious and time-consuming process of evaluating these procedures 'by hand'.[1-3] The starting point in quantitative electron-probe microanalysis involves deducing the concentration of each element in a sample from a comparison between the characteristic X-ray intensity measurements of the sample and standards under identical experimental conditions. Castaing[4] showed that to a first approximation the ratio of the intensities from the specimen and from a pure metal standard is equal to the mass concentration of the element A in the specimen, i.e.

$$K_A = C_A \qquad (1)$$

Corrections have to be made to the intensity ratio to convert it more accurately to a mass concentration. These correction procedures include 'dead-time' associated with the finite resolving time of the counter and associated electronic circuitry, a correction for X-ray absorption, a correction for X-ray fluorescence and a correction for the effective penetration of the electron beam. The latter, generally referred to as the "atomic number" effect, applies to the generation of X-rays and according to Duncumb and Reed[5] should be treated as a separate factor.

Computer Programs

Three computer programs have been prepared for the correction of raw intensity data from materials containing combinations of up to eight elements in order to select an acceptable procedure to give consistent agreements between microprobe and bulk analysis data for commercial and experimental high temperature materials. The correction procedures used in the calculations can be visualised by reference to the flow diagram shown in Fig. 1. The programs are initially based on comparing the characteristic X-ray intensity generated in a specimen to that generated in a pure element standard under the same conditions after correction of both peak and background intensities for "dead-time". The dead-time correction is given by

$$N_t = \frac{N_o}{1 - N_o T} \qquad (2)$$

where N_t and N_o are (respectively) the true and measured counting rates and T is the dead-time (μsec.) for the entire counting system. Measured relative intensities are then obtained by calculating the ratio of sample to standard intensities. At this stage the three programs, although based on the same theories for absorption, fluorescence and atomic number, differ.

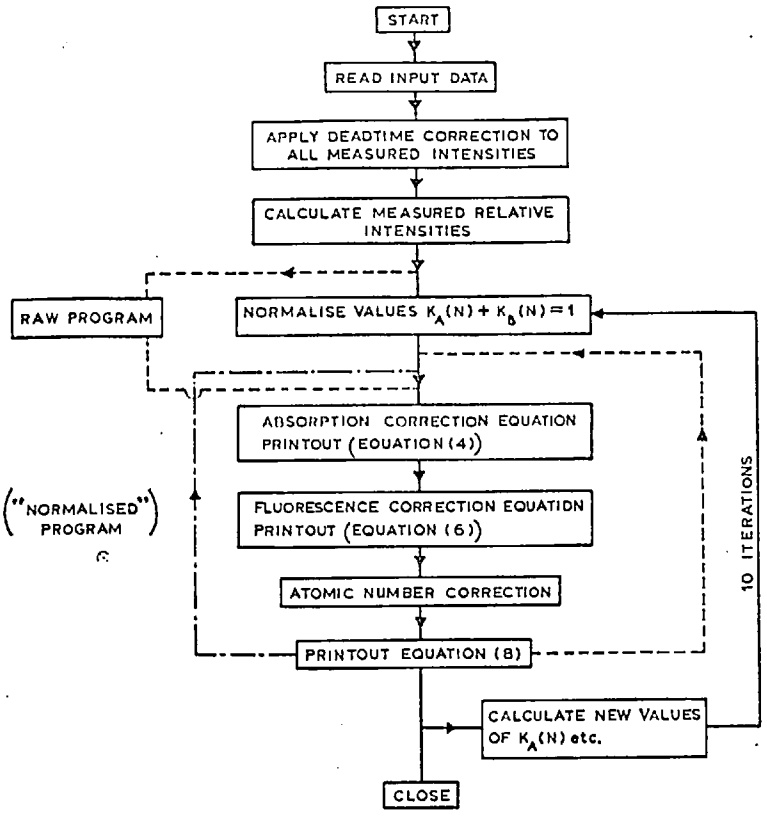
The absorption correction procedure used throughout the programs is based on the Philibert[6] expression:

$$f(\chi) = \frac{1 + h}{\left(1 + \frac{\chi}{\sigma}\right)\left[1 + h\left(1 + \frac{\chi}{\sigma}\right)\right]} \qquad (3)$$

using the Duncumb and Shield value of electron mass absorption coefficient

$$\sigma = \frac{2{\cdot}39 \times 10^5}{E_o^{1{\cdot}5} - E_c^{1{\cdot}5}}$$

In these equations $h = 1{\cdot}2\,A/Z^2$, and A and Z are atomic weight and atomic number, respectively. $\chi = (\mu/\rho)\,\mathrm{cosec}\,\theta$ where μ/ρ is the X-ray mass absorption coefficient and θ the take-off angle of the emitted radiation. E_o and E_c are respectively, the electron accelerating voltage and critical excitation voltage (kV.) for the element being analysed. Values of μ/ρ and h for the sample compositions are calculated by summing the product of the variable multiplied by its weight fraction, for the composition



NOTE.

(i) "Standard" program uses measured relative intensities multiplied by correction coefficients (absorption, etc.) based on normalised concentrations.

(ii) "Raw" program uses similar correction procedure to the above except that the concentrations are not normalised at any stage.

(iii) "Normalised" program uses similar correction procedure to (i) but results are based on $K_A(N)$ multiplied by appropriate coefficients.

Fig. 1.—Flow diagram of "standard" computer program.

being considered. The mass concentration of an element corrected for absorption is given by:

$$C_A = K_A \cdot \frac{f(\chi)_A^A}{f(\chi)_A^S} \qquad (4)$$

where $f(\chi)_A^A$ and $f(\chi)_A^S$ refer respectively to the pure element and sample respectively.

In addition to the primary characteristic emission of a particular wavelength generated by the incident electron beam, other more energetic ($> E_c$) X-radiation can cause additional emission of the same wavelength by fluorescence excitation. When the fluorescence effects are significant Equation (4) must be modified for calculating composition. The procedure used throughout the three programs is based on Castaing's method modified by Reed:[7]

$$\frac{I_f}{I_a} \quad C_B \cdot J_{(A)} \cdot D \cdot \frac{(\mu/\rho)_A^B}{(\mu/\rho)_B^S} [g(X) + g(Y)] \qquad (5)$$

where C_B is the mass concentration, J_A is a function of the element being analysed, D is a function of the accelerating voltage and difference in atomic number between the element causing fluorescence and the element being excited to fluorescence emission,

$$g[X] = \frac{\ln (1 + X)}{X} \text{ where } X = \frac{(\mu/\rho)_A^S}{(\mu/\rho)_B^S} \cdot \operatorname{cosec} \theta$$

$$\text{and } g[Y] = \frac{\ln (1 + Y)}{Y} \text{ where } y = \frac{\sigma}{(\mu/\rho)_B^S}$$

The mass concentration of an element corrected for both absorption and fluorescence is given by:

$$C_A = K_A \cdot \frac{f(\chi)_A^A}{f(\chi)_A^S} \cdot \frac{1}{1 + (I_f/I_a)} \qquad (6)$$

The atomic number correction, which takes into account the non-linearity in the relationship between K_A and C_A which remains after the other corrections have been applied, is based throughout the programs on the method of Duncumb and Reed.[5] The ability of a target material to slow down incident electrons is described in terms of stopping power, S, which is evaluated from the Bethe formula:

$$S = \text{const} \frac{Z}{A} \cdot \frac{1}{\bar{E}} \cdot \ln \left(\frac{1{\cdot}166\bar{E}}{J} \right) \qquad (7)$$

where Z and A are the atomic number and atomic weight of the element concerned, $\bar{E} = (E_o + E_c)/2$, and J the mean ionisation potential determined empirically from microprobe analysis. Values of the stopping power for E_c electrons for the pure element and sample are calculated from tabulated data of Z/A, $\bar{E}$ and J. Bishop's values of the backscatter coefficient R, as a function of overvoltage ratio E_o/E_c and atomic number for both standard and specimen are used to give at the first iteration the corrected mass concentration of an element, A, thus,

$$C_A = K_A \cdot \frac{f(\chi)_A^A}{f(\chi)_A^S} \cdot \frac{1}{1 + (I_{f(A)}/I_{a(A)})} \cdot \frac{S_{S(A)}}{S_{A(A)}} \cdot \frac{R_{A(A)}}{R_{S(A)}} \qquad (8)$$

The differences between the three programs, designated "standard", "raw" and "normalised" respectively may be visualised from Fig. 1. Until the stage of calculating the absorption correction the measured relative intensities are obtained by calculating the ratio of the sample to standard intensities after the "dead-time" correction has been applied. In the "standard" program the initial estimate of composition of the sample is obtained by normalising (i.e., $\Sigma Ci = 1{\cdot}0$) the relative intensities in order to obtain coefficients for absorption, fluorescence and atomic number. The corrected mass concentration

of an element at the first iteration is obtained by multiplying the measured relative intensities, corrected for dead-time, by these coefficients. The concentrations thus obtained are normalised to 100% as a base for calculating new absorption, fluorescence and atomic number "coefficients" that are subsequently multiplied by the measured relative intensities to give a second estimate of composition. The iteration sequence is repeated ten times. Thus:

$$C_n = K_A \text{ (corrected for dead-time)} \times \alpha \,.\, C_{n-1}$$

where C_n is the concentration of the n^{th} iteration, C_{n-1} is the concentration of the previous iteration and α is a coefficient calculated from the absorption, fluorescence and atomic number correction procedures. The "raw" program did not use "normalisation" (i.e., $\Sigma Ci \neq 1{\cdot}0$) of the measured raw intensities corrected for dead-time (MRIDT). The coefficients for absorption etc. are calculated using the MRIDT for the weight fractions, and are subsequently multiplied by the MRIDT in the iterative sequences. The "normalised" program included the normalising of the MRIDT for calculation of the coefficients for absorption, etc. The first estimate of composition involves multiplication of the *MRIDT normalised* by the calculated coefficients. This result is normalised in turn and the correction coefficients calculated in the iterative sequence to give second and subsequent estimates of concentration. The programs will enable combinations of up to eight elements commonly analysed in electron-probe microanalysis ($Z > 12$) to be corrected simultaneously. With regard to specimens containing combinations of "heavy" ($Z > 12$) and "light" elements ($Z < 12$), e.g., oxides, nitrides and carbides, the correction procedures were intended for analysis of the heavy components, but not of the light elements. Although facilities are now available for qualitative detection of the lighter elements the success of the evaluation procedure depends largely on prior knowledge of the system, and for confidence the tentative results on carbides, etc. should be supported by data from techniques other than microprobe analysis, e.g. X-ray or electron diffraction for confirmation of structure.

Materials and Experimental Detail

A JEOLCO JXA–3A microprobe analyser, with normal incidence of the electron beam, an X-ray take-off angle of 20° and a "dead-time" of 6·5 μsec. was used for the analysis of several high temperature materials. The accelerating voltage used throughout was 25 kV. Phases analysed included: molybdenum disilicide prepared by a hot pressing technique, nickel-aluminium compounds Ni_3Al and NiAl prepared in bulk form, a commercial dispersion-strengthened high temperature material TDNiC (nominal composition Ni–20%Cr–2%ThO_2) and an experimental niobium alloy (nominal composition Nb–5%Mo–10%Ta–10%W–1%Hf–0·5% Zr–0·5%C) and carbide precipitates in a nickel alloy prepared by different routes. These materials were selected for testing because of the range of analytical problems they represented in addition to their technological significance and ready availability. For example the molybdenum disilicide was analysed using K spectra for silicon and L spectra for molybdenum and significant corrections are required for absorption and atomic number effects. Nickel-aluminium compounds are present in most high temperature nickel alloys used in aircraft gas turbine engines and from the microanalysis viewpoint the high X-ray absorption coefficient of Al in Ni results in extremely low values for the measured raw intensity of Al in the nickel aluminium compounds (see Table I). The TDNiC material was used as a convenient reference and involved the use of K spectra for both Ni and Cr, the ThO_2 component was not analysed. The nickel alloy samples, chosen at random, were prepared by different processes; conventional casting in a shell mould to produce an equiaxed grain structure and directional solidification to produce a grain structure with a preferred orientation. Carbide precipitates in the respective samples were found to be significantly different in composition. Microanalysis was carried out using K spectra for Cr, Co and Ni; and L spectra for W. Carbon was detected using a lead stearate crystal. The niobium alloy, developed under Mintech contract, was analysed by the microprobe because conventional analysis of Nb and Ta in combination is difficult and results are normally quoted as (Nb + Ta)%. The alloy was analysed in carbide-free zones for the four principal refractory elements using L spectra throughout.

Discussion of Results

The results arising from the three programs are listed in Table I which includes a comparison of using the mass absorption coefficients listed by Birks and Heinrich, respectively, for the same measured raw intensities of the elements. The data refers to the corrected composition evaluated at the fifth iteration as no significant changes in composition occurred above this. In general the data tended to converge in all instances after the second iteration.

Examination of Table I shows that the measured "raw" concentrations of both molybdenum and silicon in the bulk molybdenum disilicide are low, relative to the appropriate stoichiometric concentrations. The "standard" program using Birks' mass absorption coefficients (MAC) gives a silicon concentration [Si] 1·1% low and a molybdenum concentration [Mo] 5·4% low. Using Heinrich's MAC both [Si] and [Mo] are even lower. The "raw" program and "normalised" program data yield unacceptably low and high values, respectively, for both [Si] and [Mo], irrespective of which of the two sets of MAC are used. However for any of the programs if the [Si] and [Mo] at the fifth iteration are normalised (i.e., $\Sigma Ci = 1{\cdot}0$) both [Mo] and [Si] agree to within 2% of their stoichiometric proportions.

Examination of the raw intensity data for Ni_3Al reveals the aluminium concentration (2·5% detected) to be very low and the nickel to agree to within 1% of the bulk analysis figures. The "standard" program using Birks' and Heinrich's MAC, respectively, yields [Al] to be 4·5% and 0·6% low to the bulk analysis data, whilst the [Ni] is 1·5% and 2·1% high in each instance. Reference to the "raw" program data for Ni_3Al using Birks' MAC yields an [Al] 5·0% lower whilst the [Ni] is 1·2% high. Under the same conditions using Heinrich's MAC the [Al] is 0·2% low and the [Ni] 2·3% high. Examination of "normalised" program data for Ni_3Al for both Birks' and Heinrich's MAC shows the [Ni] to be unacceptably high whilst significant differences occur in the [Al]. The effect of normalising the data at the fifth iteration for any of the programs gives better agreement between the microprobe and bulk analysis data using Heinrich's rather than Birks' MAC.

The measured intensity data for NiAl shows the [Al] to be a factor of approximately four times lower than the bulk concentration, whereas the [Ni] is less than 1% low. Examination of the "standard" program data using

TABLE I.—RESULTS OF CORRECTION PROCEDURES

Material		$MoSi_2$		Ni_3Al		NiAl		'TDNiC'				Nickel Alloy Carbide (equiaxed)				Nickel Alloy Carbide (directionally solidified)				Niobium Alloy			
Nominal Composition of Bulk Material (%)		Si 36·8	Mo 63·2	Al 13·3	Ni 86·7	Al 34·4	Ni 65·6	Cr 21·4	ThO_2 (2·4)	Ni 76·2		Cr	Co	Ni	W	Cr	Co	Ni	W	Nb	Mo	Ta	W
												Not Determined				Not Determined				Bal	5	10	10
Electron Probe Microanalysis Measured Raw Concentration (%)		24·2	36·9	2·5	87·8	8·9	64·7	23·2	(ND)	76·2		26·6	2·3	23·6	33·3	22·2	1·0	12·7	40·0	49·8	2·1	9·5	11·1
'Standard' Program Corrected Concentration at 5th Iteration	Using Birks' MAC	35·7	57·8	8·8	88·2	27·3	67·0	23·1	(ND)	79·5		28·2	3·5	21·4	42·4	23·3	1·0	12·5	48·3	54·9	2·5	10·9	12·9
	Using Heinrich's MAC	34·5	57·1	12·7	88·8	37·0	67·9	23·6	(ND)	79·8		28·5	3·5	21·3	41·9	23·6	1·0	12·4	47·9	67·9	2·9	11·2	13·3
'Raw' Program Corrected Concentration at 5th Iteration	Using Birks' MAC	26·8	42·7	8·3	87·9	24·6	66·3	23·2	(ND)	79·9		27·6	3·4	21·0	41·8	21·7	0·9	11·9	46·2	42·1	1·9	10·2	12·2
	Using Heinrich's MAC	25·1	40·1	13·1	89·0	40·9	68·6	23·8	(ND)	80·3		28·0	3·5	20·9	41·4	22·1	1·0	11·9	46·2	62·0	2·6	11·0	13·1
'Normalised' Program Corrected Concentration at 5th Iteration	Using Birks' MAC	63·6	103·2	9·9	99·4	38·4	94·2	23·9	(ND)	82·1		34·3	4·3	26·0	51·6	31·5	1·4	16·9	65·3	76·6	3·5	15·2	18·0
	Using Heinrich's MAC	61·6	101·8	14·3	100	52·1	95·4	24·4	(ND)	82·4		34·7	4·3	25·9	51·0	31·9	1·4	16·8	64·8	94·7	4·0	15·7	18·6

Birks' MAC shows the [Al] to be 7·1% lower and the [Ni] 1·4% higher than the bulk concentration. Using Heinrich's MAC for the same conditions the [Al] is 2·6% high and the [Ni] 2·3% high. Reference to the "raw" program data shows the [Al] to be extremely low and 6·5% high using Birks' and Heinrich's MAC, respectively. For the same conditions the [Ni] is 0·7% and 3·0% high, respectively. The results for both [Al] and [Ni] in the "normalised" program are significantly higher than the bulk analysis figures irrespective of which MAC data are used. The effects of normalising the data at the fifth iteration for any program using Birks' MAC lead to poor agreement between the microprobe and bulk analysis data, whereas the maximum disagreement in [Al] using the same procedure and Heinrich's MAC occurs in the "raw" program.

The measured raw intensity data on the TDNiC specimen show the [Cr] to be 1·8% high whilst the [Ni] from the microprobe agrees with the bulk analysis data. From the standard program using Birks' MAC the [Cr] at the fifth iteration is 1·7% high and the [Ni] 3·3% high relative to the bulk analysis data. For the same conditions using Heinrich's MAC the [Cr] is 2·2% high and the [Ni] 3·6% high. The effects of normalising the data at the fifth iteration using either set of MAC lead to agreement within 1·0% of the actual concentrations between microprobe and bulk analysis data for both elements. Examination of the data for both [Cr] and [Ni] at the fifth iteration using either set of MAC in both the "raw" and "normalised" programs shows increasing disagreement between microprobe and bulk analysis results. However, normalising these data at the fifth iteration gives agreement to within 1·0% for both [Cr] and [Ni].

There are no comparative bulk analysis data available for the carbide phase in the nickel alloy cast by either process. However, assuming the microprobe data refer to an $M_{23}C_6$ phase in the "equiaxed-cast" nickel alloy the sum total concentration of the metallic elements, fifth iteration "standard" program using both Birks' and Heinrich's MAC is of the right order of magnitude: 95·5% and 95·2%, respectively. Comparison of the individual data for the metallic elements under the same conditions for the "raw" and "normalised" programs shows their numerical value to differ, but the ratio of their composition remains sensibly constant.

Examination of the measured intensity data for the elements in the directionally-solidified alloy shows the sum total of the metal concentration to be similar to that of the "equiaxed" carbide. However, the sum total concentration at the fifth iteration "standard" program, using either Birks' or Heinrich's MAC is only 85%, compared to 95% in the case of the "equiaxed" carbide. X-ray diffraction studies have shown the carbides to be "different", although they have not been characterised in the two cases. The sum total concentration of the metallic elements is sufficiently high if the phase is an MC-type carbide but low if it is an $M_{23}C_6$ type. No significant differences occur in the analysis results for the four elements using either set of MAC. The "raw" and normalised program data give differing numerical values for the concentration of the elements at the fifth iteration, but the ratio of the composition remains sensibly constant.

The sum total of the measured intensity data for the elements in the niobium alloy is low relative to the nominal bulk analysis data, and although the [Ta] and [W] appear to correlate with their nominal bulk concentration, the [Mo] and [Nb] appear low. The microprobe data refer to measurements at ten areas across the specimen in carbide-free zones (the alloy containing 1%Hf, 0·5%Zr, 0·5%C for carbide dispersion strengthening). From the "standard" program, fifth iteration, using Birks' MAC the sum total concentration of the elements is 81·2% and the [Nb] seems rather low. Using Heinrich's MAC the sum total concentration is 95·3% and the [Ta] and [W] appear high (although the latter has been determined at 10·8% by wet chemical analysis) and some Nb and Mo may combine with the Hf and Zr as a complex carbide. Comparison of the fifth iteration data, Birks' MAC for the "raw" and "normalised" programs shows the numerical value of the concentrations of the elements to differ according to the program type. The ratio of their concentrations also differs. Using Heinrich's MAC the numerical values of the element con-

centrations vary with the program type, but their ratios remain fairly constant.

Conclusions

From the three correction procedures examined, the "standard" program, in which the composition of a material is estimated by normalising the measured relative intensities of the constituents in order to obtain correction coefficients for absorption, fluorescence and atomic number, tended to give the best agreement between microprobe and bulk analysis results for: molybdenum disilicide, two nickel-aluminium compounds and a commercial dispersion-strengthened nickel alloy. The use of Heinrich's (rather than Birks') X-ray mass absorption coefficients tended to give better agreement between the microprobe and bulk analysis data. Data were evaluated for two carbide phases in a nickel alloy, and an experimental niobium alloy was analysed for four elements including tantalum.

Acknowledgments

The author gratefully acknowledges the assistance of Dr. K. N. Dodd, of Royal Aircraft Establishment, Farnborough with the computer programming and Mr. A. J. Hewins for the data tape punching.

REFERENCES

1 J. D. Brown, "Comprehensive Computer Programme for Electron-probe Microanalysis", *Analytical Chemistry*, 38 (7), 890 (1966).
2 M. G. Hobby and G. C. Wood, "Computer Correction of Raw Electron-probe Microanalysis of Alloys and Oxides", *Laboratory Methods*, LXXV (449), 143 (1967).
3 S. S. So and H. R. Potts, "Computer Programs for Quantitative and Semi-quantitative Analysis with the Electron-Microprobe Analyser". *J. Electrochem Soc.*, 115 (1), 64–68 (1968).
4 R. Castaing, Ph.D.Thesis, Paris University, (1951).
5 P. Duncumb and S. J. B. Reed, "The Calculation of Stopping Power and Backscatter Effects in Electron-probe Microanalysis", Quantitative Electron-Probe Microanalysis, National Bureau of Standards Special Publication 298 (1968). Editor, K. F. J. Heinrich.
6 J. Philibert, "A Method for Calculating the Absorption Correction in Electron-probe Microanalysis. X-ray Optics and X-ray Microanalysis", p. 379, Pattee *et al.*, Editors, Academic Press (1963).
7 S. J. B. Reed, "Characteristic Fluorescence Corrections in Electron-probe Microanalysis", *Brit. J. Appl. Phys.*, 16, 913 (1965).

Digital Conversion of Analogue Signals

NEW instrumentation introduced by Ether, Ltd., Caxton Way, Stevenage, Herts., for industrial process-control applications, enables many operations at present performed by analogue instruments to be performed digitally. The basic unit is the Type 8500 Digital Indicator, which accepts analogue signals from such sensor elements as thermocouples, resistance thermometers, strain-gauge transducers and load-cells, digitises and displays them on four neon numerical indicator tubes. The indicated value in binary coded decimal is also made available externally for control purposes or for print-out.

The instrument will accept any D.C. millivolt signal, and an important feature is that this signal need not be related linearly to the quantity (temperature, pressure, flow, etc.) that it represents. For each type of sensor element, individual 'characterising' circuitry is provided to carry out the necessary conversion. This circuitry works, in principle, by dividing the non-linear graph representing the relationship between, for example, millivolts and temperature into a number of short sections, each of which individually can be considered linear within the accuracy required. Poor resolution at the lower end of the scale (as exhibited by many analogue instruments) is thus eliminated, and the full range of output of the sensor element can be utilised.

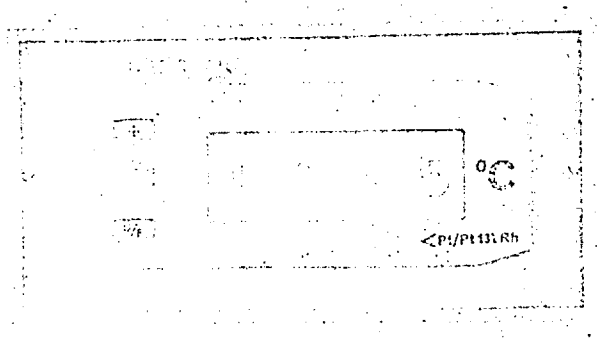
Setting Limits

The output from the indicator can be monitored by 'set-point' units which provide logic output and relay contact signals whenever pre-set limits are reached. The Type 8551 single-channel unit enables one upper or lower limit to be set, while the Type 8552 double-channel unit provides two such settings. These may be an upper and a lower limit, or two upper or two lower. For example, corrective action might be initiated at the first limit, followed by complete shutdown if the second is reached. The limits are set in digital form by means of thumb-wheel switches. Manual or automatic cancellation of the output signals can be provided.

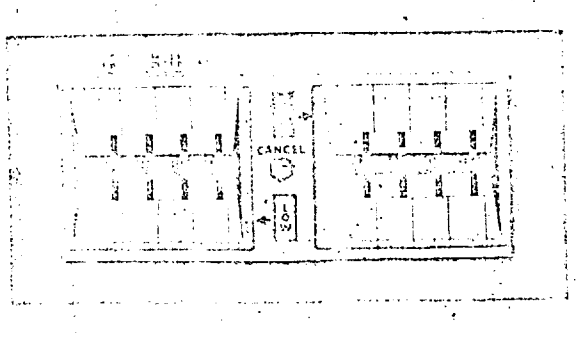
Multiple Indication

The indicator itself can be used to display signals from any number of sensor elements of the same type—for example, thermocouples. A push-button selector enabling up to 42 sensors to be supervised in this way can be supplied. The indicator can also indicate parameters of two different kinds in quick succession—for example, temperature and flow-rate or temperature and pressure. Here a push-button switches from one 'characterising' circuit to the other.

In conjunction with standard thermocouples, the instrument measures temperature with an instrument



Type 8500 digital indicator.



Type 8552 double channel unit.